Politecnico di Milano

Department of Physics

Photoactive polymer systems in aqueous environment: from the 2D to the 3D space

Gabriele Antonio Giuseppe Tullii

Ph.D Dissertation
Doctoral Programme in Physics – XXX cycle

Supervisor: Dr. Maria Rosa Antognazza
Tutor: Prof. Guglielmo Lanzani
Coordinator: Prof. Marco Finazzi

2014-2018

Index

Summary

In the latest thirty years semiconducting polymers have been extensively investigated for their optoelectronic properties, reaching in many cases the performance required for commercial applications. Only more recently, they started to attract attention also for devices requiring the exposure to an aqueous environment. Several application fields have been emerging, ranging from photo-electrochemistry to bioelectronics, given the possibility to exploit their optoelectronic properties in saline electrolytes, together with their biocompatibility and their inherent softness and conformability. In particular, systems based on regio-regular poly-hexyl-thiophene (rr-P3HT), a work-horse material for photovoltaics, have been profitably employed for (i) the fabrication of photo-electrochemical cells and for (ii) the modulation of the activity of living systems. In the first case, the creation of free charges upon polymer semiconductor photo-excitation has been successfully employed to sustain reduction/oxidation processes at the polymer/electrolyte interface. In fact, the energy alignment at the polymer/electrolyte interface is favorable for both oxygen and proton reduction reactions, thus allowing the application of rr-P3HT in optically driven oxygen sensors and in photocathodes for hydrogen reduction and water splitting. In the second case, the use of conjugated polymers as photoactive transducers at the interface with living systems is very promising, since it bears the opportunity to trigger the biological component simply by light, without any need for viral transfection. Polymer-mediated optical modulation guarantees high spatial and temporal resolution and minimal mechanical stress on the cells, as compared to standard electrical stimulation methods. rr-P3HT was demonstrated to efficiently modulate a number of biological models *in-vitro*, for instance by inducing depolarization/hyperpolarization in secondary line cells, firing/silencing of neurons in single cells, brain slices, explanted retinas, and activating temperature-sensitive channels in human cells. The same material was also at the base of the realization of a fully organic, implantable retinal prosthesis that led to the long-tern recovery of light sensitivity and visual acuity in visually-impaired animal models.

In this scenario, the detailed characterization of hybrid interfaces between conjugated polymers, saline electrolytes and living cells plays a crucial role, since a deep understanding of the processes involved is the only key to further improve the performance of polymer-based devices and to fully uncover all their application potential. In particular, this thesis work is focused on the study of the influence of the device structure engineering with the interfacial properties of bio-organic interfaces established between rr-P3HT photoactive platforms and living cells.

The dissertation starts with a detailed investigation of the electrochemical phenomena occurring at the planar rr-P3HT/electrolyte interface, in dark and upon light excitation. We show that the ITO/P3HT device presents a photoinduced capacitive collection of positive charges at polymer surface balanced by negative electrolyte ions, i.e. the Helmholtz double layer formation. We then investigate the influence of the device structure engineering on the interfacial phenomena by considering two main strategies: (1) implementation of rr-P3HT-based planar devices with charge selective materials; (2) engineering of the rr-P3HT/electrolyte interface morphology, without introducing additional materials.

We demonstrate that by following the first approach it is possible to control the sign of the charges collected at the device surface after photoexcitation. We present the modification of the ITO/P3HT configuration with an evaporated electron selective layer (ESL) of Phenyl-C61-butyric acid methyl ester (PCBM) partially intercalated within the rr-P3HT bulk, achieving a p-type/i-type/n-type (p-i-n) configuration. This device implementation leads to a collection of electrons instead of holes on top of the device surface, revealed by electrochemical measurements. We explore also different configurations comprising both hole and electron selective layers (HSL and ESL respectively) interfaced with the photoactive material, demonstrating that this has dramatic impact on the efficiency of charge transfer phenomena occurring at the device/electrolyte interface. In particular, we present the development of highly efficient hybrid organic/inorganic photocathodes for hydrogen evolution, constituted by rr-P3HT:PCBM active layer sandwiched between copper iodide (CuI) HSL and

2

titanium dioxide (TiO$_2$) ESL and coupled with a Pt catalyst. We show that this device architecture allows to achieve hydrogen evolution reaction (HER)-associated photocurrents up to 7.1 mA cm^{-2} at 0 V vs. RHE and an onset potential for HER equal to 0.702 V with 100% faradaic efficiency. Furthermore, we interface multilayered architectures with human embryonic kidney (HEK)-293 cells. The different fabricated configurations, comprising the rr-P3HT active layer alone or coupled with both CuI and TiO$_2$ or with PCBM only, are tested as photoactive platforms for the optical excitation of this cell line. By carrying out patch clamp recordings of HEK-293 grown on top of the different devices upon light stimulus, we show that there is a direct correspondence between the sign of the device optically-induced surface charging and the cell membrane response, in terms of electrical potential variation.

Regarding the second strategy (morphology engineering), we develop a light-sensitive mesoporous rr-P3HT/electrolyte interface by taking advantage of an all-solution fabrication procedure and we compare it with the correspondent planar topography. Interestingly, the mesoporous structure induces two orders of magnitude increase in the polymer/electrolyte interface surface area and this increment strongly affects the interfacial dynamics at the polymer surface in contact with the electrolyte. In particular the morphological change leads to an increased efficiency of the photo-induced O$_2$ reduction, and an inhibition of the capacitive charging at the rr-P3HT/electrolyte interface that instead dominates in the case of the flat configuration. In addition, we demonstrate that the mesoporous photoactive platform is fully bio-compatible and that HEK-293 cell population cultured on top of the polymer surface fully preserves its biological functionality. However, based on the comparison between the results obtained by patch clamp recordings with cells and surface potential measurements without cells, the electrical coupling between device and cells remains scarce.

Accrodingly, the dissertation continues with the description of a strategy for the enhancement of the electrical coupling between the photoactive platforms and living cells, based on the tightening of the cellular adhesion by using rr-P3HT microstructures. We present the successful fabrication of high

aspect ratio rr-P3HT micropillars of conical shape, by coupling the femto-second micromachine and the push-coating technique. We show that polymer pillars can be used as highly biocompatible substrates for both primary cortical neuronal cells and HEK-293 cells. From scanning electron microscopy (SEM) images we see that the adopted shape and density of polymer pillars leads to establish a close contact with both HEK-293 and neuronal cell membrane, with a localized thinning of the cell membrane, without however negatively affecting cells viability and also the neuronal intrinsic electrophysiological properties and synapses expression. Interestingly, we observe a remarkable change in the morphology of HEK-293 cells, showing a pronounced tendency to develop in the three-dimensional space when interfaced to rr-P3HT pillars. However, by performing patch clamp recordings upon light excitation we do not observe a clear benefit in terms of signal transduction coming from the tight cellular adhesion achieved. We attribute it to a reduced charge dissociation efficiency in proximity of the pillar top structures, due to the polymer thickness, much higher than in the case of polymer substrates.

Furthermore, in-view of in-vivo applications, we explore the use of micro- and nano-patterned silk/P3HT substrates as antifouling surfaces, able to sizably hinder the bacteria adhesion. We develop different nano- and micro-structured silk substrates, presenting micro-wells or nanogrooves on their surfaces, following a simple, inexpensive and high throughput, soft lithographic fabrication procedure. Interestingly, we observe that all considered patterns, both rr-P3HT-covered and uncovered, efficiently inhibit the adhesion of E.Coli bacteria without affecting the proliferation of HEK-293 cells.

Finally, we study, for the first time, the interaction of rr-P3HT with plant systems. In particular, we interface rr-P3HT thin films and nanoparticles (NPs) with plant cells. We study the effects induced by the rr-P3HT photo-excitation on the intracellular calcium ion dynamics of *Arabidopsis Thaliana* leaves guard cells. It is widely recognized that calcium ions flux plays a central role on cellular signaling, acting both as a signal transducer and as a second messenger. We find a remarkable and

reversible down-regulation of the spontaneous guard cells cytosolic calcium oscillations, directly related to the illumination of the photoactive polymer in form of nanoparticles. Given the strict relation between the activity of this type of cells and the stomatal functions, we investigate the effects of rr-P3HT NPS photoexcitation on the stomatal aperture. Interestingly, we find a deterministic relationship between polymer NPs light excitation and inhibition of the stomatal opening. Furthermore, in-view of applications at systemic plant level, we verify the rr-P3HT NPs uptake by *Arabidopsis Thaliana* seedlings roots by performing confocal imaging experiments, finding that NPs are efficiently internalized within the roots tissue.

In conclusion, in this thesis the characterization of the interfacial properties between different rr-P3HT-based systems, aqueous electrolytes and living cells is presented. Proper engineering of the device structure reveals to be key for successfully targeting specific applications within biology and energy fields Some examples are successfully demonstrated here, but many others remain to be discovered and fully characterized in view of practical applications.

1. Stimulation and recording of biological functions: the role of conjugated polymers

1.1 Electrical methods for stimulation and recording

The possibility to control or implement the biological functions of the human body with electricity has attracted the mankind since the ancient times, when people from Greece and Egypt exploited the electricity produced by Catfishes and eels in pain therapy treatments and for improving blood circulation [1]. Later, in the middle of 1600s Jan Swammerdam laid the basis of experimental electrophysiology, triggering the contraction of frog leg muscles by inserting needles inside the adherent nerves [2]. However, he did not explain the mechanism by which the nerves transduce the external stimuli. At the end of the 17th century, Luigi Galvani examined in depth the contraction of frog muscles, by improving the experimental set up. He discovered the electrical nature of the signal propagation between nerves and muscles, developing the theory for the electrical stimulation [3]. Starting from the pioneering experiments made by Galvani, a huge number of studies and methods for the control of the bioelectricity rapidly came out, allowing the excitation and recording of living tissues and singles cells activity both intracellularly and extracellularly [4]. The electrical techniques are widely consolidated and they are employed for a large variety of applications in-vivo and in-vitro [1], since they have the clear advantage of dealing with signals of the same type of the bioelectrical ones. The first examples of electrodes for the intracellular stimulation and recordings were sharp metal or glass electrodes with sub-micrometer size tip, required for minimizing the mechanical stress on the cells and the current leakage at penetration site [5–7]. Recently metal nanoelectrodes have been proposed, sensibly reducing the device invasiveness [8]. However, the small dimension increases also the impedance of the contact, leading to a very low signal to noise ratio (SNR) [1,8]. An important step forward was made by Neher and Sakmann between the end of the 1970s and the beginning of the 1980s, with the development of the patch clamp technique [9]. This method rapidly became the electrophysiology gold standard, since it allows to study the activity of both single ion

channels and entire cells, using a glass micropipette electrode with an aperture size in the range of 1-2 µm, allowing to perform measurements with a much lower background noise as compared with previously employed electrodes. The pipette is placed in contact with the membrane of the cells adhered to the samples surface, using a micromanipulator coupled with an optical microscope. By applying a suction, it is possible to establish a close contact between a membrane patch and the pipette tip (the so-called giga-seal), thus allowing the study of single ion channels. By applying an additional depression to the pipette tip, it is possible to selectively remove the cellular membrane portion in contact with the tip, making the pipette interior in direct contact with the cell cytoplasm. In this configuration (Whole-cell configuration) the micropipette electrode is filled with an electrolytic solution that resembles the cell cytoplasm and it is possible to study the average response of the entire cell. Both in the intracellular and extracellular cases, the cells activity can be recorded in potentiostatic (voltage clamp) or galvanostatic (current clamp) configurations, measuring respectively the potential difference and the current flowing across the membrane with respect to a reference electrode placed inside the extracellular bath. Additionally, electrical stimulation can be performed simultaneously by injecting intracellular currents, making this method highly versatile [10]. Patch clamp, however, presents also four main drawbacks: (1) this technique is very powerful for the study/stimulation of single cells but not for the study/stimulation of multiple cells, since it is possible to address one or few cells at a time; (2) The viability of the patched cells is limited to less than one hour; (3) the use of micrometer-size electrode is associated with impedance-related reduced SNS; (4) the flow of the electrode inner solution inside the cell interior induces the dilution of the cytoplasm [8,11,12].

These limitations can be overcome by employing devices for the extracellular recording and stimulation. In general, extracellular techniques are less invasive, offering the possibility to study cells and tissues for a longer time, up to several months [12]. The traditional extracellular bioelectronic devices are based on metals and inorganic semiconductors. One of the first architecture employed are the Multi electrode arrays (MEA) allow to come over the first two aforementioned

patch-clamp limitations. These devices are composed by a large number of planar electrodes distributed in defined highly ordered geometries and give the possibility to address a large number of cells at the same time. These devices were firstly employed for interfacing cells by Gross et.al in 1977 [13,14], and were used extensively for dual stimulation and recording, both in-vivo and in-vitro [15]. At the moment, MEAs with more 10000 electrodes are employed in in-vitro studies [16–18]. Regarding *in-vivo* studies, it is worth to mention Neuropixels probes, employed for the in-vivo recording of the brain activity [19]. The striking characteristic of these devices is represented by large number recording sites (960) comprised in a single shank that can be selectively addressed by 384 recording channels. The porous TiN single electrodes, characterized by low impedance and high stability in aqueous environment, allowed the long-term investigation of large populations of neurons from different brain segments of freely moving rats.

Field effect transistors (FET) have also been employed for the extracellular recording of the cellular activity [20]. in this configuration, the current flowing from source to drain is modulated by the extracellular potential of the cells that act as the gate signal of the transistor. The key advantage related to the use of these devices is the possibility to completely overcome the impedance-related problems, since the signal transduction mechanism involved in the recording process using FETs does not rely on charge transfer [11].

1.2 Conjugated polymers-based electrical methods

The use of inorganic materials for the fabrication of devices for bioelectronics presents different advantages that rely on their excellent electrical properties and to the possibility to exploit the standard lithographic techniques for their fabrication, leading to a large variety of sizes and shapes, allowing for many possibilities in terms of recording and excitation [12]. However, the mechanical and the chemical mismatch between these rigid abiotic components and the soft biological counterparts represents a limit for in-vivo applications, since it can lead to increased inflammatory

responses from the tissues. For this reason, organic materials have attracted a lot of interest in the bioelectronics field, since they are generally softer and present a better biocompatibility as compared to metals and inorganic materials. Moreover, they can be easily chemically functionalized for achieving additional functional properties [21,22]. In particular, conjugated polymers (CPs) have been extensively employed for bioelectronic applications, mainly for lowering the electrodes impedance and in devices that exploit their dual electronic and ionic conductivity [23]. Regarding the former application, polypyrrole (PPy) and poly(3,4-ethylenedioxythiophene) (PEDOT) have been used in the vast majority of reports [24–29]. PEDOT was generally preferred for its higher stability [30], thus becoming the workhorse material in bioelectronics applications. Inorganic MEAs covered by electropolymerized PEDOT allowed to achieve higher charge injection limit and SNR during long-term in-vivo stimulation and recording, as compared to the uncovered electrodes [24,25,31]. The ease of processability of PEDOT was exploited for locally restoring the charge transport properties of brain tissues after the formation of glial scars due to metal implants. Martin et. al. demonstrated that PEDOT can be electrodeposited directly around metal electrodes implanted inside neural tissues of animal models, lowering the system impedance without impairing the brain functions [32,33]. The other fundamental property of CPs, that had a crucial impact in biological applications, is the ionic conductivity [21]. The latter depends mainly on the morphology and on the type of the counter ion employed for counterbalancing the charge during polymerization [34]. In the case of PEDOT, the most employed counterion is poly(styrene sulfonate) (PSS) that confers to the final material, PEDOT:PSS, an enhanced level of swelling. This increases the ionic penetration and mobility within the material bulk. This characteristic was exploited in organic electrochemical transistors (OECTs) [21,23]. The peculiarity of this class of transistors is that the electrolyte acts as gate electrode and the conductivity of the organic semiconductor is modulated by the percolation of the electrolyte ions inside the material. This leads to a 3D modulation of the active material conductivity, conferring to OECTs a better sensitivity as compared to FETs. Besides many excellent reports of *in-vitro* applications, he Malliaras' group was the first to translate this technology *in-vivo*, employing ultra-

flexible OECTs for recording low-amplitude brain activities in animal models for epilepsy. Superior signal-to-noise ratio in comparison with standard surface electrodes was demonstrated [35].

1.3 Optical stimulation and recording

The possibility to modulate and record the biological functions with light is attracting a lot of interest since it allows to overcome several drawbacks related to the use of standard electrical techniques. First of all, the use of optical methods is expected to be less invasive, since light, at specific wavelength and intensities, can be delivered through living tissues without requiring physical contact or wiring [36,37]. Furthermore, the use of light allows to address specific subcellular compartments with higher spatial and temporal resolution as compared to electrical techniques, and it confers more flexibility in terms of stimulation and recording, since its shape can be varied in real time for obtaining different excitation and recording geometries. However, the use of optical tools is complicated by the light insensitivity displayed by the vast majority of living cells. Different types of transducers have been developed, both for monitoring and exciting the bioelectrical activity [37,38]. Regarding the recording techniques, the use of fluorescent indicators is now largely accepted and employed. The transmembrane potentials variations can be investigated by employing fluorescent molecules that present a strong dependence of the light emission from the presence of an external electric field [39,40]. By monitoring their emission is then possible to quantify the membrane potential oscillations. The early examples of this kind of systems are voltage sensitive dyes (VSDs) [40], generally characterized by a low sensibility, due to an aspecific staining of the cells compartments. More recently genetically encoded voltage indicators (GEVIs), allowing the precise targeting of the subcellular components, have been proposed [41]. The living cells activity can be optically assessed by monitoring the concentration of molecules directly involved in cellular processes. The calcium ion is the most significant example, given its central role on cellular signaling, acting both as a signal transducer and as a second messenger. Calcium-sensitive dyes displayed a high sensitivity, sufficient for recording the variations due to the opening of a synaptic spine single calcium channel [42,43].

The optical stimulation of living cells can be performed by taking advantage of four main strategies: (1) introduction of genetically expressed light sensitive actuators in the cell structure (figure 1.1 a); (2) thermal stimulation induced by infrared radiation (IR) (figure 1.1 b); (3) optical bio-modulation mediated by photoactive molecules (figure 1.1 c); (4) light sensitive solid-state devices (figure 1.1 d). Regarding the first category, the possibility to transfect cells with light sensitive ion channels was firstly proposed by Boyden et. al. [44] in 2005, laying the basis of optogenetics (figure 1.1 a). By using this technique both neural activation and inhibition was obtained, together with receptor-initiated biochemical signalling pathways [45]. The great advantage of optogenetics corresponds with the high transfection selectivity, allowing the study of the activity of small population of cells inside complex biological tissues. The main drawbacks are related to the safety risks associated with need for viral transfection and to the immune response of the host system due to the expression of heterologous proteins [46].

The stimulation of cells using IR is based on the change of the bioelectrical parameters induced by the local temperature increase due to the water IR absorption (figure 1.1 b). It was firstly employed by Wells et. al. [47] for the in-vivo excitation of the nerves and muscles of frogs and rats. Later, the same technique was employed for the depolarization of HEK cells and Oocytes [48] and photoactivation of neurons [49,50]. This approach is very simple, since no biochemical alteration of cells is needed, and may have important applications, for instance in the thermal treatment chronic pain. However, there are some issues that limit its application in medicine. In particular, cells may be damaged by the high radiation intensities required and it is not possible to have an optimal control on the excitation volume [37,51].

Another method for the optical excitation of cells activity exploits the property of molecular photoswitches or photo cleavable compounds, molecules that present a variation in their structure/functionality upon light exposure (figure 1.1 c) [52]. Systems in the former category usually comprise an azobenzene unit and show reversible cis-trans isomerization. By using these compounds, it is possible to target specific cellular components like ion channels, transporters and pumps, G

protein-coupled receptor (GPCRs), enzymes and elements of the cytoskeleton [52]. In the case of ion channels, a control of the cells membrane potential can be achieved. The acrylamide-azobenzene-quaternary ammonium (AAQ) is an example of this class of molecules that have been employed for the recovery of light sensitivity of blind rat retinas[53]. Photo cleavable molecules are composed by a functional molecule, like a neurotransmitter or enzyme, encapsulated inside a photolabile cage compound. The exposure to a certain wavelength allows the selective release of the inner molecule [54–56]. The application of both these classes of compounds is limited by the fact that the most part of them requires UV irradiation that can damage the biological matter after prolonged exposure and it is characterized by limited penetration trough living tissues. For this reason current efforts are focused on the development of a second generation of molecules with red-shifted absorption [52,57].

The last type of transducers are solid state devices for the extracellular optically-mediated stimulation of living cells and tissues (figure 1.1 d). This category includes different kinds of devices based on both inorganic and organic semiconductors. The state of the art in this field is presented in detail in the next paragraphs.
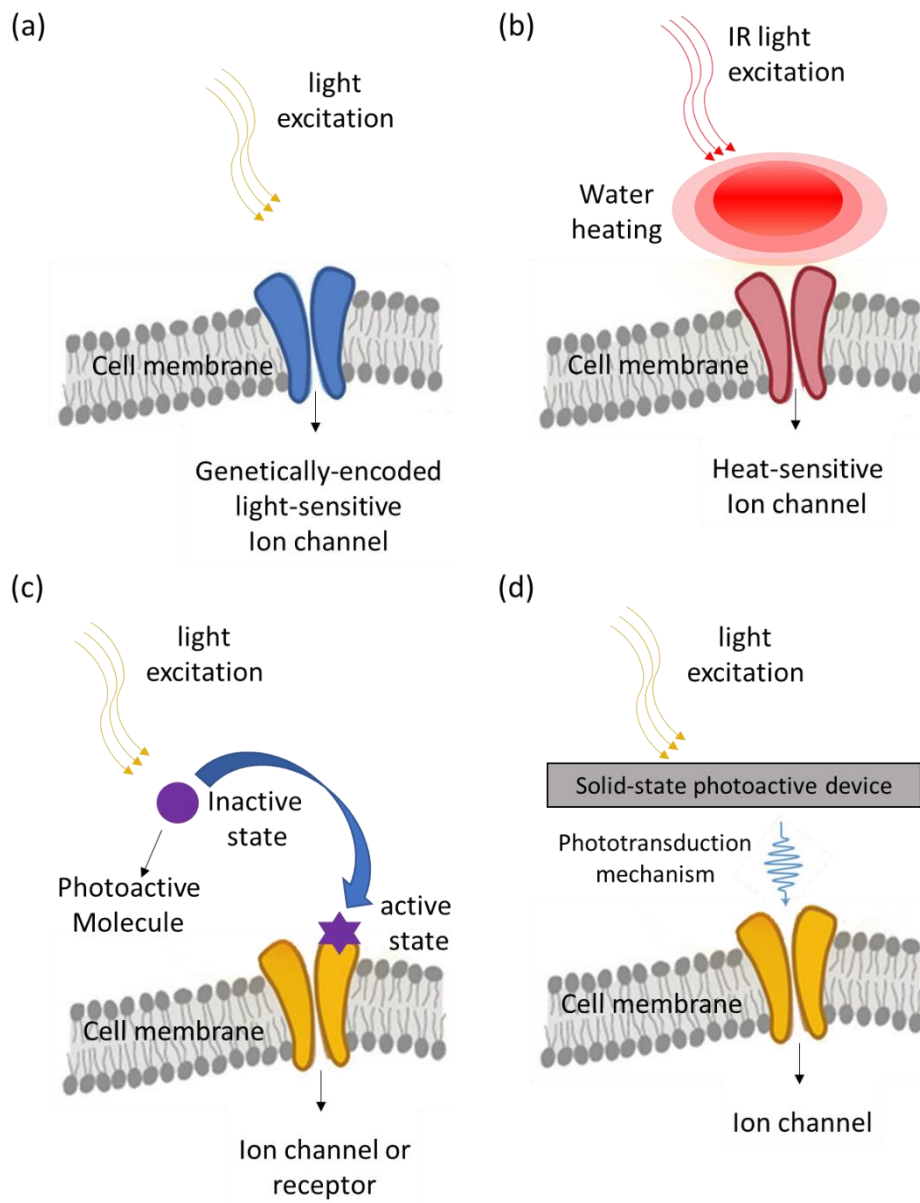
Figure 1.1. Schematic representation of the optical stimulation of living cells performed by genetically expressing light sensitive ion-channels in the cell structure (optogenetics) (a), by inducing a local temperature increase with IR light excitation (b) and by interfacing cells with photoactive molecules (c) or solid-state devices (d).

1.4 . Optical stimulation mediated by flat silicon-based devices

The first examples of photovoltaic devices for the optical modulation of the biological activity were based on oxidized silicon. The bioelectrical properties of primary nerve cells on top of this material were firstly investigated by Fromherz et. al. [58–61], who proposed an electrical model for the device/cell interface and demonstrated that by using a passivated layer of silicon it is possible to

13

perform an electrical capacitive stimulation, excluding the contribution of faradaic phenomena and electroporation of the cellular membrane. Later, Colicos et. al. [62] proposed for the first time the possibility to exploit the optically induced change in conductivity of silicon for the excitation of primary hippocampal neurons. In this configuration a p-type silicon wafer, covered by thin (2 nm) SiO_2 layer, was maintained at a constant bias with respect to a reference electrode in the bath. The illumination promotes the electron migration at the cell/device interface, and the bioelectrical activity of the neurons grown on top is then elicited capacitively by the established voltage gradient in the electrolyte solution [62]. More recently, the same technique was employed by the same group for the study of the correlation between the neuronal and astrocyte activity and the microglia formation [63]. Regarding in-vivo applications, Palanker et al.[64] developed a retinal prosthesis based on silicon photodiodes. The system is composed by a video camera that acquires the images from the environment, a small-size computer that processes the images, and a photodiode array, implanted in subretinal position. The photocurrent elicited in the silicon pixels is then transferred to iridium oxide electrodes that transfer the excitation to the retina. Since the size of the pixels is fixed by design, this device does not benefit of the increased spatiotemporal resolution associated to optical methods, but only avoids the use of the wires necessary for performing the electrical stimulation.

All the approaches presented in the current paragraph suffer from the lack of biocompatibility provoked by material stiffness, already discussed in section 1.2. In order to overcome this problem, solid state devices based on organic semiconductors have been developed.

1.5 . **Planar solid state rr-P3HT-based devices for the optical stimulation of living cells**

Conjugated polymers, as previously discussed, allow to achieve several advantages as compared to the inorganic ones, in terms of biocompatibility and mechanical properties. Despite the fact that this class of materials can reach a lower charge concentration than that of silicon, their morphological structure leads to unique device/cell interactions, due to the formation of a diffused intermixed interfacial region where the electrolyte species, like molecules and ions, can penetrate and interact [21]. Different semiconducting polymers have been studied as solid state transducers for the extracellular optical stimulation [65]. Polythiophene derivatives have proven to be the best choice, in terms of biocompatibility and electrochemical stability. In particular, Vaquero et. al.[66] tested two thiophene based polymers with different absorption properties, poly[2,1,3-benzothiadiazole-4,7-diyl[4,4-bis(2-ethylhexyl)-4H-cyclopenta[2,1-b:3,4-b']dithiophene-2,6-diyl]] (PCPDTBT) and regio-regular poly(3-hexylthiophene) (rr-P3HT) and compared them with a poly-phenylene vinylene-based polymer, poly(2-methoxy-5-(2-ethylhexyloxy)-1,4-phenylene-vinylene) (MEH-PPV) and a polyfluorene derivative, poly(9,9-dioctylfluorenyl-2,7-diyl) (PFO). rr-P3HT, PCPDTBT and MEH-PPV all showed good biocompatibility, but only the first two presented also good stability in aqueous environment, making them suitable for long-term in-vivo studies. PFO, instead, was reported to be phototoxic and not electrochemically stable.

Thin films of thiophene-based polymers, in particular rr-P3HT, were extensively studied for light induced stimulation purposes, by interfacing them *in-vitro* with different cellular models and explanted tissues, including: primary neuronal cells [67–69], explanted retinas [68,69], brain slices [69], astroglial cells [70] and non-excitable line cells [69,71]. The rr-P3HT-mediated optical excitation of isolated neurons was firstly assessed by Ghezzi, Antognazza et. al. [67] in 2011. The rr-P3HT-based device consisted in a planar indium tin oxide (ITO) electrode covered by a thin layer (~ 150 nm) of rr-P3HT blended with an electron acceptor molecule, [6,6]-Phenyl C61 butyric acid

methyl ester (PCBM), forming a bulk heterojunction (BHJ) structure. Primary hippocampal neurons cultures were successfully prepared on top of the polymer-based devices and the effect of the active material photo-excitation on the neurons bioelectrical activity was monitored by performing patch clamp recordings (figure 1.2 a). The results revealed that 20 to 50 ms light pulses ($\lambda = 560$ nm, 10 mW/mm^2) trigger neuronal action potentials with a success rate higher than 85 % (figure 1.2 a) [67]. More recently the same authors demonstrated that the light excitation of bare rr-P3HT films on ITO electrodes, without PCBM, can elicit neuronal firing in an equivalent manner as the BHJ-based devices [68]. Moreover, in the same report they successfully interfaced a blind retina with a ITO/P3HT device, by placing the photoreceptor-degenerated rat retinas both on the photoactive devices and on control ITO substrates, in subretinal configuration. Then, the system was illuminated with short light pulses (10 ms, 10 nW/mm^2 to 4 mW/mm^2, $\lambda = 532$ nm) and the output retinal response to light was monitored through an extracellular electrode placed in the retinal ganglion cell layer. The retinas interfaced to ITO/P3HT samples presented a significantly higher response to light stimulus and lower activation threshold than the one placed on ITO, demonstrating that rr-P3HT can be exploited as an artificial photoreceptor layer.

Regarding the mechanism that mediates the optical stimulation, in these first reports a capacitive coupling between the polymer-based devices and the cells was proposed[67,68]. This hypothesis was supported by other works [72,73], in which the electrochemical characterization of polythiophenes/electrolyte interfaces revealed that, upon light excitation and in presence of an underneath electrode, a surface charge displacement takes place. This leads to an accumulation of charges at the polymer/electrolyte interface, potentially exploitable for the depolarization/hyperpolarization of living cells. However, despite the fact that the study of neurons *in-vitro* represents an essential step for important applications in neuroscience, this class of cells is not a good model for understanding the mechanism behind the cell/device interaction, since it is characterized by a codified response, the action potential, which is independent from the nature of

the stimulus. For investigating the photo-transduction mechanism, it is better to study non-excitable biological models that do not show an intrinsic electrical activity, allowing a direct correlation between the origin of the stimulus and the specific variation of the cell membrane electrical properties [71]. In particular, Human Embryonic Kidney 293 (HEK-293) cells, a non-excitable genetically immortalized cellular line, was selected [71]. This cellular model was isolated from the kidney of a human embryo in the laboratories of prof. Alex van der Eb in 1973 [74]. This cell line offers easiness in handling, together with a compact shape that allow to reduce space clamp artifacts during electrophysiological measurements [75]. Martino et al. [71] demonstrated that the local rise in temperature due to the rr-P3HT or rr-P3HT:PCBM photoexcitation is able to modulate the HEK-293 cells membrane potential. Two different cell bioelectrical behavior were detected, corresponding to cell membrane depolarization and hyperpolarization, achieved by illuminating the system with 20 and 200 ms light pulses ($\lambda = 475$ nm, light intensity between 1 and 50 mW mm^{-2}) respectively (figure 1.2 b,c). The device thermal response in the employed illumination conditions was characterized, finding a local temperature increase up to 7 °C using 200 ms light pulses, with a buildup time constant of about 50 ms. These cellular responses were attributed to thermally-induced changes in cell membrane capacitance, according to the Goldman-Hodgkin-Katz (GHK) equation. The most probable physical explanation of this phenomenon lies in a thinning of the cellular membrane as a consequence of a spatial reordering of the lipid bilayer induced by the temperature gradient, as supported by a recent work [76]. The author reported also the presence of an additional signal component during HEK-293 patch clamp recordings, measurable only when the active material is deposited on top of an ITO electrode (figure 1.2 d). This effect was attributed to an electrical phototransduction process, due to the optically induced capacitive charging of the polymer surface. However, the authors did not provide a detailed description of the effects of the photo-capacitive response on the HEK-293 bioelectrical activity [71]. The photothermal modulation of HEK-293 cells membrane potential was later demonstrated also using other conjugated polymers, in particular PCPDTBT, characterized by a light absorption peak in the NIR region, very promising for in-vivo

applications, given the higher transparency displayed by living tissues in this range of wavelengths [66].

More recently, the thermal effect induced by the polymer photoexcitation was exploited in two distinct, possible applications: (i) the inhibition of neuronal firing and (ii) the modulation of temperature-activated transient receptor potential cation channels, in particular the Vanilloid Receptor 1 (TRPV1) channels. Regarding (i), Feyen et al. [69] demonstrated that the prolonged illumination of rr-P3HT and PCPDTBT thin films (550 ms, $\lambda = 530$, 16 to 30 mW mm^{-2} and $\lambda = 780$ nm, 24 mW mm^{-2} for the rr-P3HT and PCPDTBT cases respectively) silences both spontaneous and elicited action potentials in hippocampal primary neurons (figure 1.2 e), reduces the firing dynamics of mouse brain slices under induced epileptic activity and inhibits the spiking patterns of blind explanted retinas. These results demonstrate the potential use of these photoactive systems for antiepileptic therapy and for the realization of artificial retina implants. Regarding (ii), we recently employed thin layers of rr-P3HT for the optical triggering of TRPV1 channels, with an increased temporal and spatial resolution as compared to standard activation protocols [77]. This class of ion-channels can be activated by several chemical and physical stimuli, including heat, molecules like capsaicin, voltage, spider toxins, acidic pH, several fatty acids such as the endocannabinoid anandamide. Regarding the thermal activation, TRPV1 can be opened at a temperature higher than 43°C, but the combination with other type of stimuli may reduce the threshold temperature. We showed the TRPV1 activation in HEK-293T cells adhered on top of illuminated glass/P3HT devices (figure 1.2 f), with a photoexcitation density corresponding to a local heating of the bath up to an absolute temperature of 30°C, suggesting the presence of a concomitant stimulation effect. We proposed that the observed decrease in activation threshold can be due to a local photo-induced acidification of the medium, since by increasing the medium buffering capability, a reduction in TRPV1 activation is noticed. This view is also supported by other reports, in which the electron

accumulation on the photoexcited rr-P3HT surface and the subsequent formation of a charge

balancing layer of acidic polarized water molecules is demonstrated [78,79].
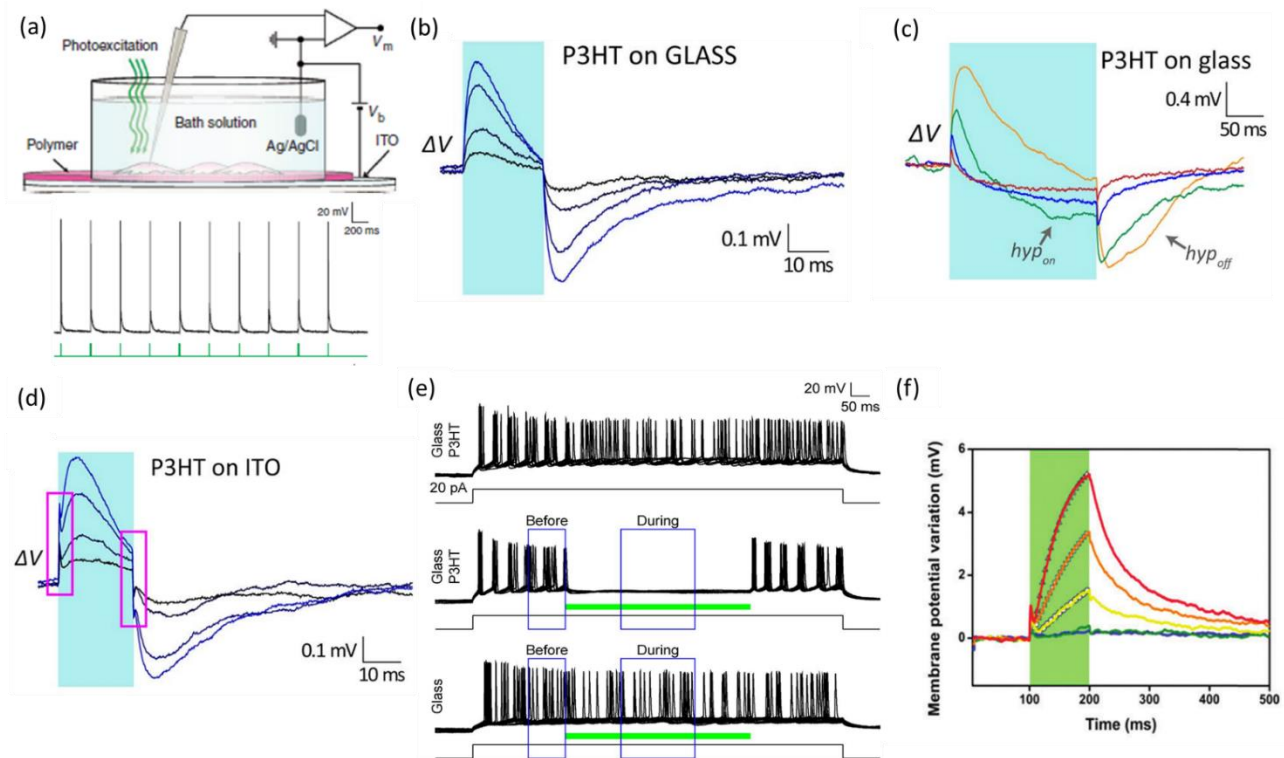
Figure 1.2. (a) Schematic representation of the set up used for the rr-P3HT-mediated optical excitation of isolated hippocampal neurons (upper panel) and representative patch clamp recording showing the neuronal action potential firing induced by 50 ms light pulses ($\lambda = 560$ nm, 10 mW/mm^2, lower panel). Reproduced from ref. [67]. Membrane potential (ΔV) changes recorded in HEK-293 grown on glass/P3HT upon excitation with 20 ms (b) and 200 ms (c) light pulses ($\lambda = 475$ nm) at increasing light intensities (7.7 mW/mm^2, 15 mW/mm^2, 35 mW/mm^2, 47 mW/mm^2). (d) Membrane potential (ΔV) variation acquired in HEK-293 cells grown on top of ITO/P3HT devices under the same light excitation conditions of panels c and d. Pink boxes highlight the ΔV component attributed to the capacitive charging occurring at the polymer surface. Panels b,c and d are reproduced from ref. [71]. (e) Silencing of the firing activity of hippocampal neurons seeded on rr-P3HT thin films induced by light excitation (green bars, 550 ms, $\lambda = 530$, 16 to 30 mW mm^{-2}). Reproduced from ref. [69]. (f) Membrane potential change recorded in HEK-293 cells stably expressing human TRPV1 grown on top of rr-P3HT upon photostimulation with 100 ms visible light pulses, at increasing photoexcitation densities (from 26 to 343 mW mm^{-2}). Light stimulus is represented by green shaded areas. Reproduced from ref. [77].

The in-vitro studies on the cells optical stimulation mediated by rr-P3HT-devices lead the Benfenati's

and Lanzani's research groups to test these systems as retinal prosthesis *in-vitro* [80]. They fabricated

a fully organic device that comprises a conformable silk substrate covered by PEDOT:PSS and rr-

P3HT layers, acting respectively as the electrode and the photoactive component [81]. The prosthesis

was implanted in the subretinal region of a rat model for retinitis pigmentosa and Electrophysiological and behavioral experiments were carried out. Recovery of both light sensitivity and visual acuity up to 6–10 months after surgery, directly associated to the presence of the implant [80], was demonstrated. These experiments open the way to the development of a new approach for the treatment of degenerative blindness, based on the use of organic functionally autonomous implants, overcoming the low biocompatibility, the need of power supplies and external cameras associated to the use of silicon and metal-based prosthesis.

1.6 Enhanced living cells stimulation and monitoring by engineered device morphologies

In recent years, materials scientists, biotechnologists and neuroscientists invested joint, extensive efforts towards the realization of three-dimensional structures suitable for interfacing with living cells cultures and tissues [8,11,12]. Different geometries (nanowires, nanopillars, mushrooms, nanoparticles), structures densities, materials and fabrication technologies, as well as diverse cellular models, have been investigated. The implementation of the planar technologies discussed in the previous paragraphs, with nano- and micro-structures, can lead to enhanced device capabilities in terms of stimulation and recording, opening the way to an increased number of applications in biotechnology, spanning from regenerative medicine to neuroscience, from pharmacology and physiology to neural computing and tissue engineering [8,11]. Regarding the study and modulation of the bioelectrical activity, a large part of the implementation strategies was aimed to the enhancement of the extracellular electrical stimulation efficacy and of the SNR during recordings [8,12]. Although extracellular electrical methods introduce some striking advantages respect to the patch clamp technique and standard intracellular electrodes (see section 1.1), they suffer from intrinsic limitations related to the presence of a cell/device interface. Concerning the recording process, by using external electrodes/FETs it is not possible to measure the actual bio-electrical signal

but the so-called "local field potential", that is composed by the superimposition of the electrical signals related to the different cellular activities, such as action potentials, synaptic currents and calcium waves. The signal deconvolution is usually complicated and requires specific software and great computational power. In addition, the reduced cell/device coupling that is possible to achieve using standard planar morphologies, lowers the SNR, leading to a poor recording quality [82]. Furthermore, the low cellular adhesion may lead to a reduction in the extracellular stimulation effectiveness [12]. Both recording and stimulation are based on the need for efficient signal transduction between the electronic device signals and the ionic response of the biological systems. For this reason, both processes would benefit of a device implementation able to promote the cell/device coupling [8,12]. Considerable effort was undertaken in the engineering of specific device morphologies for enhancing the cellular coupling. In particular, two main strategies have been followed: (1) direct intracellular access by the electrodes; (2) electrode engulfment by the cell membrane. Regarding the former approach, as already discussed in section 1.1, the introduction of metal electrodes inside the cells body leads to low SNR, as a consequence of the small dimensions needed for reducing the invasiveness. A way for overcoming this problem consists in the employment of nano FETs devices, since this class of devices is associated to a negligible input impedance, as presented in section 1.1. Tian et al. [11,83] fabricated nano FETs on top of kinked silicon nanowires and interfaced them with cardiomyocytes. After the devices internalization inside the cells, the authors were able to carry out action potential recordings, comparable to simultaneous patch clamp control measurements. In this manner they demonstrated the ability of these devices to perform reliable, high SNR intracellular recordings. More recently, this work was extended by developing new platforms in which the source and drain electrodes are deposited on a planar substrate and the cell cytosol is put directly in contact with the Si nanowires through SiO_2 nanotubes grown onto the nanowires [84]. This approach is particularly interesting because it can lead to the fabrication of arrayed nanoFETs [11].

The second strategy relies on the use of pillar-like microstructures engulfed inside the cellular membrane for achieving high electrode/cell coupling. In this configuration the cellular membrane is not perforated, ensuring the absence of detrimental effects on the cells physical properties. However, the stimulation and recording performance depends dramatically by the ratio between the transmembrane conductance and seal conductance [8,58,85]. In particular, for obtaining a high signal transduction efficiency the conductance associated to the cellular membrane should be maximized and the one associated to the seal minimized. The seal conductance can be minimized by reducing the thickness of the cleft region, increasing in this way the resistance associated to this portion of the electrolyte. For this purpose, Spira et. et. al. [16,82] have developed gold pillars microstructures with a mushroom like structure, characterized by a tight cellular adhesion. This micropillar-based platforms have been employed for the recording of the membrane dynamics of several cellular models, including cardiomyocytes [86] and hippocampal neurons [87], with an enhanced SNR during signal acquisition, enabling the measurement of subthreshold events with minimal filtering [16]. A way for further increasing the recording performance consists in combining the benefits generated by the pillar-induced tight-seal with an increased cell membrane conductance obtained by making tiny pores (10-20 nm) in the lipidic membrane [88]. A notable example is the electroporation approach, recently employed with high aspect ratio conical nanopillars [89].

The design of implemented cell/device interfacial morphologies was explored also for the development of biocompatible scaffolds for 3D cell cultures. The need for in-vitro cultures in three dimensions comes from the fact that the growth of eukaryotic cells in conventional 2D substrates leads to a cell monolayer that cannot give an accurate representation of the extracellular matrix found in living tissues [90]. The most part of the complex biological responses found in organ or tissues, like cellular proliferation and migration, apoptosis, receptor expression, transcriptional expression, differs dramatically from that of the conventional 2D cultures [90,91]. A large variety of synthetic and bio-derived polymers have been investigated, including inert polymer substrates (among many

others, PDMS, SU-8, polycarbonate, PLA) [92–94] and CPs [91,95,96], mainly for tissue engineering and regenerative medicine applications. In particular, the use of CPs for this purpose allows to combine the advantage of growing the cells in three dimensions with the possibility to electrically modulate and monitor the biological functions. A notable example is represented by PEDOT:PSS that has been proposed for the realization of 3D bioscaffolds [95,97], able to electrically modulate the activity of excitable cells [98] and to use electrical stimuli to guide cell proliferation and stem cells differentiation [96,99]. In many cases, devices transparency remains an issue, thus hampering the use of bioimaging analysis techniques. Very recently, an interesting work by S. Inal and colleagues [91] reported on the fabrication of a PEDOT:PSS-based macroporous device, integrating electrochemical sensing capabilities for in situ live cells monitoring. They demonstrated that the proliferation of epithelial cells on the conductive hydrogel-like scaffold can be quantified by measuring the changes in the PEDOT:PSS impedance before and after cells seeding, similarly to what already performed using planar electrodes [100,101].

Nanostructured material morphologies have also been investigated for the engineering of wireless platforms for the optical stimulation of living cells. Concerning the solid-state silicon based devices, the Tian's research group has recently developed amorphous Si mesostructures showing a fibril-based structure that resembles the natural biomaterials [102–104]. This material architecture displays very interesting mechanical properties, characterized by a Young's modulus value two orders of magnitude lower than the one of crystalline silicon. The material stiffness is further lowered after the immersion in water electrolyte, displaying a Young's modulus value closer to collagen [104,105]. This new class of silicon-based devices has proven to be suitable for the optically mediated thermal stimulation of living cells, given the reduced thermal conductivity and capacity induced by the porous architecture [11]. They were employed for the thermal activation of dorsal root ganglia (DRG) neurons action potentials with a lower illumination intensity than the one commonly required for the photothermal stimulation mediated by inorganic materials [104,106].

An alternative approach consists in the use of nanoparticles (NPs), both of inorganic and organic nature, as highly specific light-activated actuators for the localized, non-invasive modulation of the biological activity [22,107–109]. The striking advantage of NPs is associated to the possibility to deliver them to the cells and tissues trough injections like drugs, reducing the invasiveness during *in-vivo* medical treatments [109]. The most employed inorganic NPs for cellular stimulation are gold Nps, very interesting for their ease of functionalization and optical properties tunability. By modifying the particles morphology and consequently altering the gold surface plasmon resonance it is possible to obtain gold NPs with optical absorption maximums spanning from the visible range to the NIR [110,111]. These systems have been employed for the photothermal modulation of the activity of several cells typologies, in particular neurons [106,109,112,113]. Benzanilla et al. [106] have recently developed gold Nps functionalized with ligands for the targeting of specific neuronal membrane proteins, showing the thermal stimulation of DRG neurons with a minimum amount of NPs, given the superior resistance to washout displayed by the ligand-conjugated gold NPs.

However, the employment of gold NPs in *in-vivo* applications is limited by the increased toxicity presented by the gold metal passing from the inert bulk form to NPs [114,115]. Au NPs toxicity mostly depends on the particle shape, size and surface charge, and it is associated to increased levels of cellular oxidative stress and apoptosis, as observed on retinal neurons [114]. Organic semiconductor NPs are very interesting in view of the development of highly biocompatible artificial nanostructured light-actuators. They are easier to synthesize and functionalize, as compared to inorganic NPs, and they show good environmental stability, high brightness and large absorption cross section [109,116]. This class of NPs can be prepared by direct monomers polymerization in a heterophasic system [117–120] or by nano-precipitation or mini-emulsification of preformed oligomers or polymers [121,122]. These systems have been recently employed for the optically driven modulation of biological processes [123,124] and as intracellular temperature sensors [125]. Starting from the results obtained using rr-P3HT-based photoactive platforms discussed in section 1.5,

Lanzani, Antognazza et al. have developed sterile rr-P3HT NPs by taking advantage of the nanoprecipitation method. These polythiofene-based NPs were tested in two different configurations: bare and N-hydroxysuccinimidyl ester groups (NHS)-functionalized rr-P3HT NPs. The biocompatibility of both NPs types was tested by performing viability assays and electrophysiological experiments with HEK-293 cells lines in-vitro, finding that the cells physiological functions are not altered by the presence of the NPs [126,127]. Laser scanning confocal microscopy experiments revealed that the bare rr-P3HT NPS are rapidly internalized by the cells, probably through micropinocytosis or protein corona formation [128]. Instead, the presence of the NHS group leads to the NPs attachment to the cellular membrane, presumably as a consequence of the interaction between the NHS functional groups and the primary amines of the cells membrane proteins [129]. The different NPs/cell interaction leads to dissimilar cellular photoinduced responses. HeK-293 cells treated with bare rr-P3HT NPs in fact, do not show any response during patch clamp recordings upon light excitations [126]. The same experiments performed on cells treated with rr-P3HT-NHS NPs showed instead a photoactivated response similar to the thermally activated-one obtained using rr-P3HT thin films [66,71]. Recently we reported that the unfunctionalized rr-P3HT NPs, upon photoexcitation, increase the intracellular Ca^{2+}concentration of HEK-293 cells, through a reactive oxygen species (ROS)-mediated mechanism [130]. This picture is supported by performing calcium imaging experiments and measurements with fluorescent indicators and pharmacological agents for the ROS detection/suppression respectively in presence of the light stimulus. The photo-electrochemical characterization further consolidates the thesis, suggesting the a ROS production pathway similar to the one observed in rr-P3HT thin films [78,131,132], involving the initial photo-activated oxygen reduction at polymer/electrolyte interface, forming the superoxide ion that further evolves leading to the generation of different ROS [130].

Furthermore, it was demonstrated that rr-P3HT NPs directly affect the light sensitivity and the behavior of Hydra vulgaris, eye-less polyps [133]. The results obtained reveal that the exposure of rr-

P3HT treated hydras increases their tendency to be more contracted, differently from to the untreated ones that tend to be more elongated. When the light stimulus is interrupted, the NPs-treated animals maintain the enhanced contraction state, while the untreated ones recover their contraction/elongation behavior. Moreover, it was found the polyps treated both with light and rr-P3HT Nps display a higher expression of an opsin-like gene, directly involved in the light transduction mechanism of the animals. These results put a step forward in the employment of rr-P3HT based photo-transducers for the in-vivo restoration of the light sensitivity, opening the way to a new medical approach based on the direct injection of the nanostructured photoactive material in the body, reducing the invasiveness of the associated surgical procedure.

In the next chapters we present different strategies to engineer hybrid interfaces established between rr-P3HT-based photoactive platforms and aqueous electrolytes, focusing in the characterization of the biological effect on living cells activity and functionality.

2. Planar rr-P3HT-based devices interfaced with aqueous electrolytes and living cells

2.1 Introduction

In the previous chapter (in particular in section 1.5 and 1.6) we presented different applications in which rr-P3HT was exploited for the polymer-mediated optical modulation of the activity of a number of biological models *in-vitro* and for the recovery of light sensitivity and visual acuity in visually-impaired animal models *in-vivo*. In this scenario, the detailed characterization of hybrid interfaces between conjugated polymers, saline electrolytes and living cells plays a crucial role for the understanding of the processes involved and for developing strategies for the improvement of device performance. In this chapter we focus on the investigation of the electrochemical phenomena occurring at the planar rr-P3HT/aqueous electrolyte interface in dark and upon light excitation. We propose an approach for controlling the interfacial electrochemical properties based on the implementation of rr-P3HT-based planar devices with charge selective materials. We start by showing the photocurrent and photovoltage trends of the simplest configuration employed, that comprises a thin rr-P3HT film deposited on a standard ITO electrode (figure 2.1 a). We then present different device implementation strategies based on the coupling of the active semiconducting layer with different hole and electron-selective layers (HSL and ESL respectively). We consider two implemented device architectures: (1) a p-type/i-type/n-type (p-i-n) structure, obtained by coupling rr-P3HT with an ESL (figure 2.1 b); (2) a multilayered configuration constituted by an active layer of rr-P3HT, blended with an ESL material and sandwiched between a HSL and an ESL (figure 2.1 c).
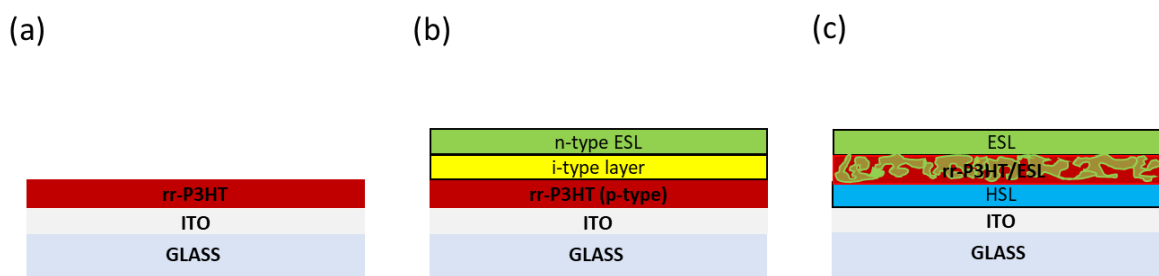
Figure 2.1. Schematic drawing depicting the standard ITO/P3HT (a) and the implemented photoactive device architectures composed by rr-P3HT coupled with ESL in a p-i-n configuration (b) and rr-P3HT sandwiched between HSL and ESL (c).

We discuss the changes induced by charge selective layers on the photo-electrochemical capacitive and faradaic phenomena occurring at device/electrolyte interface. In particular, we demonstrate that the architecture (2) is particularly suitable for the development of highly efficient organic/inorganic photocathodes for hydrogen evolution. In the last part of the chapter we show the photoinduced modulation of non-excitable line cells membrane potential, using the different fabricated architectures, by performing whole-cell patch clamp recordings. In addition, we extend the electrochemical characterization by measuring the light-induced changes in the device local surface potential, using the same set up employed for the electrophysiological recordings.

The results related to the fabrication and characterization of photocathodes for hydrogen evolution are included in the following publications: (1) F. Fumagalli, S. Bellani, M. Schreier, S. Leonardi, H.C. Rojas, A. Ghadirzadeh, G. Tullii, A. Savoini, G. Marra, L. Meda, M. Grätzel, G. Lanzani, M.T. Mayer, M.R. Antognazza, F. Di Fonzo, *Hybrid organic–inorganic H$_2$ -evolving photocathodes: understanding the route towards high performance organic photoelectrochemical water splitting*, J Mater Chem A. 4 (2016) 2178–2187. doi:10.1039/C5TA09330A (2) H.C. Rojas, S. Bellani, F. Fumagalli, G. Tullii, S. Leonardi, M.T. Mayer, M. Schreier, M. Grätzel, G. Lanzani, F.D. Fonzo, M.R. Antognazza, *Polymer-based photocathodes with a solution-processable cuprous iodide anode layer and a polyethyleneimine protective coating*, Energy Environ. Sci. (2016). doi:10.1039/C6EE01655C.

2.2 ITO/P3HT: fabrication and electrochemical characterization

Thin films of bare rr-P3HT represent the starting point for the study of the device/electrolyte properties carried out in this work. The fabrication of this device is based on a single spin coating deposition, followed by a thermal annealing, for improving the crystallinity of the material and enhancing its charge dissociation performance (see appendix A.1 for details). The films are deposited on top of ITO-covered glasses that act as electrodes.

The electrochemical properties of the rr-P3HT/electrolyte interface can be directly evaluated by carrying out galvanostatic and potentiostatic measurements using an electrochemical cell connected to a potentiostat. Here, a three-electrode configuration of the electrochemical cell is employed, comprising ITO/P3HT as the working electrode, an Ag/AgCl electrode as the potential reference (RE) and a Pt wire that completes the current path as the counter electrode (CE). In this scheme, it is possible to avoid voltage drops due to the current flow. All the electrochemical experiments are done by immersing the two/thirds of the device inside an electrolyte (NaCl 0.2M, unless otherwise stated) both in dark and by illuminating the samples with a light source (LED or Xe light source). For additional information on electrochemical experiments set up see Appendix A.2.

Figure 2.2 panel a shows the typical photocurrent trace recorded during a potentiostatic, chronoamperometry measurement by shining a 100 ms pulse of light to a ITO/P3HT device from the ITO direction and by applying a voltage equal to the open circuit potential (OCP, on average close to 0.2V vs. Ag/AgCl), in order to maintain the system close to the electrochemical equilibrium. The behavior is capacitive, with fast current spikes at the beginning and at the end of the illumination, characterized by a decay time constant in the order of few milliseconds. Instead, the photopotential measured between the device and the RE during galvanostatic, potentiometry measurements, upon the same photoexcitation conditions (figure 2.2 b), is characterized by an initial downward dynamic when the light is switched on, reaching a negative value that start to slightly decrease towards positive values after few milliseconds.
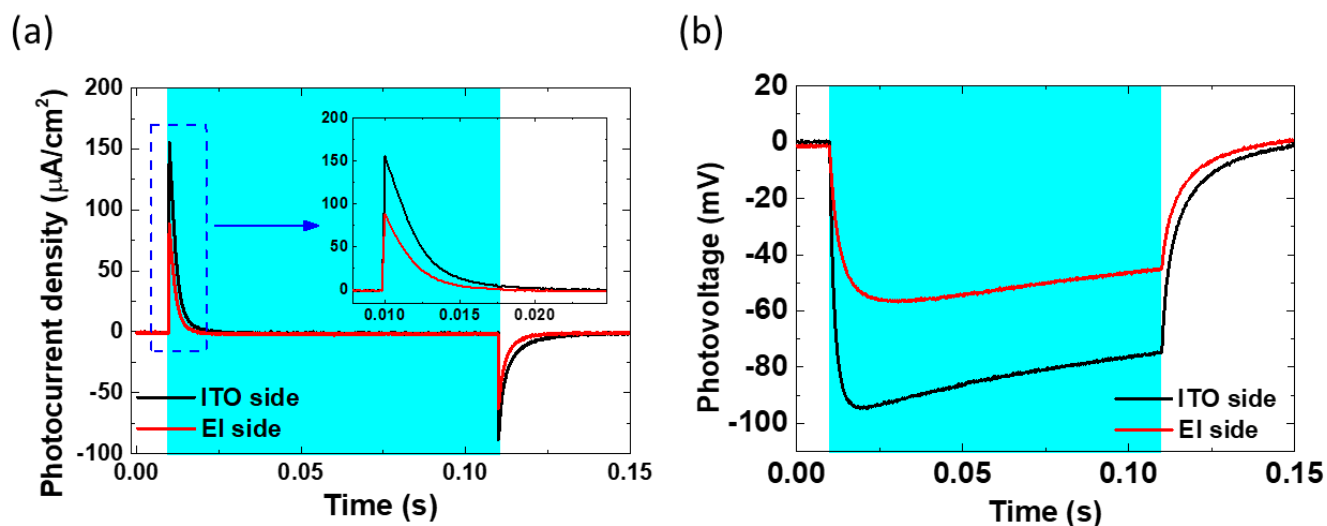
Figure 2.2 Representative photocurrent (b) and photovoltage (b) traces measured in a three-electrodes electrochemical cell upon excitation with a 100 ms light pulse (470 nm, 2.8 mW/mm^2) impinged both from the ITO or electrolyte (El) side. During the photocurrent recording a constant bias of 0.2 V vs. ag/AgCl, equal to the device open circuit potential (OCP), is applied. The cyan shaded area represents the light excitation interval.

This behavior is related to a positive charging of the polymer surface, that attracts negative ions from the bath, forming a Helmoltz double layer at the rr-P3HT/electrolyte interface. The ITO electrode instead acts as a sink for electrons (figure 2.3) [78]. This picture is corroborated by observing the data acquired by illuminating the sample from the opposite direction (electrolyte (El) side). In this case both the photocurrent and photopotential values are lower, reflecting the fact that the ITO/P3HT interface, where the exciton dissociation occurs, is now at the opposite side leading to an increased electrons recombination probability within the polymer bulk, whose thickness (in general between 30 and 250 nm [69,71,77,134]) is higher than the diffusion length of the exciton (approx.. 10 nm, [135,136]).
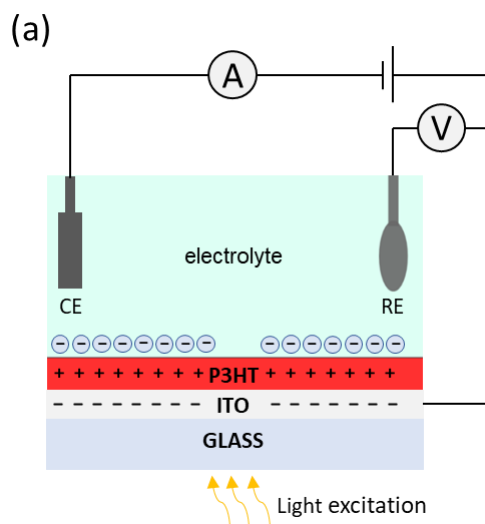
Figure 2.3 Schematic representation of the three electrodes electrochemical cells during operation that highlights the charging that occurs at the ITO/P3HT and P3HT/electrolyte interfaces, induced by exciting with light pulses in the millisecond time domain.

2.3 Device implementation using charge selective layers

2.3.1. ITO/p-i-n architecture

The charging at the polymer/electrolyte interface can be controlled by introducing charge selective layers inside the structure. In particular, we have modified the standard ITO/P3HT flat obtaining a p-type/i-type/n-type (p-i-n) structure, widely employed in solar cells and photoconductors [137–139]. In general, this architecture is constituted by a blend of donor/acceptor semiconductors (i-type layer) sandwiched between a p-doped hole transport layer (p-type layer) and an n-doped electron transport layer (n-type layer). Here, we use rr-P3HT as the p-type layer and Phenyl-C61-butyric acid methyl ester (PCBM) as the n-type layer, blended together forming the i-type layer in-between, following a fabrication strategy employed for enhancing the sensitivity of Organic thin film photoconductors (OTFPs) [137]. In particular, we modified the ITO/P3HT device (P3HT film thickness about 80 nm) by depositing a PCBM film (thickness ~ 20nm) on top of its surface by evaporation, followed by a solvent annealing for the permeation of the PCBM inside the rr-P3HT structure, forming the P3HT:PCBM i-type layer. In order to intercalate the PCBM within only a part of the rr-P3HT layer, without affecting its semi-crystalline structure, it is necessary to carry out the annealing for a short

time (60 seconds) and use dichloromethane (DCM) as the solvent, given the poor solubility of rr-P3HT in DCM [140](see appendix A.3 for additional fabrication details). It was demonstrated that this fabrication route leads to a i-type layer depth very close to the thickness of the starting evaporated PCBM layer [137]. The device is then completed by evaporating the PCBM n-type layer (thickness ~20 nm) (figure 2.4 panel a). SEM image of the full ITO/p-i-n sample cross-section is depicted in figure 2.4 b (see appendix A.4). Unfortunately, the instrument resolution is not sufficient to identify the P3HT:PCBM i-type layer and to clearly distinguish it from the overlying PCBM layer.
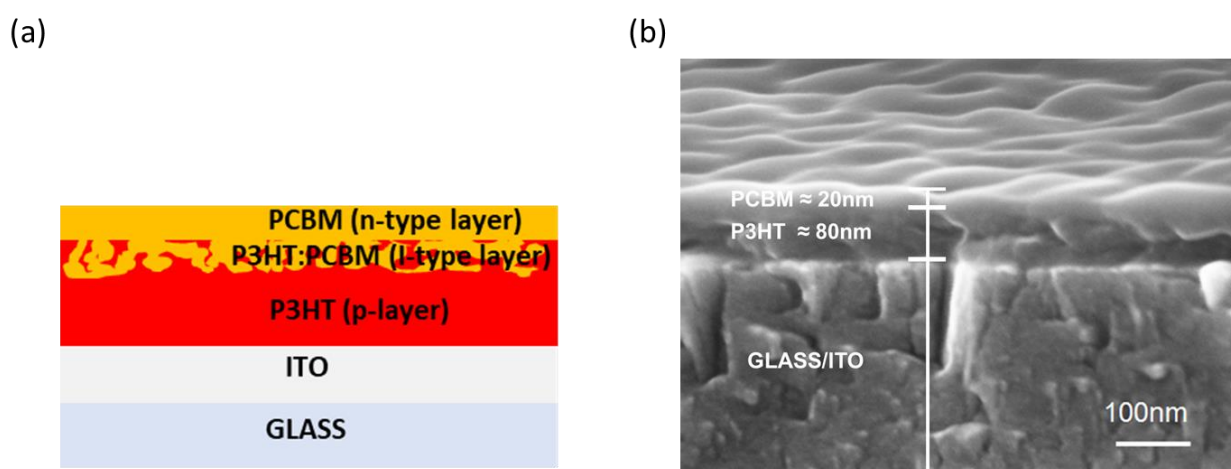
Figure 2.4 (a) Cartoon depicting the p-i-n device structure. (b) SEM micrograph of the p-i-n structure cross-section.

Further structural analysis would be needed to directly describe the layered architecture and morphology of the device. However, the photoelectrochemical characterization provides a convincing, though indirect, demonstration, showing a sizable change in the predominant photocurrent and photovoltage dynamics. In fact, the photoelectrochemical response of the p-i-n device, as in the ITO/P3HT case, is purely capacitive but shows a strong dependence from the light excitation incidence direction. In particular, when the light comes from the ITO side, the p-i-n architecture exhibits the same behavior of the ITO/P3HT case, characterized by positive/negative photocurrent spikes when the light is switched on/off, related to the positive charging/discharging of the polymer/electrolyte interface (figure 2.5 a). Instead, when light is impinging from the El side, the photocurrent sign is reversed (figure 2.5 a). Accordingly, to the ITO/P3HT case, ITO/p-i-n shows the

same sign for the photovoltage and photocurrent signal, being negative/positive when light is impinging from ITO/El sides (figure 2.5 b). A difference in the photovoltage dynamics in dependence to the light incidence direction is noticeable in the ITO/p-i-n case (figure 2.5 b). In particular, when light comes from the ITO side the photovoltage trace displays a spiky variation during the first 3 ms from the photoexcitation beginning, absent in the case of El light incidence direction (figure 2.5 b). The explanation of this discrepancy is not straightforward and requires additional experiments for being clarified. The different photocharging behavior displayed by the ITO/p-i-n configuration in dependence from the photostimulation direction, can be explained by considering that when light comes from the ITO side is mainly absorbed by the bare rr-P3HT layer, leading to a predominant dissociation of the excitons by the closer ITO/P3HT interface. Instead, when light impinges the opposite device side, the majority of the excitons are dissociated by the P3HT/PCBM interface within the i-type layer, obtaining the collection of electrons at the PCBM surface. A similar photocharging dependence behavior was observed by Gautam et. al. on BHJs of P3HT:N2200 immersed in a water based electrolyte [72].
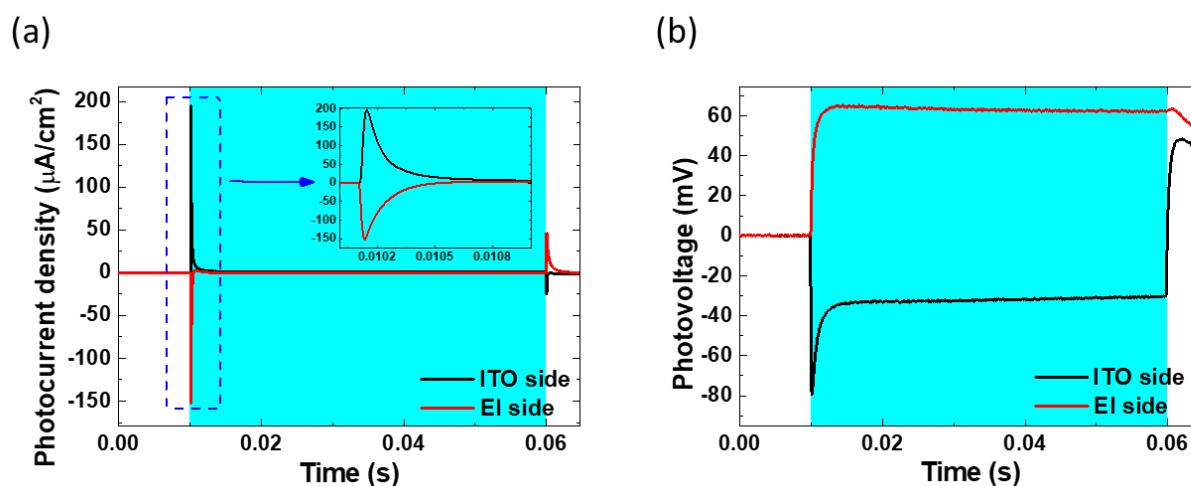
Figure 2.5. Representative photocurrent (b) and photovoltage (b) signals obtained by exciting the ITO/p-i-n device with a 50 ms light pulse (470 nm, 2.8 mW/mm2) from different directions. A constant bias of 0.1 V vs. ag/AgCl, equal to the device OCP, is applied during the photocurrent recording The cyan panel represents the light excitation.

These measurements show that through a proper engineering of the hybrid polymer/electrolyte architecture it is possible to select the sign of majority charges facing the aqueous environment.

2.3.2. rr-P3HT-based hybrid organic-inorganic photocathode for hydrogen evolution

In the previous paragraph we saw that the introduction of a PCBM layer between rr-P3HT and electrolyte changes the sign of the capacitive photocharging occurring at the device/electrolyte interface. In this paragraph we consider a different strategy based on a rr-P3HT/ESL material blend as the photoactive layer, sandwiched between a HSL and an ESL. We exploit this architecture for enhancing the efficiency of interfacial faradaic photo-electrochemical processes. In particular we present the development of hybrid organic/inorganic photocathodes for hydrogen evolution. We explore different HSL and ESL materials, obtaining the best results with an architecture that comprises (from bottom to top): (1) a semitransparent electrode of fluorine-doped Indium Tin Oxide (FTO); (2) a spin-coated layer of copper iodide (CuI) as HSL; (3) a spin-coated photoactive layer of rr-P3HT and PCBM blended together (P3HT:PCBM) forming a bulk heterojunction (BHJ) configuration; (4) a layer of amorphous TiO_2, deposited by Pulsed laser deposition (PLD), that act as ESL; (5) a sputtered layer of Pt, a good catalyst for HER (figure 2.6 a) [141]. The electrochemical characterization of this photocathode reveals a high efficiency towards the hydrogen evolution reaction (HER). In particular, we record HER-associated photocurrents up to 7.1 mA cm^{-2} at 0 V vs. RHE and an onset potential for HER equal to 0.702 V with 100% faradaic efficiency. The complete description of the device fabrication and characterization, together with the results obtained by considering different device architectures, is reported in appendix A.5.

2.4 Coupling planar rr-P3HT-based devices with HEK-293 cells

2.4.1. HEK-293 cells cultures and viability on planar rr-P3HT-based devices

HEK-293 cells are plated on the different device architectures presented in section 2.3, in particular on ITO/P3HT, ITO/p-i-n, ITO/P3HT:PCBM (appendix A.1) and ITO/CuI/P3HT:PCBM/TiO$_2$ samples. Regarding the latter sample type employed for hydrogen evolution, we use this specific configuration that lacks the Pt catalyst because the presence of Pt would in principal enhance the efficiency of the oxygen reduction reaction, leading to a possible ROS overproduction that has proven to be detrimental, mainly for an induced oxidative stress [142] and non-specific damage of DNA, proteins and lipids [143] (see appendix A.6 for further fabrication details). The preparation of the cells cultures on top of the different samples is carried out following a procedure described previously [71], that implies the use of a glycoprotein of the extracellular matrix, fibronectin, that is deposited on the polymer surface, acting as an interlayer for enhancing cells adhesion as firstly reported by Scarpa et. al. for promoting the adhesion of different kind of cells on P3HT [144] (see appendix A.7 for details about the preparation of cells cultures).

The first step in the characterization of the hybrid HEK-293/device bio-interface is the assessment of cells viability. This was already assessed by Martino et al. [71] in the case of bare rr-P3HT and P3HT:PCBM samples, both using the 4',6-diamidino-2-Phenylindole (DAPI)/propidium iodide (PI) method and the tetrazolium salt (MTT) assay. The former consists in the staining of the cells with two different fluorescent dyes, DAPI, specific for all cells nuclei, and PI, that stains only dead cells. The evaluation of the number of viable cells is then carried out by counting the cells over different fields of view, obtaining the percentage of healthy cells at a specific cell culture time point. MTT assay, is based on the evaluation of the quantity of the MTT dye reduced by the cell to its formazan form trough mitochondrial activity [145]. The quantity of formazan is related to the number of cells and can be evaluated by measuring the optical density of the MTT-treated cell cultures at a selected wavelength (λ = 570 nm) and at different time points, giving information about the proliferation of

the cells. The results obtained on rr-P3HT and P3HT:PCBM thin films showed 96 % of viable cells from DAPI/PI staining and an increase in cells proliferation during time (1,2,3,4 and 7 days in-vitro) exhibiting a similar rate as in the control glass substrates case (figure 2.6) [71].
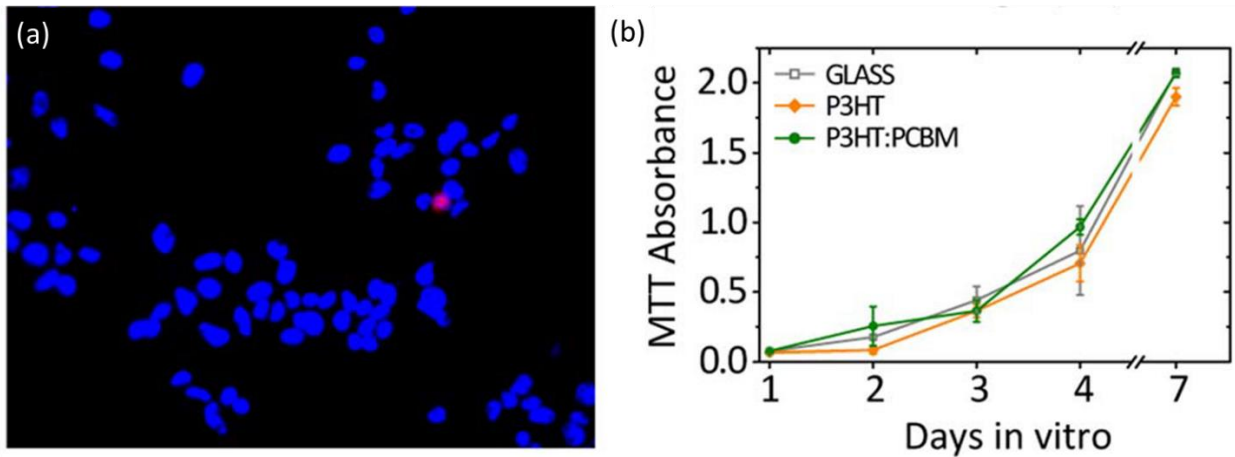
Figure 2.6 (a) representative fluorescence image of the HEK-293 cells nuclei of alive and dead cells stained with DAPI (blue) and PI (red) respectively. (b) absorbance of the MTT dye in contact with HEK-293 cultures measured at different time points.

We do not directly assess the HEK-293 cells viability on the ITO/p-i-n and ITO/CuI/P3HT:PCBM/TiO$_2$ samples, since in the first case we expect a similar behavior as for P3HT:PCBM devices and in the other one the biocompatibility of the TiO$_2$ exposed layer is already well-documented [146–149].

2.4.2. HEK-293 cells electrophysiology

Among the methods employed for recording of the cells bioelectrical activity, Patch-clamp technique in whole-cell configuration represents an optimal choice for the study of the biophysical interaction between cells and photoactive devices in-vitro, since it gives the possibility of monitoring the actual variations of membrane potential and of the currents that flow through the membrane, as introduced in section 1.1. In particular, the devices with the cells grown on top are immersed in a proper

extracellular solution, in floating configuration, i.e. without contacting the ITO electrode to any external circuit. Whole-cell recordings in current clamp configuration are then performed, both in dark and in light conditions, in order to investigate the direct effect of the illumination on the cells electrochemical behavior. The light is impinged on the samples using a LED system fiber-coupled to the fluorescence microscope integrated in the patch-clamp set up, achieving a focalized light spot (540 µm diameter) with an intensity of about 1 order of magnitude higher as compared to the one employed during the electrochemical characterization discussed in section 2.2. Since the microscope is in an inverted configuration, light comes from the ITO direction (see section A.7 for additional details about patch clamp recordings). The typical cellular response recorded in current clamp experiments during the ITO/P3HT device photoexcitation with light pulses in the millisecond time domain ($\lambda = 470$ nm, light intensity ranging from 8 to 46.5 mW mm^{-2}) is reported in figure 2.7. As briefly presented in paragraph 1.5, when the polymer is excited with 20 ms light pulses the membrane potential variation (ΔV) is characterized by two main components, both dependent on incident light intensity: (1) fast spikes at the beginning and at the end of the illumination, that resemble the capacitive response discussed in section 2.2; (2) slower depolarization during light excitation followed by a hyperpolarizing signal when the light stimulus is switched off (figure 2.7 a). When the stimulus duration is increased to 200 ms, the cell experiences a depolarization/hyperpolarization switch during the illumination time (figure 2.7 b). The origin of this signals was clarified in a previous report [71]. In particular, it was demonstrated that the fast signal component is most probably related to the photocharging of the polymer/electrolyte interface, since it disappears when ITO electrode is removed. The slower component instead, was attributed to a variation in the cell membrane capacitance due to the local heating of the bath induced by the thermal energy released by the polymer as a consequence of non-radiative recombination of excited states [71].
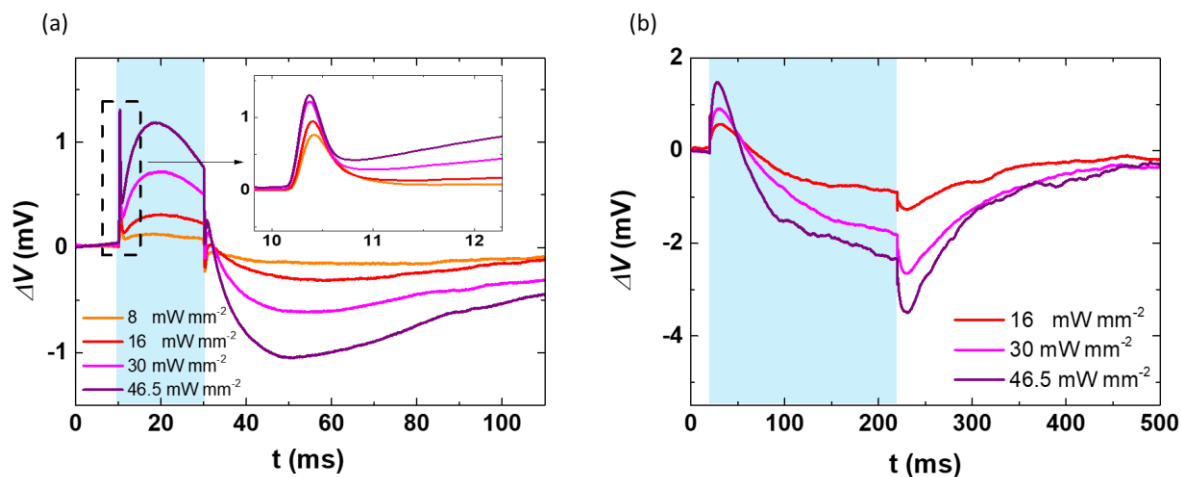
Figure 2.7. Current clamp recordings of the HEK-293 grown on top ITO/P3HT devices upon light excitation (λ = 470 nm) with 20 ms (a) and 200 ms (b) light pulses. The illumination interval is represented by the cyan shaded areas.

When the ITO/P3HT device is modified obtaining the p-i-n structure, the thermal contribution of the cell membrane variation is comparable, both when 20 or 200 ms light pulses are impinged on the rr-P3HT layer (figure 2.8). Instead, the fast transients observed in the ITO/P3HT case are still present, but with an opposite sign and a reduced intensity (figure 2.8 a).
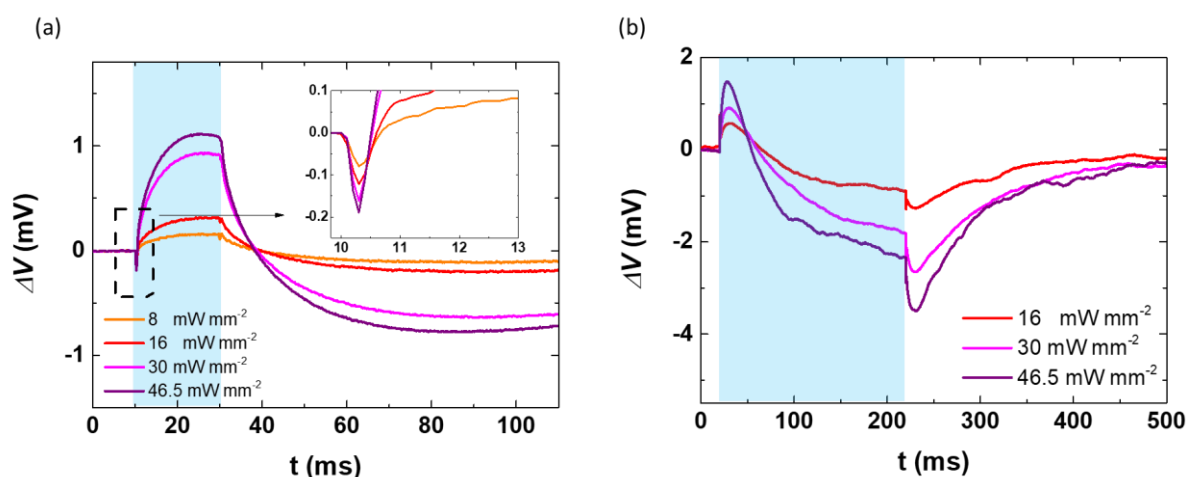
Figure 2.8 Current clamp recordings of the HEK-293 grown on top ITO/p-i-n devices upon light excitation (λ = 470 nm) with 20 ms (a) and 200 ms (b) light pulses. The illumination interval is represented by the cyan shaded areas.

The introduction of a P3HT:PCBM BHJ sandwiched between hole and electron selective layers, leading to the ITO/CuI/P3HT:PCBM/TiO$_2$ configuration, induces a photoinduced HEK-293 cells membrane potential variation trace similar to the ITO/p-i-n case, but with an increased intensity of the fast electrical component (figure 2.9). In order to understand the specific contribution of the charge selective layers to the photomodulation of the cells membrane potential, we repeat the experiments on HEK-293 cells grown on top of ITO/P3HT:PCBM samples, focusing on the response related to the device surface charging. The results show that the BHJ-based architecture alone does not affect the sign of the fast membrane potential variation, thus confirming the crucial role of the charge selective materials for the control of the sign of the charges accumulated at the polymer/electrolyte interface. However, an improvement of the signal intensity in the ITO/P3HT:PCBM case is noticeable, reflecting the better charge dissociation efficiency within the inter-diffused BHJ phase .
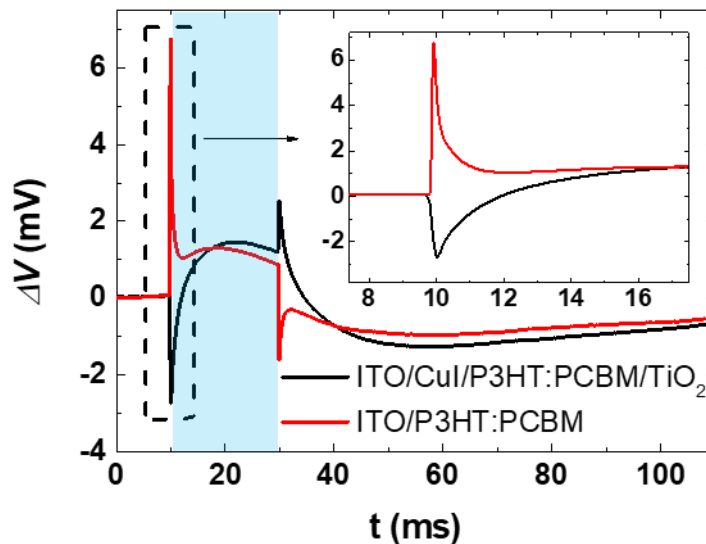

Figure 2.9 Current clamp recordings of the HEK-293 grown on top P3HT:PCBM-based devices upon light excitation (λ = 470 nm) with 20 ms light pulses. The illumination interval is represented by the cyan shaded area.

The fast contribution to the membrane potential variation, due to the device/electrolyte interface photocharging, can be further characterized by performing experiments without cells, for the evaluation of the potential established at the device surface, using the same set up employed during patch clamp measurements. In this configuration the bath and the electrode-filled micropipette are loaded with the same electrolytic solution used during patch clamp electrophysiology, in order to avoid the establishment of junction potentials. The pipette is then micro-manipulated close to the floating device surface (~2 µm) and voltage-clamp measurements are carried out by simultaneously photostimulating the device using the LED-coupled microscope. The surface potential is then obtained by multiplying the acquired current traces by the pipette resistance. This experiment allows to extend the electrochemical characterization discussed in section 2.2, studying the system in the same conditions of the electrophysiological experiments, i.e. without contacting the ITO to the external circuit and by illuminating only a small fraction of the device area (a detailed description of the experimental conditions adopted during surface potential measurements is reported in appendix A.8).

The surface potential (V_{surf}) variation upon light excitation with 20 ms light pulses ($\lambda = 470$ nm, light intensity = 46.5 mW mm^{-2}) recorded on top of the four different samples is depicted in figure 2.10. Firstly, we can appreciate the correspondence between the surface potential trace and the fast spikes recorded during current clamp acquisitions, confirming the electrical origin of the signal. All the tested devices show a capacitive behavior. ITO/P3HT and ITO/P3HT:PCBM samples exhibit positive potential transients that decay to zero after few milliseconds after the light onset, corresponding to a positive charging of the device surface. ITO/p-i-n and ITO/CuI/P3HT:PCBM/TiO$_2$ present a capacitive behavior with similar dynamics, but corresponding to a negative surface charging. These results are in agreement with the photo-charging mechanism presented in sections 2.2 and 2.3, exception made for the ITO/p-i-n architecture, that shows negative photogenerated charges at its surface, even though the light excitation comes from the ITO side. This difference can be explained

by considering that in surface potential experiments the light excitation intensity is about one order of magnitude higher than the one employed in the electrochemical characterization. This situation leads to a higher penetration of light within the device, increasing the contribution of the P3HT/PCBM interface to the charge dissociation. From the Lambert-Beer law, considering a rr-P3HT absorption coefficient of about 10^5 cm^{-1} [150], it is possible to estimate an intensity abatement of about 37% at 100 nm, corresponding to ~1 mW mm^{-2} and ~17 mW mm^{-2} in the p-i-n and P3HT cases respectively. Furthermore, it is possible to make different considerations regarding the maximum surface potential values achieved by the different architectures: (1) ITO/P3HT:PCBM exhibits the highest surface potential intensity (~7 mV, figure 2.10 a), reflecting the enhanced charged extraction due to the diffuse P3HT/PCBM interface given by the bulk-heterojunction configuration. (2) The addition of HSL and ESL to P3HT:PCBM do not increase the capacitive contribution to the surface potential (~7 mV and ~ - 3 mV in the ITO/P3HT:PCBM and ITO/CuI/P3HT:PCBM/TiO$_2$ respectively, figure 2.10 a) and a constant negative contribution to the surface potential appears during all the illumination time (~ -0.2 mV figure 2.10 c). The presence of the sustained negative signal is consistent with a negative device surface charging, immediately followed by a faradaic electron transfer, similarly to what observed during light-chopped linear sweep voltammetry experiments (appendix A.5.2 figure A.5.4 b). (3) ITO/p-i-n shows a lower capacitive charging of the surface as compared to ITO/P3HT (~ 1 mV and ~ 3.5 mV respectively, figure 2.10 b), that is not in agreement with the comparable photocurrent peaks the two device architectures shown in section 2.2 and 2.3. Again, the explanation of this discrepancy comes from the different light excitation intensity employed in the two experiments, that leads to the different charge dissociation mechanism already discussed.
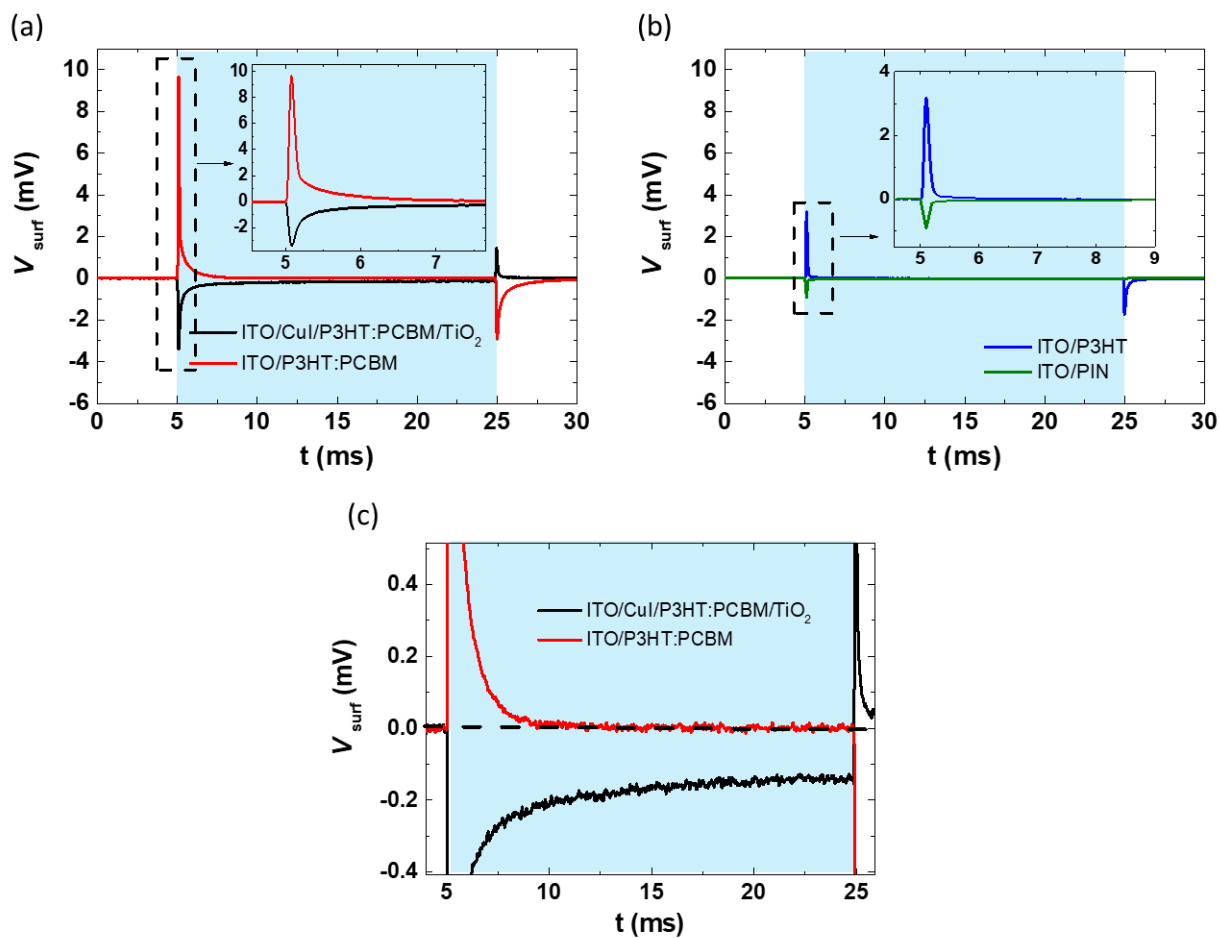
Figure 2.10. Surface potential recordings performed on the rr-P3HT devices implemented with charge selective layers (a) or with the p-i-n architecture (b). (c) Magnified view of the panel (a) that highlights the faradaic contribution to the surface potential signal acquired on the ITO/CuI/P3HT:PCBM/TiO$_2$ device surface. Illumination conditions: $\lambda = 470$ nm, 46.5 mW mm^{-2}, light pulse duration = 20 ms. Light excitation is represented by the cyan shaded area.

3. rr-P3HT-based mesoporous devices

3.1 Introduction

In chapter 2 we showed that by modifying the simple ITO/P3HT architecture by introducing different materials, with hole or electron selective capabilities, it is possible to change the photoinduced electrochemical properties of the device/electrolyte interface. In particular, ms light pulses induce a positive purely capacitive charging of the P3HT/electrolyte interface and the sign of the accumulated charges can be reversed by introducing the p-i-n configuration. In addition, the implementation of a standard P3HT:PCBM bulk-heterojunction with HSL (CuI) and ESL (TiO$_2$) together with a Pt catalyst leads to an enhanced efficiency towards light driven faradaic processes, exploited for hydrogen evolution. The ITO/P3HT:PCBM/TiO$_2$ partial configuration allow instead to have a balance between faradaic and capacitive processes in the ms time domain, as shown by linear sweep voltammetry and surface potential measurements. In this chapter we describe a different strategy for the control of the device/electrolyte interface electrical parameters, based on the engineering of the device morphology without introducing additional materials. A mesoporous rr-P3HT based architecture is obtained by taking advantage of an all-solution processed fabrication, introducing a ITO nanoparticles (ITO NPs) layer between the flat ITO electrode and the rr-P3HT photoactive layer. The variation of the electrochemical behavior of the resulting device is characterized, demonstrating that the increase in device surface area leads to the possibility of controlling the type of charges accumulated at the device surface, changing then the balance between photoinduced faradaic and capacitive events at the polymer/aqueous electrolyte interface.

3.2 Fabrication and morphological characterization

The fabrication of the mesoporous rr-P3HT-based configuration starts with the deposition of an ITO NPs (ITO NPs average diameter ~ 50 nm) dispersion on a flat ITO electrode by four subsequent spin coating steps, followed by a thermal treatment at 200°C. The device is then completed by filling the ITO-based porous electrode with rr-P3HT by spin coating and by subsequent thermal annealing. ITO/P3HT samples (rr-P3HT thickness ~ 30 nm) are fabricated as a control, by employing the same spin coating and annealing parameters. (see appendix B.1 for more fabrication details). The two different device architectures are depicted in figure 3.1 panels a and b.
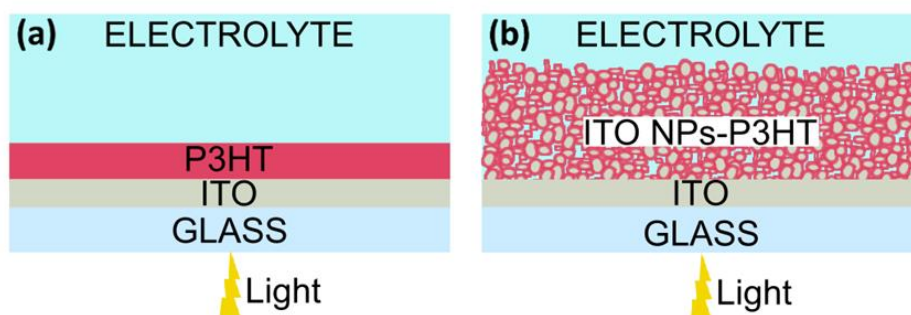
Figure 3.1. A cartoon depicting the planar (ITO/P3HT, panel a) and the mesoporous (ITO/ITO NPs/P3HT, panel b) device structures.

The mesoporous configuration is characterized by acquiring SEM cross-sectional images that show the surface area increase associated to the new morphology (figure 3.2 a). SEM images are acquired in the same experimental conditions of the ITO/p-i-n samples (see section A.4). A proper rr-P3HT solution concentration (10 g l^{-1}) leads both to a perfect intercalation of the rr-P3HT inside the nanostructure, highlighted by the comparison between the full device architecture (figure 3.2 a) and the uncovered ITO NPs-based electrode (figure 3.2 b), to obtain a rr-P3HT optical absorption comparable to the one obtained with the planar ITO/P3HT sample (figure 3.2 c).
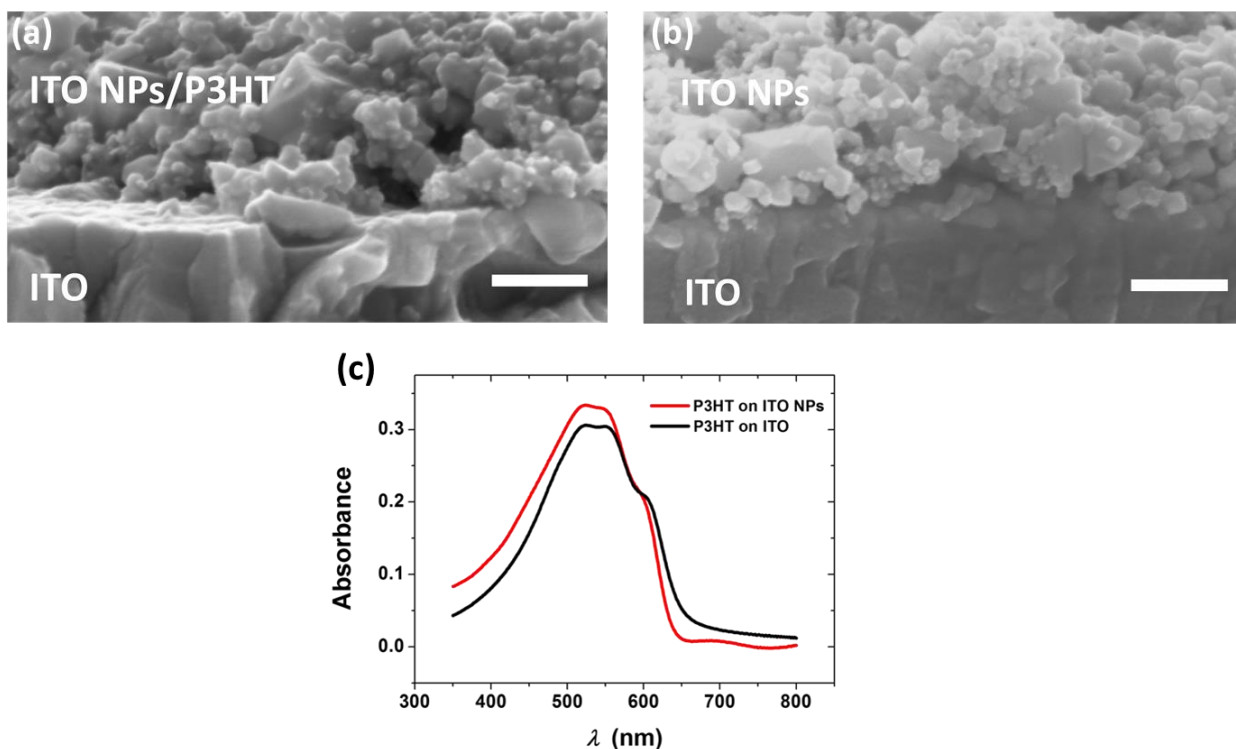
Figure 3.2. SEM cross-section image of the ITO/ITO NPs/P3HT (a) and the ITO/ITONPs (b) architectures. Scale bar, 100 nm. (c) Optical absorbance spectra of rr-P3HT layers deposited on top of ITO NPs (red line) and planar ITO (black line).

The observations made by looking at the SEM images are confirmed by carrying out Kr physical adsorption experiments (appendix B.2). The ITO/ITONPs/P3HT device exhibits a surface area value very close to the one of the ITO/ITONPs uncovered electrode (212 ± 21 cm^2 and 186 ± 19 cm^2, for 1 cm x 1 cm slides, respectively), associated to an enhancement factor of 186 ± 19 respect to the geometrical surface area.

Atomic force microscopy (AFM) images (appendix B.2) complete the morphological characterization, highlighting the surface roughness increase passing from the planar (figure 3.3 a) to the mesoporous (figure 3.3 b) rr-P3HT based devices, associated to a Roughness Mean Square (RMS) value of 6 nm and 16 nm respectively.
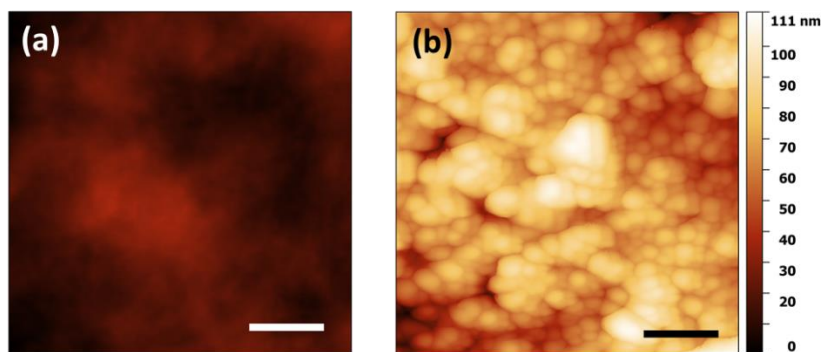
Figure 3.3. AFM topography images of the planar and mesoporous rr-P3HT-based devices, respectively. Scale bar, 200 nm.

3.3   Electrochemical characterization

A variation in the electrode morphology can lead in principle to a different position and occupation of its energy levels [151]. For this reason, the work function (WF) of the ITO/ITO NPs electrode is firstly checked by performing Kelvin probe measurements (appendix B.2), finding a comparable WF value for the ITO NPs modified and unmodified ITO electrodes (4.6 and 4.5 eV respectively). This indicates that in this specific case the electronic structure is not affected by the morphological change.

Furthermore, the electrochemical properties of the full device architecture are investigated, since the porous structure can affect the length of the depletion region inside the semiconductor layer, the Helmoltz layer capacitance and the charge transfer processes at the polymer/electrolyte interface [151–153]. A useful technique that allows to have an overview on all these properties is the electrochemical impedance spectroscopy (EIS). EIS is performed with the same electrochemical set up employed for the photocurrent and photovoltage measurements (see appendix A.2 and B.2 for more details) and it consist in the evaluation of the impedance of the system by applying voltage sinusoidal perturbations (in the order of tens of millivolts) superimposed to a constant bias between the sample (WE) and the RE. The experiment is carried out by varying the frequency at a single voltage oscillation amplitude. Since the system is subject to a small perturbation, it is possible to consider only the linear part of the current-voltage curve, simplifying the frequency analysis. The

impedance response can be modeled with equivalent electrical circuits, where the single components are related to the specific physical processes that take place at the device/electrolyte interface, such as the double layer capacitance build-up and charge transfer processes. EIS is carried out on planar an mesoporous rr-P3HT based devices, both in dark and upon CW light excitation ($\lambda = 470$ nm, 2.8 mW mm^{-2}) and by applying a constant potential equal to the open circuit potential (V_{eq}) in dark (0.2 V vs. Ag/AgCl for the ITO/P3HT device and 0.19 V vs. Ag/AgCl for the ITO/ITO NPs/P3HT device) and light (0.36 V vs. Ag/AgCl for the ITO/P3HT device and 0.33 V vs. Ag/AgCl for the ITO/ITO NPs/P3HT device) conditions, in order to maintain the system close to the electrochemical equilibrium. The impedance phase and modulus vs. frequency traces (Bode plots) are reported in figure 3.4 panels a-d. The phase diagrams of the ITO/P3HT device (figure 3.4 panels a and b, for dark and light conditions, respectively) are composed by three distinct regions, exhibiting one minimum at frequency values higher than 10 kHz, one maximum between 100 Hz and 10 kHz and one maximum at frequencies less than 100 Hz. The equivalent circuit that best model this system (figure 3.4 e and f) comprises, accordingly, three main circuital loops: (1) capacitance and resistance values Cs and Rs that describe the electrolytic solution; (2) an RC circuit related to the polymer/electrolyte interface, composed by the charge transfer resistance, R_{CT}, and by a constant phase element Q_{DL} that models the Helmholtz double layer. The constant phase circuital component describes the behavior of an imperfect capacitor, allowing to take into account non-ideal processes that affect the polymer/electrolyte interface double layer capacitance, such as ionic contributions to surface conductivities, ion diffusion into the polymer layer or surface heterogeneities [154,155]; (3) a resistor and a capacitor in parallel, described by R_p and C_p values, that model the charge reorganization processes that can take place within the polymer semiconductor or on its surface, leading to the formation of a space charge layer at the rr-P3HT/electrolyte interface or surface states that mediate the charge transfer to the electrolytic solution [151,156]. In order to understand the phenomenon that is related to the presence of C_p and R_p terms, additional experiments are required, falling out from the scope of the present work. The illuminated devices exhibit a substantial decrease of both the

impedance modulus and the phase angle in the low frequency region (<10 Hz), probably as a consequence of ions percolation within the polymer bulk and photo-oxidation phenomena (figure 3.4 b). For this reason, the equivalent circuit related to the experiment light condition requires the addition of a Warburg element, commonly employed for modeling the diffusion of ions inside electrodes [157].

Interestingly, the ITO/ITO NPs/P3HT device shows a very different behavior (Figure 3.4 panels c and d for dark and light conditions, respectively). The correspondent equivalent circuit lacks both the RC circuital loop associated to the polymer semiconductor (R_p and C_p) and the Warburg component (figure 3.4 g). This situation can be explained by the presence of a diffused semiconducting polymer/electrolyte interface throughout the device bulk that leads to shallower surface traps and/or to a condition in which a space charge layer cannot be supported [152,153]. The fitting curves obtained by considering the equivalent circuit just discussed are in optimal agreement with the experimental data (figure 3.4 a-d, solid lines). The numerical values extracted from the fitting are depicted in table 3.1.
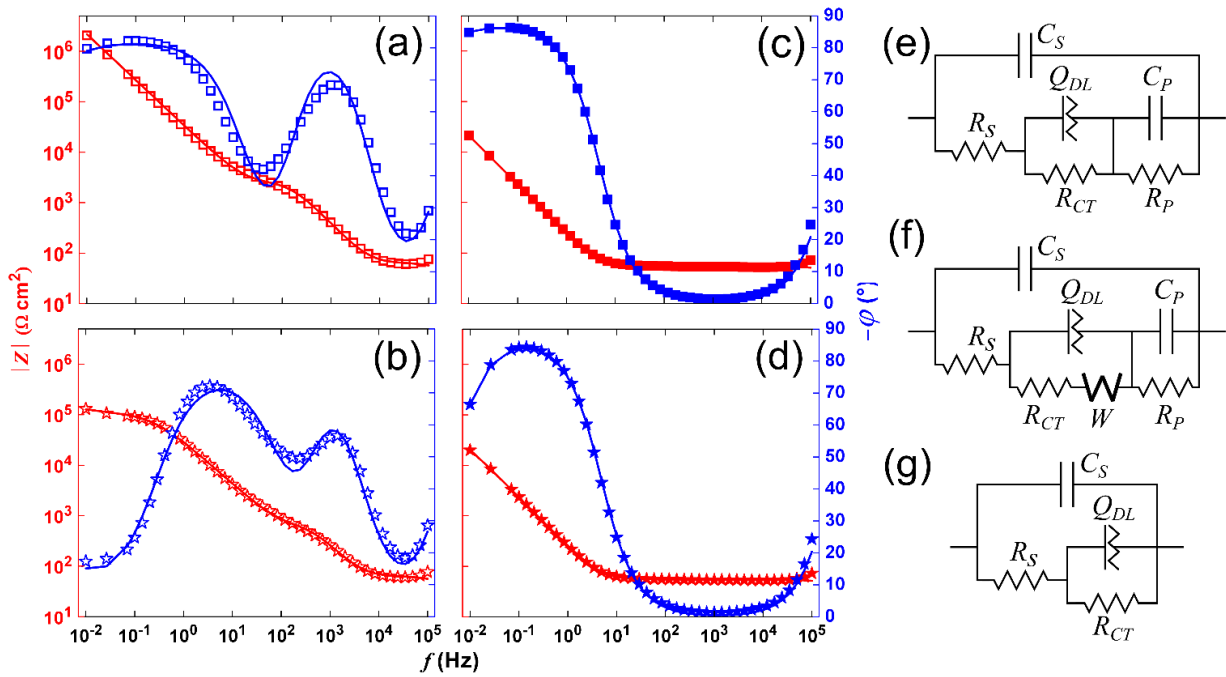
Figure 3.4. (a,c) Experimental Bode plots for the ITO/P3HT (empty squares, panel a) and ITO/ITO NPs/P3HT (filled square symbols, panel c) devices, in dark conditions. (b,d) Experimental Bode plots for the ITO/P3HT (empty stars, panel b) and ITO/ITO NPs/P3HT (filled stars symbols, panel d) devices, upon photoexcitation (central emission wavelength, 470 nm; photoexcitation density, 2.7 mW/mm2). Impedance values are normalized to the geometrical device area in all cases. Equivalent circuits used to model experimental data are shown in panels (e) and (f), for the ITO/P3HT devices, in dark and light conditions respectively, and (g), for the ITO/ITO NPs/P3HT devices, for both dark and light conditions. Fitting curves are shown as solid lines in all considered cases (chi-squared values χ^2 = 0.432; 0.207; 0.138; 0.135 for fitting curves reported in panels (a), (b), (c) and (d), respectively).

Device	Y_0 (μS cm^{-2})	n	R_{CT} (Ω cm^2)	R_S (Ω cm^2)	C_S (μF cm^{-2})	W (μS cm^{-2})	R_P (Ω cm^2)	C_p (μF cm^{-2})
ITO	7.4	0.92	-	53	$1.4 \cdot 10^{-2}$	-	-	-
ITO/ITO NPs	782	0.97	-	55	$1.2 \cdot 10^{-2}$	-	-	-
ITO/P3HT (Dark)	5.7	0.91	$43 \cdot 10^6$	65	$1.2 \cdot 10^{-2}$	-	$2.1 \cdot 10^3$	0.5
ITO/P3HT (Light)	6.4	0.87	$1 \cdot 10^5$	62	$1.1 \cdot 10^{-2}$	111	$4.1 \cdot 10^2$	0.9
ITO/ITO NPs/P3HT (Dark)	685	0.97	$5.1 \cdot 10^5$	55	$1.1 \cdot 10^{-2}$	-	-	-
ITO/ITO NPs/P3HT (Light)	671	0.97	$5.6 \cdot 10^4$	55	$1.1 \cdot 10^{-2}$	-	-	-

Table 3.1. Numerical values of the circuital components used to fit the EIS experimental data obtained at the equilibrium potential in dark (0.2 V *vs.* Ag/AgCl for the ITO/P3HT device and 0.19 V *vs.* Ag/AgCl for the ITO/ITO NPs/P3HT device) and light conditions (0.36 V *vs.* Ag/AgCl for the ITO/P3HT device and 0.33 V *vs.* Ag/AgCl for the ITO/ITO NPs/P3HT device).

EIS measurements are also performed on the ITO and ITO/ITO NPs electrodes. The central role of rr-P3HT in the photoinduced changes in both the impedance modulus (figure 3.5 a) and phase (figure 3.5 b) is highlighted by the exact correspondence of the bode plots acquired in light and dark conditions (figure 3.5).
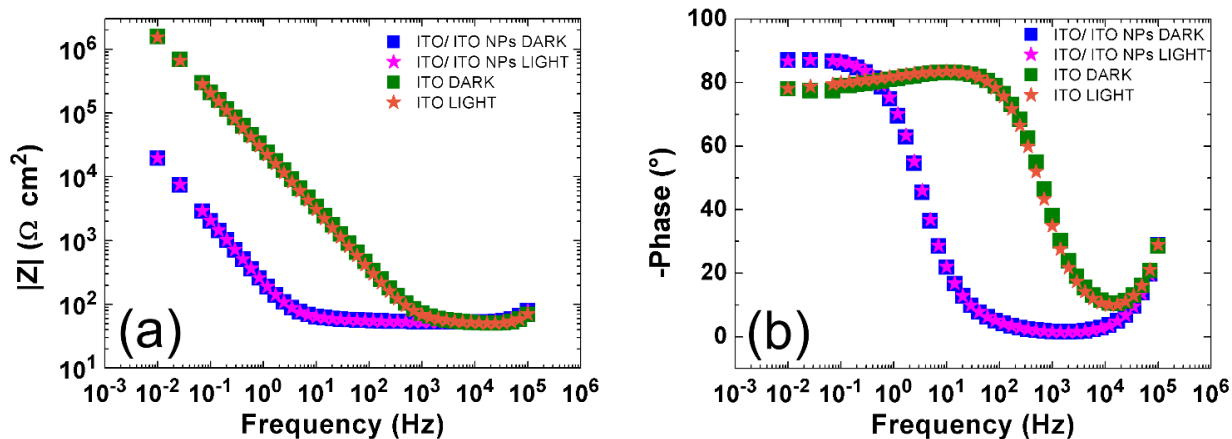
Figure 3.5. Impedance modulus (a) and phase (b) of ITO and ITO/NPs samples, obtained from EIS measurements acquired in dark and upon light excitation (central emission wavelength, 470 nm; photoexcitation density, 2.8 mW mm^{-2}). Impedance moduli are normalized to the geometrical device area.

In order to obtain a direct comparison of the interfacial properties of the planar and mesoporous rr-P3HT-based devices, the charge transfer resistance (R_H) and Helmholtz double layer capacitance (C_H) quantities are calculated from the Helmholtz RC circuital loop from the following equations:

$$\frac{1}{Z_{eq,H}} = \frac{1}{R_{CT}+Z_W} + \frac{1}{Z_{Q_{DL}}} ; \quad C_H = -\frac{\text{Im}(Z_{eq,H})}{\omega|Z_{eq,H}|^2} ; \quad R_H = \frac{|Z_{eq,H}|^2}{\text{Re}(Z_{eq,H})}$$

where $Z_{eq,H}$ represents the impedance of the Helmholtz circuital loop. R_H and C_H values are calculated at the lowest measured frequency (0.01 Hz), since the Helmholtz loop contribution is mainly related to ionic diffusion processes and become predominant at low frequencies. In particular, in the low frequency regime, C_H in dark is directly related to surface area increase introduced by the porous morphology, R_H and C_H in light provide information about the photoelectrochemical processes that take place at the device/electrolyte interface. In dark conditions C_H correspond to 7.2 µF cm^{-2} in the ITO/P3HT case (in agreement with previous reports [154,158,159]) and 742 µF cm^{-2} for the ITO/ITO NPs/P3HT device, corresponding to an enhancement factor of about 100, the same order of magnitude of the one obtained from Kripton physical adsorption experiments (212 ±21). The difference between the values can be related to the different atomic radii between the ionic species in the electrolyte and

Kripton. When the devices are photoexcited, the difference between the porous and planar C_H values is reduced, corresponding to a decrease in the enhancement factor to about 20. This is related to the photoinduced accumulation of charges at the planar rr-P3HT/electrolyte interface, that increases the C_H value for the flat case to about 37 µF cm^{-2}, while the C_H value for the mesoporous rr-P3HT-based sample upon light is comparable to the one in dark (723 µF cm^{-2}). The ITO/ITO NPs/P3HT device exhibits lower R_H values both in dark and light conditions as compared to the planar morphology (245 and 51 kΩ cm^2 respect to 11000 and 146 kΩ cm^2 for the ITO/P3HT sample, in dark and upon light, respectively), reflecting an enhanced propension of developing interfacial charge transfer processes at the mesoporous polymer/electrolyte interface.

In order to extend the EIS characterization to the regime out of equilibrium, i.e. by applying a constant potential shifted from V_{eq}, it is convenient to adopt a simplified approach, based on the modeling of the system with a frequency dependent RC circuit and considering it in the low frequency regime [154,159–161]. First of all, effective capacitance and resistance, $C(\omega)$ and $R(\omega)$, are calculated from the measurements in equilibrium conditions using the following equations:

$$C(\omega) = -\frac{\text{Im}(Z)}{\omega|Z|^2} \; ; \quad R(\omega) = \frac{|Z|^2}{\text{Re}(Z)}$$

Being Z the measured impedance. $C(\omega)$ and $R(\omega)$ values at 0.01 Hz are closely comparable to C_H and R_H (Table 3.2), confirming the reliability of the simplified model and that the response in the low frequency domain is mainly due to processes that take place in the Helmholtz layer.

	C_H (µF cm^{-2})	$C(\varpi)$ (µF cm^{-2})	R_H (kΩ cm^2)	$R(\varpi)$ (kΩ cm^2)
ITO/P3HT (dark)	7.2	7.7	11000	11000
ITO/P3HT (light)	37	36	146	136
ITO/ITO NPs/P3HT (dark)	742	748	245	234
ITO/ITO NPs/P3HT (light)	723	730	51	50

Table 3.2. Capacitance and resistance values for the planar and the mesoporous device architecture, in dark and light conditions, as obtained by the EIS data fitting (C_H and R_H) and by assuming a frequency-dependent, equivalent circuit ($C(\omega)$ and $R(\omega)$). Reference frequency, $\varpi = 2\pi \cdot 0.01$ Hz. All data are normalized to the geometrical device area.

$C(\omega)$ and $R(\omega)$, calculated for both the planar and the mesoporous samples, are displayed respectively in figure 3.6 a and c as a function of the frequency. The ITO/ITONPs/P3HT device exhibits higher capacitance values at low and intermediate frequencies, respect to the planar case. Furthermore, it does not present relevant differences between dark and light conditions. The ITO/P3HT architecture instead, at the lowest frequencies (<0.1 Hz) upon light, shows a higher capacitance as compared to dark values, probably due to intercalation of ions within the polymer bulk that leads to an increased rr-P3HT/electrolyte interface effective area. By comparing $R(\omega)$ in the two device architectures at low frequencies, and in dark/light conditions, it is possible to confirm that (i) The occurrence of charge transfer reactions is promoted by light ($R(\omega)$ during light excitation is lower than in dark, for both samples), and (ii) the mesoporous rr-P3HT-based morphology facilitates the occurrence of interfacial charge transfer reactions, highlighted by the fact that $R(\omega)$ value is lower than in the flat case. $C(\omega)$ and $R(\omega)$ are also calculated at 0.01 Hz ($C(\varpi)$ and $R(\varpi)$) from the measured Z in the out of equilibrium condition, varying the applied bias in the range − 0.3 V ÷ 0.36 V (figure 3.6 b and d, respectively). $R(\varpi)$ is substantially lowered at − 0.3 V in all conditions, respect to their corresponding equilibrium values (relative decrease of 97%, 79% for planar rr-P3HT-based device in dark, light; 97%, 78% for the mesoporous one in dark, light), indicating that a cathodic process is occurring at this specific value of the applied bias. $C(\varpi)$ presents a slight increment as the external bias becomes more negative (about 85% and 40% relative increase at – 0.3 V in the planar and mesoporous devices, respectively). One explanation for this phenomenon may reside in the occurrence of reversible

intercalation of redox ions at the interface, which results from faradaic processes, corresponding to a pseudo-capacitance contribution [162]. Moreover, a peculiar dependence of C(ϖ) on the external bias of the illuminated ITO/P3HT sample around 0 V vs. Ag/AgCl is noticeable. The interpretation of this effect is not straightforward and requires additional experiments that will be the object of a future work.
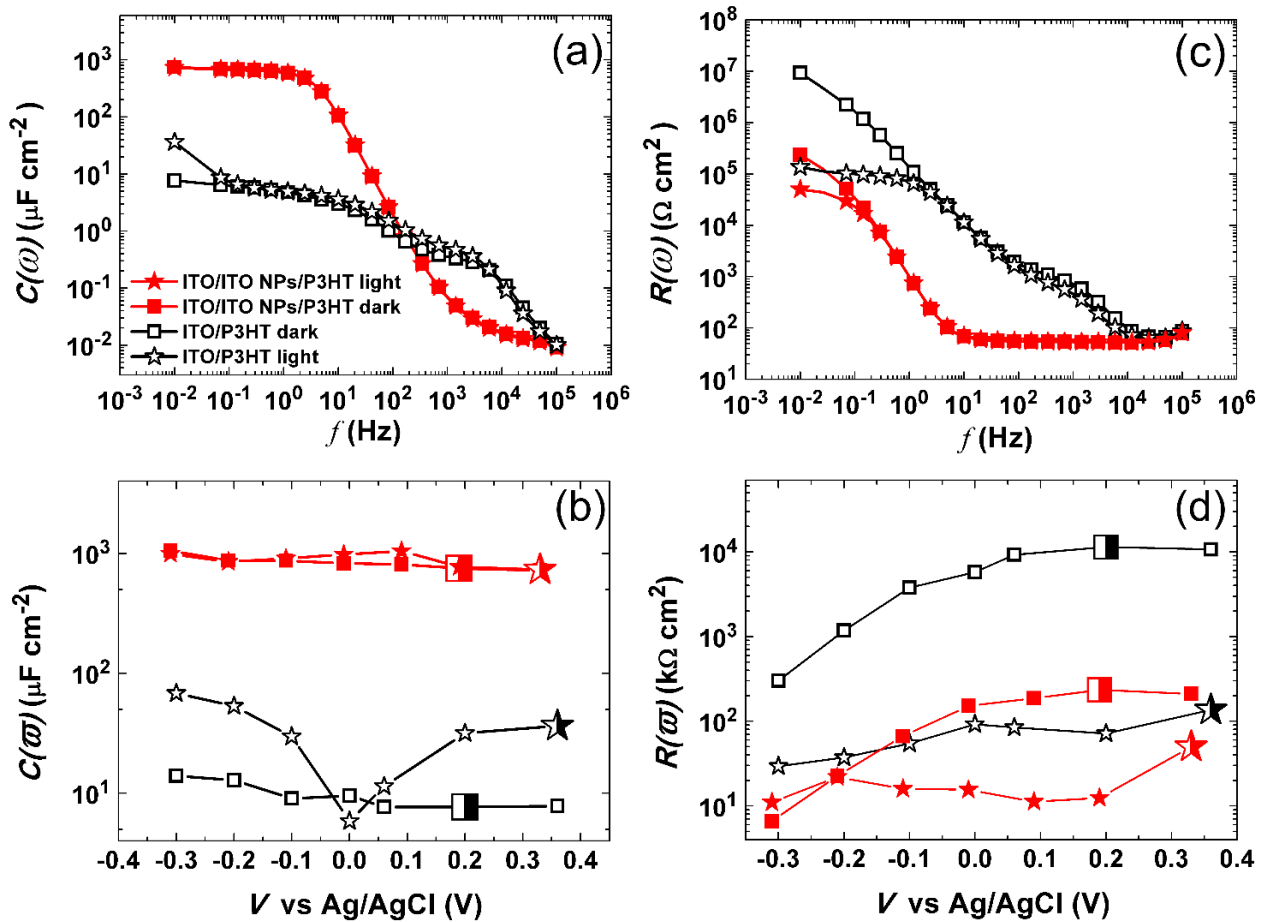
Figure 3.6. Device/electrolyte interface electrochemical behavior for ITO/P3HT in dark (empty squares, black) and upon light stimulation (empty stars, black), ITO/ITO NPs/P3HT in dark (filled squares, red) and upon light excitation (filled stars, red). Panels (a) and (c) show the effective capacitance C(ω) and resistance R(ω) as a function of the frequency, as obtained from EIS experimental data acquired at the corresponding equilibrium potential. Panels (b) and (d) report C(ϖ) and R(ϖ), calculated at $\varpi = 2\pi \cdot 0.01$ Hz, as a function of the external bias. Light excitation: 470 nm, 2.73 mW mm^{-2} photoexcitation density. All data are normalized to the geometrical device area.

In order to characterize the charge transfer processes taking place at the device/electrolyte interface photocurrent measurements are carried out (figure 3.7 panels a and b, see appendix B.2 for additional

experimental details). The photocurrent (J_{ph}) traces recorded by exciting the ITO/P3HT device with 250 ms light pulses ($\lambda = 470$ nm) in equilibrium conditions, show the capacitive behavior fully discussed in section 2.2 (figure 3.7 a). Conversely, the ITO/ITO NPs /P3HT sample exhibits a purely faradaic photocurrent, represented by a constant signal during the whole illumination time (figure 3.7 c). When a negative bias is applied between the samples and the RE, the intensity of the capacitive spikes presented by the planar device are reduced and a constant faradic component does appear (figure 3.7 a). However, the ITO/ITO NPs/P3HT at $-$ 0.2V is about one order of magnitude higher than in the flat case (figure 3.7 a and c, amounting to $\sim$ 100 μA cm^{-2} and $\sim$ 10 μA cm^{-2} respectively). The overall difference in the photocurrent response that is noticed between the two architectures reflects the reduced charge transfer resistance displayed by the mesoporous device. In order to investigate the origin of the charge transfer events, the J_{ph} experiments are repeated by fluxing N_2 inside the electrolytic solution, for removing the dissolved molecular oxygen (figure 3.7 b and d). In this condition the faradaic contribution to the photocurrent drops to zero in both cases, confirming the central role of oxygen in the charge transfer processes, in agreement with previous works [78,131], and already discussed in chapter 2.
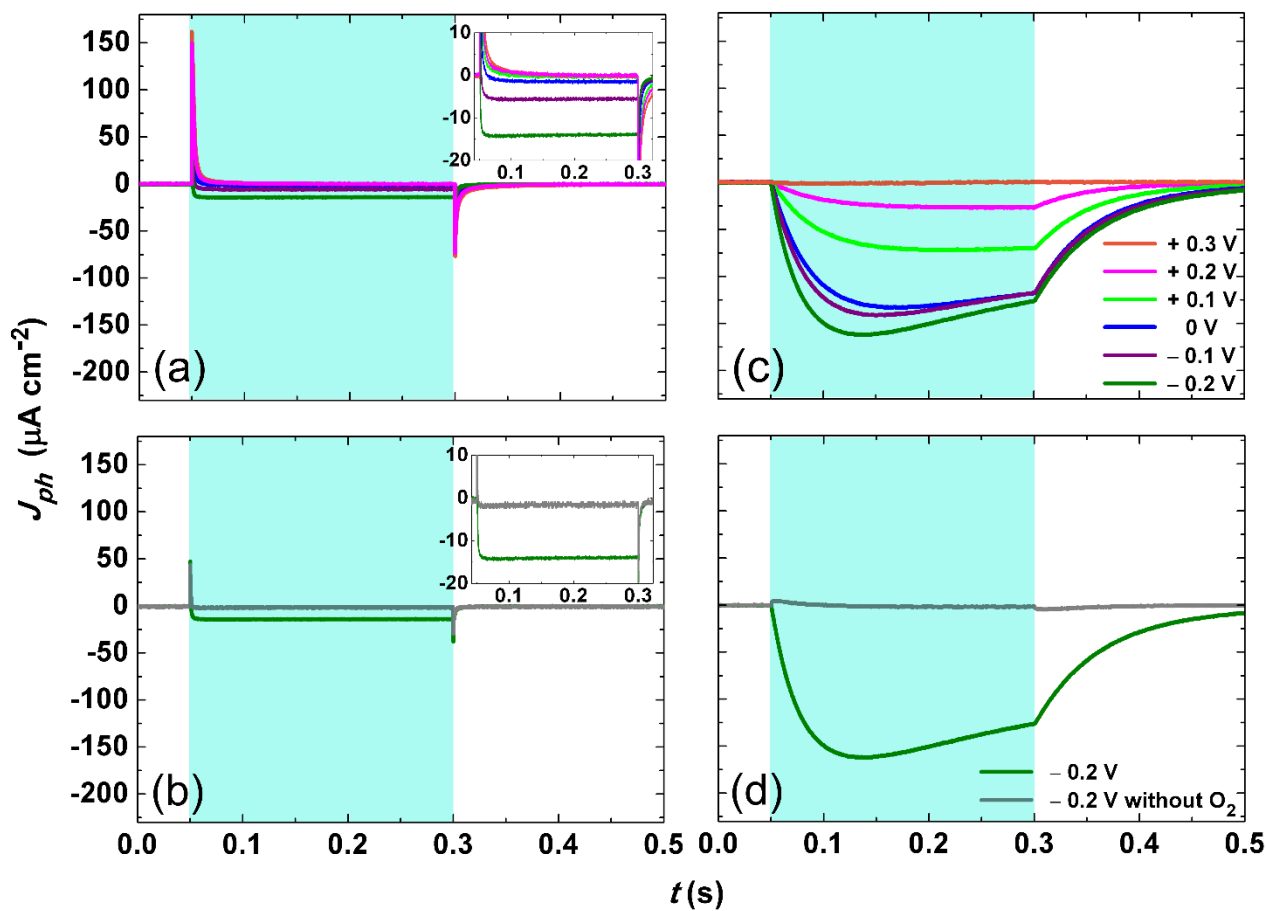
Figure 3.7. Photocurrent response of the ITO/P3HT (a) and ITO/ITO NPs/P3HT (c) devices, upon visible light excitation (470 nm, 250 ms, 2.7 mW mm^{-2} photoexcitation density) and under external bias (values are referenced to the Ag/AgCl reference electrode). The inset in panel (a) is a zoom over the steady state photocurrent signal in planar devices. Panels (b) and (d) report a comparison of the photocurrent density recorded in ITO/P3HT (b) and ITO/ITO NPs/P3HT (d) devices, before (green solid line) and after (grey solid line) oxygen removal. The faradaic contribution to the photocurrent is completely suppressed in both cases. All data have been normalized to the geometrical device area

The dependence of J_{ph} from the light stimulus direction is also assessed (figure 3.8). When the light comes from the electrolyte side, a decrease in the capacitive spike amplitude is noticeable (figure 3.8 a). As discussed in section 2.2, this phenomenon is due to the fact that the ITO/P3HT interface, where the exciton dissociation occurs, is now at the opposite side. Since the thickness of the planar rr-P3HT-based sample is higher than the exciton diffusion length (approx. 10 nm [135,136]), excitons face an increased recombination probability within the polymer bulk. The mesoporous device response instead, does not show any dependence from the light excitation direction (figure 3.8 b). This is

probably due to the establishment of a diffused polymer/electrolyte interface within the porous ITO/ITO NPs/P3HT device bulk.
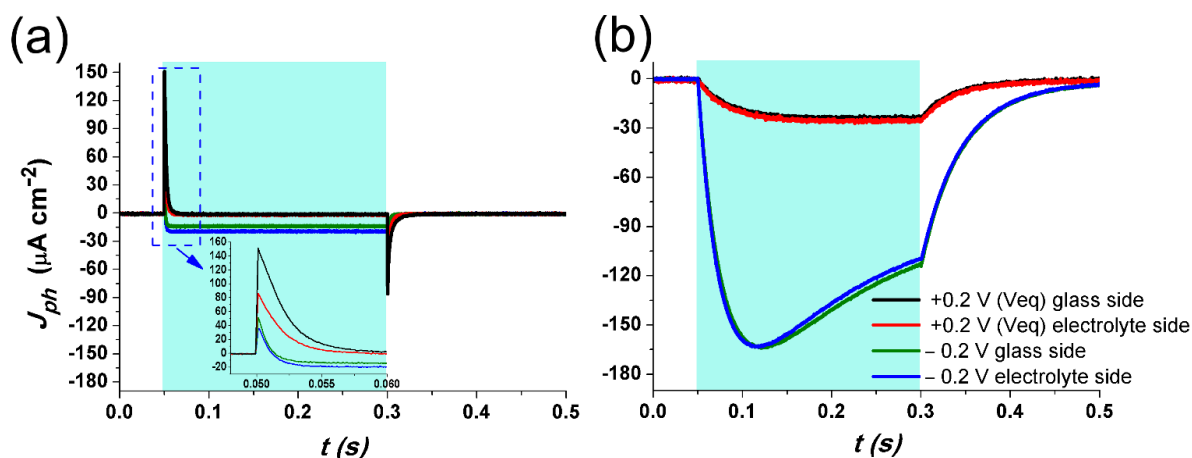
Figure 3.8. Photocurrent response of the ITO/P3HT (a) and ITO/ITO NPs/P3HT (b) devices, upon visible light excitation (470 nm, 250 ms, 2.8 mW mm^{-2} photoexcitation density), under external bias (potential values *vs.* Ag/AgCl reference electrode) and for different light incidence directions. All data are normalized to the geometrical device area.

The electrochemical characterization is concluded by testing the devices stability, since the optical and electronical properties of the organic semiconductor may be affected by the photoinduced faradaic reactions. Despite rr-P3HT has already shown an optimal durability when employed as the photoactive layer in electrochemical [131,141,163] and biological *in-vivo* [81] applications, it is necessary to check if this is the case of also for the mesoporous morphology and in the experimental conditions adopted in the present work. For this purpose, UV-Vis spectra of the ITO and ITO/ITO NPs electrodes (figure 3.9 a,b) and of the full device architectures (figure 3.9 c,d) are acquired before and after the electrochemical experiments, showing no significant differences and confirming the excellent rr-P3HT stability. In addition it is possible to appreciate the optimal stability of the uncovered ITO-based substrates, in line with recent literature [164].
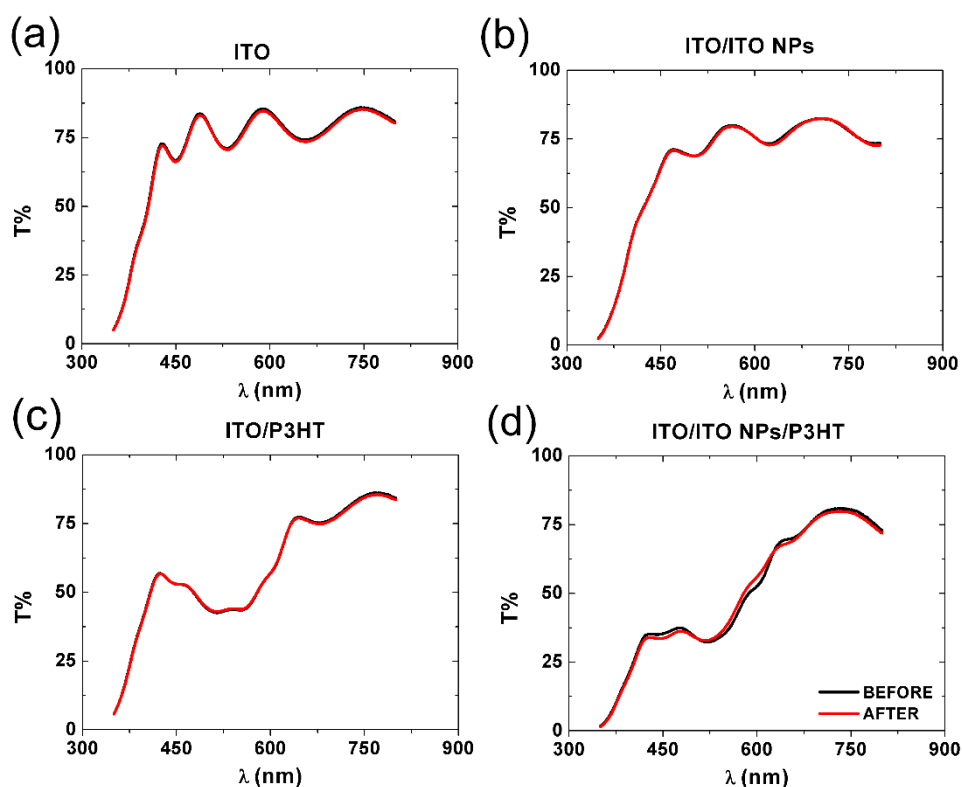
Figure 3.9. UV-Vis transmission spectra of the ITO (a), ITO/ITO NPs (b), ITO/P3HT (c) and ITO/ITO NPs/P3HT (d) devices, before and after all the electrochemical measurements discussed in section 3.3 (total illumination time during the electrochemical measurements: 60 minutes; external bias range: -0.3 ÷ 0.36 V vs. Ag/AgCl).

3.4 Surface potential measurements

Before testing the new mesoporous device architecture with living cells, the photoinduced polymer surface charging is characterized in the same conditions of the electrophysiological experiments, by carrying out surface potential measurements, introduced in chapter 2 (see appendix A.8). Figure 3.10 panel a and b depicts the results obtained by photoexciting the flat and mesoporous rr-P3HT based morphologies with 5 ms, 470 nm, light pulses. Differently from the photocurrent measurements case, the ITO/ITO NPs/P3HT sample shows a capacitive charging at the polymer/electrolyte interface, probably as a consequence of the different electrical scheme associated to the surface potential experiments, in which the ITO-based electrode is floating (figure 3.10 a). The positive spike related to the surface photocharging is about one order of magnitude lower than in the planar case, but presents a similar dependence from the illumination intensity (*I*) (figure 3.10 panel b). In addition to

the capacitive behaviour, the mesoporous morphology introduces a negative variation of the surface potential, that is superimposed to the fast non-faradaic photocharging and reaches a constant value after 2 ms. The negative plateu remains unchaged for the whole illumination period (figure 3.10 a), and does not decay to zero even when the photoexcitation is extended to 200 ms (figure 3.10 panel c). Accordingly to photocurrent experiments, this behavior can be attributed to the negative charging of the polymer surface and to the subsequent establishment of redox reactions at the device/electrolyte interface.
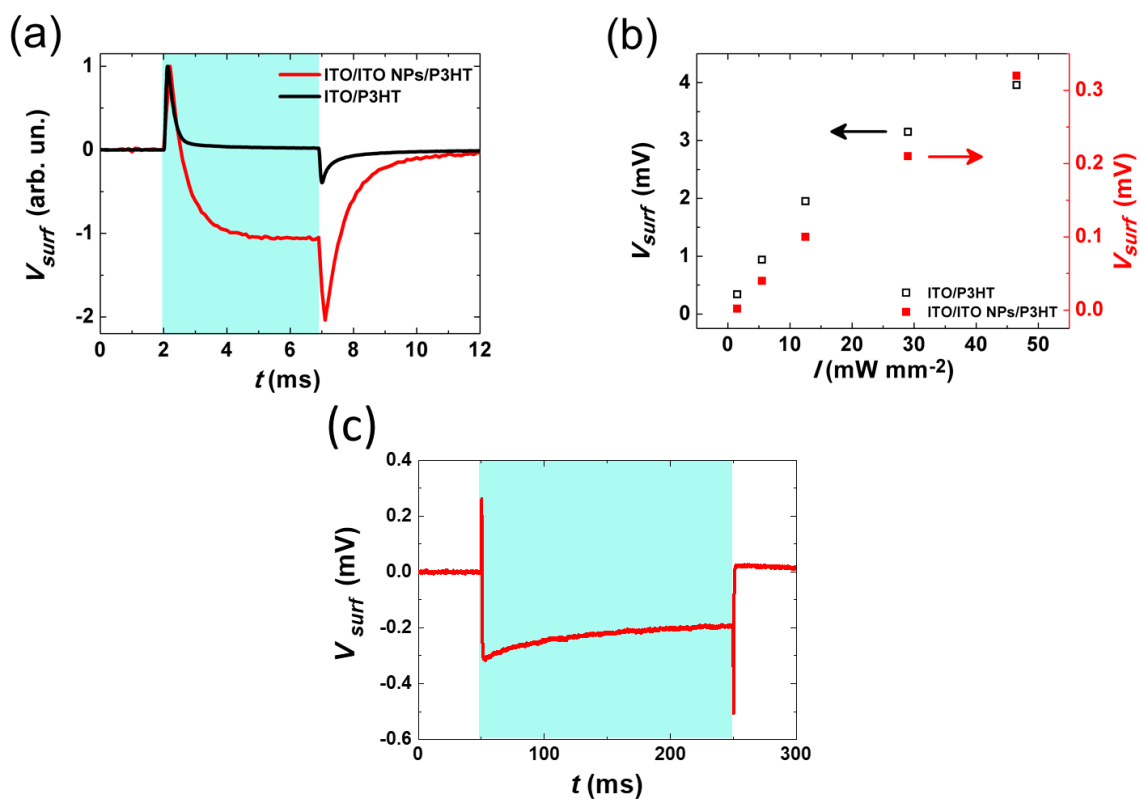
Figure 3.10. (a) Normalized surface potential V_{surf} recorded in the close proximity ($\sim 2\ \mu$m) of the polymer surface, in the case of flat devices (black solid line) and mesoporous devices based on ITO NPs (red solid line). Photoexcitation (pulse duration, 5 ms; excitation wavelength, 470 nm; illumination density, 46.5 mW mm^{-2}) is represented by the cyan shaded area. (b) Dependence of the surface potential positive peaks on photoexcitation density I. (c) V_{surf} trace acquired by exciting the ITO/ITO NPs/P3HT device with a 200 ms light pulse (excitation wavelength, 470 nm; illumination density, 46.5 mW mm^{-2}).

3.5 HEK-293 cells electrophysiology

HEK-293 cells cultures on top of ITO/P3HT and ITO/ITO NPs/P3HT are prepared as previously described in chapter 2 (see also Appendix A.7). In order to verify that the porous structure does not introduce any change in the cellular proliferation and morphology, bright-field and fluorescence images of the cells adhered on the different devices are acquired. DAPI and phalloidin-FITC are employed for the labeling of cells nuclei and cytoskeleton respectively (Appendix B.3). The acquired images do not show significant differences between single and multiple cells cultured on the planar (figure 3.11 a,b and figure 3.12 a,b) and mesoporous (figure 3.11 c,d and figure 3.12 c,d) architectures.
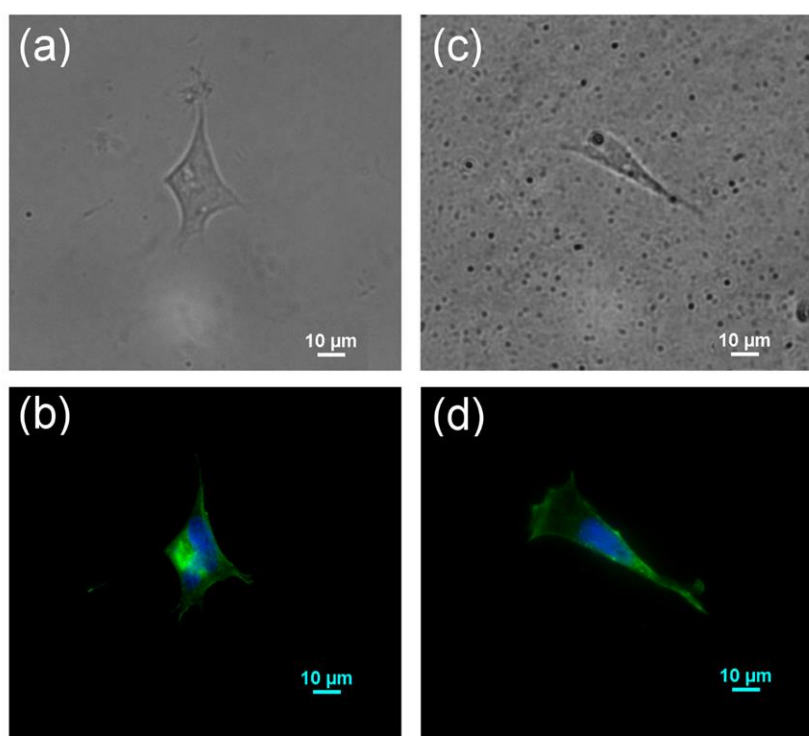
Figure 3.11. Representative bright field and Immunofluorescence images of single HEK-293 cells plated on top of ITO/P3HT (a, b) and ITO/ITO NPs/P3HT (c, d) devices, after 72 hours incubation. HEK-293 cells F-actin is stained with Phalloidin (green) and their nucleus with DAPI (blue).
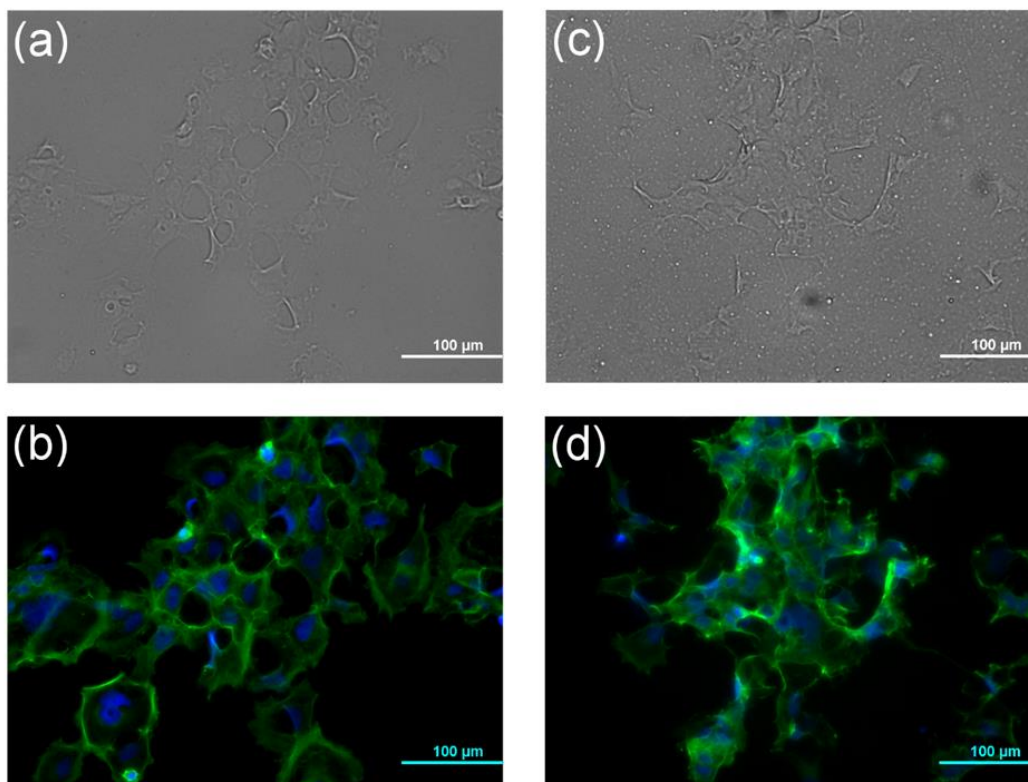
Figure 3.12. Representative bright field images of multiple HEK-293 cells plated on top of ITO/P3HT (a) and ITO/ITO NPs/P3HT (c) devices. Immunofluorescence images of HEK-293 cells, plated on top of ITO/P3HT (b) and ITO/ITO NPs/P3HT (d) devices, collected in the same field of view of the bright field images in panel a and b. Cells incubation time: 72 hours. HEK-293 cells F-actin is stained with Phalloidin (green) and their nucleus with DAPI (blue).

Whole-cell patch clamp electrophysiology recordings are then performed, in current clamp configuration (I=0) and upon light excitation, adopting the same experimental conditions employed for the surface potential measurements (5 ms light pulses, $\lambda = 470$ nm; illumination intensity ranging from 1.5 to 46.5 mW mm^{-2}, figure 3.13 a and b) During the first 1ms after illumination onset, the variation of the potential inside the cells grown on top of the two device morphologies exhibits a similar dynamic but with a different intensity, being about two times lower in the mesoporous case. This signal contribution resembles the capacitive charging of the rr-P3HT/electrolyte interface discussed in paragraph 3.4. Over a longer timescale, the situation is markedly different. The cells inner potential variation induced by the flat interface is related to the membrane capacitance change

due to the photoinduced heating of the polymer surface (figure 3.13 a and schematized in figure 3.15). The cells grown on top of the rr-P3HT-based mesoporous device show an opposite behavior, consisting in a negative constant variation of the membrane potential until the light is switched off, resembling the photoinduced surface potential trend (figure 3.13 b).
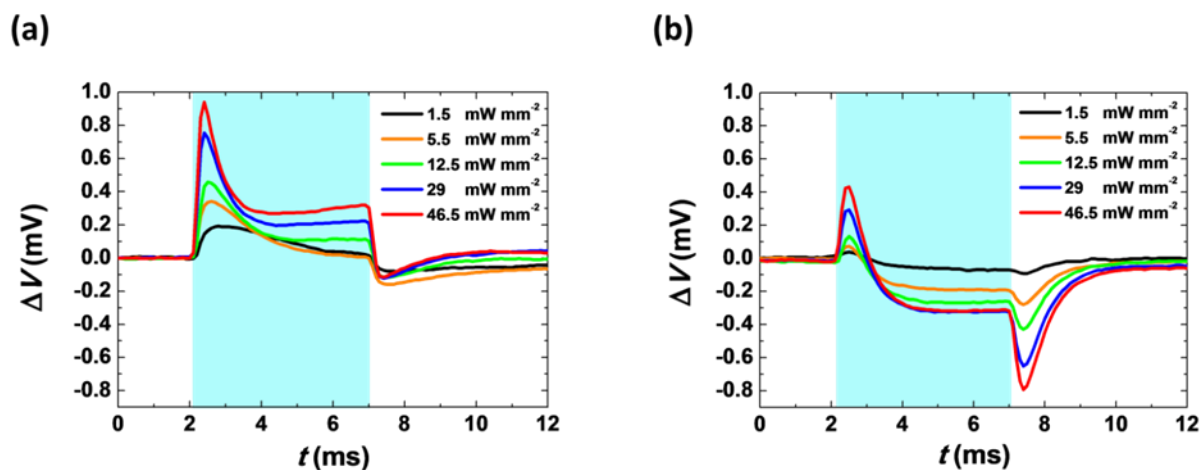
Figure 3.13. Variation of the potential inside HEK-293 cells grown on top of ITO/P3HT (panel a) and ITO/ITO NPs/P3HT (panel b) samples for different photoexcitation densities (5 ms light pulses, 470 nm maximum emission wavelength, photoexcitation is represented by the cyan shaded area).

The mechanism behind the HEK-293 cells electrophysiological response, can be clarified by considering the different effects that it is possible to photo-induce at the device/electrolyte interfaces, resumed in figure 3.14. The photoexcited flat rr-P3HT-based device (figure 3.14 panel a) presents a positive charging of the polymer/electrolyte interface, counterbalanced by an accumulation of electrons in the ITO layer. This fast capacitive photo-charging causes a transient positive photocurrent peak and a positive surface potential signal, observable during the first 1 ms after the optical excitation starts. The non-radiative recombination of excitons instead, gives rise to a heating of the polymer surface. This two different processes elicit the cells electrical response in the $t < 1$ ms and $t > 1$ ms time scales, respectively, as already discussed in paragraph 2.4.2. The mesoporous sample, when optically stimulated, exhibits a bimodal electrical response, characterized by a capacitive positive surface photocharging at $t < 1$ ms (figure 3.14 panel b1) and a surface collection of electrons followed by a faradaic electron transfer taking place at $t > 1$ ms (figure 3.14 panel b2), attributed to the oxygen reduction reaction. These phenomena are evidenced during photocurrent and surface potential experiments and their correspondence is found in cells membrane potential variation traces.
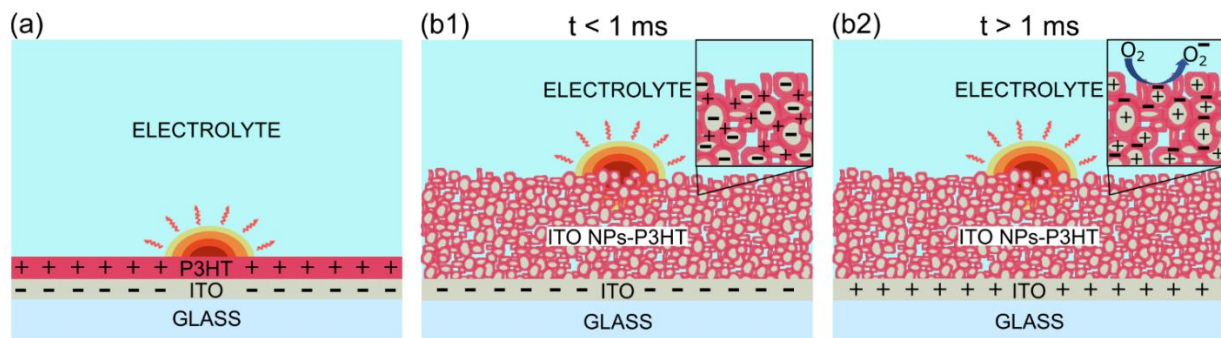
Figure 3.14. Schematic drawing of the main processes occurring in the planar ITO/P3HT (a) and in the mesoporous ITO/ITO NPs/P3HT (b) devices. Initial photo-capacitive current, due to hole accumulation at the polymer/electrolyte interface, is observed in both cases (panels (a) and (b1)); 1 ms after photoexcitation, however, thermal effects are observed in the first case (a), leading to cell membrane depolarization, while faradaic currents predominate in the second case (b2), mainly due to electron transfer phenomena.

At this point it is important to make some considerations about the shape of the signals recorded in the experiments with and without cells. A clear correspondence between the surface potential and cell potential variation traces attributed to electrical effects, both in the planar and mesoporous cases, is noticeable. A possible interpretation lies in the absence of an actual variation of the membrane potential. The signal acquired can be the result of a coupling of the surface signal to the recording electrode. For understanding the possible reasons of this effect, it is useful to consider the cell/device interface with a two-compartment model introduced by Fromherz et al., depicted in figure 3.15 [58,59]. The cell membrane can be divided in two regions: the basal membrane, adhered to the device surface leaving a confined space in between, the cleft region; the lateral membrane which is in direct contact with the extracellular bath. The resistance R_{cleft} that connects the cleft and the extracellular spaces, is a very useful parameter for the modeling of the cellular adhesion, as discussed in paragraph 1.6 and in several studies conducted on silicon-based semiconductor electrodes [59,165] and on gold micro electrodes [12]. Effective extracellular stimulation is possible only when cells adhere tightly to the surface of the device, achieving a R_{cleft} value much higher than the electrolyte resistance (R_{el}) [12,60]. Upon illumination and in current clamp configuration, the potential inside the cell (V_{cell}) is measured with respect to the reference bath electrode and it does not correspond to the lateral

membrane potential. The latter is indeed the difference between V_{cell} and the extracellular lateral potential (V_{surf}), corresponding to the surface potential of the illuminated region depicted in figure 3.15 a. For $R_{cleft} = 0$, no current passes through the membrane. When $R_{cleft} \approx R_{el}$ the variation of the three relevant potential values (V_{cleft}, V_{cell} and V_{surf}) is comparable, $\Delta V_{cleft} \approx \Delta V_{cell} \approx \Delta V_{surf}$, resulting in a negligible variation of the lateral membrane potential. In fact, this is observed by comparing surface potential recordings (figure 3.10) and whole cell patch clamp traces (figure 3.13), considering that in the latter case a thermal depolarization of the cell is also established, leading to a slight difference of the signal dynamics respect to the surface potential case. In light of these considerations, it is clear the necessity of adopting new fabrication strategies aimed to the enhancement of the cellular adhesion on the photoactive platforms, in order to achieve an effective electrical stimulation of the cells.
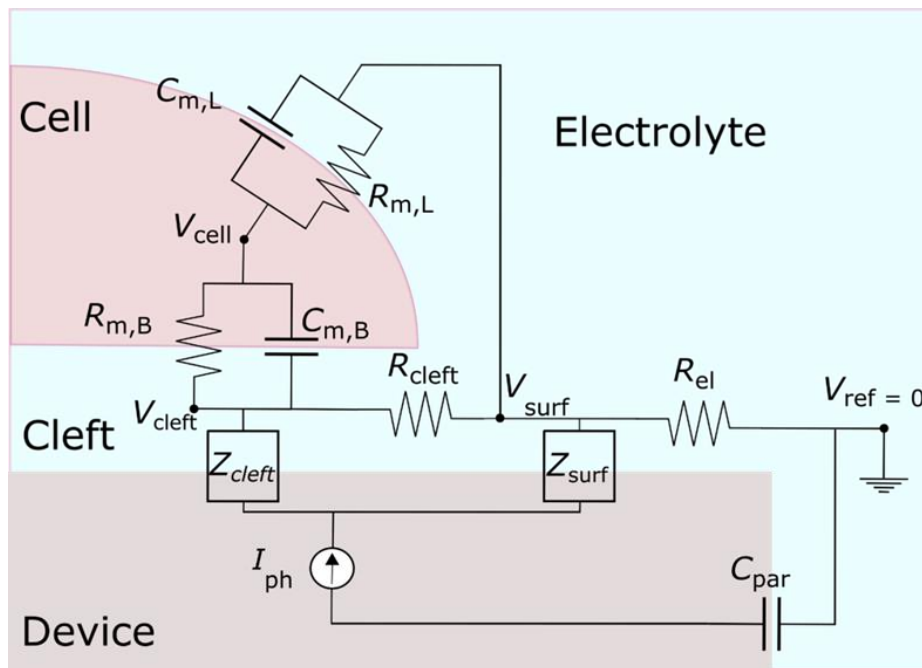
Figure 3.15. Electrical schematization of the two-compartment model applied to the case of cell stimulation. The cell membrane is divided in two different parts: the basal membrane and the lateral membrane, that are represented by a resistor and a capacitor in parallel, $C_{m,B}$ and $R_{m,B}$ and $C_{m,L}$ and $R_{m,L}$ respectively. The space confined between the basal membrane and the device is called cleft and is connected to the extracellular solution via a resistance, R_{cleft}. When the device is illuminated, a current I_{ph} circulates in the system, and the behavior of the device/electrolyte interface is described by the impedances Z_{cleft} and Z_{surf} in the cleft and extracellular regions, respectively. This situation can be established even if the device is not directly contacted to the remaining part of the circuit, because the circuit is closed on a parasitic capacitance (C_{par}) at the device/electrolyte interface. During the patch-clamp experiments in current-clamp, the potential inside the cell (V_{cell}) is measured, with respect to the counter-electrode potential V_{ref}, that can be considered equal to zero.

4. rr-P3HT pillars-based devices for living cells optical stimulation

4.1 Introduction

In the previous chapter we described the implementation of the photoactive rr-P3HT based device with a mesoporous topography, showing that it leads to a different electrochemical behavior of the polymer/electrolyte interface, characterized by an increased efficiency towards faradaic processes. However, the patch clamp experiments with HEK-293 cells highlighted the presence of a scarce device/cells electrical coupling, both in the planar and mesoporous cases, that causes a decrease in the photoinduced electrical stimulation efficacy. For this reason, we oriented our attention towards new fabrication strategies aimed to the enhancement of the electrical signal transduction at the device/cell interface. As discussed in section 1.6, one possible solution relies on the employment of microstructures for the tightening of the cellular adhesion through the cell membrane engulfment. In this chapter we present the fabrication and characterization of arrays of high aspect ratio (HAR) pillars entirely made of rr-P3HT. To the best of our knowledge, light-responsive micro- and nano-structured devices, recently reported in literature and described in paragraph 1.6, are all based on inorganic semiconductors [11,166]. The size of the HAR micropillars permits to combine the higher grade of cellular adhesion with the possibility to grow the cells in three dimensions, exploiting the advantages of 3D cell cultures. The use of structurally defined scaffolds, like polymer-based HAR pillar arrays, is strongly affecting the cell culture field since it leads to a better control over the 3D cell cultures parameters as compared to hydrogel-like scaffolds that are commonly employed for this purpose [167]. Firstly, we present the rr-P3HT pillars fabrication process, based on a highly repeatable push-coating technique [168,169], and we discuss the pillars morphological properties characterized by performing SEM and EIS measurements. Then, we show the effects of the pillars-based architecture on both primary (cortical neurons) and secondary line (HEK-293) cells in terms of viability and morphology, evaluated by SEM and fluorescence microscopy studies. Moreover, we study the cortical neurons electrical functionality and synaptic espression on top of the micro-structured

substrates by performing patch clamp recordings in dark and through the staining with specific fluorescent synaptic markers. Finally, we investigate the optically-induced effects on both HEK-293 cells and neurons mediated by the rr-P3HT pillars platforms by carrying out patch clamp recordings in presence of a light stimulus. The results presented in this chapter are included in G. Tullii, F. Giona, F. Lodola, S. Bonfadini, C. Bossio, S. Varo, A. Desii, L. Criante, C. Sala, M. Pasini, C. Verpelli, F. Galeotti, M. R. Antognazza, *High Aspect Ratio semiconducting polymer pillars for 3D cell cultures*, in preparation.

4.2   rr-P3HT microstructures fabrication and morphology

The fabrication of the rr-P3HT micro-structured substrates is carried out by taking advantage of the push-coating technique (appendix C.1). Push-coating is an adaptable and ecofriendly process for manufacturing thin polymer films, which was originally developed for organic field effect transistors [168], and recently applied also to light-emitting diodes and solar cells [169]. In push-coating, a small volume of polymer solution is sandwiched between the substrate and a millimeters-thick PDMS layer. The solution spreading between the substrate and the PDMS through capillary forces facilitates the solvent diffusion into PDMS, to form uniform thin films. Because the surface roughness of the PDMS layer determines the morphology of the push-coated film, this technique has been very recently proposed also to create nanostructured light-emitting polymer layers [170]. However, push-coating has never been employed so far to fabricate high aspect-ratio pillared structures.

rr-P3HT nano- and microstructures are typically obtained by self-assembly or by imprinting processes [171–173]. Whether the former approach is not suitable for high aspect-ratio structures, the latter requires to heat the solid polymer film well above its glass transition and crystallization temperatures before imprinting (around 170 °C for rr-P3HT), and to apply a controlled pressure on a lithographed hard stamp. By contrast, in our approach the pillared film is formed from solution, in a few seconds, at room temperature, without any other applied pressure than the weight of the PDMS layer, and only a mild thermal treatment is required to facilitate the final stamp detachment. In addition, a soft PDMS

stamp is used, and very small amounts of semiconducting polymer solution (20 times smaller than in spin-coating) are employed [169].

The first step to manufacture the rr-P3HT pillars by push-coating is the fabrication of the PDMS mold (appendix C.1.1). The process, schematically depicted in figure 4.1 a, is carried out in collaboration with the L. Criante's research group (Center for Nano Science and Technology, Istituto Italiano di Tecnologia, Milano) and starts with the fabrication of a PDMS layer by thermal crosslinking of a commercial silicone oil precursor. In this work a 5 mm thick stamp is employed, since a PDMS thickness in the mm-scale guarantees a good retention of the solvent inside the PDMS layer and optimal mechanical properties, necessary for the success of the push-coating procedure [169]. The second step consists in the micro-patterning of the PDMS mold by femto-laser micromachining, in order to obtain a negative stamp of the pillars' structure. The PDMS stamp is then employed in the push-coating process, ending up with an array of rr-P3HT pillars surrounded by a planar rr-P3HT region (thickness = 180 nm, obtained from profilometry measurements) deposited on top of standard glass/ITO substrates (see appendix C.1.2 for additional details). Because the process is not damaging for PDMS, the same stamp can be used for a large number of depositions with high reproducibility of the obtained pillared structure.

The developed fabrication process offers a number of advantages. Besides the excellent repeatability and speed of the overall process, the use of femtosecond micromachining to fabricate the mold allows to finely tune ($\sim$ 1 μm) the geometrical parameters of the polymer pillars (three-dimensional shape, size, aspect ratio, pitch). The combination of all these characteristics is known to be key in the interaction with the living cells, since it strongly influences cells viability, adhesion and proliferation [174–178]. In fact, HAR micro and nano-pillars have been recently, successfully employed to probe cellular tractions, for stem cells differentiation or to gain intracellular access for delivery [175,177,179,180]. In all these cases, the fabrication technique should ideally be highly repeatable, fast, and simple, while providing at the same time high versatility and capability to rapidly adapt parameters to the specific cellular model.

In our case, the pillars size and aspect ratio can be easily, finely tuned by properly changing the writing parameters and conditions employed during the PDMS mold maskless fabrication, namely the laser source pulse power, number of pulses, repetition rate, pressure of the vacuum chamber, etc. Scanning electron microscopy (SEM) images (appendix C.5) show the high aspect ratio conical shape of the individual pillars (figure 4.1 b) and provide an idea of the repeatability of the overall fabrication procedure (figure 4.1 c,d). Average pillars height, base diameter and half-height width are, respectively, $6.4 \pm 0.3 \, \mu m$, about $2.3 \pm 0.1 \, \mu m$ and about $1.2 \pm 0.2 \, \mu m$. The mean distance between two adjacent pillars (from center to center) is $7.2 \pm 0.2 \, \mu m$ (the values are displayed as mean ± standard error of mean (s.e.m)). From figure 4.1 b it is possible to appreciate the increased surface area due to the nanometer-scale roughness of the organic semiconducting pillars usually achieved in HAR inorganic structures through expensive and time-consuming methods [181]. It was demonstrated that the presence of nanogrooves on micro pillars side walls is an essential parameter for the formation of 3D neuronal networks *in-vitro*, since it enhances the adhesion of neuronal processes to the pillars body [182]. Importantly, the conical shape of the HAR structures presented here (figure 4.1 b) allows to combine the advantages of micro and nano scale topographies. In particular, the micrometer size base confers to the soft rr-P3HT pillars good mechanical stability, while the sub-µm rounded tip is expected to establish a tight interface with the living cell membrane.

The distance between HAR pillars is another key parameter. In fact, high density pillar arrays (adjacent pillars pitch lower a critical value of about 2 □m) usually lead to a limited cellular adhesion and proliferation. This effect has been unanimously attributed to a reduced contact area with the underlying flat substrate [175,177]. Conversely, when the inter-pillar distance is much higher (pillars density <30 pillars 100 μm^{-2}), the adhesion and proliferation of cells is enhanced. Interestingly, it was observed that Si and InAs pillar arrays, with a density in the range of the one employed in our case (2 pillars 100 μm^{-2}), promotes cells to spread out, with a larger area, higher aspect ratio and a tighter adhesion than in the other cases, without seriously affecting cells viability [183,184].
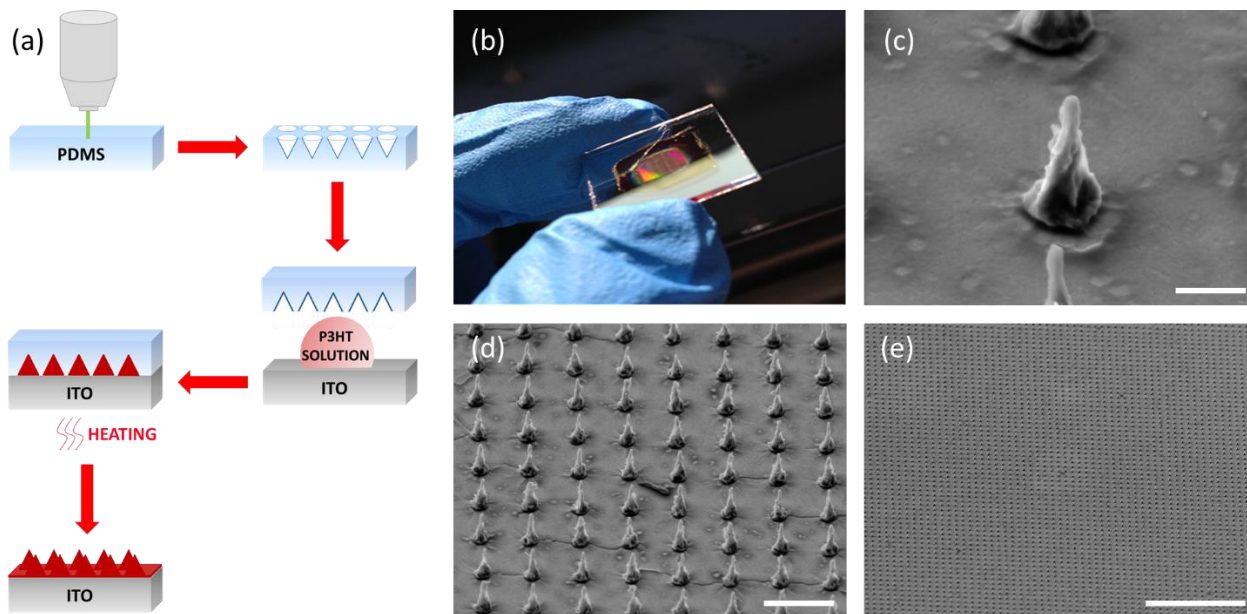
Figure 4.1. (a) rr-P3HT micro-pillars fabrication process. (b) Photograph of the rr-P3HT pillars-based device, taken at the end of the fabrication process. SEM images depicting the single rr-P3HT pillar structure (c, scale bar, 2 µm) and an overview of the pillars array at decreasing magnification (d,e, scale bars, 10 and 100 µm respectively).

4.3 rr-P3HT pillars-based substrates electrochemical characterization

Aiming at interfacing the realized polymer micro-structured substrates with a biological environment, it is important to preliminarily characterize their electrochemical behavior in contact with an aqueous, saline medium. To this goal, we carry out EIS measurements (appendix C.2) at the electrochemical equilibrium, i.e., at potential values corresponding to the device open circuit potential, by employing KRH extracellular solution as the electrolyte, in order to study the system in the same condition of the *in-vitro* electrophysiological experiments.

As discussed in section 3.3, by modeling the system with a simple frequency-dependent RC circuit and considering it at frequencies below 10 Hz, it is possible to obtain information about the device/electrolyte interface. In particular, within this low frequency range, the capacitor well approximates the Helmholtz double layer established at the interface [134,159–161,185].

The $C(\omega)$ trend below 10 Hz (figure 4.2 a), shows that the flat rr-P3HT reaches a plateau at frequencies < 1Hz, whose amplitude corresponds to the Helmholtz double layer capacitance. Conversely, in the case of the rr-P3HTpillars/electrolyte interface, $C(\omega)$ is characterized by a distinct behavior, being almost constant between 1 and 0.2 Hz and increasing at frequency values < 0.2 Hz, reaching 53 μF cm^{-2} at 0.01 Hz. The latter regime can be ascribed to the establishment of a volumetric capacitance, due to an enhanced percolation of ionic species trough the organic semiconductor that expand the electrochemical active surface area [157,185]. A detailed understanding of this phenomenon, however, requires deeper investigations and falls out the scope of the present work. Here, we focus our attention on the 0.1-1Hz frequency range, where the $C(\omega)$ is constant and the volumetric capacitance contribution is negligible, thus making possible to evaluate the increase in the surface area exclusively depending on the pillars morphology. We observe that $C(\omega)$ at 0.2 Hz is equal to 12.2 μF cm^{-2} (normalized on the geometrical device area), almost 3 times higher than the corresponding value in the flat case (4.4 μF cm^{-2}), in line with the existing literature [134,158,159]. The active surface area increment, due to both the ions percolation and surface topography, leads to the decrease of the device impedance modulus of about 15 times (figure 4.2 b), passing from the flat rr-P3HT morphology to the micro-structured one. This result is promising in view of the implementation of low impedance polymeric electrodes for electrically-assisted cell proliferation and differentiation applications, as well as for electrical stimulation and recording of living cells activity, since it is related to a higher signal-to-noise ratio and higher charge injection limit [26,181].
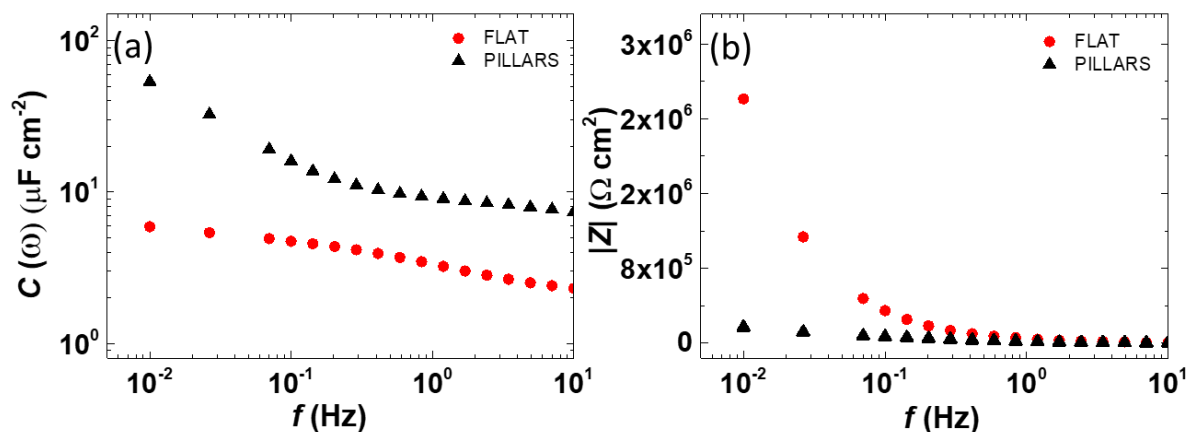
Figure 4.2. Equivalent capacitance C(ω) (a) and impedance modulus (b), extracted from EIS data, normalized to the devices geometrical surface area.

4.4 Neurons and HEK-293 cells interfaced with rr-P3HT pillars: viability and morphology

Although the good viability of several cell models on top of rr-P3HT thin-films was extensively verified [68,71], cell growth and proliferation on top of rr-P3HT micro-structures may be strongly affected by the underlying topography, and need to carefully assessed. Thus, viability of cells cultured on top of HAR rr-P3HT pillars is directly evaluated, by employing both primary (cortical neurons) and secondary line cells (HEK-293) (see appendix C.3 for additional details on cell cultures preparation). HOECHST/NucGreen staining (appendix C.4) was used to evaluate the relative percentage of healthy cells on the two substrates (figure 4.3), obtaining > 90% viable cells both for HEK-293 and neuron cell cultures after 1 and 14 days in vitro (DIV) respectively. No significant differences are detected between rr-P3HT planar and micro-structured regions (figure 4.3i and 4.3j).
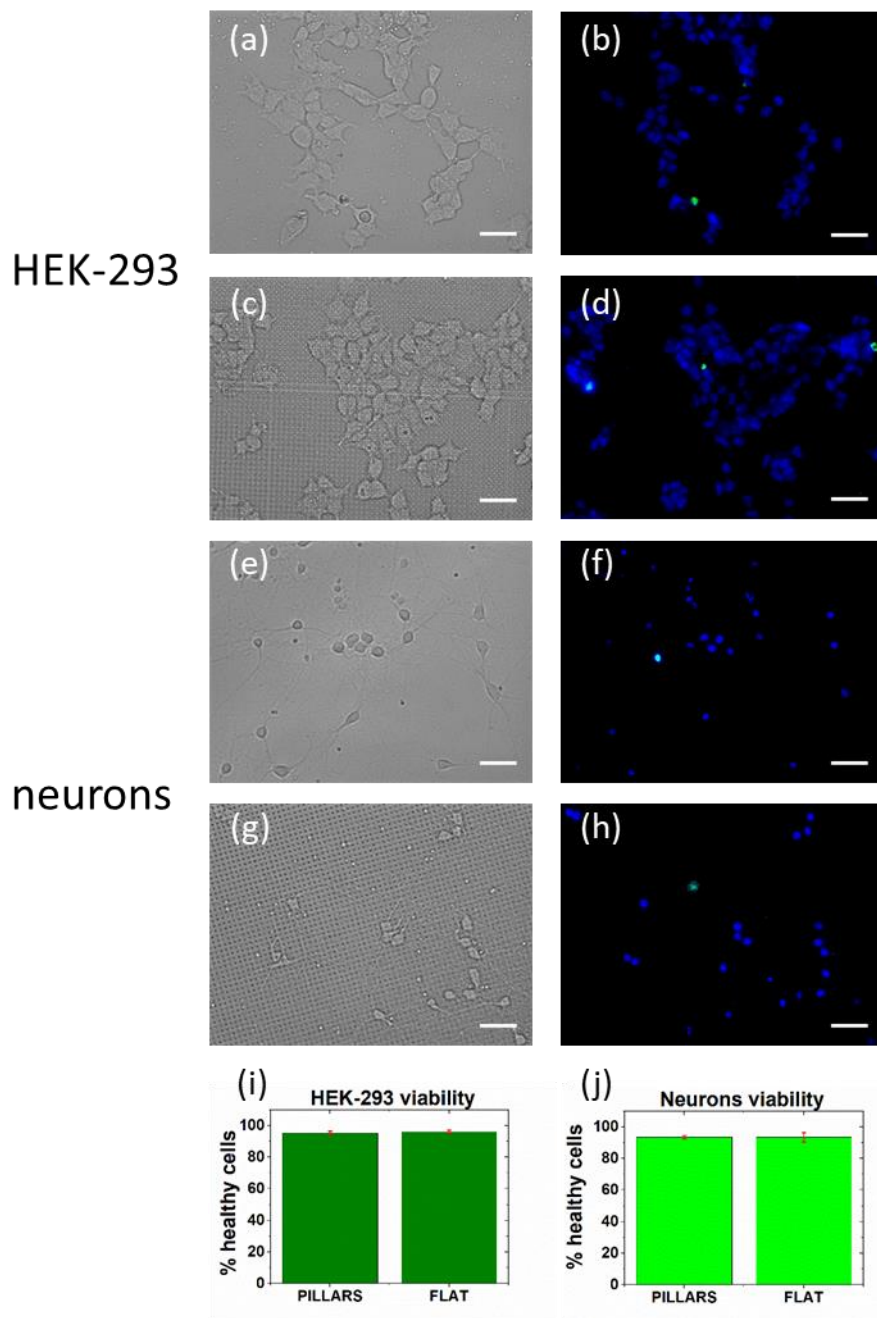
Figure 4.3. Bright field and fluorescence images of HEK-293 cells and cortical neurons cultured on flat rr-P3HT (a,b,e,f) and rr-P3HT pillars (c,d,g,h), respectively. All cells nuclei are stained by HOECHST (blue), dead cells nuclei are stained by NucGreen (green). Scale bars, 50 µm. Histograms showing the percentage of viable HEK-293 cells (i) and cortical neurons (j) on the different device morphologies. n = 450 cells for each substrate type. Error bars represent the s.e.m..

The morphology of HEK-293 and cortical neurons grown on top of polymer flat and micro-structured substrates is qualitatively assessed by SEM. Figure 4.4 clearly shows a significant difference in the morphology of the cells plated on the two different substrates. Both HEK-293 and primary neuronal cells cultured on flat rr-P3HT present a planar, 2-dimensional shape. Conversely, when cultured on

top of polymer microstructures, HEK-293 cells and neuronal bodies remain largely suspended on top of the pillars, rarely reaching the underlying substrate. It can be also appreciated how the selected arrays geometry leads to a more elongated morphology of the cells body, especially in the case of HEK-293 cells. Interestingly, the cells membrane thinning in the proximity of the pillars tips points to the attainment of a tight cell/material interface.
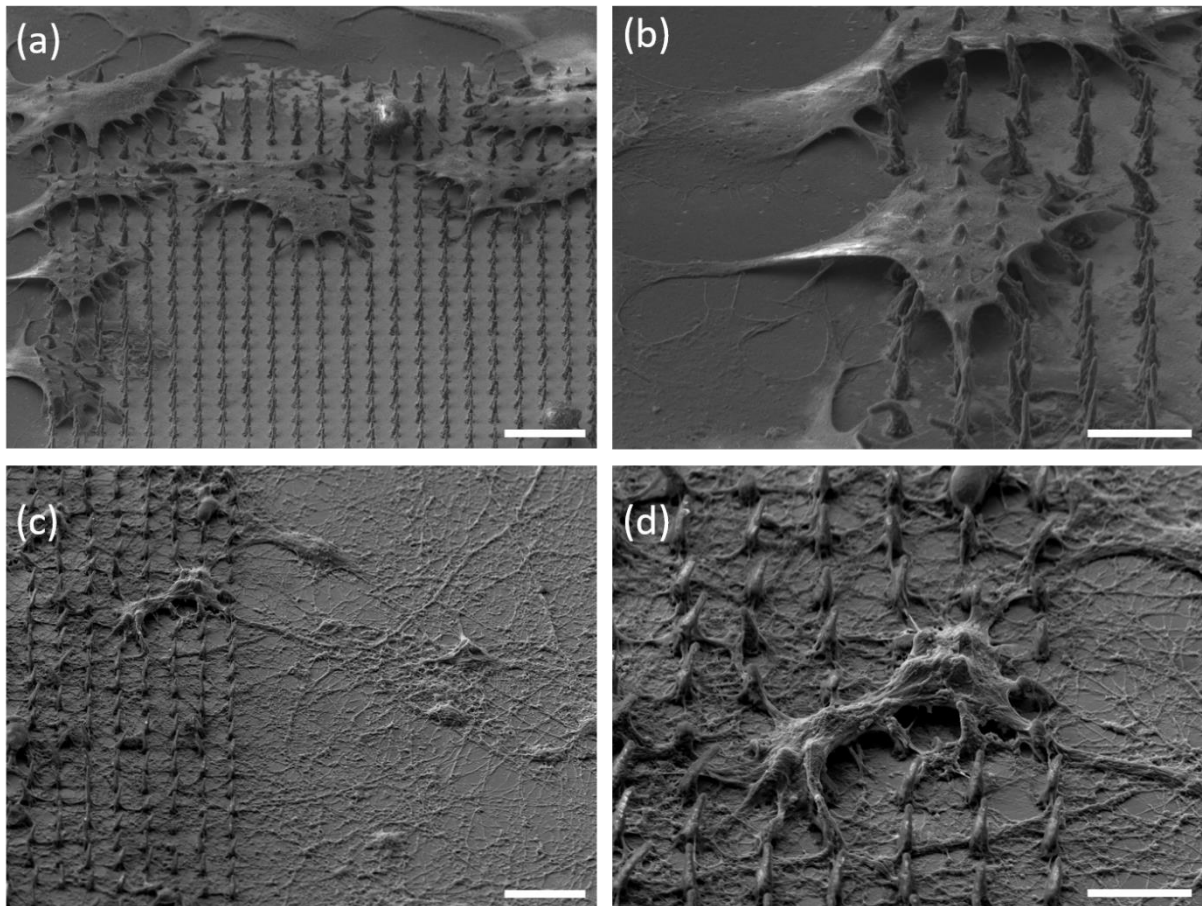
Figure 4.4. Top-view SEM images of HEK-293 cells (a,b) and cortical neurons (c,d) after 1 and 14 DIV respectively. Scale bars, 20 and 10 µm for panels a,c and b,d respectively.

4.5 HEK-293 cells morphological analysis

In order to corroborate and quantify the observed changes in the morphology of HEK-293 cells cultured on top of rr-P3HT micro structured substrates, we carry out immunofluorescence imaging experiments (see appendix C.6). Figure 4.5 depicts some representative fluorescence images of the nuclei and cytoskeleton, marked with DAPI (blue) and phalloidin-FITC (green) respectively, of the

cells grown on top of planar (Figure 4.5a) and pillars-modified (Figure 4.5 b) regions. The cells plated on rr-P3HT pillars show a more elongated shape (figure 4.5 c) than the ones grown on the flat controls, in line with the obtained results of HEK-293 plated on similar densities of HAR microstructures [183] and also with other cell types [186]. The pillar microstructures induce a sizable shrinking of the cell membrane in the x-y plane and a parallel spreading in the z-direction, qualitatively observed in the SEM images (Figure 4.4) and quantitatively confirmed also by the measurement of the average top-view surface area of cells (Figure 4.5 d).
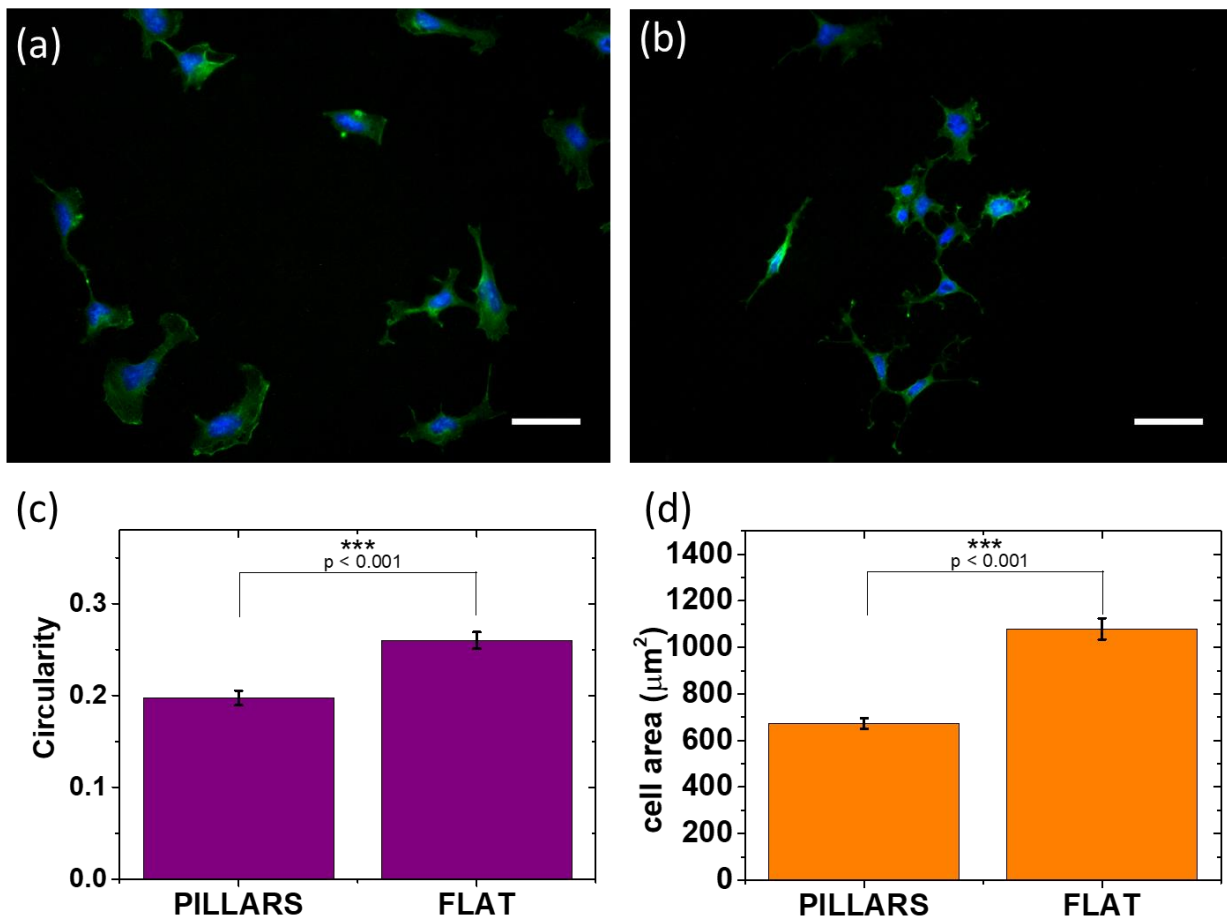
Figure 4.5. Immunofluorescence images of HEK-293 cells cultured on top of rr-P3HT flat (a) and rr-P3HT pillars (b). Cells nuclei and cytoskeleton are stained with DAPI (blue) and phalloidin-FITC (green), respectively. Scale bar, 50 μm. Quantification and comparison of cells morphological parameters in terms of circularity (c) and average cells top-view surface area (d). Mean values are averaged over a statistical ensemble of n = 100 cells for each substrate type. Error bars represent the s.e.m. ***, $p < 0.001$ (Student t-test)

Interestingly, the quantitative evaluation of the average cell perimeter (normalized to the cell area, Figure 4.6) shows that the cells adhered on the rr-P3HT pillars develop more cellular projections, similarly to what already observed in the case of cells cultured on HAR silicon pillars with an inter-distance > 2µm [184], as well as on silicon nanowires [187,188].
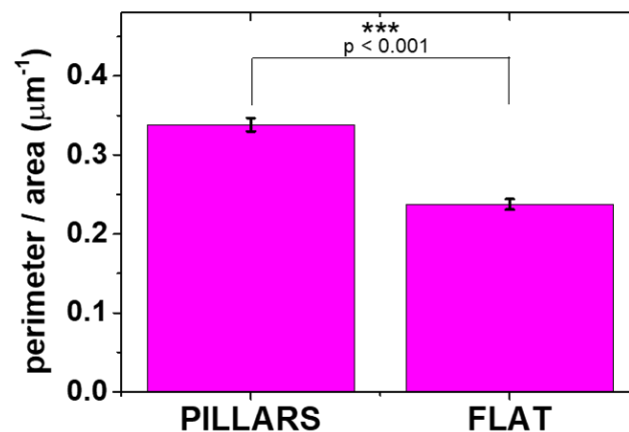
Figure 4.6. Average perimeter normalized to the cell area on rr-P3HT flat and micro-structured substrates. ***, p< 0.001 (Student t-test). Error bars represent s.e.m..

4.6 Morphological analysis of cortical neuronal cells

In collaboration with the C. Sala's research group (Istituto di Neuroscienze, CNR, Milano) we investigate the effect of the rr-P3HT pillars architecture also on the cortical neuronal cells morphology, by performing confocal imaging experiments (appendix C.6). In this case we focus on the neurons arborization, i.e. the arrangement of neuronal processes (axon and dendrites) forming a tree-like structure, since it is directly related to the neurons functionality [189].

Microtubule-associate protein 2 (MAP2) is employed for the selective staining of dendritic trees. The confocal images depicting the dendritic morphology of cortical neurons growth in absence of the polymer (figure 4.7 a**),** on top of rr-P3HT pillars (figure 4.7 c) and on planar rr-P3HT (figure 4.7 e) are compared. The neurons cultured in presence of the rr-P3HT polymer (flat or pillar) have a slight

decrease in the number of primary and secondary dendrites (figure 4.7 b-d), as well as branching points (figure 4.7 f) in comparison to neurons cultured on glass-coverslips. Interestingly, there are no significant differences between rr-P3HT pillars and flat conditions (figure 4.7 panels b,d,f). This result suggests that the neuronal cells functional properties are preserved on the rr-P3HTpillars-based substrates, given the intimate relationship between the dendritic expression and the neurons electrical activity [189].

The effect of substrate topography on neuronal morphology was previously assessed with several micro- and nano-structured morphologies, including continuous geometries, like grooved substrates or electro-spun fibers [190–192], and discontinuous geometries as pillar arrays [191,193]. The most part of the micro pillars employed for this purpose are made of silicon and they have been interfaced with dorsal root ganglion (DRG) neurons [194], spiral ganglion neuronal cells [195] and hippocampal neurons [182,196–199]. In general, it has been reported that the neurons outgrowth on micro pillars is strongly affected by the pillars density [193,195–197]. In general, it was found that pillars spacing lower than 4.5 um highly affects the neurons outgrowth. Instead, when the interpillar distance is increased, the neurons morphology is comparable to the one of the flat control substrates [182,197], in line with our results. However, we cannot make a precise comparison between our results and the ones obtained in these reports, since the employed pillars material composition, type and maturation stage of neuronal cells are very different from the ones used in the present work [194].
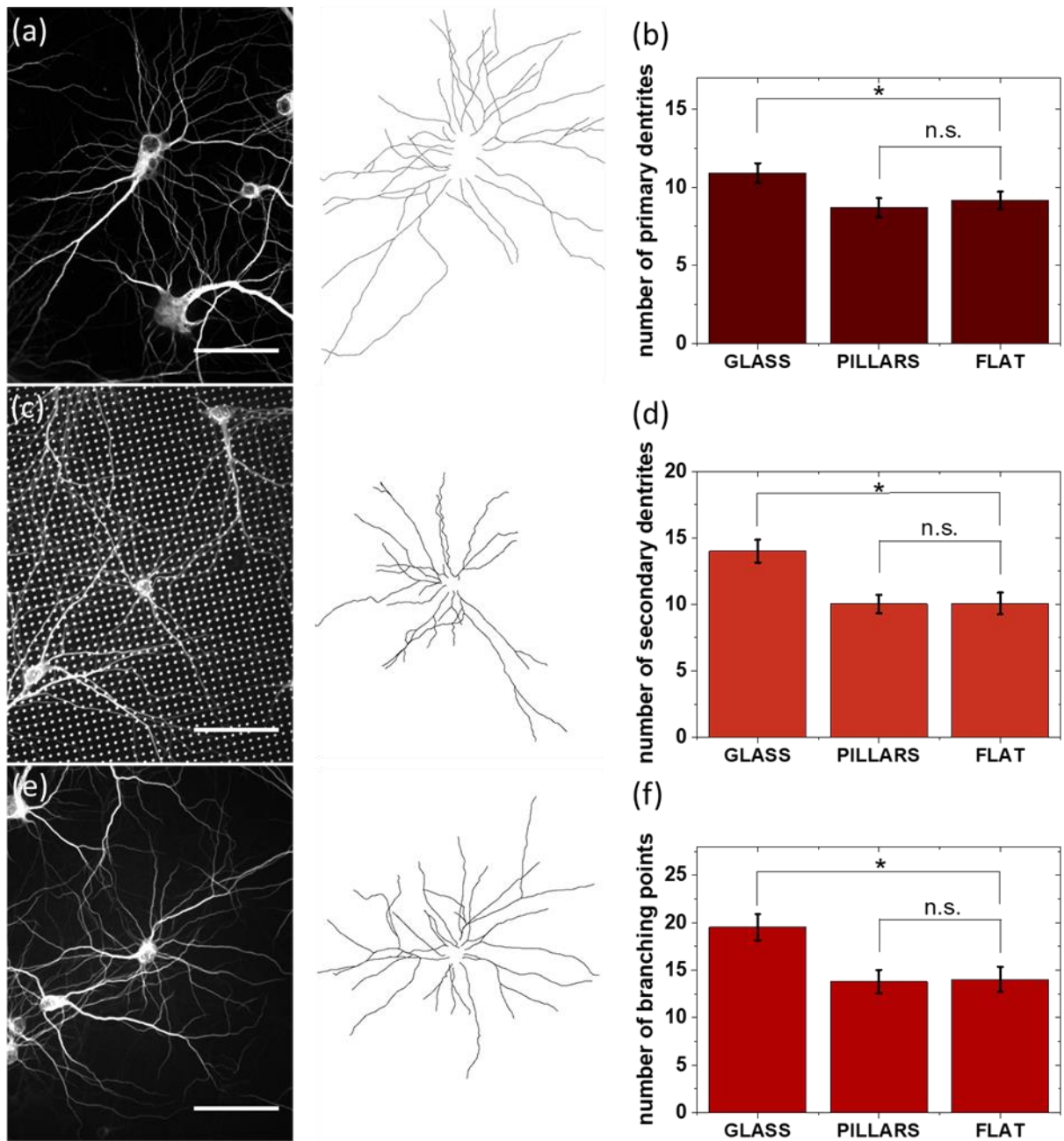
Figure 4.7. Rat cortical neurons cultured on top of glass (a), rr-P3HT pillars (c) and rr-P3HT flat (e) stained for MAP2. Histograms showing the number of primary dendrites (b), secondary dendrites (d) and branching points (f) of neurons on different devices. n= 30 cells for each condition. Error bars represent the s.e.m. Scale bars 50 µm. One way ANOVA, followed by Bonferroni correction.

4.7 Neurons electrophysiological characterization in dark conditions

In order to verify whether the membrane passive properties and the electrophysiological activity of primary cortical neurons cultured on rr-P3HT HAR-pillars are preserved, we carry out patch clamp recordings in whole-cell configuration and in dark conditions (figure 4.8, see appendix C.7 for further experimental details). Figure 4.8 a and 4.8 b compare the equilibrium parameters of the cells plated both on flat and on micro-structured rr-P3HT areas. The average cell membrane resting potential (V_m = −68 ± 1 mV and V_m = −66 ± 1 mV on pillars and flat regions respectively, displayed as mean ± s.e.m.) does not show significant dependence on the substrate type, showing, in both cases, the typical value recorded *in-vitro* (figure 4.8 a). Conversely, the average cell membrane capacitance C_m is significantly higher in the case of rr-P3HT pillars, possibly due to the increase in the cell membrane surface area (Figure 4.8 b). Since the C_m value reported in figure 4.8 b is normalized by the cells body top-view surface area, it is possible to relate the surface area increment only to the cell membrane elongation observed in the SEM images (figure 4.4). Figure 4.8 c and 4.8 d show whole-cell recordings in current clamp configuration carried out on neurons cultured on both the micro-structured and the planar polymer substrates, respectively. The intracellular current injection in subsequent steps of 20 pA amplitude and 20 ms time duration, and the simultaneous recording of the membrane potential, allows to evaluate the threshold current value (I_{th}) for action potential firing. I_{th} is very similar in the two cases, with no statistically significant difference (figure 4.8 e). The action potential characteristics are also not affected by the substrate morphology, as displayed by the similar time to peak vs. intensity trends of the neurons grown on pillars and flat regions (figure 4.8 f).
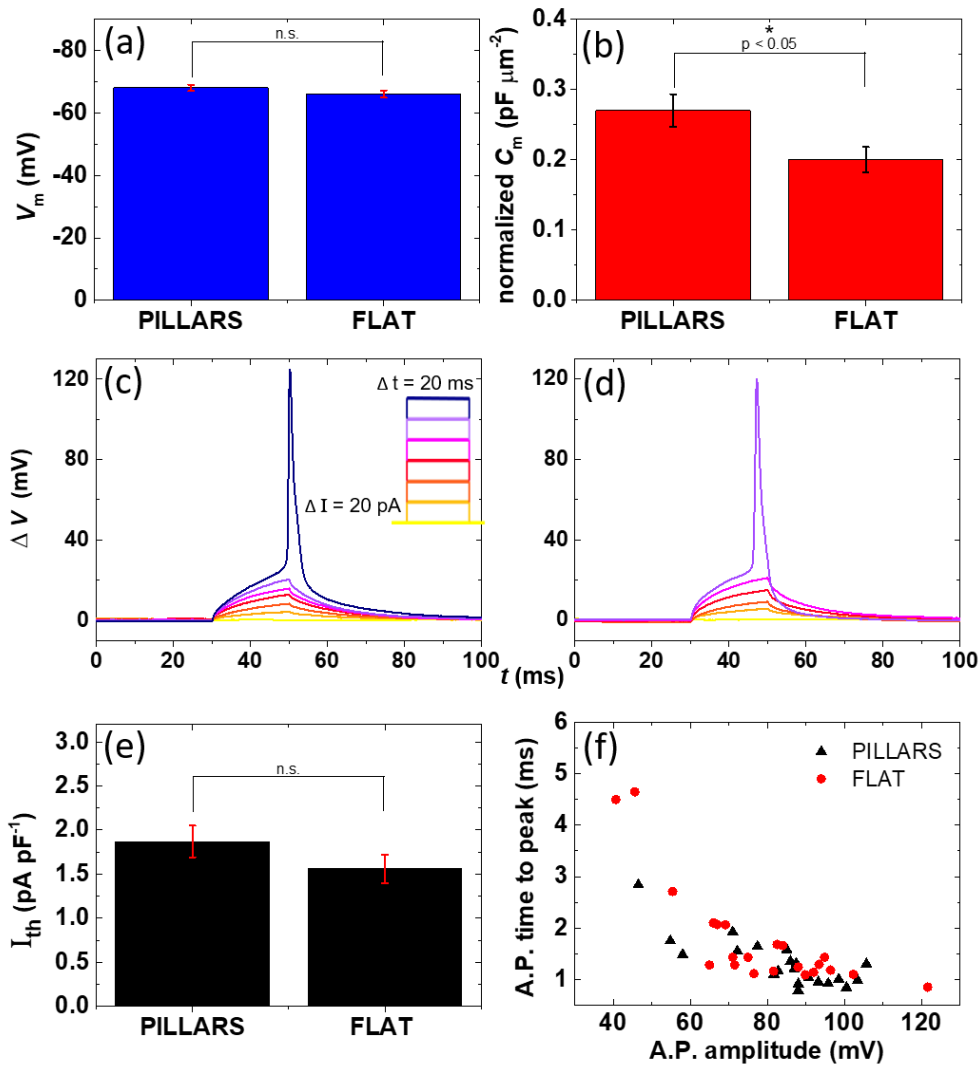
Figure 4.8. Average cell membrane resting potential V_m (a) and cell membrane capacitance C_m (b) of neurons grown on planar and micro-structured substrates. C_m values are normalized to the cells surface area in the x-y plane. *, $p < 0.05$ (Student t-test). Representative action potentials traces elicited in neurons plated on rr-P3HT pillars (c) and rr-P3HT flat (d) by 20 ms current steps of 20 pA amplitude. (e) Average threshold current intensity, as normalized to the cell membrane capacitance. (f) Neurons action potentials time to peak versus amplitude. The error bars in the histograms represent the s.e.m.

Overall, whole-cell configuration patch-clamp experiments demonstrate that the main electrophysiological properties of primary cortical neurons cultured on top of polymer pillars are well preserved, at least at the level of the overall, macroscopic behavior. Interestingly, the observed, sizable increase of the cell membrane capacitance, represents an indication that a more intimate cell/material interface is successfully established, as a consequence of the cell membrane stretching induced by the pillar structure.

4.8 Characterization of cortical neurons synaptic morphology

As a further step, we investigate whether the micro-structured polymer structures affect the expression of excitatory or inhibitory synapsis. To test if rr-P3HT micro-structured substrates affect synapses formation, we carry out confocal imaging experiments in collaboration with the C. Sala's group (Istituto di Neuroscienze, CNR, Milano, see appendix C.8 for additional experimental details). The excitatory synapses are stained with the presynaptic marker vesicular glutamate transporter (vGLUT) and the post synaptic density protein 95 (PSD-95) marker, whereas the inhibitory ones are labeled with the presynaptic marker vesicular GABA transporter (vGAT). Overall, no statistically significant difference among neurons growth on top of rr-P3HT pillars and neurons growth on flat polymer or glass coverslips is noticeable (figure 4.9). Altogether these data demonstrate that the micro structured polymer structures do not negatively affect synapse formation.
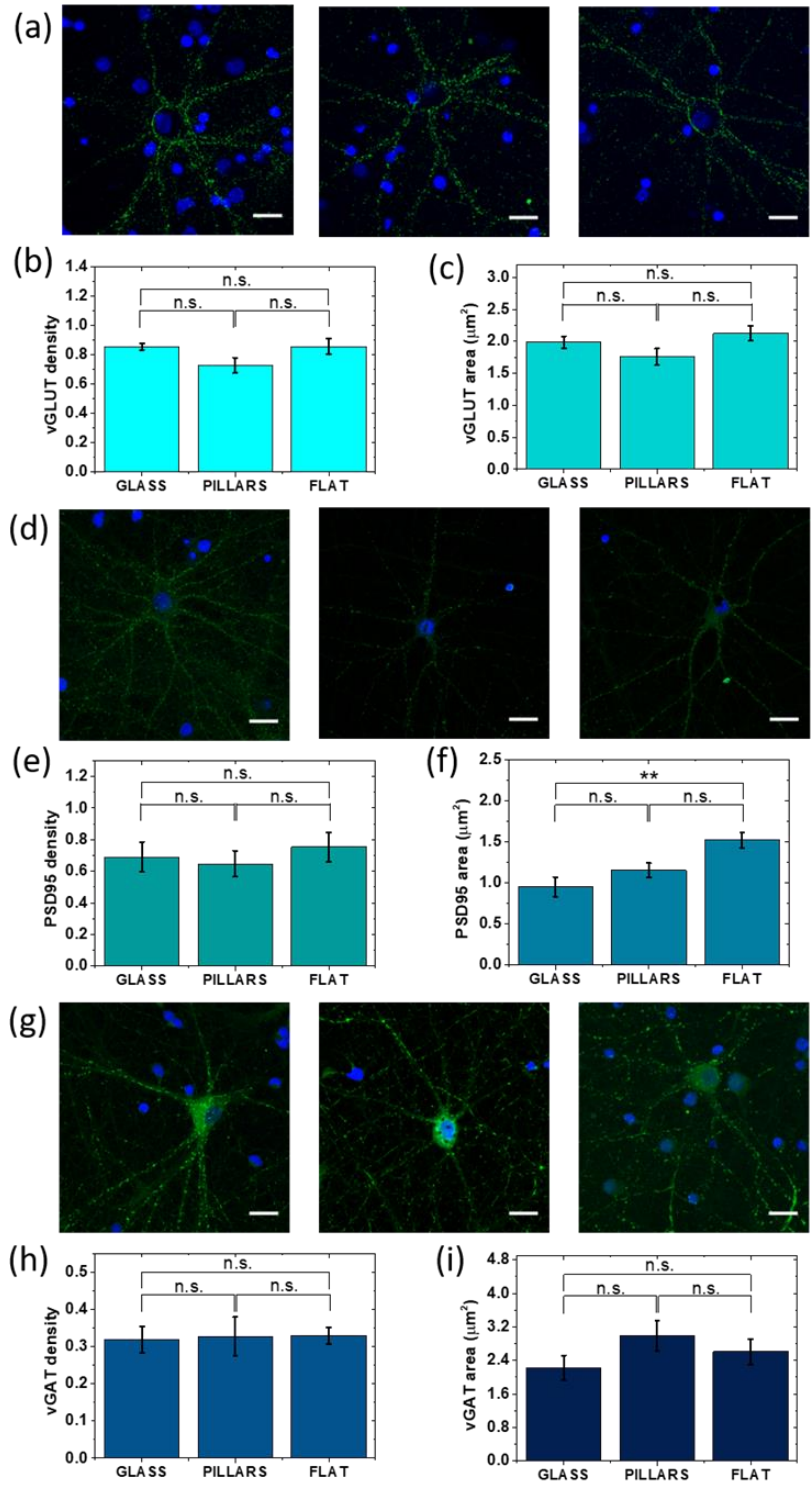
Figure 4.9. Merged confocal images showing the cells nuclei labeling (DAPI, blue) and vGLUT (green) (a), PSD-95 (green) (d) and vGAT (green) (g) stainings of rat cortical neurons cultured on top of (from left to right): glass, rr-P3HT pillars and rr-P3HT flat. Scale bars 20 µm. Histograms showing the vGLUT cluster density (b) and area (c). Histograms reporting PSD-95 cluster density (e) and area (f). Histograms depicting vGAT cluster density (h) and area (i). n= 8/16 neurons for each substrate. Error bars represent s.e.m. (one way ANOVA, followed by Bonferroni correction).

4.9 Electrophysiological recordings upon light excitation

In the previous paragraphs it has been demonstrated that rr-P3HT pillars structures do not negatively affect the viability and the functional properties of model primary and secondary cells. In this section the optical stimulation capabilities of the micro-structured photoactive platforms are addressed.

As discussed in section 1.6 and at the end of chapter 3, the extracellular stimulation effectiveness increases as the thickness of the cleft region between cell and device is decreased. The SEM images of the HEK-293 cells and cortical neurons grown of top of rr-P3HT pillars (figure 4.4) suggest that the microstructure allows to establish a more intimate interaction with the cells membrane as compared to the planar thin films. In order to verify whether this effect translates into an enhanced electrical coupling at the cells/device interface, whole-cell patch clamp recordings, in current clamp configuration and upon light stimulation, are carried out using the same set up and experimental conditions employed in the case of planar rr-P3HT-based devices presented in section 2.4.2 (see also appendix A.7), but with a different photostimulation protocol. The patched HEK-293 cell (figure 4.10 a) transmembrane potential variation (ΔV) induced by the polymer photoexcitation with 20 ms light pulses ($\lambda = 470$ nm, 46.5 mW mm^{-2}) is depicted in figure 4.10 panels b and does not display significant differences with the one recorded on planar rr-P3HT thin films presented in section 2.4.2 (figure 2.7 a). The presence of fast capacitive components at the beginning and at the end of the photoexcitation together with a subsequent thermally induced cell depolarization are still noticeable (figure 4.10 b). In particular, both the peak amplitude (in the order of 1 mV, figure 4.10 b) and the dynamics (figure 4.10 c) of the positive capacitive component measured on top of rr-P3HT pillars are fully comparable with the ones recorded on the planar ITO/P3HT device in the same illumination conditions (refer to figure 2.7 a for the signal intensity and to figure 4.10 c for the dynamics).

This result is an evidence of the fact that the rr-P3HT pillars morphology does not improve the electrical coupling between HEK-293 cells and rr-P3HT-based photoactive devices.
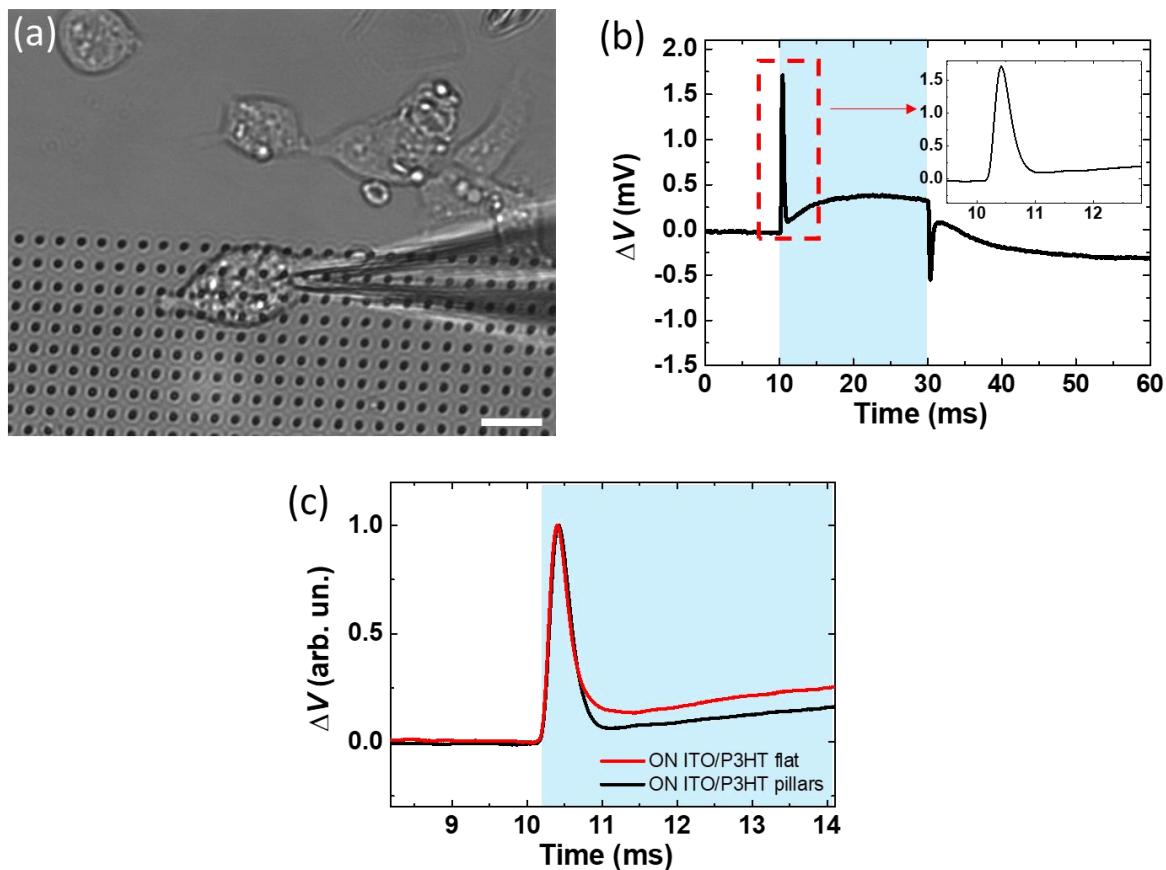
Figure 4.10. (a) Bright field image depicting a HEK-293 grown on rr-P3HT pillars array and attached to a patch clamp micropipette. Scale bar 20 µm. (b) Representative HEK-293 membrane potential (ΔV) variation recorded during whole-cell patch clamp recording upon photostimulation with 20 ms light pulses ($\lambda = 470$ nm, 46.5 mW mm^{-2}). Light excitation is represented by the cyan shaded area. (c) Normalized comparison between the fast HeK-293 cell membrane potential variation component, related to the polymer surface charging, recorded on rr-P3HT flat/pillars-based devices. ΔV traces have been normalized to the peak maximum.

The patch clamp experiments are repeated in light conditions with cortical neurons grown on top of ITO/P3HTpillars devices (figure 4.11 a), employing the same experimental conditions adopted for the electrophysiological recordings in dark presented in paragraph 4.7, exception made for the presence of a light stimulus and the absence of intracellular current injection. Figure 4.11 panel b depicts the photoinduced neuron ΔV changes induced by 20 ms light pulses ($\lambda = 540$ nm). Data highlight that no action potential is elicited and that the ΔV trend is consistent with a passive electrical response of the neuron, most likely due to the combination of the surface charging and local heating at the polymer surface, similarly to what observed with HEK-293 cells [71].
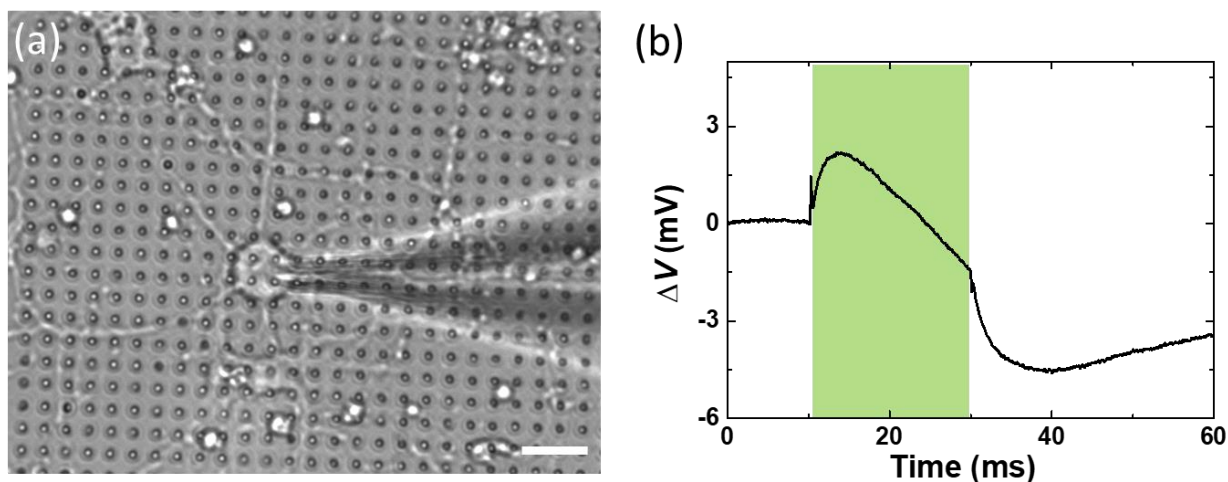
Figure 4.11. (a) Bright field image depicting a cortical neuron grown on rr-P3HT pillars array and attached to a patch clamp micropipette. Scale bar 20 µm. (b) Representative HEK-293 membrane potential (ΔV) variation recorded during whole-cell patch clamp recording upon photostimulation with 20 ms light pulses ($\lambda = 540$ nm, 220 mW mm^{-2}). Light excitation time duration is represented by the green shaded area.

The results obtained in the electrophysiological experiments do not show an improvement of the electrical coupling between cells and the photoactive platforms. The cell membrane stretching observed in SEM and fluorescence images and confirmed by the increased C_m values of neurons, suggests that the problem is not related to the cellular adhesion. The most probable explanation relies on the poor charge dissociation efficiency of the micro-structured device in correspondence with the pillar structures, due to the high polymer thickness. In order to validate this assumption, surface potential experiments are performed (figure 4.12), using the same set up and experimental conditions adopted in the case of planar rr-P3HT-based devices presented in section 2.4.2 (see also appendix A.8), but with a different photoexcitation protocol. The surface potential trend recorded on pillar arrays (figure 4.12 a) is comparable with the one displayed by ITO/P3HT planar devices (figure 2.10 b), characterized by fast capacitive spikes at the beginning and the end of the photoexcitation ($\lambda = 540$ nm, 220 mW mm^{-2}). However, it has to be considered that during this type of measurement the micropipette electrode senses the average local potential variation from an area much larger than the pillar size (about tens of µm^2). The signal acquired during surface potential measurements on semiconducting pillars arrays is composed by the superimposition of the contributions of both the rr-P3HT microstructures and planar polymer film between them. The measurement of the surface

84

potential contribution of the single rr-P3HT pillar is not straightforward, and it cannot be done with the patch clamp set up. It is possible to make a rough estimation by performing surface potential recordings on top of rr-P3HT films with a thickness comparable with the height of the pillars. Figure 4.12 panel b shows the photoinduced potential trend acquired on top of a 6μm-thick rr-P3HT film (see appendix C.9 for details on the film fabrication) with the same illumination conditions employed in the case of the pillar arrays. In this case the surface potential trace has still a capacitive behavior but the positive spike intensity is lowered of about 1 order of magnitude as compared to the case of the microstructures array (~ 0.1 and ~ 2.5 mV in the rr-P3HT thick film and pillars cases respectively, figure 4.12 a and b). This result suggests that the high polymer thickness in proximity of the microstructures may account for the low phototransduction efficiency observed, explaining also the absence of the light-induced neurons action potential firing previously showed by Ghezzi et al. using planar rr-P3HT [67]. These findings orient future works to the optimization of the pillars-based photoactive platforms, in order to decrease the semiconducting polymer thickness in proximity of the device/cell interface.
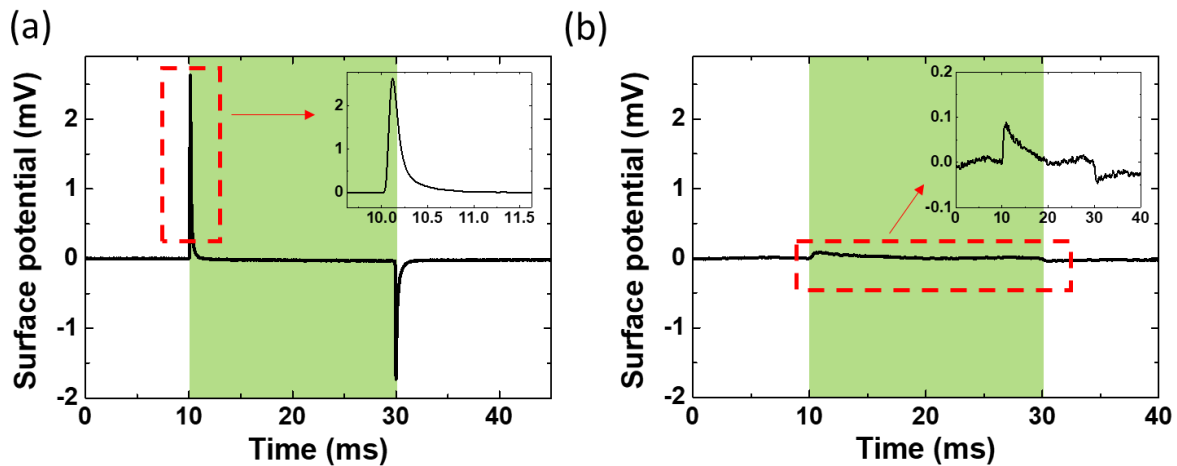
Figure 4.12. Surface potential traces recorded on rr-P3HT pillar arrays (a) and on a 6μm-thick rr-P3HT film (b). Illumination conditions: $\lambda = 540$ nm, 220 mW mm^{-2}. The photoexcitation time duration is represented by the green shaded area.

5. Antifouling properties of micro and nano-patterned silk/P3HT substrates

5.1 Introduction

The use of medical implants for the treatment of irreparable damages to the human body, like prosthetic joints, dental implants, and vascular grafts, has become very diffused nowadays, leading to dramatic improvements in patients quality of life [200]. For this reason, a lot of effort is undertaken to minimize the risk of implants failure, principally due to the development of device associated infections (DAI) caused by microbial contamination [200,201]. Bacteria preferentially adhere and proliferate on the implant surface, producing a biofilm, i.e. a layer of aggregated bacteria bound together by a polysaccharide extracellular matrix [202]. The presence of the biofilm confers to the microorganisms a much higher resistance than the unattached bacteria, requiring 500–5000 times higher doses of antibiotics[202,203]. The consequence is the extensive use of antibiotics that leads to an enhanced bacterial resistance towards the common antibiotic agents. A solution consists in the hindering of the formation of the biofilm by the proper engineering of implanted material and devices [204]. Three main strategies do exist to this purpose: (1) the functionalization of the implant material with antimicrobial agents for imparting antimicrobial, i.e. direct killing of bacteria, properties [204]; (2) the modification of the prosthesis surface properties for limiting the microbial adhesion (i.e. antifouling) through steric hindrance, hydrophobicity, Van der Waals forces or electrostatic interactions [205–209]; (3) the combination of the strategies (1) and (2) [204,210].

Silk fibroin is a well-known biocompatible material, extensively employed for several biomedical *in-vivo* applications, such as tissue engineering [211–213], drug release [214,215] and implantable electronics [216,217]. In particular, it was used for the fabrication of functionally autonomous rr-P3HT-based photovoltaic prostheses for the recovery of light sensitivity and visual acuity in blind retinas, discussed in section 1.5 [68,80,81]. Even though the functionalization of silk with antimicrobial agents was extensively studied [218–222], to the best of our knowledge the antifouling properties of micro and nano-structured silk fibroin substrates have not yet been explored. In this

chapter we present the study of the influence of micro and nano-patterned sillk surface topographies on the attachment of HEK-293 cells and E.Coli bacteria. After assessing that the micro and nano-structured morphologies do not hinder the HEK-293 cells by performing MTT viability assays, the adhesion grade of GFP-encoded E.Coli is evaluated by fluorescence microscopy imaging. Then, in view of optoelectronic in-vivo applications, we investigate the antifouling properties of rr-P3HT-covered silk substrates.

The results presented in this chapter are included in G.Tullii, F.Galeotti, S.Donini, C.Bossio, F.Lodola, M.Pasini, E.Parisini and M.R. Antognazza, *Micro and nano-patterned silk substrates for antifouling applications,* in preparation.

5.2 Micro and nano-patterned silk substrates: fabrication and morphological characterization

The fabrication of the micro- and nano-patterned silk fibroin substrates studied in this thesis work is based on a soft lithographic approach and it is carried out in collaboration with Dott. Francesco Galeotti (Istituto per lo Studio delle Macromolecole (ISMAC), CNR, Milano) following a method reported elsewhere [223] and in appendix D.1. The procedure, summarized in figure 5.1, starts with the extraction of the silk fibroin protein from the *bombyx mori* degummed silk fibers trough dissolution in LiBr solution and subsequent dialysis against mQ-water. The silk fibroin solution obtained is drop casted on top of PDMS molds that present the negative structure of the final micro and nano-patterns. Once solidified, the fibroin films are subjected to a water vapor annealing for increasing the crystallinity of the silk-based material obtained, making them insoluble in water [224].
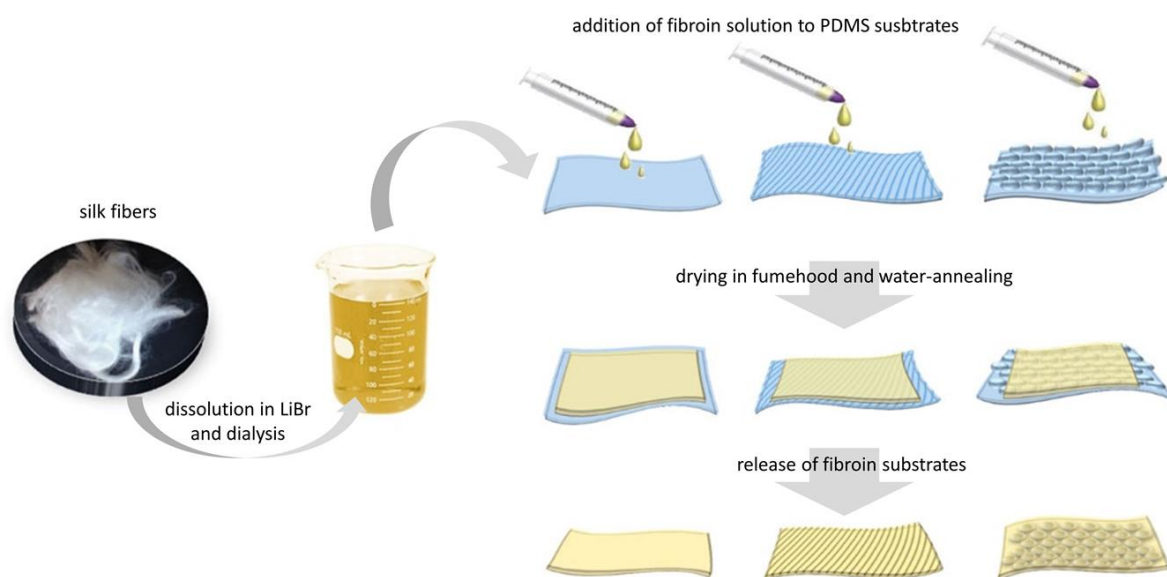
Figure 5.1. Scheme of the soft lithographic fabrication route followed for the preparation of micro and nano-patterned silk substrates.

The surface topography of the obtained silk substrates is characterized by acquiring top-view SEM micrographs (figure 5.2, see appendix D.2 for details about the sample preparation for SEM), from which it is possible to appreciate the different micro- and nano- patterned morphologies in comparison with the planar unmodified silk fibroin surface (silk flat, figure 5.2 a). Three different structured topographies are prepared: (1) a nanostripes-patterned silk fibroin surface, composed by grooves of ~ 800 nm width (nano stripes, figure 5.2 b); (2) a surface modified silk fibroin substrate that comprises micro-wells of different diameters, ranging from 3.5 to 5 µm (µwells 1, figure 5.2 c); (3) a micro-wells patterned silk fibroin surface morphology that displays wells with a similar shape of µwells 1, but with a diameter in the range 1-2 µm (µwells 2, figure 5.2 d).
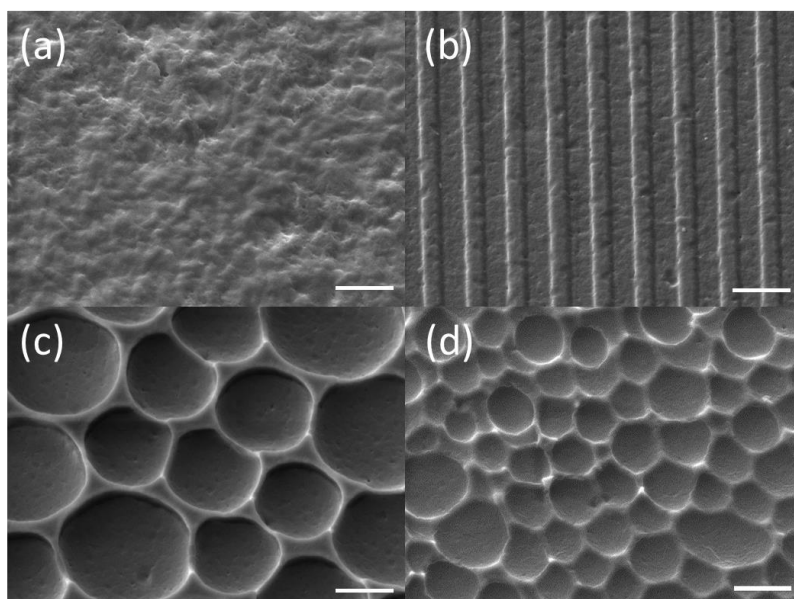
Figure 5.2. Top-view images of silk flat (a), nano stripes (b), µwells 1 (c) and µwells 2 (d). Scale bars 2 µm

5.3 HEK-293 cells cultures on micro/nano-patterned silk substrates

Silk fibroin, once obtained from *bombyx mori* silk by a proper purification route [225], show optimal biocompatibility, well documented in several studies *in-vivo* and *in-vitro* [81,226,227]. In order to investigate whether the structured topography negatively affects the viability of living cells, HEK-293 cells cultures are prepared on the different micro- and nano- patterned silk fibroin-based substrates and their proliferation is monitored by performing the MTT assay (figure 5.3), introduced in section 2.4.1 (for further details see appendix D.3). The formazan absorption of the MTT treated cells cultures on the different morphologies is evaluated after 1, 2 ,3 and 4 DIV, showing a general reduction in cells proliferation after 1 DIV both on flat and patterned silk samples in comparison to control glass substrates (figure 5.3). Starting from DIV 2 the proliferation of HEK-293 cells on silk-based samples starts to recover, reaching a comparable formazan absorption value respect to the one observed on glass slides at DIV 4. Furthermore, there are no significant differences between flat and patterned silk cases, confirming that the micro and nanostructures proposed do not affect the HEK-293 cells viability and proliferation.
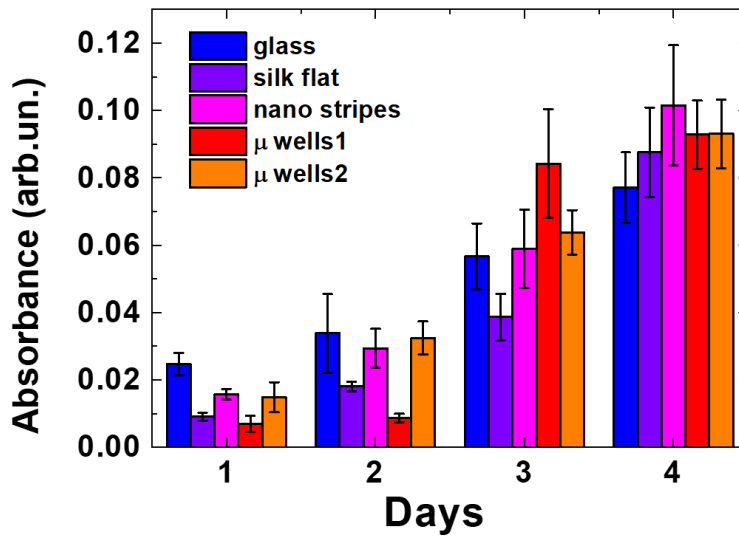
Figure 5.3. MTT viability assay on HEK293 cells plated on top of silk substrates and on glass slides as control. Data are reported as average over n = 2 samples ± s.e.m.

5.4 Evaluation of E.Coli adhesion on silk-based substrates

The antifouling capability of the different micro/nano-patterned silk samples is evaluated by employing the E.Coli bacterial model, genetically modified to express green fluorescent protein (GFP) for fluorescence imaging. The preparation and maintenance of the bacterial cultures are carried out in collaboration with Dr. Parisini's research group (Center for Nano Science and Technology, Istituto Italiano di Tecnologia, Milano), and all the related details can be found in appendix D.4. Prior to evaluating the samples antifouling properties, the substrates are incubated with the GFP-expressing E.Coli for 24h, washed by subsequent immersions in mQ-water for removing all unattached bacteria and covered with a mQ-H_2O drop. The number of adherent bacteria is then quantified by acquiring GFP fluorescence emission (figure 5.4 a-e), (appendix D.5). All the silk-based samples display a lower number of adhered bacteria in comparison to the glass control (figure 5.4 f). The interpretation of the result obtained on the planar silk topography is not straightforward and additional experiments would be necessary for clarifying the origin of this effect, falling out from the scope of the present work. Most importantly to the goals of the present work, the micro- and nano-patterned silk samples

present a significant reduction in the number of E. Coli attached to their surfaces in comparison with the flat silk morphology, amounting at 49 % ($p < 0.05$), 64 % ($p < 0.01$) and 66 % ($p < 0.001$) for the nano stripes, µwells 2 and µwells 1 cases respectively (figure 5.4 f).
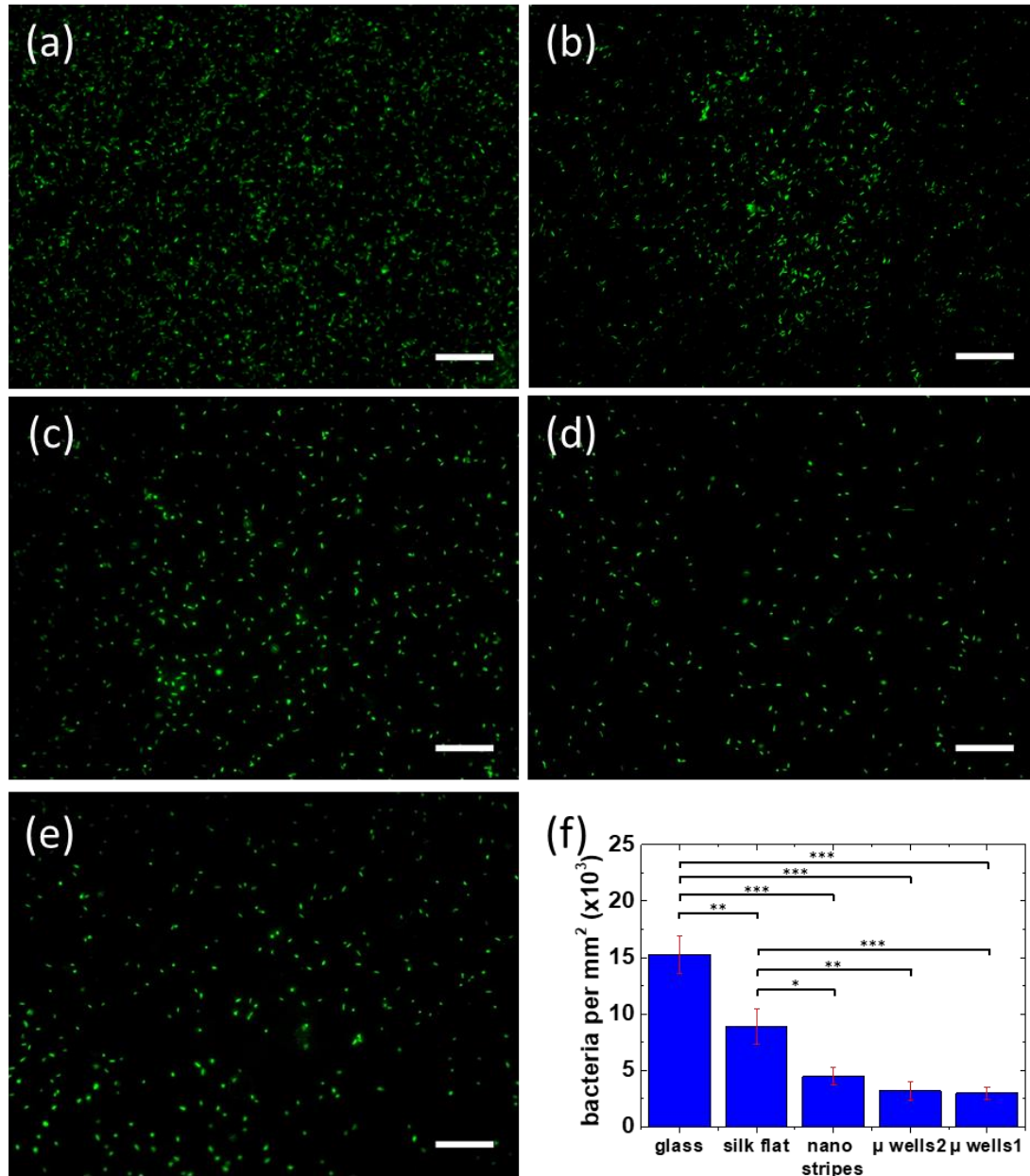
Figure 5.4. Fluorescent microscopy images of GFP expressing bacteria cultured on glass (a) and flat (b), nano-striped (c), µwells 2-patterned (d), µwells 1-patterned (e) silk substrates, after 24h. Scale bars 50 µm(f) Quantitative analysis of bacteria observed in a-e. *p <0.05, **p< 0.01, ***p< 0.001.

This result can be attributed to a topography-driven antifouling mechanism. In literature, two main effects were found to have a central role in the inhibition of bacterial adhesion: (1) a steric effect due to the presence of a regular micro-patterned morphology characterized by a features size lower than

bacterial dimension [204,205,228]; (2) an effect related to the high hydrophobicity induced by micro-structured surfaces [204,206,229,230]. In both cases the driving force of the antifouling process relies in the reduction of the surface area to which the organisms can adhere. The reduced bacterial adhesion achieved with silk nano stripes and μwells 2 can be explained by considering the former mechanism, since the E. Coli average length (~ 2 μm) and diameter (~ 1 μm) [231,232] are higher than both the nano stripes silk grooves width (~ 800 nm) and μwells 2 silk wells mean diameter (between 1 and 2 μm). On the contrary, this argumentation is not valid for explaining the bacterial adhesion reduction induced by μwells 1, because the diameter of the wells that composes this architecture (in the range 3.5-5 μm) is about 2 times higher than the E. Coli average dimension. In order to clarify the origin of the antifouling effect observed, experiments for the evaluation of the samples hydrophobicity are carried out by measuring the static contact angle (figure 5.5, further details are reported in appendix D.6). Generally, the limit between hydrophilicity and hydrophobicity is set at a contact angle value of 90° [233]. Planar silk and control glasses are hydrophilic, presenting a closely comparable water contact angle (69 ± 1 and 68 ± 1° respectively). Silk nano stripes and μwells 2 samples show increased water contact angle values (73 ± 0.5° and 82 ± 2° respectively), but they still fall in the hydrophilic regime, confirming that the reduced E.Coli adhesion observed is most likely due to a steric effect exerted by the surface topography and it is not related to the surface wettability. μwells 1 substrates display a hydrophobic behavior, characterized by a water contact angle of 100 ± 1°. This result is in line with the existing literature, where similar honeycomb surface topographies were observed to influence the wettability of polymer films. In particular, this behavior was explained by the formation of air pockets between substrate surface and water droplets when the latter are much larger than the dimension of the substrate topological features [234]. This phenomenon may account for the μwells 1 antifouling properties, since it determines the amount of surface that is available for bacterial attachment. In particular Manabe et al. [229] observed that when the size of the pores lies between 3.5 and 11 μm and the contact angle of the culture medium is high, as in the μwells 1 case, bacteria experience a limited contact with the surface.
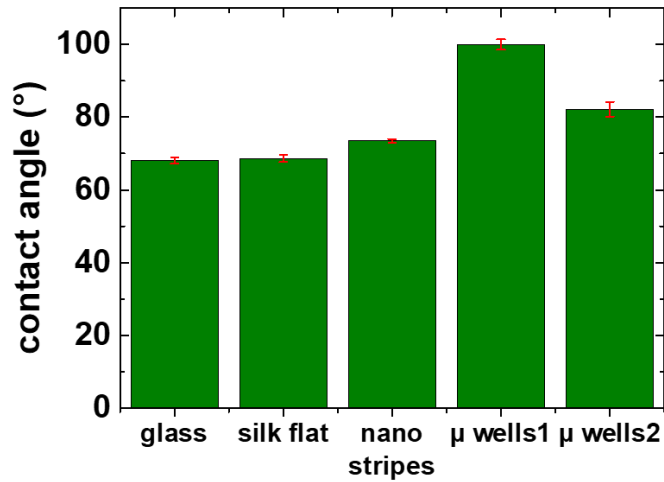
Figure 5.5. Static contact angles established by water drops over the different micro/nano-patterned silk morphologies and bare glasses.

5.5 Evaluation of E.Coli adhesion on rr-P3HT-covered silk substrates

In view of possible optoelectronic applications *in-vivo*, we implement the silk fibroin-based substrates with a thin layer of rr-P3HT. We focused our attention on the substrate that gave the best antifouling result, μ wells1, and on the planar silk morphology as a control.

The deposition of the semiconducting polymer layer is carried out by spin-coating, by selecting the proper rr-P3HT concentration and spin parameters that do not lead to a passivation of the micro-structured topography (appendix D.7). SEM images of the rr-P3HT-covered/uncovered samples (figure 5.6 panels a, b and c, d for silk flat and μwells 1 respectively) confirm that the samples surface morphologies are not altered after the semiconducting polymer deposition.
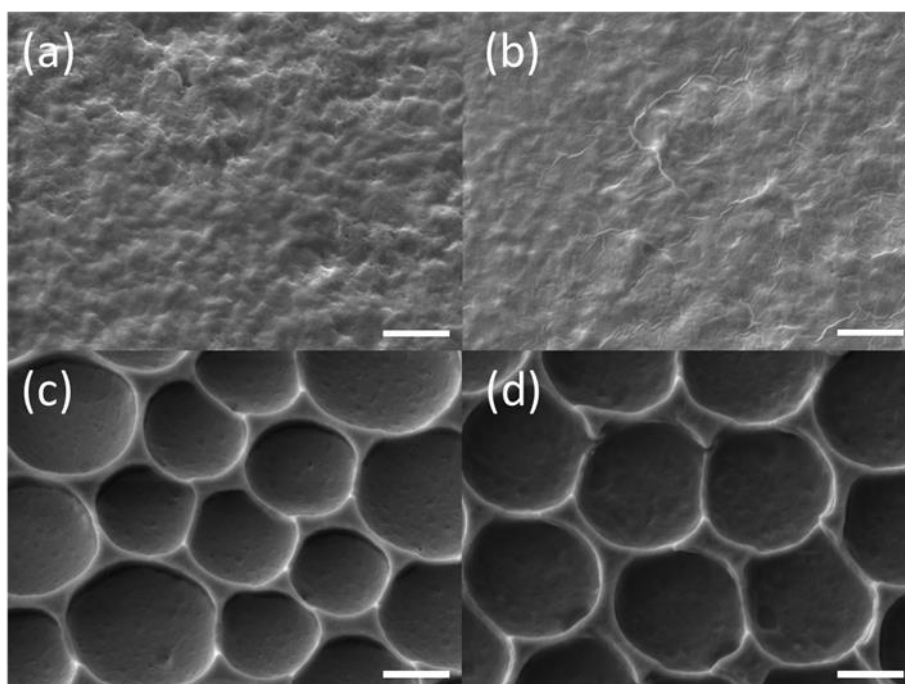
Figure 5.6. Top-view SEM images of silk flat without (a) and with rr-P3HT on top (b) and of µwells 1 sample before (c) and after (d) rr-P3HT deposition. Scale bar 2 µm

Experiments for the evaluation of the E. Coli attachment are then repeated using the rr-P3HT-covered silk samples (figure 5.7). The µwells 1/P3HT sample displays reduction of 41 % ($p < 0.05$) in the number of adhered bacteria with respect to the flat control, demonstrating that in the presence of rr-P3HT the topography-driven antifouling effect is still effective.
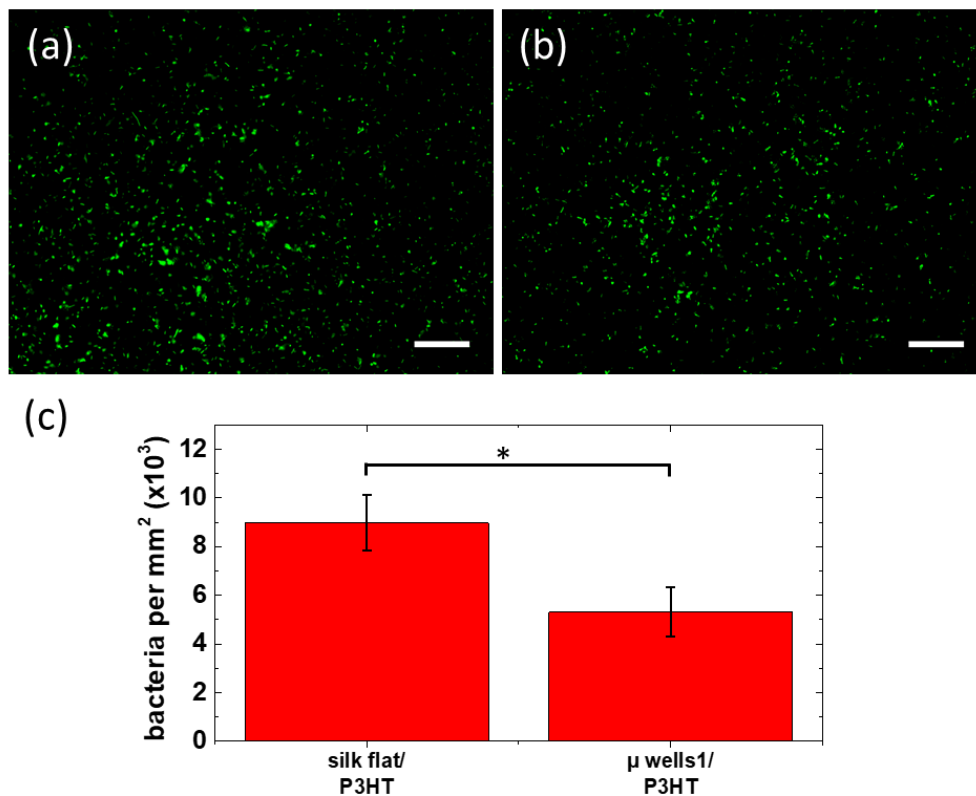
Figure 5.7. Fluorescent microscopy images of GFP expressing E.Coli bacteria cultured on top of silk flat/P3HT (a) and µwells 1/P3HT (b), after 24h. Scale bars 50 µm. (c) Quantitative analysis of bacteria observed in a,b. *p <0.05.

In order to corroborate our findings, we carried out experiments for the quantification of the bacterial growth inside the culture medium in presence of all the tested substrates. This experiment allows to understand whether the results obtained depend only on a hindered bacterial adhesion or on a coupling of this effect with bactericidal one, i.e. the killing of bacteria [235]. E.Coli cultures are prepared following the same procedure described in section D.4 but without transfecting the bacteria with the GFP construct. The bacterial growth is then evaluated by measuring the culture medium optical absorption at 600 nm after 24h. The results obtained, depicted in figure 5.8, show that there are no significant differences between the case where no substrate is present and the one where bacteria are incubated with both rr-P3HT-uncovered (figure 5.8 a) and rr-P3HT-covered (figure 5.8 b) samples. On the basis of these findings, we can conclude that the reduction of the surface-attached bacteria is only due to an unfavorable bacterial adhesion induced by the micro/nano-patterned topographies, excluding the presence of a concomitant bactericidal effect.
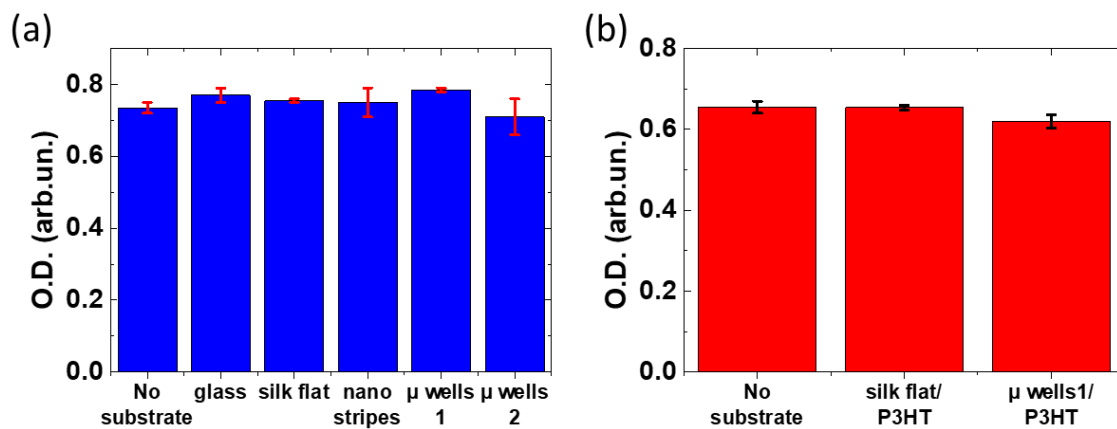
Figure 5.8. Bacterial growth in solution after 24h incubation with rr-P3HT-uncovered (a) and rr-P3HT-covered (b) substrates in comparison to the case where no substrate is present inside the growth medium. Bacterial growth is evaluated as the optical density (O.D.) at 600nm.

6. rr-P3HT-mediated optical stimulation of plant cells

6.1 Introduction

The central role that plants play both in the ecosystem, as regulators of water cycles and atmospheric oxygen, and in human life as a source of food, chemicals, heat and materials, aimed researchers to find solutions for augmenting plant growth and functions [236]. The methods employed to this purpose are mainly based on the use of fertilizers and on the genetic modification of plants; these strategies however are often related to environmental risks due to the release of chemicals in the environment and uncontrollable changes in the ecosystem. Smart materials have been introduced as an alternative to these approaches, for both the monitoring and the improvement of plants functions. For example, using inorganic nanoparticles, effects on root elongation, seed germination and plant growth were observed [237,238], whereas the treatment with carbon nanotubes led to the enhancement of the photosynthesis process [239]. Very recently, the M. Berggren's research group interfaced organic semiconductors with plant systems, introducing the concept of electronic plants (e-plants) [240]. In particular, they reported the fabrication of hydrogel-like conducting wires within the plant vascular tissues using water soluble thiophene-based polymers and oligomers, respectively self-organized and *in situ* polymerized inside *R. floribunda* plants tissues [240,241]. Moreover, they exploited the plant-integrated electronic systems obtained for the fabrication of OECTs and supercapacitors inside the vegetable structure [240,241]. Another recent work reported the recording of the plant physiological parameters with textile-based OECTs integrated into the vegetable structure [242].

Taking a cue from these works and in light of the results obtained by interfacing rr-P3HT-based devices and NPs with animal cells (presented in paragraphs 1.5 and 1.6), we explore the opportunity to establish a functional interplay between conjugated polymer systems and plants. We chose *Arabidopsis Thaliana* as a plant model, widely accepted in a variety of different studies, including plant physiology, population genetics, evolution and environmental science [243,244]. The functional

interaction between conjugated polymers and plant systems is tested here at the single cell level. To this goal, functional interfaces between rr-P3HT, both in the form of thin films and nanoparticles, and guard cells (GCs) are realized. Guard cells are highly specialized, kidney-shaped cells, which juxtapose to form a pore, the stoma. Importantly, they contain photosynthetically active chloroplasts, and their volume variations govern stomata movement. GCs play a key-role in both carbon dioxide uptake from the environment and respiration process, and they ultimately rule plant growth and survival [245]. Guard cells volume variation are the macroscopic result of a complex network of molecular processes, occurring at different hierarchical scales [245]. We decided to monitor the functional interaction between the thiophene-based material and the plant systems by measuring the variations in the cytosolic calcium (Ca^{2+}) concentration ($[Ca^{2+}]_{Cyt}$), in dark and light conditions, since Ca^{2+} signalling participates in many regulatory processes and is involved in nearly all aspects of plant development as a second messenger [246]. Ca^{2+} oscillations are widely employed to elucidate different plant processes, including metabolism and stimuli responsiveness [247]. Ca^{2+} signals consist in transient increases in $[Ca^{2+}]_{Cyt}$ that arise from Ca^{2+} fluxes coming from the extracellular environment or from internal compartments of the cells [247]. External stimuli, such as temperature changes, salt, or osmotic stresses, light, and plant hormones, produce specific Ca^{2+} responses with defined spatial and temporal characteristics, called Ca^{2+} signatures [246,248]. We monitor the $[Ca^{2+}]_{Cyt}$ by performing calcium imaging experiments, employing *Arabidopsis Thaliana* plants genetically encoded with the cytosol-localized calcium indicator yellow Cameleon (YC). YC probes are based on the fluorescence resonance energy transfer (FRET). They comprise two GFP variants, cyan and yellow fluorescent proteins (CFP and YFP respectively) bound together by the calmodulin-binding peptide M13 and the Ca^{2+} -binding protein calmodulin [249]. When Ca^{2+} ion binds to calmodulin, a conformational change in the YC indicator takes place, enabling enhanced FRET between CFP and YFP. The quantitative measurement of Ca^{2+} dynamics is performed by acquiring the YFP/CFP ratio shift [249].

In this chapter, the study of the interaction between the photoexcited rr-P3HT and plant systems starts with the evaluation of the GCs viability in presence of the semiconducting polymer. Then, the effects of light stimulation on the $[Ca^{2+}]_{Cyt}$ oscillations of *Arabidopsis* leaves GCs, in presence of rr-P3HT polymer thin films and NPs, are investigated. In addition, NPs-induced variations in the stomatal aperture size are studied by fluorescence imaging. Moreover, the NPs coupled to the plant sample are visualized by acquiring confocal microscopy images. In view of future applications at a systemic level, in the last part of the chapter a preliminary study of the rr-P3HT NPs uptake by *Arabidopsis* seedlings, i.e. very young plants grown from a seed, is investigated. In particular, the NPs uptake within the root tissue is successfully assessed by confocal imaging experiments.

To the best of our knowledge, this is the very first report of use of rr-P3HT conjugated polymer in combination with a vegetable system and the presented results will be included in: G. Tullii, A. Costa, M. R. Antognazza, *Conjugated polymers optically regulate signalling in Arabidopsis Thaliana models at single and multicellular level*, in preparation.

6.2 *Arabidopsis* guard cells interfaced with rr-P3HT: viability assay

The *Arabidopsis Thaliana* plants used for all the experiments presented in this chapter are grown and maintained in collaboration with Prof. A. Costa (Department of Biosciences, University of Milan).

As a necessary preliminary step, we evaluate the cells viability in contact with the photoactive material, both in dark and upon photoexcitation (figure 6.1). 6-week-old *Arabidopsis* leaves are attached to glass slides and the upper epidermal cells are remove using a razor blade. The exposed guard cells are placed in a proper imaging solution and put in physical contact with spin coated rr-P3HT thin films (film thickness: 150 nm, for additional details refer to appendix E.1) on planar ITO electrodes. Then, a viability study based on fluorescein-diacetate (FDA) assay is carried out (appendix E.1). FDA is a consolidated probe for the study of both animal and plant cells viability [250,251].

FDA is a non-fluorescent compound that switch to the fluorescein fluorescent form when hydrolysed by the intracellular esterases of cells that display intact membranes and regular enzymatic activities. Thus, only healthy cells become fluorescent. Figure 6.1 shows representative bright-field optical microscope images (panels a, c and e) and FDA fluorescence staining over the very same field of view (panels b, d and f). The comparison with bright-field conditions allows to distinguish viable from not-viable cells. The experiment has been carried out without the polymer in dark and upon CW light excitation ($\lambda = 540$ nm, 64 mW/mm^2, time duration = 2 minutes), both in presence and absence of the ITO/P3HT device interfaced to GCs. The statistical analysis is based on 50 cells belonging to 3 statistically independent samples for each condition (Figure 6.1 g). No statistically significant differences are evidenced among the three samples cohorts, being the percentage of healthy cells 72 ± 6 %, 81 ± 8 % and 74 ± 13 % in the case of control in dark, light treated, and light+polymer samples, respectively (Student's t-test $p > 0.05$ in all considered cases).
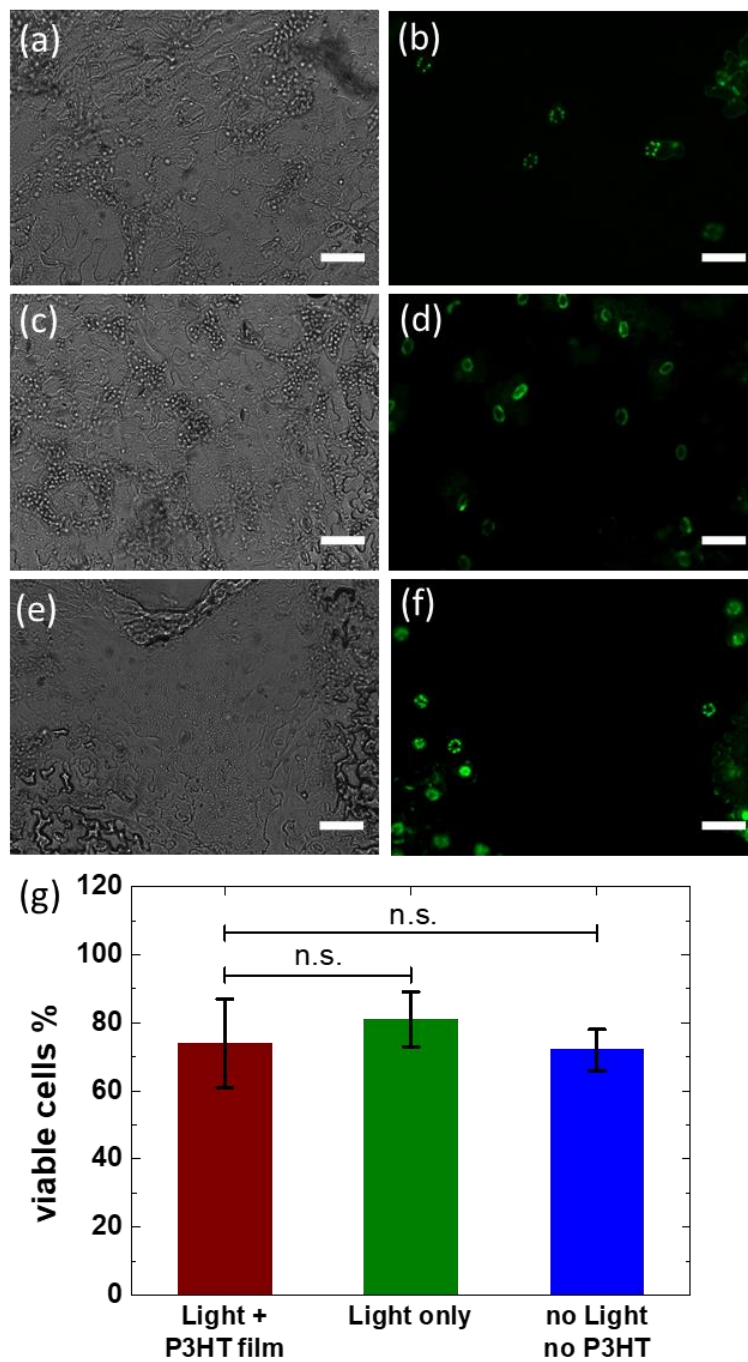
Figure 6.1. Representative bright field and fluorescence images depicting FDA-treated GCs without any treatment (panels a,b), after green light excitation (panels c,d) and after green light excitation in presence of rr-P3HT film (panels e,f). Light stimulation conditions: $\lambda = 540$ nm, 64 mW/mm^2, time duration = 2 minutes. Scale bars: 50 µm. Panel g shows the percentage of viable cells for each condition.

6.3 Modulation of *Arabidopsis* guard cells intracellular Ca^{2+} by polymer photoexcitation

Functional interaction between photoexcited conjugated polymer and GCs is evaluated by carrying out calcium imaging experiments. To this purpose, *Arabidopsis* plant leaves genetically encoded with a variant of the cytosol-localized yellow cameleon probe (NES YC3.6 [252,253]), are employed. The leaves are anchored to glass substrates and immersed in imaging solution in the same way as for the viability study (appendix E.1). Then, the plant samples are interfaced with ITO/P3HT devices and rr-P3HT NPs (average hydrodynamic radius 237 ± 82 nm). rr-P3HT nanoparticles synthesis and characterization has been reported elsewhere, and briefly summarized in appendix E.2 [126]. Leaves guard cells are incubated for 20 minutes with NPs, diluted in the bath solution up to a final concentration correspondent to Nps optical density (OD) = 0.1. As aforementioned in paragraph 6.1, the YC probe fluorescence emission (YFP/CFP ratio) is directly proportional to the cytosolic Ca^{2+} concentration and can be measured using a fluorescence microscope. We monitor the spontaneous [Ca^{2+}]$_{Cyt}$ oscillations before and after stimulating the system with CW light ($\lambda = 540$ nm, intensity :64 mW/mm^2, time duration: 2 minutes, figure 6.2) in presence and absence of rr-P3HT. In dark, the [Ca^{2+}]$_{Cyt}$ trend is comparable in all cases, recording the typical spontaneous [Ca^{2+}]$_{Cyt}$ oscillations profile already observed in *Arabidopsis* GCs (figure 6.2 panels a-c, see appendix E.3 for experimental details) [254–256]. Although the nature of the spontaneous [Ca^{2+}]$_{Cyt}$ oscillations has not yet fully elucidated, experiments performed on GCs of intact plants have confirmed that this spontaneous Ca^{2+} activity is a conserved feature of this cell type, and it is probably related to physiological processes taking place in response to environmental stimuli (e.g., water balance, light conditions, CO^2 levels) [256]. The comparable [Ca^{2+}]$_{Cyt}$ dynamics recorded in dark suggests that in absence of a light stimulus, the GCs functional properties are not affected just by the contact with the organic semiconductor. When the optical excitation is provided, the situation changes. It has been reported that photoexcitation at blue and red wavelengths can substantially affect calcium signalling, leading to an increase in the [Ca^{2+}]$_{Cyt}$ mediated by the action of specific photoreceptors, phototropines and

phytochrome for blue and red light respectively [246,257–260]. The use of green light excitation in principle allows to exclude any effect mediated by light sensitive proteins. This assumption is fully confirmed by the results obtained with the rr-P3HT-untreated guard cells (CTRL), with no relevant changes in the $[Ca^{2+}]_{Cyt}$ peaks amplitude and number considered in the pre- and in the post-excitation temporal windows (figure 6.2 a). The variation is quantified by calculating the ratio between the average peaks amplitude after/before light (I_{AFTER}/I_{BEFORE}) and the ratio of the mean number of peaks recorded after and before the light stimulus occurrence (N_{AFTER}/N_{BEFORE}). Both quantities are very close to unity in the CTRL case ($N_{AFTER}/N_{BEFORE} = \sim 1$, $I_{AFTER}/I_{BEFORE} = \sim 0.8$, figure 6.2 panels d-e). Conversely, the illumination of the polymer film leads to a remarkable silencing of the calcium activity (figure 6.2 b), associated to N_{AFTER}/N_{BEFORE} and I_{AFTER}/I_{BEFORE} values about 88% and 69% lower than in the CTRL case (figure 6.2 d,e). The same experiment carried out upon administration of rr-P3HT NPs shows comparable results with the solid state film (figure 6.2 c), even though the overall effect is less evident in this case (N_{AFTER}/N_{BEFORE} and I_{AFTER}/I_{BEFORE} values reduced respectively by 51% and 49% as compared to the CTRL case, figure 6.2 d,e).
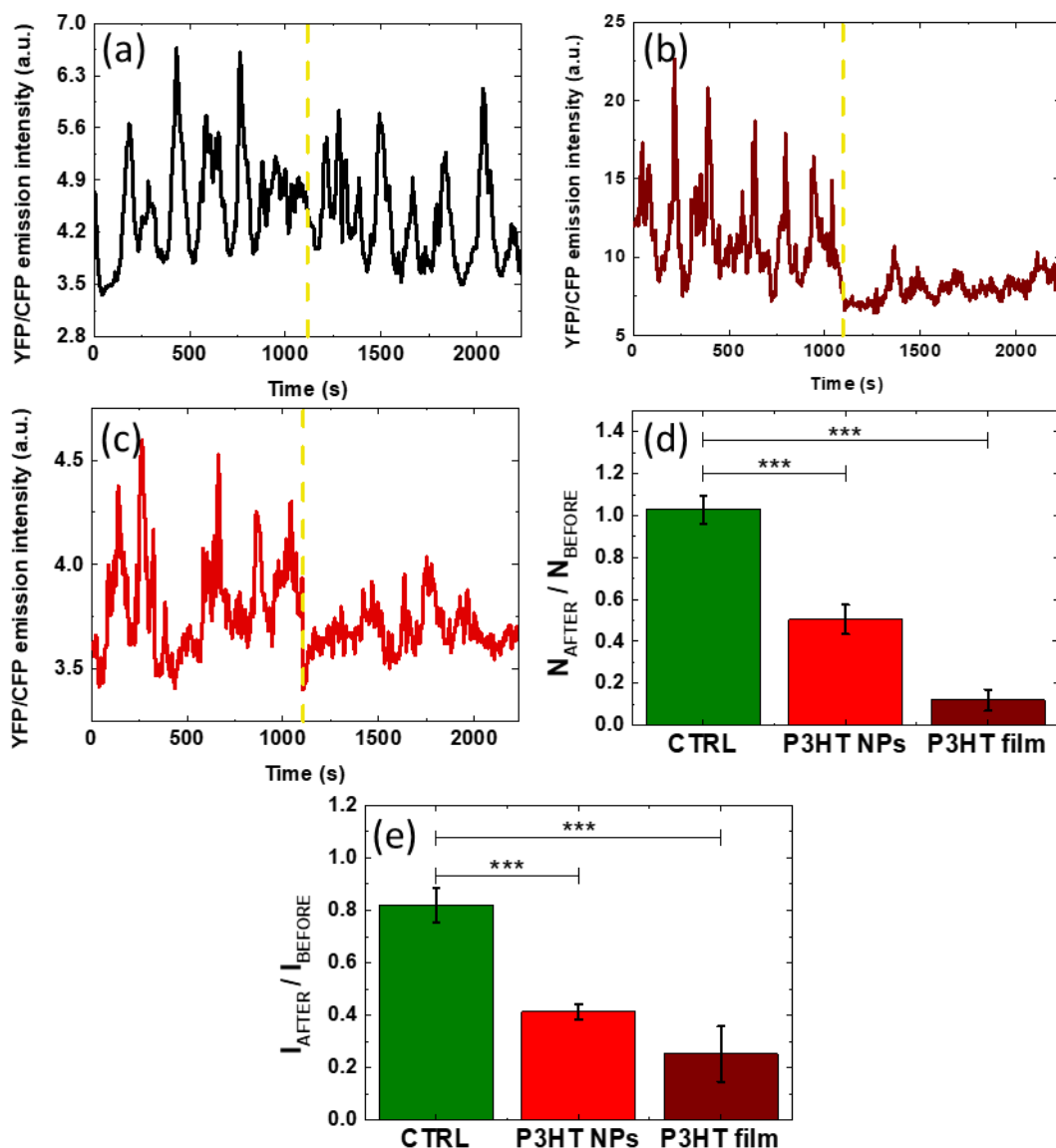
Figure 6.2. Ca^{2+} dynamics monitored in *Arabidopsis* guard cells expressing Cameleon YC3.60 before and after optical excitation in terms of YFP/CFP emission, in absence of rr-P3HT (panel a) and in presence of rr-P3HT film (panel b) or rr-P3HT NPs (panel c). The yellow dashed line represents the optical excitation ($\lambda = 540$ nm, intensity :64 mW/mm^2, time duration = 2 minutes). (d) Mean ratio between the average number of YFP/CFP emission peaks after and before illumination. (e) Average ratio of the YFP/CFP emission intensity recorded after and before optical excitation. Mean values are averaged over a statistical ensemble of n = 10 cells for each condition. Error bars represent the s.e.m.. ***, p < 0.001 (Student's t-test).

These results demonstrate that the use of polymer photoactivity in combination with visible light excitation may provide a useful tool to down-regulate on demand, in a drug-free and fully controllable way the calcium activity in single guard cells. Moreover, the use of rr-P3HT NPs gives the possibility

to further reduce the invasiveness of the method and allows to exploit the ease of delivery of the NPs, particularly attractive in view of applications that involve entire plant systems. For this reason, from now on, we focus only on the interaction between rr-P3HT NPs and plants.

Reversibility of the observed down-regulation in intracellular Ca^{2+} dynamics must be assessed. To this purpose, two different approaches are adopted: (1) administration of excess extracellular Ca^{2+} concentration after light-induced partial silencing; (2) repetition of calcium imaging experiments after leaving the samples resting in dark (figure 6.3, appendix E.3). The addition of Ca^{2+} ions in the extracellular bath represents a standard stimulus for eliciting $[Ca^{2+}]_{Cyt}$ spikes in leaves GCs [254,261–263]. We observe that the Ca^{2+} addition in the bath elicits a sizeable increase in both the amplitude and number of $[Ca^{2+}]_{Cyt}$ spikes, turning back to be comparable to the values measured before the light excitation protocol (figure 6.3 a). This demonstrates that the GCs functionality is preserved. However, although this test represents a direct and easy way for assessing the reversibility of the photoexcited rr-P3HT NPs-induced effect, it implies the alteration of the GCs physiological conditions (delivery of excess Ca^{2+} ions respect to physiological conditions). The recovery of the $[Ca^{2+}]_{Cyt}$ spontaneous oscillations is thus verified also without any external stimulus, by taking advantage of the method (2). In this case, calcium imaging recordings of rr-P3HT NPs-treated guard cells upon light excitation are repeated (figure 6.3 b). Additional calcium imaging recordings are then performed after leaving the samples 20 minutes in dark, revealing that the guard cells recover almost completely the frequency (95%) and partially the amplitude (58%) of the $[Ca^{2+}]_{Cyt}$ spontaneous spikes recorded before the light stimulation event (figure 6.3 c).
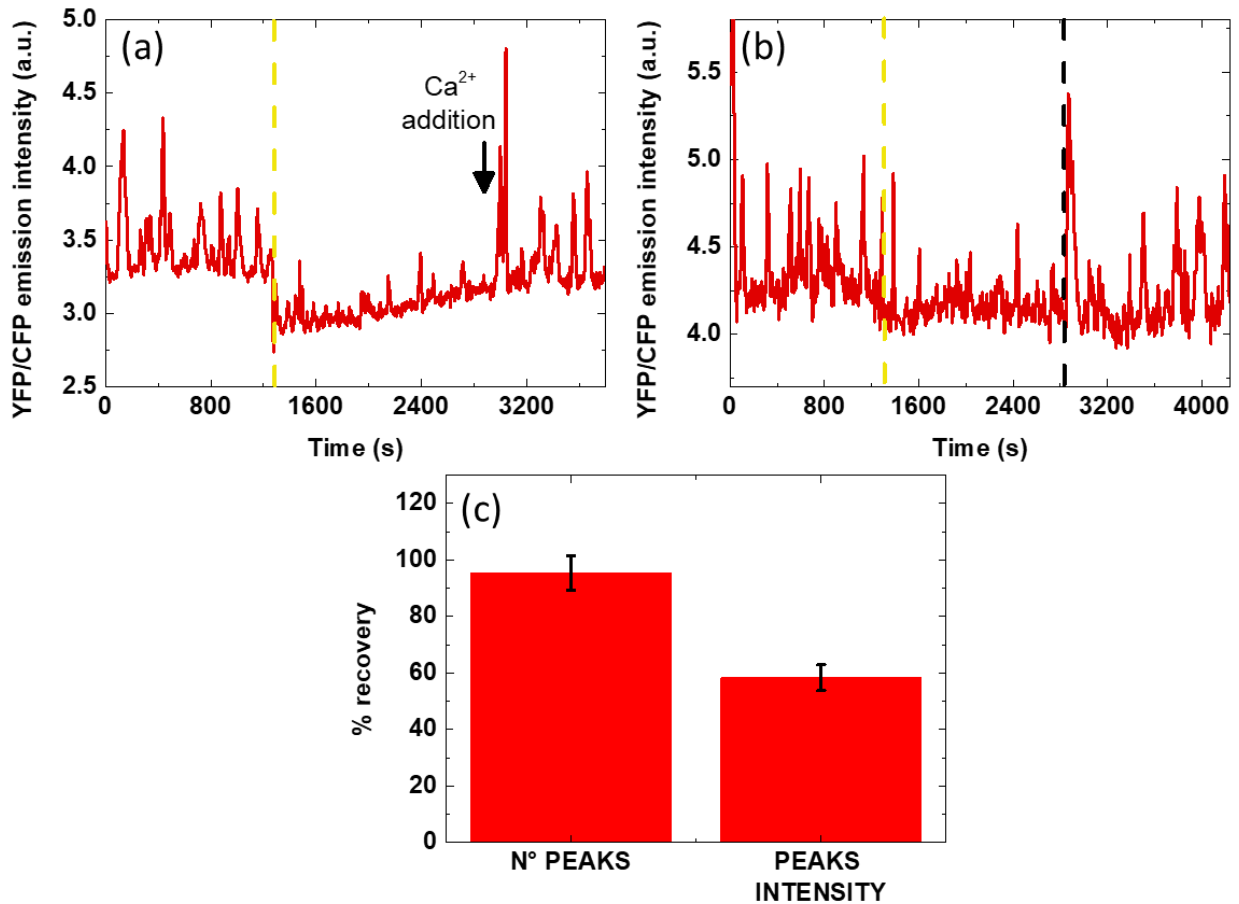
Figure 6.3. Calcium imaging experiments on rr-P3HT NPs-treated *Arabidopsis* guard cells genetically encoded with Cameleon YC3.60 for the evaluation of the reversibility of the optically-induced $[Ca^{2+}]_{Cyt}$ oscillations silencing phenomenon, performed by extracellular Ca^{2+} addition (a) or by leaving the plant sample resting in dark (b). The yellow and black dashed lines represent the optical excitation ($\lambda = 540$ nm, intensity :64 mW/mm^2, time duration: 2 minutes) and the time spent in dark (20 min) respectively. (c) % recovery of the average number and amplitude of YFP/CFP spikes after leaving the guard cells in dark with respect to the values in the pre-light excitation time window. Mean values are averaged over a statistical ensemble of n = 20 cells. Error bars represent the s.e.m..

These results show that the optically-induced silencing in the guard cells $[Ca^{2+}]_{Cyt}$ spontaneous oscillations, mediated by rr-P3HT NPs, is not an irreversible effect, excluding the occurrence of detrimental consequences on guard cells functionality.

The explanation of the mechanism involved in the rr-P3HT NPs-mediated modulation of $[Ca^{2+}]_{Cyt}$ in *Arabidopsis* guard cells is not straightforward. The analogy with the results obtained with ITO/P3HT devices suggests that the phenomenon is guided by an extracellular mechanism. In order to validate this assumption, the distribution of NPs within the plant sample is assessed by acquiring confocal

microscopy images of rr-P3HT NPs-treated leaves GCs. During images acquisition, the entire sample area is scanned from bottom to top, incrementing each focal plane in steps of 250 nm. The confocal detection system permits the collection of the emitted light coming only from planes close to the considered focal plane, allowing the precise localization of the NPs. Figure 6.4 depicts the single stack focal planes acquired, by which it is possible to appreciate that the nanoparticles are not internalized within the GCs cytosol, remaining suspended in the extracellular bath solution. This result corroborates the assumption that the photoexcited rr-P3HT NPS down regulate the GCs $[Ca^{2+}]_{Cyt}$ spontaneous oscillations trough an extracellular mechanism.
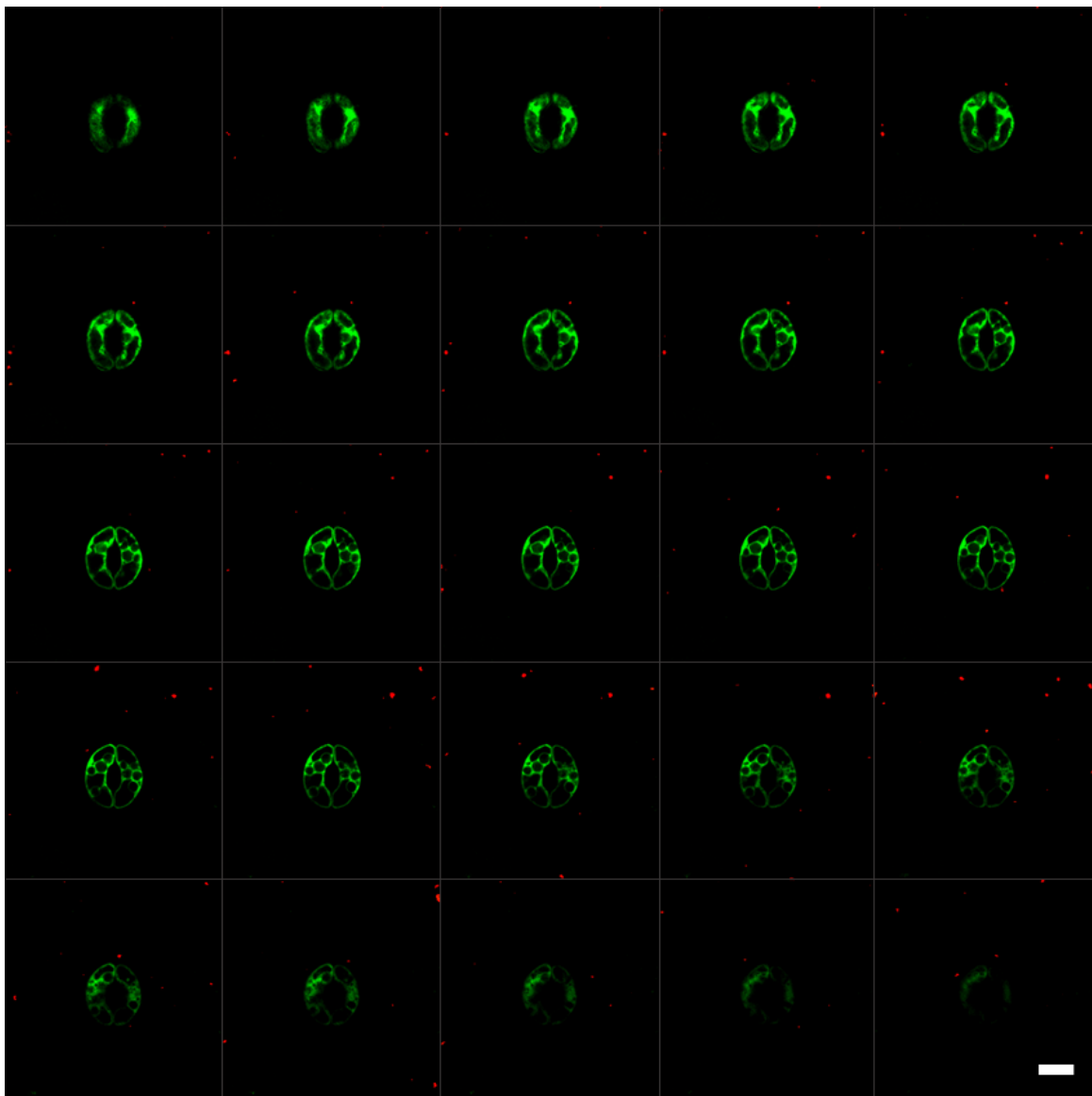
Figure 6.4. Confocal optical sections depicting an *Arabidopsis* GCs treated with rr-P3HT NPs. GC is stained with YC3.6 (green). Red emission corresponds with rr-P3HT NPs. Scale bar: 10 µm.

Given the role of Ca^{2+} as second messenger, the guard cells $[Ca^{2+}]_{Cyt}$ can be modulated by a large variety of external stimuli, including auxin, CO_2, abscisic acid (ABA), extracellular Ca^{2+} addition and ROS [264]. The response to most of these extracellular stimuli corresponds with transient elevations in guard cells $[Ca^{2+}]_{Cyt}$. However, in some cases effects on the spontaneous $[Ca^{2+}]_{Cyt}$ oscillations were also observed. In particular, the increase of the CO_2 concentration and the addition of ABA in the bath solution have been demonstrated to reduce the rate and both the amplitude and the frequency of spontaneous $[Ca^{2+}]_{Cyt}$ transients in *Arabidopsis* guard cells, respectively [264,265]. Moreover, in the case of ABA, a reactivation of the $[Ca^{2+}]_{Cyt}$ spontaneous oscillations after a quiescent period of 30-40 minutes was noticed, similarly to what observed with rr-P3HT NPs. Both ABA and CO_2-induced dampening of the spontaneous $[Ca^{2+}]_{Cyt}$ oscillations were attributed to a depolarization of the GCs. In analogy with these reports, we can thus tentatively attribute the silencing of the $[Ca^{2+}]_{Cyt}$ activity observed in our case to a cell depolarization induced by the photoexcited rr-P3HT NPs. However, a precise explanation of the mechanism requires additional experiments.

6.4 Optically-induced effects on stomatal opening mediated by rr-P3HT NPs

We proceed the study of the interaction between rr-P3HT NPs and guard cells by investigating the presence of optically-induced effects on the stomata functionality. In particular, we assess the presence of changes in stomatal aperture induced by the treatment with photoexcited rr-P3HT NPs by performing fluorescence microscopy imaging (appendix E.4).

Arabidopsis leaves samples, genetically-encoded with the YC probe, are treated with rr-P3HT NPs with the same concentration and incubation time employed in calcium imaging measurements. The leaves are also incubated with optically insensitive silica nanoparticles (SiO_2 NPs, average diameter = comparable to polymer nps, concentration = 0.25 mg ml^{-1}) that serve as a control experiment, for assessing the presence of stomatal aperture variations only due to the NPs sterical effect. The NPs-

treated leaves GCs are exposed to white light (4000 lux) for 90 minutes. In this case the light excitation serves both as a stimulus for NPs and for the stomata, since the guard cells photoexcitation (in particular with blue and red wavelengths) have been demonstrated to provoke the stomatal opening [266]. Thus, by measuring the stomatal aperture size after the optical treatment it is possible to evaluate the influence of the NPs on the light-induced stomatal aperture. Fluorescence images of the YC-encoded guard cells after the treatment with light and NPs are acquired and the stomatal aperture width (d) is measured through a post-processing analysis of the images. In this case the YC probe acts only as a visual indicator, since the superimposition of the YFP and CFP emissions is recorded. Representative fluorescence images of open and closed guard cells are depicted in figure 6.5 panels a and b respectively. The analysis of the stomatal aperture size (figure 6.5 c), conducted in double-blind conditions, reveals a significant decrease in stomatal aperture both in the SiO_2 and rr-P3HT NPs cases in comparison to the untreated samples (CTRL) (correspondent to 7 % and 21 % in the SiO_2 and rr-P3HT cases respectively). Interestingly, the treatment with rr-P3HT NPs leads to the lowest value of the stomatal aperture width (figure 6.5 c).
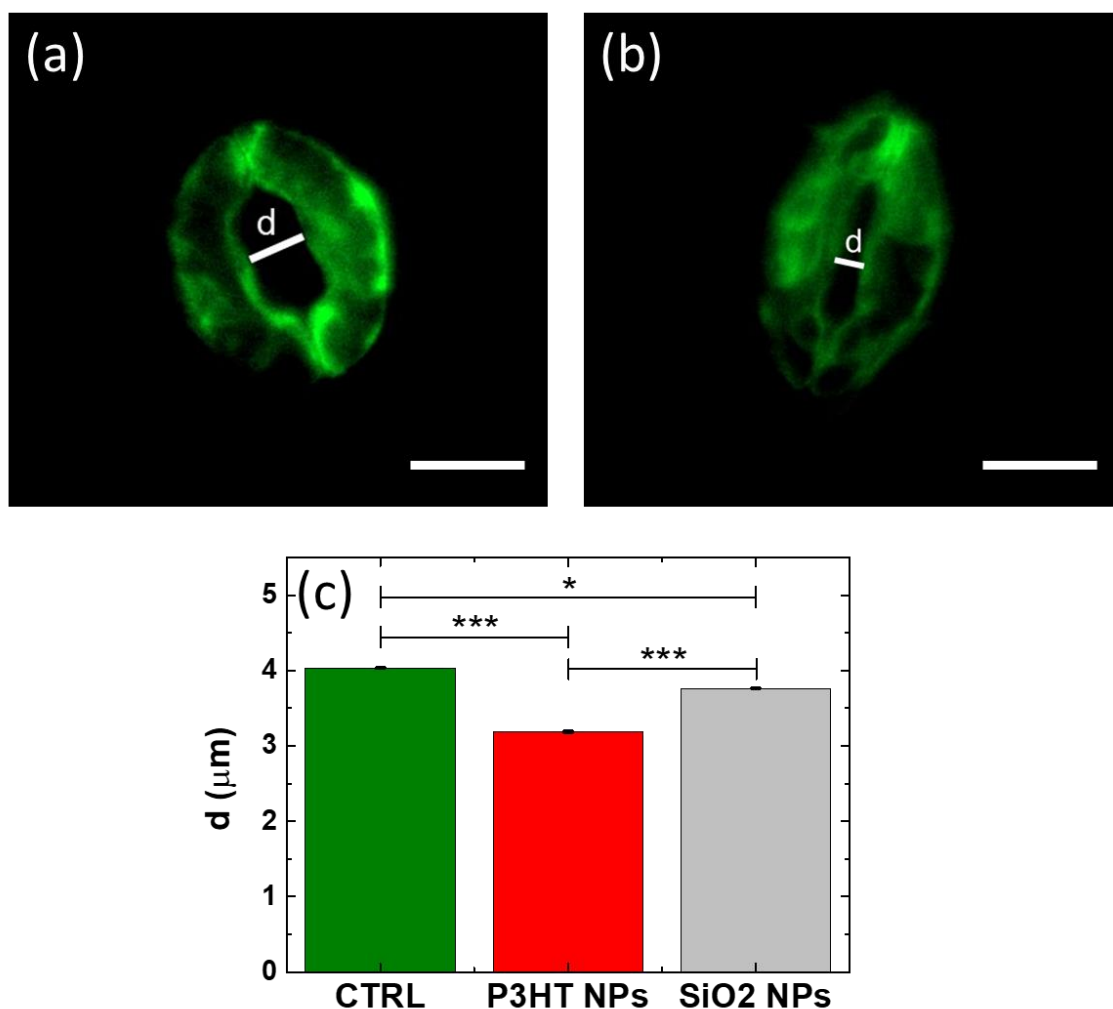
Figure 6.5. Representative fluorescence images of YC 3.6-encoded GCs in open (a) and closed (b) states. Scale bars: 10 µm. (c) Histogram reporting the average stomatal aperture width (d) measured after exposure to white light without any NPs (CTRL) present and in presence of rr-P3HT or SiO_2 NPs. Error bars represent the s.e.m.. *, $p < 0.05$, ***, $p < 0.001$ (Student's t-test).

In literature, the inhibition of the stomatal opening was demonstrated by the treatment with ABA, extracellular Ca^{2+}, Nitric oxide (NO) and H_2O_2 [267–271]. In particular, the addition of exogenous H_2O_2 has been shown to inhibit the stomatal opening provoked by light excitation in *Arabidopsis Thaliana* plants [272]. As discussed in sections 1.6 and 2.2, rr-P3HT presents a favorable energy alignment at the polymer/electrolyte interface for the oxygen reduction reaction (ORR) [78,273], that leads to the photoinduced production of ROS at the polymer/electrolyte interface. In particular, we recently demonstrated that the rr-P3HT NPs photo-stimulation produces an increase in the

intracellular concentration of ROS in HEK-293 cells [130]. The presence of ROS was verified by using different ROS fluorescent probes, including 2,7-dichlorodihydrofluorescein diacetate (H2DCF-DA) that is sensible to various ROS species, including H_2O_2 [130]. We attributed the ROS production to a direct photocatalytic effect of the NPs, demonstrated in different electrolyte compositions through electrochemical experiments [130]. Thus, it is likely that this phenomenon can occur also in the extracellular environment in contact with the GCs. In light of these considerations, a tentative explanation of the inhibition of the stomatal opening exerted by rr-P3HT NPs can be made by considering a local photo-induced production of H_2O_2 in the close proximity of *Arabidopsis* guard cells (figure 6.6). The validation of this assumption will be the object of future experiments.
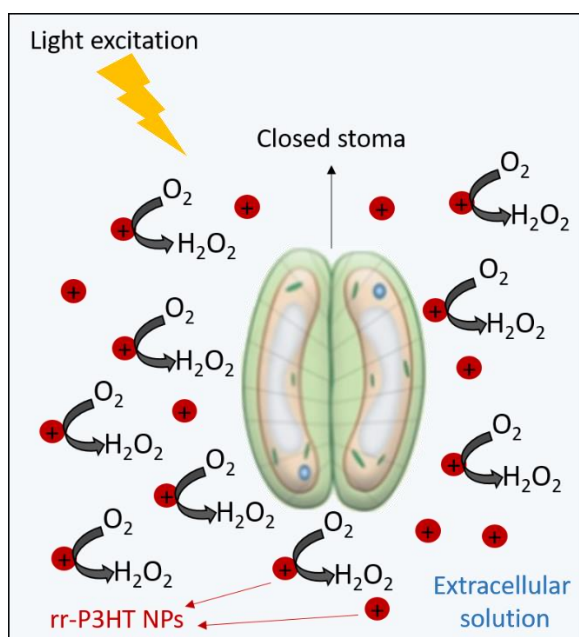
Figure 6.6. Schematic drawing of the inhibition of the light-induced stomatal opening due to the presence of extracellular H_2O_2 produced by the rr-P3HT NPs photoexcitation.

6.5 rr-P3HT NPs uptake by *Arabidopsis Thaliana* seedlings roots

We extend the study of the interaction between rr-P3HT NPs and *Arabidopsis Thaliana* plants to an increased level of biological complexity, by investigating the Nps uptake by 7-days-old *Arabidopsis Thaliana* seedlings roots.

Arabidopsis seedlings are incubated for 60 minutes with rr-P3HT NPs, diluted in the bath solution up to a final concentration correspondent to Nps optical density (OD) = 0.25. The Nps, coupled with the root tissue, are visualized by performing confocal imaging experiments (figure 6.7). The inspection of subsequent stacks, acquired from the bottom to the top of the root sample (1.5 µm steps), reveals that nanoparticles have a great tendency to accumulate along the root tip surface and also to be internalized within root tissue in proximity of the tip cap (white arrows, figure 6.7). This constitutes a promising result and opens the way to an in-depth study of the NPs delivery to entire plants *in-vivo*.
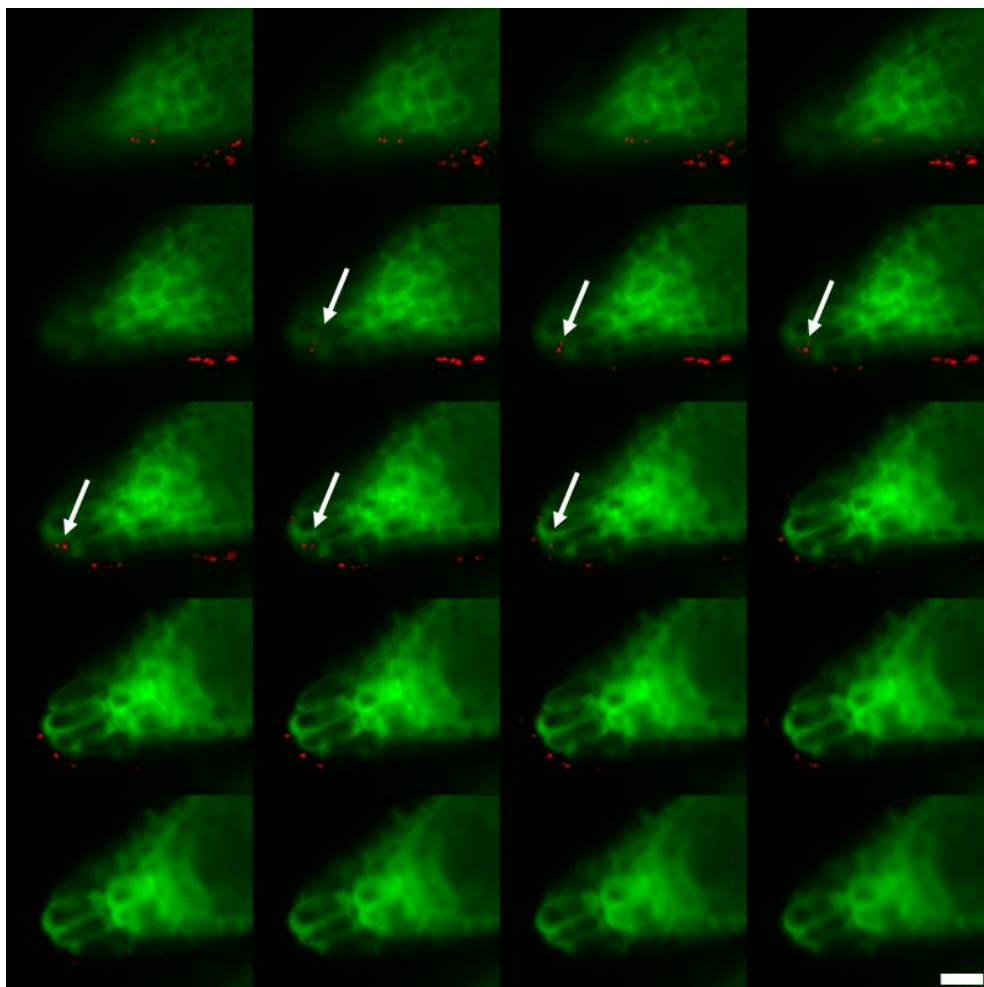
Figure 6.7. Confocal optical sections of the *Arabidopsis* Thaliana seedlings incubated with rr-P3HT NPs. Root tip cells are stained with YC3.6 (green). Red emission corresponds with rr-P3HT NPs. Nps internalized within the plant tissue are indicated by white arrows. Scale bar: 20 µm.

7. Conclusions and perspectives

In this thesis work we have developed different strategies to engineer hybrid interfaces established between rr-P3HT-based photoactive platforms and aqueous electrolytes, and we have characterized in depth the biological effect on living cells activity and functionality. In chapter 2 we present the fabrication and characterization of multilayered planar devices that comprise a rr-P3HT active layer sandwiched between charge selective materials. By performing electrochemical measurements, we show that the ITO/P3HT device presents a predominant photoinduced capacitive behavior, characterized by the accumulation of positive charges at the polymer surface, balanced by negative ions in the electrolyte solution. This property can be selectively modulated by coupling the rr-P3HT layer with hole-selective layers (HSL) or electron selective layers (ESL) materials. We demonstrate that by depositing an ESL layer of PCBM on top of the semiconducting polymer, ending up with ITO/p-i-n architecture, the prevailing device response is still capacitive, but with opposite sign (i.e., electrons accumulate at the surface). Moreover, we show that by developing a more complex architecture, and in particular by introducing both ESL and HSL materials coupled with a catalyst, the efficiency of faradaic charge transfer phenomena at the device/electrolyte interface is dramatically enhanced. In particular we describe the fabrication and characterization of highly efficient organic/inorganic photocathodes for hydrogen evolution. We explore different multilayered architectures, obtaining the best results with FTO/CuI/P3HT:PCBM/TiO$_2$/Pt configuration, characterized by photocurrent value up to 7.1 mA cm^{-2} at 0 V vs. RHE, associated to hydrogen evolution reactions with 100% faradaic efficiency . This result indicates that conjugated polymer-based photocathodes are suitable devices for efficient photocatalytic hydrogen generation.

In the following, we describe the successful interfacing of ITO/P3HT, ITO/P3HT:PCBM, ITO/p-i-n and ITO/CuI/P3HT:PCBM/TiO$_2$ architectures with HEK-293 line cells. We observe that the presence of ESLs (PCBM, TiO$_2$) leads to modulate HEK-293 cells membrane potential respect to the ITO/P3HT and ITO/P3HT:PCBM cases. In particular, we record opposite signs of the fast membrane potential variation component, previously attributed to the capacitive device photocharging, in the

two cases. By performing surface potential measurements, we confirm the direct relationship existing between the fast membrane potential change and the capacitive charging occurring at the device surface. These results highlight the fact that the coupling of rr-P3HT with interlayers can be exploited for the achievement of different capacitive stimulation patterns, leading either to cell membrane depolarization or hyperpolarization.

In chapter 3 we propose an alternative strategy for balancing the capacitive vs. faradaic photoinduced effects occurring at the rr-P3HT/electrolyte interface, based on the engineering of the ITO/P3HT device morphology. We present a mesoporous device constituted by a rr-P3HT active layer intercalated into a mesoporous ITO NPs-modified ITO electrode, fabricated through an all-solution process. By performing electrochemical measurements and by modeling the experimental data with an equivalent electrical circuit, we show a strict relationship between the mesoporous morphology and the polymer/electrolyte interface dynamics. In more detail, we find that the surface area increment (about two orders of magnitude) due to the mesoporous architecture leads to a remarkable increase of the efficiency of the optically-induced faradaic charge transfer phenomena occurring at the polymer/electrolyte interface. Oxygen reduction reactions (ORR) represent the predominant photoinduced faradaic phenomena in both the mesoporous and planar cases, in agreement with previous reports that identified a favorable energy alignment at the rr-P3HT/electrolyte interface for this specific reaction. The possibility to balance capacitive and faradaic processes is particularly appealing for biological applications since it opens the way to the possibility to achieve a bimodal stimulation pattern, by coupling for example capacitive and faradaic stimulation mechanisms. In light of this, we test the mesoporous device morphology for the living cells optical excitation by performing extracellular surface potential measurements in presence of a light stimulus and whole-cell patch-clamp recordings on HEK-293 cell models. We demonstrate that the mesoporous photoactive platform is bio-compatible and fully working even in the presence of a living cell population cultured on top of its surface. However, we do not evidence any clear variation, possibly due to an 'active' response from the cells, between the surface potential trace recorded in absence of

cells and the electrical component of the HEK-293 cells membrane potential variations. We attribute this to a scarce electrical coupling between the mesoporous photoactive platforms and the cells. This observation prompted us to explore new strategies to enhance the electrical coupling between the rr-P3HT-based device and living cells.

In chapter 4, we propose an approach for the improvement of the cellular adhesion based on the implementation of micro-structured devices. We present the successful fabrication of rr-P3HT microstructures of conical shape, by coupling femto-second micromachining and push-coating wet-deposition technique. The fabrication process allows for the realization of devices, in a highly versatile, fast, straightforward and repeatable way. Realized semiconducting polymer pillars are characterized by a high aspect ratio and usefully combine the advantages of micro- and nanoscale topographies, as a highly desirable characteristics which, in the case of inorganic electrodes, can be achieved only by making recourse to complex fabrication techniques. In fact, the micrometer-sized base confers to the soft rr-P3HT pillars good mechanical stability, while the sub-um rounded tip establishes a tight interface with the living cell membrane, key for achieving efficient and reliable extracellular stimulation and recording and also for other interesting applications, such as the localized delivery of biomolecules into the cell cytosol. We show that polymer pillars can be used as highly biocompatible substrates for both primary cortical neurons and HEK-293 cells. The adopted shape and density of polymer pillars leads to establish a close contact with both HEK-293 and neuronal cell membrane, with a localized thinning of the cell membrane, without however negatively affecting cells viability. In the case of cortical neurons, we notice also that their intrinsic electrophysiological properties and synapses expression are fully preserved on top of the pillar microstructures. Interestingly, we observe a sizable change in the morphology of HEK-293 cells, showing a pronounced tendency to develop in the three-dimensional space when interfaced to structured polymer substrates. Importantly, the rr-P3HT structured devices maintain a certain degree of optical transparency, thus making possible optical access to the cell culture. However, despite the successful attainment of optimal cellular adhesion in the close proximity to pillar microstructures, we

do not observe any clear improvement in the cellular response upon polymer photoexcitation. We attribute this to the high polymer thickness in correspondence with the rr-P3HT-based microstructures, which implies, in absence of a corresponding microstructuring of the underlying electrode, poor charge dissociation efficiency. In light of this, future work will target the implementation of the rr-P3HT pillars-based platform for the thinning of semiconducting polymer active layer. A possible strategy consists in the fabrication of the high aspect ratio microstructures with a transparent and inert material and in the subsequent deposition of the ITO and semiconducting polymer layers.

Given the high interest of organic bioelectronics devices for in vivo use, in chapter 5 we describe the exploitation of micro- and nano-structured device topographies for antifouling applications, i.e., to limit the adhesion of bacteria. We develop micro-structured silk substrates, presenting micro-wells or nanogrooves on their surfaces, following a simple, inexpensive and high throughput, soft lithographic fabrication procedure. Interestingly, we observe that all the micro and nano-patterned silk substrates efficiently inhibit the adhesion of E.Coli bacteria without hindering the proliferation of HEK-293 cells. We notice that the sample patterned with micro-wells in the 3.5-5 μm range provides excellent antifouling properties, due to a hydrophobicity-driven mechanism, which are preserved also when the silk substrate is covered by the rr-P3HT polymer layer. This opens the way to the exploitation of polymer-coated biocompatible and bioresorbable devices enhanced with antifouling capability for optoelectronic *in-vivo* applications. In the future, prior to the application of this substrate as a medical implant, its antifouling properties will be assessed *in-vitro* using clinically-relevant bacterial pathogens (e.g. *Pseudomonas aeruginosa and Staphylococcus aureus)*. Moreover, its antifouling efficiency will be also assessed *in-vivo* by evaluating the influence of the micro-patterned morphology on the amount of antibiotics necessary for completely eradicate bacterial infections, by performing pharmacodynamic analysis.

Finally, in chapter 6, we present the first attempt of interfacing rr-P3HT conjugated polymer with vegetal systems. In particular, we show that rr-P3HT can be safely coupled with *Arabidopsis Thaliana* guard cells without affecting their viability. Interestingly, we observe down-regulation of guard cells spontaneous $[Ca^{2+}]_{Cyt}$ oscillations upon photoexcitation of the semiconducting polymer, in the form of either thin solid films or of nanoparticles. This effect has proven to be safe and reversible, since the guard cells recover almost completely their Ca^{2+} activity after optical stimulation. Even more importantly, we demonstrate that the optical treatment of rr-P3HT NPs interfaced with *Arabidopsis Thaliana* leaves leads to remarkable inhibition of the light-induced stomatal opening. In view of future applications with entire plant systems, we preliminarily investigated the uptake of photoactive rr-P3HT NPs by *Arabidopsis Thaliana* seedlings roots, showing that NPs are efficiently intercalated within the roots tissue. Overall, our results reveal an optically-induced, functional interaction between rr-P3HT and plant systems, demonstrated at the single cells level with guard cells. However, a clarification of the mechanisms involved is needed and will be the object of future experiments, by using specific plant knock-out mutants, able to selectively deactivate the enzymes implicated in the plant response to external stimuli [274]. In light of the preliminary results obtained with rr-P3HT NPs and seedlings roots, we will continue the test of the NPs delivery to plants *in-vivo*. To this end, different strategies will be explored, as the vacuum-assisted NPs delivery to whole plants, the direct NPs injection into the leaf lamina or the simple uptake of NPs dispersions from roots (root-to-leaf method) [275].

Appendix. Supplementary material

Appendix A. Planar rr-P3HT-based devices

A.1 Fabrication of ITO/P3HT and ITO/P3HT:PCBM devices

Glass/ITO planar substrates were cleaned by subsequent rinses in an ultrasonic bath by using distilled water, acetone and isopropanol (10 minutes each), and then dried with a N_2 flux. Chlorobenzene solutions of rr-P3HT (molecular weight $15000 \div 45000$) alone (concentration, 20 g l^{-1}) or mixed at 1:1 weight ratio with PCBM (concentration, 20 g l^{-1} on a polymer basis) were stirred at 50 °C for 15 hours. The solutions were then deposited by spin-coating on flat glass/ITO substrates in 2 steps: (1) speed 800 rpm, acceleration 800 rpm s^{-}1, for 3 s, (2) speed 1600 rpm, acceleration 1600 rpm s^{-}1, for 60 s). The samples are finally annealed at 120°C for 20 minutes.

A.2 Photocurrent and photovoltage measurements

Chronoamperometry and potentiometry measurements were carried out using potentiostat/galvanostat station (Autolab potentiostat PGstat 302N, Metrohm) with light incident from the ITO substrates. An electrochemical cell in a three electrode configuration was employed, comprising the rr-P3HT polymer-based device as the working electrode (WE), a platinum wire as the counter electrode (CE) and saturated-KCl Ag/AgCl as the reference electrode (RE). 0.2 M NaCl aqueous solution at room temperature was used as the electrolyte. Chronoamperometry measurements are performed by applying a fixed potential of 0.2 V vs. Ag/AgCl, equal to open circuit potential (OCP) value and by measuring the current flowing between WE and CE. During potentiometry measurements the current density flowing between the WE and CE is set to zero while monitoring the potential established between the WE and the RE. In both cases the devices are illuminated from

the ITO or the electrolyte (El) side, with a continuous light source (Thorlabs LED M470L3-C5) connected to a function generator (Keithley 50MHz 3390) modulating the illumination in pulses of 50 or 100 ms duration, depending to specific cases. The illumination density, homogeneous over the whole sample area, was A.5.3 mW mm^{-2} and the emission wavelength peak was 470 nm.

A.3 Fabrication of ITO/p-i-n devices

rr-P3HT was deposited on top of planar glass/ITO electrodes following the same procedure described in appendix A1. A PCBM layer (20 nm) is then evaporated on top of the ITO/P3HT device by thermal evaporation and the obtained device is exposed to DCM vapors in a closed vessel for 75 s in order to mix the PCBM layer with rr-P3HT, forming the P3HT:PCBM I-layer. Finally, a second evaporated layer of PCBM (20nm) completes the ITO/p-i-n architecture.

A.4 ITO/p-i-n devices: Scanning electron microscopy (SEM)

The samples are immersed in liquid N$_2$ and cut in two pieces by forcing them with tweezers. Cross-sectional micrographs of the devices were acquired by using a Zeiss SUPRA40 field-emission scanning electron microscope (SEM) using an operating voltage of 5 kV and a working distance of 2 mm.

A.5 rr-P3HT-based photocatalytic devices for hydrogen evolution

A.5.1   Introduction

The possibility to convert solar energy into hydrogen is attracting a lot of interest since it would lead, in principle, to the possibility of creating a carbon-neutral energy cycle [276]. Two main device configurations exist for the optically-induced splitting of water in hydrogen and oxygen:

photoelectrochemical (PEC) cells and photovoltaic (PV)-biased electrolytic cells. The former device type consists in an all-in-one solution in which the photon absorption and electrochemical processes take place in the same electrochemical device usually based on a semiconducting material, coupled with a catalyst, immersed in aqueous electrolyte. The second configuration comprises instead a photovoltaic module and an electrolytic cell, electrically connected together. Despite the fact that PV-biased electrolytic cells currently allow to achieve a higher solar to hydrogen conversion efficiency, PEC cells are attracting so much attention within the research community because they would allow in principle to exceed the PV-biased electrolytic cells performance [277,278].

The functioning of a PEC cell is based on the conversion of solar energy into the electrochemical energy required for the water splitting process, which is based on the following redox half-reactions:

$$4H^+ + 4e^- \rightarrow 2H_2 \qquad (1)$$

$$2H_2O \rightarrow O_2 + 4H^+ + 4e^- \qquad (2)$$

where reaction (1) and (2) refer respectively to the hydrogen evolution reaction (HER), happening at the PEC cell cathode/electrolyte interface, and the oxygen evolution reaction (OER), performed by the PEC cell anode. The solar-to-hydrogen efficiency (η_{STH}) is defined by the following equation:

$$\eta_{STH} = \left| \frac{|J_{SC}| \times 1.23 \times \eta_F}{P_{IN}} \right| AM1.5G \qquad (3)$$

where J_{SC} is the short-circuit photocurrent density, η_F is the faradaic efficiency associated to H_2 evolution, and P_{IN} is the photoexcitation power density. This formula is obtained by considering standard air mass 1.5G (AM1.5G) illumination conditions [279]. The choice of the proper semiconducting material for the PEC cell fabrication is crucial, since the η_{STH} parameter is directly related to its light absorption, charge carrier generation/separation efficiency and charge transport [279–282]. First of all the selected material must fulfill two fundamental requirements: the electrochemical potential values of the semiconductor conduction and valence bands must be lower

121

than the H⁺/H₂ redox level ($E^0_{H^+/H_2}$ = 0 V versus standard hydrogen electrode, SHE) and higher than

the O₂/H₂O redox level ($E^0_{O_2/H_2O}$ = 1.23 V versus SHE) respectively [279,283]. The outstanding

photophysical properties of inorganic semiconductors have been exploited in PEC cells. In particular

Si, III-V semiconductors and copper-based chalcogenides have been employed [284,285]. However,

the use of these materials is limited by the associated high manufacturing costs and limited stability

in aqueous environment [284]. Among the possible alternatives, semiconducting polymers are

promising candidates, mainly because: (1) their energetical properties can be tuned by the chemical

modification of their structure with functional groups or heteroatoms [286,287]; (2) they can be

synthetized and processed by taking advantage of high throughput, cost-effective techniques [288];

(3) they present a high absorption coefficient (over than 10^5 cm⁻¹[150]) within the solar spectrum; (4)

in specific configurations, their charge carrier mobility can be comparable to the one of amorphous

Si [289]. In particular, rr-P3HT demonstrated to be highly suitable for this purpose. The charges

photogenerated by rr-P3HT have the required energy for activating the HER, since this material has

a direct bandgap of 1.9 eV and its LUMO electrochemical potential value is fairly below the $E^0_{H^+/H_2}$

potential [290]. In addition, it presents a good photoelectrochemical stability in aqueous environment,

exploited in many biological applications, discussed in section 1.1 [66,72,109,132,291]. ITO/P3HT

was the first configuration tested, showing photogenerated currents in the order of tens of µA cm⁻² in

acidic environment [132,292,293]. However, HER gives only a small contribution to this signal (in the

order of sub- µA cm⁻²). The major part of the recorded photocurrent is due to the Oxygen reduction

reaction (ORR), given the favorable energy alignment at the polymer/electrolyte interface displayed

by rr-P3HT for this reaction [78,273]. The photocathodes based on the bare rr-P3HT were improved

by incorporating electron accepting molecules in the structure, such as C₆₀ [293], PCBM [132] and

metallofullerens [294,295], forming a BHJ configuration that led to about ten times higher

photocurrent response. However, this value is about two order of magnitude lower than the one

expected by considering the light harvesting efficiency of these systems and the performance that

they achieve in solid-state organic solar cells (OSCs) [290,296]. The research was thus oriented to the characterization of the charge transfer processes happening at the device/electrolyte interface, in order to optimize the device functioning in aqueous environment. In particular, Guerrero et. al. [291] gave a fundamental contribution to the understanding of the rr-P3HT-based PEC cells working principles. First of all, they studied the charge transfer properties of a P3HT:PCBM BHJ active layer by sandwiching it between hole or electron selective layers and a redox couple dissolved in an organic solvent. They showed that by properly selecting the interfacial layer and the redox couple it is possible to provide both electrons and holes to the organic electrolyte, demonstrating the possibility to extend the applicability of the system also to photo-induced anodic processes. Moreover, the authors carried out continuous-wave photoinduced absorption spectroscopy (CW-PIA) on the same device configuration, in presence of the organic electrolyte or in air, revealing that the charge photogeneration efficiency is not affected by the intercalation of the liquid electrolyte. Then, the BHJ-based photoelectrode was tested in the same organic solvent in presence of chloro(pyridine)bis(dimethylclyoximate) cobalt III (cobaloxime), a homogeneous catalyst for HER, and HCl as a proton source. In these conditions cathodic photocurrents of about 1 mA cm^{-2} were recorded, demonstrating for the first time the possibility to perform efficient HER using a semiconducting-polymer based photocathode. The results achieved by Guerrero et. al. pointed out that the poor HER efficiency of the bare BHJ-based electrodes is probably due to a scarce HER-catalytic performance of the P3HT:PCBM, highlighting the necessity of implementing the photocathodes architectures with catalysts and charge selective layers. Basing on these findings, the research was later focused to the integration of good catalyst for HER, like Pt [297], in the rr-P3HT-based photocathodes structure. An example is the work made by Haro et. al. [273], in which the ITO/P3HT:PCBM BHJ configuration was implemented by sandwiching the photoactive layer between crosslinked PEDOT:PSS and TiOx thin films, acting as the hole and electron extracting layers respectively, and by depositing on top of the photocathode surface a uniform Pt layer as the hydrogen evolution catalyst. The authors measured HER-associated photocurrents up to 1 mA cm^{-2}

and a H$_2$ generation rate of 1.6 μmol h^{-1} cm^{-2} at 0 V versus RHE. This result confirm that P3HT:PCBM maintain its photogeneration capability also in aqueous environment and opens the way to the development of new stable multi-layered semiconducting polymer-based photocathodes for hydrogen evolution.

A.5.2   hybrid organic-inorganic photocathodes for hydrogen evolution

As discussed in section A.5.1, the rr-P3HT photogeneration capabilities can be exploited for the fabrication of photocathodes for hydrogen evolution, but rr-P3HT alone cannot achieve an acceptable efficiency for this application. In order to enhance it, an improvement in the device structure is needed. In particular, charge selective materials can be added for enhancing the exciton separation efficiency and then increase the electrons available for proton reduction reaction [273,291]. For this purpose we fabricated hybrid organic/inorganic devices, comprising (from bottom to top): (1) a semitransparent electrode of fluorine-doped Indium Tin Oxide (FTO); (2) α-MoO$_3$ as the hole selective layer (HSL), obtained by Mo sputter deposition, followed by thermal oxidation (3) a spin-coated photoactive layer of P3HT:PCBM BHJ (4) a layer of amorphous TiO$_2$, deposited by Pulsed laser deposition (PLD), that act as the electron selective material (ESL); (5) a sputtered layer of Pt, a good catalyst for hydrogen evolution reaction (HER) (figure A.5.1 a) (see section A5.3 for further experimental details) [141]. In this configuration, a built-in potential is established, electron and holes are spontaneously separated and electrons are driven to the catalytic sites where the reaction occur (figure A.5.1 b). Figure A.5.1 c depicts the linear sweep voltammogram carried out in a 0.1 M H$_2$SO$_4$–Na$_2$SO$_4$ solution (buffered at pH 1.37) by illuminating the device with a solar simulator at 1 sun intensity. The light source is alternatively chopped for simultaneously comparing the device responses in light and dark conditions. From this experiment it is possible to extract two important parameters, useful for a direct comparison between the different device configurations: the onset potential (OP), defined as the applied bias at which the device reaches a photocurrent density of 10

$\mu A\ cm^{-2}$, and the maximum photocurrent density value reached at the minimum applied potential. By looking at the I-V traces of the devices constituted by only a part of the complete device, the contribute of each layer to the device performance can be evaluated. The FTO/BHJ sample, comprising only the photoactive layer, shows the lower photocurrent density at -0.3V vs. the standard reversible hydrogen electrode (RHE) (2.5 $\mu A\ cm^{-2}$). When the surface of FTO/BHJ is covered by Pt the performance is enhanced, exhibiting an OP value of 0.0 V vs. RHE and a maximum current density of 400 $\mu A\ cm^{-2}$ at -0.3 V vs. RHE. The introduction of a layer of TiO_2, having the role of both Pt support and ESL, the current density is more than doubled (about 1 mA cm^{-2} at -0.3V), increasing the OP value to 0.2 V vs. RHE. The incorporation of α-MoO_3 between FTO and BHJ lead to the complete device configuration, reaching the higher efficiency, characterized by about 3 mA cm^{-2} at 0 V vs. RHE, increasing to 3.8 mA cm^{-2} at -0.3 V vs. RHE, with an OP value of 0.55 V vs. RHE. The performance of this hybrid organic-inorganic photocathode lies among the best efficiencies reported from photocathodes comprising organic photoactive materials [298], generating a photovoltage comparable to the best P3HT:PCBM BHJ based solar cells [299], and competitive with Cu_2O and Si based photocathodes [300,301]. The stability of the photocathode is evaluated by performing chronoamperometry measurements at a fixed potential of 0.18 V vs. RHE. The photocurrent evolution during time of the complete architecture shows a peak performance corresponding to a photocurrent maximum around 25 minutes of operation and then the photocurrent starts to decline linearly reaching less than 1 mA cm^{-2} after 75 minutes (figure A.5.1 d). The comparison with complementary architectures, lacking the HSL or both the HSL and ESL layers, suggest that the peculiar trend of the current density is due to the presence of the α-MoO_3 and TiO_2 films. The peak in efficiency after 25 minutes it is ascribed to an intercalation of small cations (H^+ and Na^+) inside the α-MoO_3 structure that firstly lead to an increase in the α-MoO_3 HSL layer conductivity, favoring the injection of electrons in the BHJ, and then the photocurrent measured at the device/electrolyte interface. Unfortunately, this process implicates the reduction of α-MoO_3 to substoichiometric phases ($MoO_{3-x}OH_x$, MoO_2), probably through an H_2 insertion/H_2O extraction mechanism, leading to a decrease of

the HSL work function and a subsequent drop in the selectivity of the contact, decreasing the device performance after 25 minutes of operation. In addition, the formation of Ti^{3+} states, acting as traps for photogenerated charges, further decrease the photocurrent density and then the photocathode efficiency.
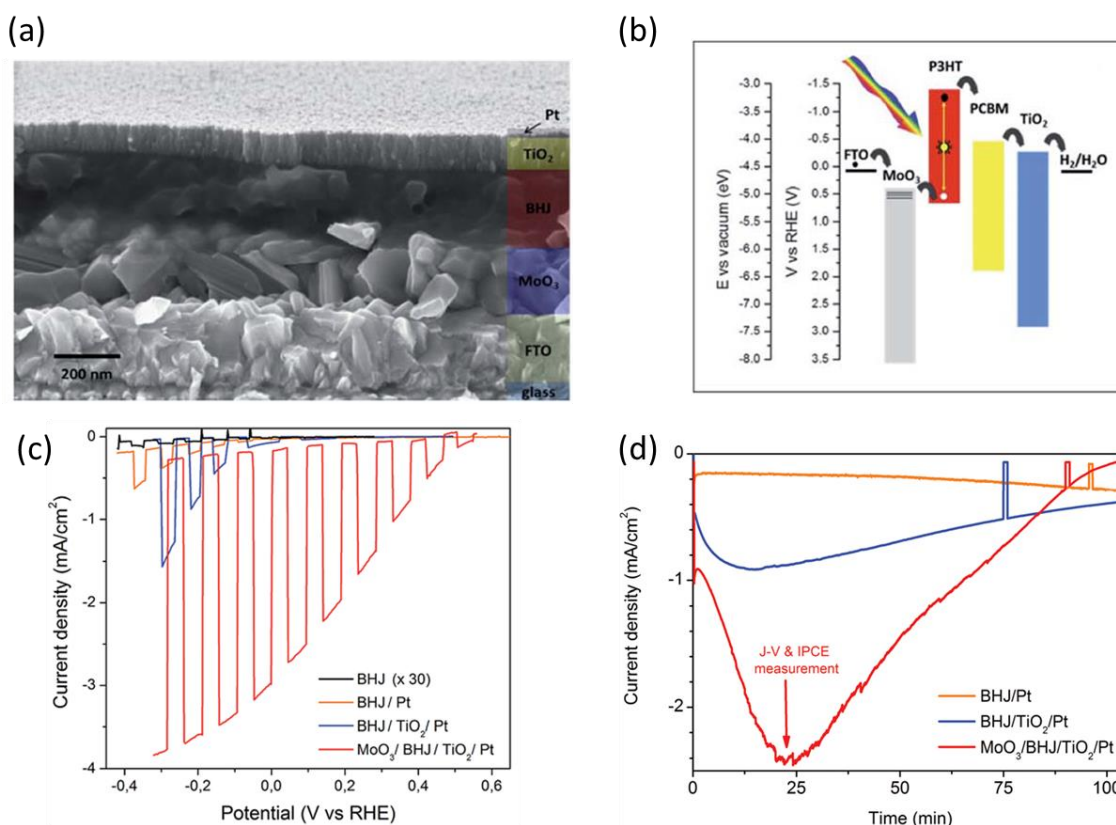
Figure A.5.1. (a) SEM micrograph depicting the complete architecture of the hybrid organic-inorganic photocathode. (b) Energy band edge positions of the different layers that compose the photocatalytic device and of the redox levels of the water reduction reaction; the electron injection is represented by black arrows; black lines inside the MoO_3 energy band diagram represent the levels coming from the protonation of the MoO_3 layer. (c) Linear sweep voltammogram of the complete photocatalytic device and the ones comprising only specific layers, acquired in 0.1 M H_2SO_4–Na_2SO_4 solution (buffered at pH 1.37) and by illuminating the device with a chopped light source (450W Xe lamp equipped with an AM1.5G filter, one sun intensity). (c) Photocurrent density recorded in potentiostatic conditions (applied bias: 0.18 V vs. RHE) of the illuminated full hybrid photocathode compared to the devices lacking only the HSL or both the HSL and ESL layers. The illumination conditions are the same of the ones employed for the linear sweep voltammetry measurements.

The quantitative evaluation of the H_2 evolving capability of the hybrid photocathode are carried out by performing chronoamperometry experiments under illumination and by simultaneously measuring

the presence of evolved hydrogen by in-line gas chromatography. The results obtained (figure A.5.2 panel a) show that the hydrogen quantity measured correlates well with the hydrogen amount expected from the photocurrent density value over time, with a faradaic efficiency very close to one. This data confirm that the charges produced by the device illumination are employed for the reduction of water to oxygen and not for other undesired processes, like non-faradaic corrosion events. The photocatalytic device under operation is shown in figure A.5.2 panel b, where it is possible to appreciate the evolving hydrogen bubbles attached to the device surface.
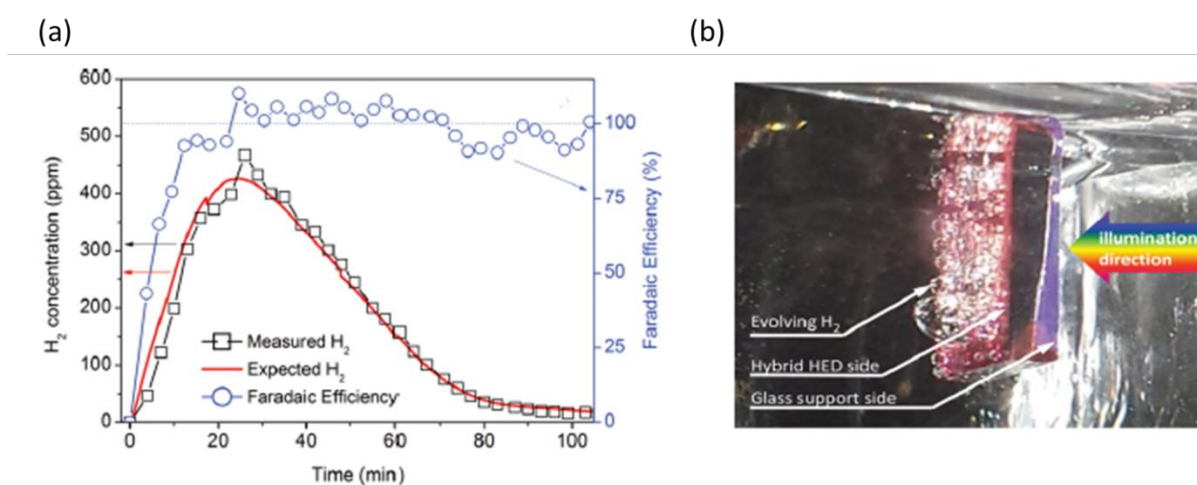
Figure A.5.2 (a) H_2 concentration monitored by GC (left y-axis) during hybrid photocathode chronoamperometry measurement under continuous illumination in pH1 electrolyte. Red trace refers to the expected H_2 concentration obtained from the measured photocurrent during chronoamperometry measurements. (b) Photograph of the hybrid photocathode during potentiostatic operation.

Recently, we proposed an improvement of the hybrid photocathode architecture, in which the hole selective contact is substituted by a thin layer of copper iodide (CuI) (thickness less 10 nm, figure A.5.3 a) [163] (see section A5.4 for further details on the fabrication process). CuI offer the advantage of easy processability, since it can be deposited directly from solution without requiring a thermal treatment and allowed to obtain an optimal alignment of the energy levels in the final device configuration (figure A.5.3 b).
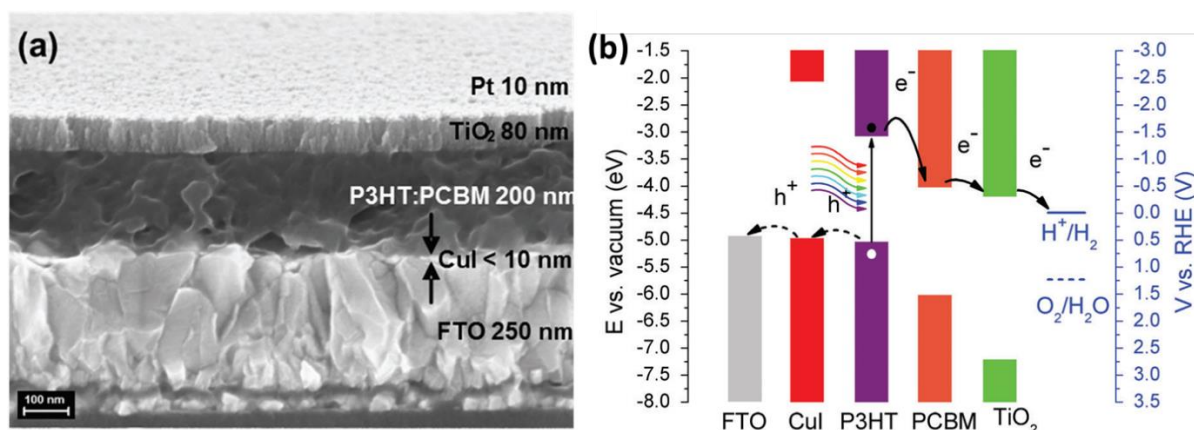
Figure A.5.3. SEM image in cross-section (a) and energy band diagram (b) of the hybrid organic/inorganic photocathode implemented with the CuI HSL.

This new configuration leads to a dramatic improvement of the photocatalytic device performance, exhibiting a maximum photocurrent density of 7.1 mA cm^{-2} at 0 V vs. RHE and a high OP value of 0.702 ± 0.007 V (figure A.5.4 a). From the comparison with the partial configurations it is clear that the CuI interlayer has the main contribution in the overall performance enhancement, since when it is not present, a photocurrent less than 100 µA cm^{-2} at 0 V vs. RHE is reached, with an OP value of 0.171 V vs. RHE (figure A.5.4 b). Instead, the devices that comprise CuI HSL and lack the TiO$_2$ ESL show a higher photocurrent (1.5 mA cm^{-2} at 0 V vs. RHE) and OP value (0.372 V vs. RHE, figure A.5.4 a). It also interesting to notice that the photocathode fabricated with both HSL and ESL but without the Pt catalyst exhibit an expected decrease in performance (600 mA cm^{-2} at 0 V vs. RHE, OP = 0.603 V) together with an increased capacitive contribution to the photocurrent, as proven by the larger fast spikes when the light is switched on, due to a less efficient electron extraction at the device/electrolyte interface (figure A.5.4 b).
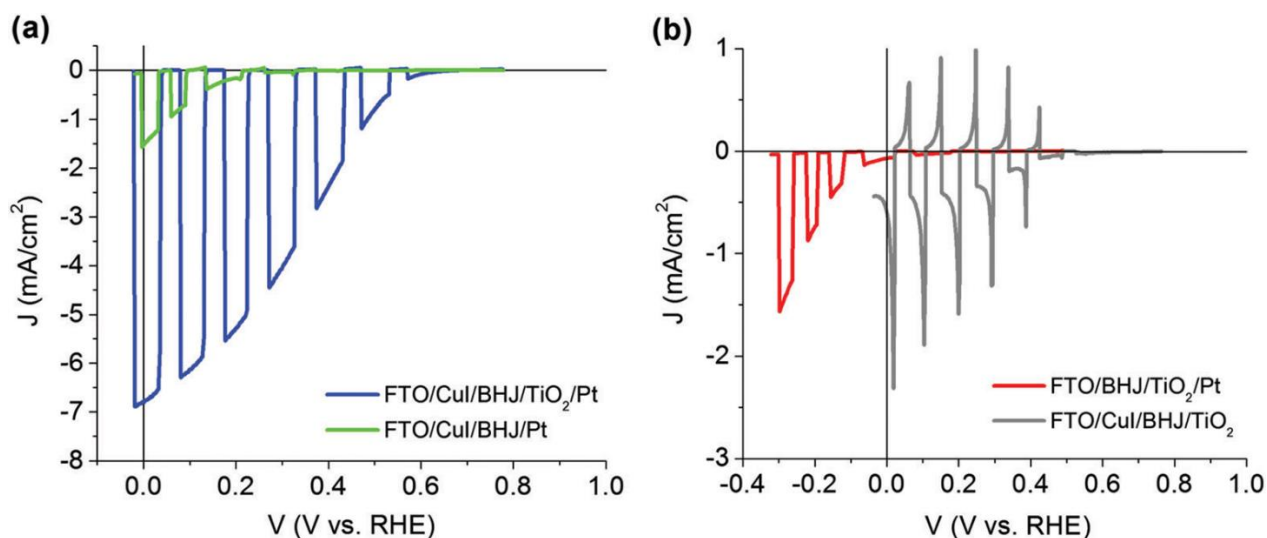
Figure A.5.4. Linear sweep voltammogram of the CuI-implemented full photocatalytic device architecture compared to the TiO2-lacking one (a) and of partial configurations without CuI and Pt (b). Measurements are carried out in 0.1 M H_2SO_4–Na_2SO_4 solution (buffered at pH 1.37) by illuminating the device with a chopped light source (450W Xe lamp equipped with an AM1.5G filter, one sun intensity).

The stability of the device is assessed by chronoamperometry measurements under continuous illumination with a 1 sun solar simulator, showing a decrease of the photocathodic current density of about 60 % after 20 minutes of operation (figure A.5.5 a), attributed to a partial delamination of the Pt catalyst layer, as proven by SEM micrographs of the device surface after 1 hour of operation (figure A.5.5 b,c).
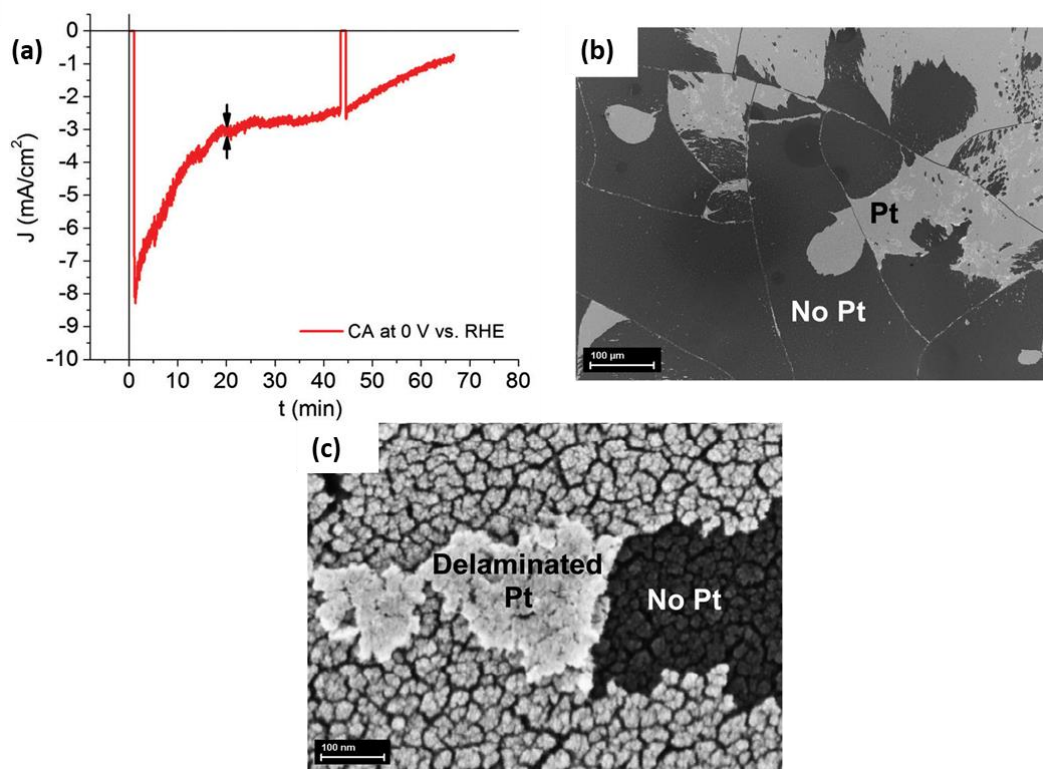
Figure A.5.5. (a) Photocurrent density recorded in potentiostatic conditions (applied bias: 0 V vs. RHE) of the illuminated CuI-implemented photocathode. The illumination conditions are the same of the ones employed for the linear sweep voltammetry measurements. Top-view SEM (b) and HR-SEM magnification (c) micrographs of the CuI-implemented hybrid photocatalytic device acquired after 1 hour of potentiostatic operation at 0 V vs. RHE, in pH1 electrolyte and under 1 sun illumination.

In order to overcome this problem, a protective coating of polyethyleneimine (PEI) is introduced on the device surface. This branched polymer is chosen for its good adhesion properties and hydrophilicity, together with proton and metal chelating properties that would allow to a decrease in Pt delamination and electrolyte permeation, without affecting the electrolytic activity of the photocathode. Furthermore, PEI is solution-processable and can be dissolved in ethanol, which guarantees a good wettability of the device surface. The linear sweep voltammogram and the chronoamperogram of the illuminated PEI-protected full device architecture confirm this picture, showing a comparable photocurrent generation at 0 V vs. RHE (figure A.5.6 a) and a delayed photocurrent decrease over time, now exhibiting a reduction of about 60 % after 50 minutes (figure A.5.6 b).

130
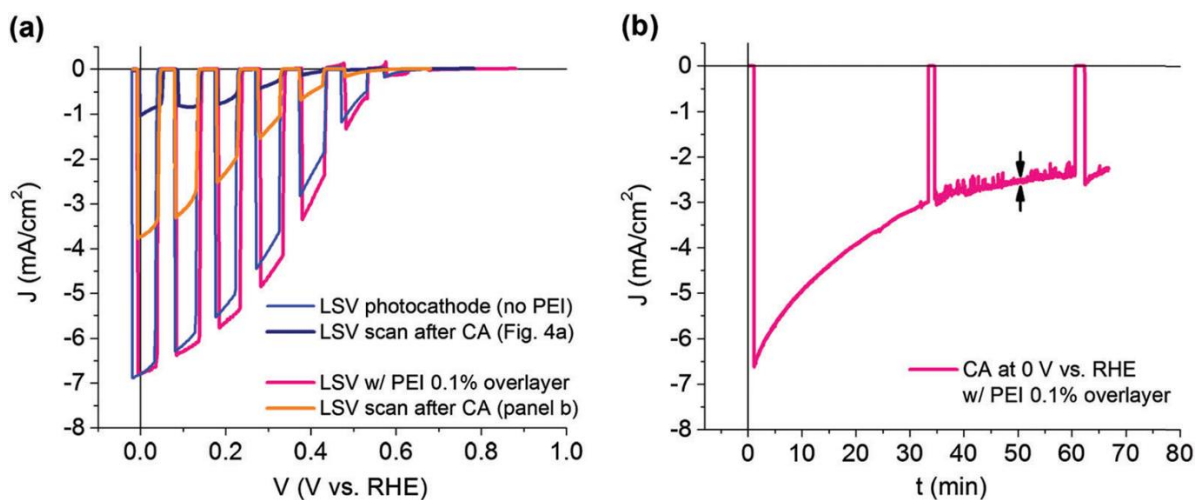
Figure A.5.6. (a) Linear sweep voltammogram of the illuminated PEI-protected full device architecture, before and after chronoamperometry recording, compared to the unprotected device (b) Chronoamperometry test of the PEI-protected photocathode.

The implemented hybrid organic-inorganic photocathode is finally tested in experiments for the quantification of the hydrogen production, in the same conditions employed in the case of the first photocathode version without the CuI and PEI layers. The results obtained (figure A.5.7) show that the device is characterized by a 100% faradaic efficiency for hydrogen evolution, confirming that the enhanced photocathodic current, due to the introduction of CuI as HSL, is related only to the water reduction reaction, and that the PEI layer does not interfere with the process.

131
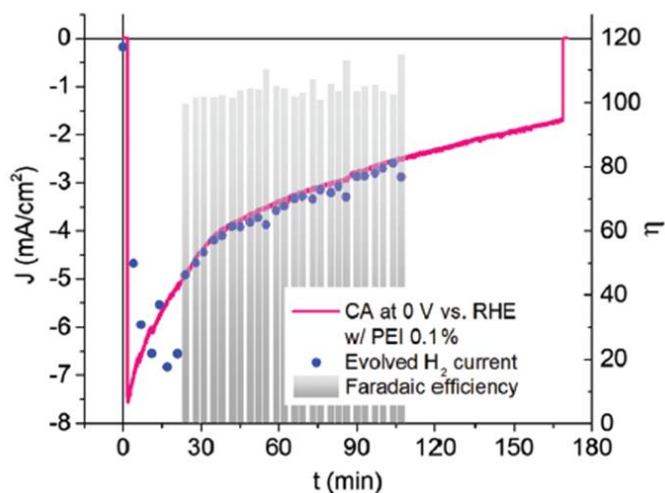
Figure A.5.7. Chronoamperogram at 0 V vs. RHE (pink trace) superimposed to the simultaneously quantified H_2 concentration (blue dots) of the hybrid photocathode implemented with the CuI and PEI layers. The faradaic efficiency is represented by gray columns (right y-axis).

A5.3   Fabrication of FTO/MoO₃/BHJ/TiO2/Pt devices

Glass/FTO coated soda-lime glass substrates (sheet resistance 15 Ω sq^{-1}) were cleaned according to the following protocols: two series of sequential sonication baths in acetone, isopropanol and demineralized water each lasting for 20 minutes, thermal annealing in a muffle furnace operating in air at 500 °C for 2 hours and plasma cleaning in an inductively coupled reactor for 20 minutes (100 W RF power, excitation frequency 13.56 MHz, 40 Pa of O_2 gas process pressure, background gas pressure 0.2 Pa). Then, A pulsed-DC magnetron sputtering source with adjustable repetition frequency and duty cycle was used for Mo deposition on FTO. The vacuum chamber was evacuated to a base vacuum pressure lower than 3.0 x 10^{-3} Pa before each deposition. The discharge operating pressure was 1 Pa and argon gas flow 110 sccm; the target–substrate distance was fixed at 50 mm. Mo metal films were thermally treated in a muffle furnace operating in air at 500 °C for 30 minutes for obtaining alpha-phase orthorhombic MoO_3 films. rr-P3HT and PCBM were dissolved in chlorobenzene at a 1:1 weight ratio and 25 mg ml^{-1} on a polymer basis and stirred at 50°C for 12 hours before use. The solution was then deposited on the FTO/MoO3 architecture by spin coating using the

132

following set of parameters: two step spinning protocol with rotation speeds of 800 rpm for 3 s followed by 1600 rpm for 60 s, respectively; for both sections set accelerations were 34 680 rpm s^{-1} and total drop-casted solution volume was 100 mL for each sample. This spin casting protocol produces an P3HT:PCBM blend (BHJ) layer 200±20 nm thick, as measured by means of profilometry experiments. TiO2 films were deposited on top of the FTO/MoO$_3$/BHJ architecture by means of pulsed laser deposition using a TiO2 target in an Ar/H$_2$ atmosphere (H$_2$ content 3.1% mol) at a total pressure of 15 Pa. A pulsed excimer laser (Coherent KrF, λ = 248 nm) was set at a pulse repetition rate of 20 Hz with 400 mJ energy per pulse and a fluence of 2.5 J cm^{-2}. Pt deposition was deposited on top of the obtained multilayered architecture using a pulsed-DC magnetron sputtering source as in the Mo case, but by setting the discharge operating pressure to 15 Pa, the argon gas flow to410 sccm and the target–substrate distance at 80 mm. Finally, the FTO/MoO$_3$/BHJ/TiO2/Pt devices were thermal annealed in a N$_2$ atmosphere at 130 °C for 10 minutes. Complementary architectures without hole or electron selective or catalyst layers were also fabricated by skipping the correspondent fabrication steps.

A5.4 Fabrication of FTO/CuI/BHJ/TiO$_2$/Pt/PEI devices

CuI (97% purity) was dissolved in acetonitrile at 10 g l^{-1} concentration. The solution was filtered by using Polytetrafluoroethylene (PTFE) filters with a cut-off dimension of 450 nm. CuI deposition on cleaned glass/FTO substrates was carried out by spin coating in one single step (3000 rpm rotation speed for 60 s). Then, the BHJ, TiO$_2$ and Pt layers were added following the same fabrication procedure described in appendix A.3.1. branched polyethyleneimine (PEI, Mw 25 000 g mol $^{-1}$) for the realization of the protective layer was dissolved in ethanol at 0.1% concentration and spin coated on top of full devices at a speed of 2000 rpm for 60 s. Post thermal annealing at 130 °C for 10 minutes in an inert atmosphere completed the fabrication of the hybrid photocathode.

A.6 Fabrication of ITO/CuI/P3HT:PCBM/TiO₂ devices

This device architecture was obtained following the same fabrication steps employed for the deposition of the CuI, P3HT:PCBM (BHJ) and TiO2 layers described in section A5.4, starting from planar glass/ITO substrates cleaned by subsequent rinses in an ultrasonic bath by using distilled water, acetone and isopropanol (10 minutes each), and dried with a N_2 flux.

A.7 HEK-293 cells cultures and electrophysiological measurements

All devices were sterilized by immersion in ethanol for few minutes. A layer of fibronectin (2 µg mL^{-1} in PBS buffer solution) was deposited on the polymer surface of all devices and incubated for 1 hour at 37 ºC, in order to promote cellular adhesion. Excess fibronectin was then removed by rinses with PBS prior to cell plating. Human Embryonic Kidney (HEK-293) cells were cultured in cell culture flasks containing DMEM with 10% FBS, 100 µg mL^{-1} penicillin and 100 µg mL^{-1} streptomycin. Culture flasks were maintained in a humidified incubator at 37 °C with 5% CO_2. When at confluence, HEK-293 cells were enzymatically dispersed using trypsin-EDTA and then plated on the different devices at a concentration of 20.000 cells cm^{-2}.

Intracellular recordings were performed with a patch-clamp setup (Axopatch 200B, Axon Instruments) coupled to an inverted microscope (Nikon Eclipse Ti). Devices were optically excited with a LED system (Lumencor Spectra X) fiber-coupled to the fluorescence port of the microscope. The samples were illuminated from the bottom, substrate side, with light pulses characterized by the central emission wavelength, intensity and time duration specified in the main text. Spot size was 0.23 mm^2. HEK-293 cells were measured after 3÷5 days in vitro (DIV) in whole-cell configuration, using glass pipettes (3÷6 MΩ) filled with the following intracellular solution [mM]: 12 KCl, 125 K-Gluconate, 1 MgCl$_2$, 0.1 CaCl$_2$, 10 EGTA, 10 HEPES, 10 ATP-Na$_2$. The extracellular solution composition was [mM]: 135 NaCl, 5.4 KCl, 5 HEPES, 10 Glucose, 1.8 CaCl$_2$, 1 MgCl$_2$. Only single HEK-293 cells were selected for recordings. All measurements were performed at room temperature.

A.8 Surface potential recordings

Surface potential measurements were performed with the same patch-clamp setup, light source and illumination protocols employed in the case of whole-cell patch-clamp measurements. Recordings were carried out in voltage clamp configuration by micro-manipulating freshly pulled glass pipettes ($3 \div 6$ MΩ) in the close proximity (~ 2 μm) of the polymer-aqueous electrolyte interface. Both the pipette and the bath were filled with electrolytic solution to avoid junction potentials artifacts. The electrolytic solution composition was the same as the electrolyte solution used during patch clamp recordings. The measured current was set to zero under dark conditions; surface potential was then calculated by multiplying the current trace measured upon illumination by the pipette resistance. All measurements were performed at room temperature. Acquisition was performed with pClamp 10 software suite (Axon Instruments) and all data were elaborated with Origin 8.0.

Appendix B. Mesoporous rr-P3HT-based devices

B.1 Fabrication of mesoporous ITO/ITO NPs/P3HT devices

Glass/ITO planar substrates were cleaned by subsequent rinses in an ultrasonic bath by using distilled water, acetone and isopropanol (10 minutes each), and then dried with a N_2 flux. For the fabrication of mesoporous substrates, an ITO nanoparticles (ITO NPs) dispersion in ethanol was prepared (100 g l^{-1}), and treated with a probe sonicator (Branson digital sonifier) for 30 minutes at 10% power. ITO NPs were then deposited onto cleaned ITO-glass substrates by spin coating (speed 1000 rpm, acceleration 1000 rpm s^{-1}). The deposition was repeated 4 times for each device, keeping the samples in vacuum after each deposition step for complete solvent evaporation. In between subsequent spin coating sessions, ITO NPs dispersion was sonicated in an ultrasonic bath at room temperature. The mesoporous ITO NPs substrate was finally annealed at 200 °C under nitrogen atmosphere. rr-P3HT chlorobenzene solution (concentration, 10 g l^{-1}) was stirred at 50 °C for 15 hours prior to spin coating deposition and finally deposited both on mesoporous and on planar ITO substrates (1500 rpm, acceleration 1496 rpm s^{-1}). Polymer thickness in the case of planar device is 30 ± 6 nm, as measured by profilometry measurements. A thermal annealing treatment (120 °C for 20 minutes, under N_2 atmosphere) completed the fabrication process.

B.2 Morphological, electrical and electrochemical characterization

The work function of the different ITO electrodes was evaluated in air by using an ambient Kelvin Probe (KP) set up (KP Technology, series 7), calibrated towards a reference gold substrate. Micrographs of the devices were acquired by using a Zeiss SUPRA40 field-emission scanning electron microscope (SEM) using an operating voltage of 5 kV and a working distance of 2 mm.

An Agilent 5500 Atomic Force Microscope (AFM) in tapping mode at 25 ºC was used for the morphology investigation of both the mesoporous and planar systems. The tip employed for the measurement was a silicon non-contact probe (NANOSENSORS PPP-NCHR, Nanoworld AG, Switzerland) with a force constant of 42 N m^{-1}, a resonance frequency of 330 kHz and a tip radius of curvature < 10 nm. Scans were performed over one-length scales (1x1 µm) at a scan speed of 0.5 Hz. Root Mean Square (RMS) roughness values were calculated from AFM topography images using Gwyddion software.

Specific surface area measurements were carried out by Kr physisorption at 77 K in a Quantachrome equipment, model autosorb iQ. The specific surface areas were calculated using the multi-point BET (Brunauer–Emmett–Teller) model, considering 9 equally spaced points in the P/P^0 range from 0.10 to 0.30. P^0 is the vapor pressure of krypton at 77 K, corresponding to 2.63 Torr. Prior to measurements, samples were degassed for 1 hour at 60°C under vacuum to eliminate weakly adsorbed species.

Electrochemical impedance spectroscopy (EIS) were carried out using potentiostat/galvanostat station (Autolab potentiostat PGstat 302N, Metrohm) both in dark and in light conditions, with light incident from the ITO substrates. A continuous light source (Thorlabs LED M470L3-C5) was used (photoexcitation density, homogeneous over the whole sample area, 2.73 mW mm^{-2}, emission wavelength peak, 470 nm). 0.2 M NaCl aqueous solution at room temperature was used as the electrolyte. An electrochemical cell in a three electrode configuration was employed, comprising the planar/mesoporous polymer device as the working electrode, a platinum wire as the counter electrode and saturated-KCl Ag/AgCl as the reference electrode. Impedance spectra were recorded in the 0.01 Hz ÷ 100 kHz frequency range with an AC amplitude of 0.02 V. For the measurements at equilibrium, a constant bias (V_{eq}) was applied, corresponding to the open circuit potential in dark (0.2 V vs. Ag/AgCl for the ITO/P3HT device and 0.19 V vs. Ag/AgCl for the ITO/ITO NPs/P3HT device) and upon light (0.36 V vs. Ag/AgCl for the ITO/P3HT device and 0.33 V vs. Ag/AgCl for the ITO/ITO NPs/P3HT device). All V_{eq} values have been specifically marked in Figure 3. For the out

of equilibrium studies, external bias was varied within the range -0.3 V $\div$ 0.36 V vs. Ag/AgCl. Nova 2.0 software was used for data analysis.

Photocurrent measurements were carried out using the same electrochemical set up employed in the case of the EIS measurements, by applying fixed potential ranging from 0.3 V to -0.2 V vs. Ag/AgCl and by illuminating the devices from the glass side, unless differently specified, with a continuous light source (Thorlabs LED M470L3-C5) connected to a function generator (Keithley 50MHz 3390) modulating the illumination in pulses of 250 ms duration. The illumination density, homogeneous over the whole sample area, was 2.73 mW mm^{-2} and the emission wavelength peak was 470 nm. Prior to measure the photocurrent without dissolved oxygen, N2 gas was bubbled in the electrochemical cell for 40 minutes before starting each experiment and a constant nitrogen flow was maintained during the whole measurement.

B.3   Immunocytochemical Studies

Cells were fixed in 4% parafolmaldehyde and 4% sucrose at room temperature for 15 min. Phalloidin was applied in GDB buffer (30 mM phosphate buffer pH 7.4 containing 0.8 NaCl, 0.2% gelatin and 0.5 Triton X-100) for 1h at room temperature; nuclei were stained with 4',6-diamidino-2-phenylindole (DAPI) 1µg ml^{-1} in PBS for 5 min. The images were acquired with a fluorescence microscope (Nikon eclipse Ti).

Appendix C. High Aspect Ratio rr-P3HT pillars-based devices

C.1 rr-P3HT pillars fabrication

C.1.1   PDMS mold

PDMS precursor was mixed with the curing agent (10:1 volume ratio) and left in vacuum for 30 minutes, in order to remove air bubbles formed during the mixing process. The degassed mixture was put inside a glass petri dish and left in an oven for 4 hours at 65°C. The bottom part of the petri dish was covered with a silicon wafer to obtain a highly planar PDMS surface. After the thermal curing, a 4x5mm2 PDMS area was patterned with micro-holes array, 2 um diameter and 7 um pitch (distance from two holes center), using a femtosecond pulse laser micromachining. The system is equipped with a regenerative amplified mode-locked femtosecond laser source based on Yb:KGW active medium (Light Conversion, Pharos) whose pulses at the fundamental wavelength of 1030 nm are characterized by duration of 240 fs, repetition rate up to 1 MHz and pulse energy up to 0.2 mJ. In order to create the desired array of holes, an intensive process of optimizing the writing parameters was carried out. As an optimal result, using the second harmonic λ = 515 nm, we obtained the following "solution": 50 pulses on the same position with 100 kHz repetition frequency and 15 mW average power. The laser beam is statically focused on the surface substrate through a microscope objective (20X, Mitutoyo, NA 0.40). The 2D structure is achieved moving the sample, placed on a high precision three axis air-bearing translation stage (Aerotech, ABL 1000 series) with a resolution up to 20 nm. Usually a direct laser ablation performed on a substrate (in our case PDMS) creates a large amount of debris that strongly affects the quality of both the surface and the geometry of the obtained structure (micro holes) in terms of morphology, aspect ratio and homogeneity. In order to overcome this serious problem and to obtain a high degree of repeatability in the realization of the holes, the micro perforation of the PDMS substrate was then performed in a controlled atmosphere using a vacuum chamber ($10^{-2} \div 10^{-3}$ bar). The low pressure promotes the separation of the ablated

material from the surface that are free to "fly" away from the unprocessed area - thanks to the increase in their average free path and to the low kinetic energy. In this way the obtained structure geometry is more easily controllable and of better quality with a residual roughness of about two orders of magnitude lower than the conventional ablation in air. After the laser process the mold was washed with EtOH for an additional surface cleaning.

C.1.2 ITO/P3HT pillars samples

Commercial glass/ITO slabs were cut into 18x18 mm^2 slides and washed by subsequent rinses in an ultrasonic bath by using distilled water, acetone and isopropanol (10 minutes each), and then dried with a N$_2$ flux. rr-P3HT was dissolved in o-dichlorobenzene (20 g l^{-1}) and stirred for one night at 50°C. A 1 µl drop of the rr-P3HT solution was pushed onto the cleaned glass/ITO surface using the micro-patterned PDMS mold. After a thermal treatment at 90°C for 2 minutes, the mold was gently removed ending up with a 4x5 mm rr-P3HT pillars array surrounded by flat rr-P3HT region deposited on top of glass/ITO substrates.

C.2 Electrochemical characterization

Electrochemical Impedance Spectroscopy (EIS) was carried out in Krebs–Ringer–Hepes (KRH) extracellular solution (composition [mM]: 135 NaCl, 5.4 KCl, 5 HEPES, 10 Glucose, 1.8 CaCl2, 1 MgCl2) at room temperature, using the same potentiostat and electrochemical cell employed in the case of mesoporous rr-P3HT-based devices (section B.2) The planar rr-P3HT part of the flat/pillar devices was removed in order to guarantee that only the impedance contribution from the pillars array is taken into account. For the comparison with the planar rr-P3HT, flat glass/ITO/P3HT devices were employed. Impedance spectra were recorded in the 0.01 Hz ÷ 100 kHz frequency range with an AC amplitude of 0.02 V and by applying a constant bias equal to the devices open circuit potential (0.11

and 0.08 V for the rr-P3HT flat and pillars cases respectively). Nova 1.8 software was used for data analysis.

Glass/ITO/P3HT flat samples for electrochemical measurements were prepared by spin-coating (speed 1600 rpm, acceleration 1600 rpm s^{-1}) a 20 g l^{-1} rr-P3HT solution in o-dichlorobenzene on top of 18x18 mm^2 glass/ITO slides.

C.3 Cell cultures preparation

HEK-293 cells were plated on the rr-P3HTpillars-based substrates following the same procedure described in the case of planar rr-P3HT-based devices (section A.7).

Primary cortical neurons cultures were prepared from 18 to 19-day-old rat embryos (pregnant females were obtained from Charles River Laboratories). Prior to neurons plating, the micro-structured rr-P3HT devices were sterilized in oven at 120 °C for two hours and treated with a poly-L-lysine solution (1mg/100ml of Buffer Borato pH 7.4) overnight at room temperature. After washing 3 times with deionized water, primary cortical neurons were plated on the substrates at a density of 60.000-75.000 cells cm^{-2} in Neurobasal medium supplemented with 1% Penicillin and Streptomycin; L-Glutammate (at final concentration of 10 mM), Glutammine (at final concentration of 2 mM) and 2% B27 prepared in the laboratory. The cells were maintained in the incubator at 37 °C with 5% CO2. After 4 DIV half of the medium was replaced with Neurobasal medium supplemented with 1% Penicillin and Streptomycin, 1% Amphotericin B, Glutammine (at final concentration of 2 mM) and 2% B27.

C.4 Cells viability assays

The evaluation of the viability of all cell types employed in this work (primary neurons after 14DIV, HEK-293 cells after 1DIV) was accomplished by HOECHST 33342/NucGreen Dead 488 ReadyProbes assay. The flat/pillar rr-P3HT substrates were incubated in KRH extracellular containing the two dyes (HOECHST 33342 10 µg ml^{-1} and NucGreen Dead 488 ReadyProbes Reagent 2 drops ml^{-1}) for 5 minutes protected from ambient light. The samples were then washed with extracellular solution and multiple images were acquired with a Nikon Eclipse Ti-S epifluorescence inverted microscope. Standard DAPI and FITC filter sets were employed for HOECHST and NucGreen respectively. The percentage of viable cells was estimated by counting the total number of cells nuclei (stained by HOECHST) and the total number of dead cells nuclei (stained by NucGreen). The results obtained on the flat and micro-structured regions were compared (n = 450 cells for each substrate type).

C.5 Scanning electron microscopy (SEM)

To evaluate cells morphology and spreading, HEK-293 cells (1DIV) and primary neurons (14DIV) plated on flat/pillars rr-P3HT substrates were prepared for SEM with the following procedure: (1) fixation in glutaraldehyde 2.5% in PBS overnight at 6°C; (2) immersion in increasing concentrations of ethanol (20%, 30%, 40%, 50%, 60%, 70%, 80%, 90% and 100%, 20 minutes for each concentration) followed by air-drying; (3) evaporation of a thin gold layer on top of samples surface (thickness 6 nm, 1.5 nm Cr adhesion layer). rr-P3HT pillars-based devices without cells instead, did not require any treatment prior to SEM images acquisition. All SEM micrographs were acquired by using a TESCAN MIRA III scanning electron microscope (operating voltage 4kV, working distance 18 mm, stage tilt angle 45°).

C.6 Quantitative evaluation of cells morphological response

HEK-293 cells grown on fibronectin-coated rr-P3HT flat/pillars substrates for 2 DIV were washed twice with PBS and fixed for 15 min in 4% paraformaldehyde and 4% sucrose in 0.12 M sodium phosphate buffer pH 7.4, at RT. Labeling with phalloidin-FITC was applied in GDB buffer (30 mM phosphate buffer, pH 7.4, containing 0.2 % gelatin, 0.5 % Triton X-100, and 0.8 M NaCl) for 2 hours at RT. Nuclei were marked with DAPI (5 minutes incubation in PBS). Fluorescence images were acquired with the same microscope employed for the viability assay, using standard FITC and DAPI filters set for recording the fluorescence emission of the phalloidin-FITC and DAPI stained actin and nuclei. Cells top-view surface area and shape parameters were quantified using Imagej software. Cells shape was evaluated in terms of circularity c ($4\pi *$ [cell area]/[cell perimeter]^2, $c = 1$ indicates a perfect circle, c close to 0 indicates a highly elongated shape). The cells projections extension was evaluated by measuring the cells perimeter and normalizing it to the cells top-view surface area. Mean values have been obtained by averaging over a statistical ensemble of n = 100 cells for each substrate type.

Rat cortical neurons were fixed at DIV14 in 4% paraformaldehyde plus 4% sucrose at room temperature. AntiMAP2 (1:200, Abcam, GR143561) was applied in GDB buffer (30 mM phosphate buffer pH 7.4, containing 0.2% gelatin, 0.5% Triton-X-100 and 0.8M NaCl). Morphologic analysis of dendrites was performed on the signal obtained by MAP2 staining, acquired using a confocal microscope (Zeiss LSM800) with a 40x objective and sequential acquisition setting at resolution of 1024x1024 pixels. Sholl analysis was performed using NeuronStudio (Computational Neurobiology and Imaging Center, Mount Sinai School of Medicine, New York, NY) to evaluate the dendritic arborization and to measure the number of branching points. Labelled neurons were chosen randomly for quantification from three to six coverslips from two to three independent experiments. The number of neurons used for quantification is indicated in the figure legends. Statistical significance was determined by one-way ANOVA Bonferroni post hoc test.

C.7 Primary cortical neurons electrophysiology in dark

Electrophysiology was performed using a patch clamp set up based on an inverted fluorescence microscope (Nikon eclipse Ti-S). Intracellular recordings of primary cortical neurons were carried out after 14DIV with an Axopatch 200B (Axon Instruments) in whole-cell configuration, using borosilicate glass pipettes (3-6 MΩ). Recordings were performed in KRH extracellular solution and in current clamp configuration, with and without applying a current ramp (20 pA current steps, ranging from 0 pA up to 200 pA) for evaluating the neuron firing threshold. The patch pipette was filled with the following solution [mM]: 126 K-Gluconate, 4 NaCl, 2 MgSO$_4$, 0.2 CaCl$_2$, 0.08 Bapta, 9.45 Glucose, 5 Hepes, 3 ATP, and 0.1 GTP. Responses were amplified and stored with pCLAMP 10 (Axon Instruments), and resting membrane potentials were corrected for a -15 mV junction potential offset, evaluated using pClamp10 junction potential calculation tool. All data were elaborated with Origin 9.0 software. Neurons top-view surface area was measured from bright field images using Imagej software.

C.8 Primary cortical neurons synapses imaging

Rat cortical neurons were fixed at DIV14 in 4% paraformaldehyde plus 4% sucrose at room temperature. Primary antibodies, anti-PSD95 (used at the concentration of 1:200, and obtained by Neuromab, cat. n. 444-1LC-49), anti-vGAT (1:100, SynapticSystem, 131002), anti-v-GLUT (1:200,SynapticSystem, 135303), anti-Synapsin (1:400, SynapticSystem, 106002) and secondary antibodies FITC- conjugated anti-mouse (1:100, Jackson ImmunoReserch, 715-095-150), FITC-conjugated anti-rabbit (1:100, Jackson ImmunoReserch, 711-095-152) and Cy5- conjugated anti-mouse (1:100, Jackson ImmunoReserch, 715-175-150) were applied in GDB buffer (30 mM phosphate buffer pH 7.4, containing 0.2% gelatin, 0.5% Triton-X-100 and 0.8M NaCl).

Confocal images were obtained using the same confocal microscope, objective and image acquisition parameters employed for the neurons morphologic analysis. Labelled neurons were chosen randomly

for quantification from three to six coverslips from two to three independent experiments. The number of neurons used for quantification is indicated in the figure legends. Morphometric measurements were performed using MetaMorph image analysis software (universal Imaging Corporation). Three single dendrites from each neuron in different condition were manually traced. The number, area and average intensity of synapses were automatically measured by computer using MetaMorph image analysis software and logged into Microsoft Excel. The synapse density was calculated as number of synapses per length of dendrites. Statistical significance was determined by one-way ANOVA Bonferroni post hoc test.

C.9 Fabrication of 6 μm-thick rr-P3HT films

Glass/ITO planar substrates (surface area = 1 cm^2) were cleaned by subsequent rinses in an ultrasonic bath by using distilled water, acetone and isopropanol (10 minutes each), and then dried with a N$_2$ flux. 1,2-diclorobenzene solution of rr-P3HT (molecular weight 15000 ÷ 45000, concentration, 60 g l^{-1}) was stirred at 50 °C for 15 hours for completely dissolving the polymer. The solution was then drop-casted on top of the glass/ITO substrate (drop volume = 20 µl), heated at 90°C for 2 minutes, and finally annealed at 120°C for 2 h. The thickness of the rr-P3HT layers obtained was measured using a profilometer.

Appendix D. Micro and nano-patterned silk and silk/P3HT substrates

D.1 Silk substrates fabrication

bombyx mori degummed silk fibers (2 g) were dissolved in a LiBr solution (9.3 M, 10 mL) at 60° C for 90 min obtaining a 20% (w/v) solution. A dialysis tubing (molecular cut off weight of 12 000 Da) was used for dialyzing the solution in water for 48 h at room temperature to remove the LiBr salt. The aggregates formed during dialysis were removed by centrifugation (4000 rpm, 25 min). After these steps the aqueous silk solution concentration was approximately 6% (w/v), determined by a gravimetric analysis performed on the dried sample. Silk solution was then casted on a PDMS masters that present the negative structure of the final micro and nano-patterns (for details about the fabrication of the PDMS masters see ref. [223]) and dried at room temperature for 24 h. Once solidified, the fibroin films were carefully removed from the PDMS master and subjected to a water vapor annealing by placing them in a desiccator together with a water reservoir. This process increases the crystallinity of the silk-based material and makes it insoluble in water.

D.2 Scanning electron microscopy (SEM)

Prior to Scanning electron microscopy (SEM) images acquisition, silk substrates were attached to glass slides using adhesive tape, air-dried and covered by a thin gold layer (thickness 6nm, 1.5 Cr adhesion layer) using a metal evaporator. All SEM micrographs were acquired using a TESCAN MIRA III scanning electron microscope (operating voltage 4kV, working distance 19 mm, stage tilt angle 30°).

D.3 HEK-293 Cells cultures preparation and viability assay

Glass and silk substrates were sterilized by immersion in EtOH 70% for 3 hours and washed 3 times with mQ-H_2O. Then, a layer of fibronectin (2 µg ml^{-1} in PBS buffer solution) was deposited on the samples surface and incubated for 1 hour at 37 ºC, in order to promote cellular adhesion. Excess fibronectin was then removed by rinses with PBS prior to cell plating. HEK-293 cells were cultured on top of the different substrates following the same procedure adopted in the case of rr-P3HT-based devices, described in section A.7. Cells proliferation was assessed after 24, 48, 72 and 96 hours in vitro performing the MTT [3-(4,5-dimethylthiazol-2-yl)-2,5-diphenyltetrazolium bromide] assay. For each time point, the growing medium was replaced with RPMI medium without phenol red containing 0.5 mg ml^{-1} of MTT and the samples were maintained in dark at 37 °C for 3 h. Then, the medium was removed, and the samples were air-dried at room temperature. Dry samples were subsequently immersed in 200 µl of ethanol in order to dissolve the formazan salt produced by cells through reduction of MTT. The proliferation cell rate was calculated as the difference in absorbance at 560 nm and 690 nm.

D.4 Bacterial cultures preparation

The gene encoding eGFP was PCR amplified from a pDONR-P2R-P3 vector carrying the eGFP coding sequence, and cloned into a pET23a(+) by conventional methods using NdeI and XhoI restriction sites (Table PRIMER). The resulting construct pET23a(+)-eGFP was sequence verified, and transformed into E. coli (DE3) Rosetta (Invitrogen).

Table PRIMER. Primer sequence (5'-3') used in this study.*[a]		
eGFP	Forward$_{Nat}$	cccccc<u>catat</u>ggtgagcaagggcgaggagc
	Reverse$_1$	ggtctgg<u>ctcgag</u>gtacagctcgtccatgcc
*: the restriction sites for NdeI (forward) and XhoI (reverse) are underlined.		

Bacterial cells were similarly cultured as previously described (ACS Biomater. Sci. Eng. 2016, 2, 1862-1866). Briefly, a single colony, from the bacteria carrying the pET23a(+)-eGFP construct, was inoculated in Luria Bertani (LB) broth in presence of Ampicillin (50 µg/ml) and incubated overnight at 37ºC until stationary phase is reached. The bacterial culture was then diluted to O.D 0.1 (1x10⁷ CFU ml⁻¹) in LB media supplemented with the same antibiotics. Then, each substrate was incubated with 5 ml of bacterial suspension and kept in 12 well culture plates. Finally, isopropyl-1-thio-D-galactopyranoside (IPTG) was added to the bacterial culture at a final concentration of 1 mM, following a 24-hours incubation at 25℃ on a platform shaker.

D.5 Evaluation of bacteria adhesion

After 24 hours the samples were removed from the bacteria growing medium, washed 3 times with mQ-H_2O and covered by a drop of water. Fluorescence images for the evaluation of the bacteria adhesion grade on the different substrates were acquired using an inverted fluorescence microscope (Nikon eclipse Ti), by exciting with a 470 nm light source (Lumencor Spectra X) and using a standard FITC filters set. The average number of bacteria adhered on each substrate type was quantified using Imagej software. Mean values has been averaged over n = 10 fields of view for each sample type, and over n = 3 statistically independent samples.

D.6 Water contact angle measurements

Silk-based samples were attached to glass slides using adhesive tape and air-dried overnight. Then, photographs of 5 µl water droplets deposited on the different substrates were taken using an optical contact angle measuring and contour analysis system (DataPhysics OCA 15EC). The calculation of the static water contact angle was carried out using the SCA 20 software (DataPhysics), according to

the sessile drop method. Representative images of the water droplets deposited on the different substrates are depicted in figure D.6.1.
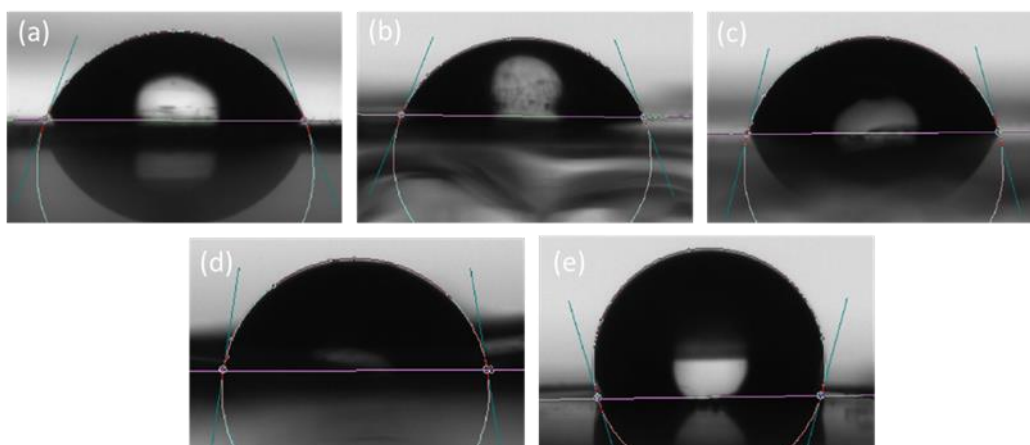
Figure D.6.1. Representative photographs of water droplets in contact with glass (a), silk flat (b), silk nano-stripes (c), μ wells2 (d) and μ wells1 (e) samples.

D.7 rr-P3HT deposition on silk substrates

Wet flat and patterned silk substrates were anchored on glass slide using adhesive tape and air-dried for one night. rr-P3HT was dissolved in o-dichlorobenzene (5 g l^{-1}) and stirred for one night at 50°C. rr-P3HT solution was deposited on dry silk substrates by spin coating (speed 1500 rpm, acceleration 1600 rpm s^{-1}) and the obtained samples were left in vacuum for 40 minutes.

Appendix E. rr-P3HT thin films and nanoparticles (NPs) interfaced with plant cells

E.1 rr-P3HT thin films fabrication and guard cells viability assay

ITO/P3HT devices were prepared by depositing a solution of rr-P3HT (Mn 54.000–75.000 molecular weight) in chlorobenzene (20 g/l, Sigma Aldrich) on top of glass/ITO substrates (15 Ω/sq) by spin-coating (two-steps recipe: i) 3 s at 800 rpm, ii) 60 s at 1600 rpm), after a careful cleaning of the substrates trough subsequent ultrasonic baths of ultrapure water, acetone and isopropanol. Polymer film thickness is about 150 nm. All films were thermally treated in an oven at 120°C for 2 h for annealing.

Prior to guard cells viability assay, 6-week-old *Arabidopsis Thaliana* leaves were attached to microscope cover glasses (0.17 µm thickness) using a Medical adhesive and by gently pressing them with a paintbrush. The leaves were then immersed in the imaging solution (5 mM KCl, 10 mM MES, 10 mM Ca^{2+}, pH 5.8 adjusted with Tris) after carefully removing the upper cells layer using a razor blade. Then, the obtained peeled leaves were incubated with fluorescein-diacetate (FDA, 4 µg/ml in imaging solution) for 20 minutes. Then, bright field and fluorescence images of the FDA-stained guard cells were acquired with an inverted fluorescence microscope (Nikon Ti-E) using a 20X objective (NA 0.75) and standard FITC filter set. Plant samples were subsequently interfaced with ITO/P3HT devices, and both rr-P3HT-treated and untreated leaves were photoexcited with green light focalized by the microscope objective ($\lambda = 540$ nm, light intensity on the sample: 64 mW/mm^2) for 2 minutes. The acquisition of bright field and fluorescence images of the FDA-stained guard cells was then repeated. The statistical analysis was done by manually counting the number of guard cells for each field of view. The % of healthy cells was obtained from the ratio between the FDA-stained cells and the total number of cells counted in bright field images. 50 cells belonging to 3 statistically independent samples for each condition were considered for the statistical analysis.

E.2 rr-P3HT Nps fabrication and characterization

rr-P3HT NPs were prepared as previously described, following the reprecipitation method [126]. Briefly, a solution of rr-P3HT in tetrahydrofuran (THF, Sigma Aldrich) was added drop-wise to mQ-water under magnetic stirring. The colloidal dispersion obtained was subjected to dialysis against 2 l of water overnight, for removing the residual organic solvent. The rr-P3HT-based colloidal suspension was centrifuged for 10min at different rates, from 2,000 to 8,000 rpm, separating every time the supernatant from the precipitate, obtaining a wide range of samples with different particle dimensions (from 100 to 600 nm) and different optical density (OD). The average hydrodynamic radius of the NPs and the solutions OD were characterized by carrying out Dynamic Light Scattering (DLS) measurements and using a TECAN Spark 10M Plate reader, respectively. The rr-P3HT Nps dispersions administered to the plant systems during the experiments described in this work are characterized by an average hydrodynamic radius 237 ± 82 nm and a polydispersity index of 0.12.

E.3 Calcium imaging experiments

Prior to guard cell Ca^{2+} imaging, *Arabidopsis Thaliana* plants leaves, genetically-encoded with NES YC3.6 probe, were attached to microscope cover glasses by following the same procedure described for the viability assay (see section E.1). The obtained peeled leaves were then immersed in the imaging solution (5 mM KCl, 10 mM MES, 10 mM Ca^{2+}, pH 5.8 adjusted with Tris) and put directly in contact with ITO/P3HT devices or incubated with rr-P3HT NPs (rr-P3HT NPs in imaging solution, OD value: 0.1) for 20 minutes. Ca^{2+} imaging analysis of the spontaneous guard cells activity were carried out with an inverted fluorescence microscope (Nikon Ti-E) using 20X objective (NA 0.75). The yellow Cameleon (YC) probe excitation was provided by a fluorescent lamp (Prior Lumen 200 PRO; Prior Scientific) at 440 nm (436/20 nm), set at 20% power. Images were acquired every 5 s with a Hamamatsu Dual CCD camera (ORCA-D2) using a FRET cyan fluorescent protein (CFP)/yellow fluorescent protein (YFP) optical block A11400-03 (emission 1, 483/32 nm for CFP;

emission 2, 542/27 nm for FRET) with a dichroic 510 nm mirror (Hamamatsu) for the simultaneous CFP and YFP acquisitions. The exposure time was set to 100 ms and the CCD binning was 4×4. The rr-P3HT photo-excitation was carried out with green light focalized by the microscope objective ($\lambda = 540$ nm, light intensity on the sample: 64 mW/mm^2, time duration = 2 minutes). Statistical analysis was performed by considering n = 10 guard cells for each condition, belonging to 3 statistically independent samples.

The experiments for the evaluation of the reversibility of the rr-P3HT Nps-induced effect were performed by adding CaCl$_2$ in the bath (5 mM) at the end of the calcium imaging measurement; or by repeating the calcium imaging experiments after leaving the plant samples resting in dark for 20 minutes.

E.4 Stomatal opening analysis

Arabidopsis Thaliana leaves genetically-encoded with NES YC3.6 probe, were attached to glass coverslips and peeled in the same way as for the viability assay (see section E.1). Then, they were incubated with imaging solution containing rr-P3HT NPs (rr-P3HT NPs solution OD value: 0.23) or SiO$_2$ NPs (average hydrodynamic radius = 260 ± 10 nm, 250 µg/ml) under white light (4000 lux) for 90 minutes. The measurement of the stomatal opening was carried out by acquiring fluorescent images of the guard cells using the same fluorescent microscope employed for calcium imaging experiments, using a 60X objective and standard FITC filter sets. The stomatal aperture size was quantified using Imagej software. The measurement of the size of the stomata aperture was performed by two different investigators in blind conditions. Mean values has been averaged over n = 120 cells, over n = 4 statistically independent samples.

Bibliography

[1] C.D. McCaig, A.M. Rajnicek, B. Song, M. Zhao, Controlling Cell Behavior Electrically: Current Views and Future Potential, Physiological Reviews. 85 (2005) 943–978. doi:10.1152/physrev.00020.2004.

[2] M. Cobb, Timeline: exorcizing the animal spirits: Jan Swammerdam on nerve function, Nat. Rev. Neurosci. 3 (2002) 395–400. doi:10.1038/nrn806.

[3] L. Galvani, Opere edite ed inedite del professore Luigi Galvani raccolte e pubblicate per cura dell' Accademia delle scienze dell' Istituto di Bologna, 1841.

[4] A. Verkhratsky, O.A. Krishtal, O.H. Petersen, From Galvani to patch clamp: the development of electrophysiology, Pflügers Archiv - European Journal of Physiology. 453 (2006) 233–247. doi:10.1007/s00424-006-0169-z.

[5] D.H. Hubel, Tungsten Microelectrode for Recording from Single Units, Science. 125 (1957) 549–550. doi:10.1126/science.125.3247.549.

[6] B. Holmgren, Conduction along the dorsal tracts of the spinal cord, The Journal of Physiology. 123 (1954) 324–337. doi:10.1113/jphysiol.1954.sp005054.

[7] C.-L. Li, H. Jasper, Microelectrode studies of the electrical activity of the cerebral cortex in the cat*, The Journal of Physiology. 121 (1953) 117–140. doi:10.1113/jphysiol.1953.sp004935.

[8] M.R. Angle, B. Cui, N.A. Melosh, Nanotechnology and neurophysiology, Current Opinion in Neurobiology. 32 (2015) 132–140. doi:10.1016/j.conb.2015.03.014.

[9] E. Neher, B. Sakmann, J.H. Steinbach, European Journal of Physiology 9 by Springer-Verlag 1978 The Extracellular Patch Clamp: A Method for Resolving Currents through Individual Open Channels in Biological Membranes, n.d.

[10] A. Molleman, Patch clamping: an introductory guide to patch clamp electrophysiology, J. Wiley, New York, 2003.

[11] M.Y. Rotenberg, B. Tian, Talking to Cells: Semiconductor Nanomaterials at the Cellular Interface, Advanced Biosystems. 2 (2018) 1700242. doi:10.1002/adbi.201700242.

[12] A. Hai, In-Cell Recording and Stimulation by Engulfment Mechanisms, in: M.D. Vittorio, L. Martiradonna, J. Assad (Eds.), Nanotechnology and Neuroscience: Nano-Electronic, Photonic and Mechanical Neuronal Interfacing, Springer New York, 2014: pp. 45–70. doi:10.1007/978-1-4899-8038-0_3.

[13] G.W. Gross, E. Rieske, G.W. Kreutzberg, A. Meyer, A new fixed-array multi-microelectrode system designed for long-term monitoring of extracellular single unit neuronal activity in vitro, Neurosci. Lett. 6 (1977) 101–105.

[14] G.W. Gross, A.N. Williams, J.H. Lucas, Recording of spontaneous activity with photoetched microelectrode surfaces from mouse spinal neurons in culture, J. Neurosci. Methods. 5 (1982) 13–22.

[15] J.L. Novak, B.C. Wheeler, Multisite hippocampal slice recording and stimulation using a 32 element microelectrode array, J. Neurosci. Methods. 23 (1988) 149–159.

[16] M.E. Spira, A. Hai, Multi-electrode array technologies for neuroscience and cardiology, Nat Nanotechnol. 8 (2013) 83–94. doi:10.1038/nnano.2012.265.

[17] M. HajjHassan, V. Chodavarapu, S. Musallam, NeuroMEMS: Neural Probe Microtechnologies, Sensors. 8 (2008) 6704–6726. doi:10.3390/s8106704.

[18] I. Delgado Ruz, S.R. Schultz, Localising and classifying neurons from high density MEA recordings, J. Neurosci. Methods. 233 (2014) 115–128. doi:10.1016/j.jneumeth.2014.05.037.

[19] J.J. Jun, N.A. Steinmetz, J.H. Siegle, D.J. Denman, M. Bauza, B. Barbarits, A.K. Lee, C.A. Anastassiou, A. Andrei, Ç. Aydın, M. Barbic, T.J. Blanche, V. Bonin, J. Couto, B. Dutta, S.L. Gratiy, D.A. Gutnisky, M. Häusser, B. Karsh, P. Ledochowitsch, C.M. Lopez, C. Mitelut, S. Musa, M. Okun, M. Pachitariu, J. Putzeys, P.D. Rich, C. Rossant, W. Sun, K. Svoboda, M. Carandini, K.D. Harris, C. Koch, J. O'Keefe, T.D. Harris, Fully integrated silicon probes for high-density recording of neural activity, Nature. 551 (2017) 232–236. doi:10.1038/nature24636.

[20] A. Poghossian, S. Ingebrandt, A. Offenhäusser, M.J. Schöning, Field-effect devices for detecting cellular signals, Seminars in Cell & Developmental Biology. 20 (2009) 41–48. doi:10.1016/j.semcdb.2009.01.014.

[21] D.T. Simon, E.O. Gabrielsson, K. Tybrandt, M. Berggren, Organic Bioelectronics: Bridging the Signaling Gap between Biology and Technology, Chem. Rev. 116 (2016) 13009–13041. doi:10.1021/acs.chemrev.6b00146.

[22] J. Rivnay, H. Wang, L. Fenno, K. Deisseroth, G.G. Malliaras, Next-generation probes, particles, and proteins for neural interfacing, Science Advances. 3 (2017) e1601649. doi:10.1126/sciadv.1601649.

[23] T. Someya, Z. Bao, G.G. Malliaras, The rise of plastic bioelectronics, Nature. 540 (2016) 379–385. doi:10.1038/nature21004.

[24] K.A. Ludwig, J.D. Uram, J. Yang, D.C. Martin, D.R. Kipke, Chronic neural recordings using silicon microelectrode arrays electrochemically deposited with a poly(3,4-ethylenedioxythiophene) (PEDOT) film, J Neural Eng. 3 (2006) 59–70. doi:10.1088/1741-2560/3/1/007.

[25] S. Venkatraman, J. Hendricks, Z.A. King, A.J. Sereno, S. Richardson-Burns, D. Martin, J.M. Carmena, In Vitro and In Vivo Evaluation of PEDOT Microelectrodes for Neural Stimulation and Recording, IEEE Transactions on Neural Systems and Rehabilitation Engineering. 19 (2011) 307–316. doi:10.1109/TNSRE.2011.2109399.

[26] R. Gerwig, K. Fuchsberger, B. Schroeppel, G.S. Link, G. Heusel, U. Kraushaar, W. Schuhmann, A. Stett, M. Stelzle, PEDOT–CNT Composite Microelectrodes for Recording and Electrostimulation Applications: Fabrication, Morphology, and Electrical Properties, Frontiers in Neuroengineering. 5 (2012). doi:10.3389/fneng.2012.00008.

[27] X. Cui, J.F. Hetke, J.A. Wiler, D.J. Anderson, D.C. Martin, Electrochemical deposition and characterization of conducting polymer polypyrrole/PSS on multichannel neural probes, Sensors and Actuators A: Physical. 93 (2001) 8–18. doi:10.1016/S0924-4247(01)00637-9.

[28] X. Cui, V.A. Lee, Y. Raphael, J.A. Wiler, J.F. Hetke, D.J. Anderson, D.C. Martin, Surface modification of neural recording electrodes with conducting polymer/biomolecule blends, J. Biomed. Mater. Res. 56 (2001) 261–272.

[29] D.-H. Kim, M. Abidian, D.C. Martin, Conducting polymers grown in hydrogel scaffolds coated on neural prosthetic devices, J Biomed Mater Res A. 71 (2004) 577–585. doi:10.1002/jbm.a.30124.

[30] M. Asplund, T. Nyberg, O. Inganäs, Electroactive polymers for neural interfaces, Polym. Chem. 1 (2010) 1374–1391. doi:10.1039/C0PY00077A.

[31] R. Green, M.R. Abidian, Conducting Polymers for Neural Prosthetic and Neural Interface Applications, Adv. Mater. Weinheim. 27 (2015) 7620–7637. doi:10.1002/adma.201501810.

[32] L. Ouyang, C.L. Shaw, C.-C. Kuo, A.L. Griffin, D.C. Martin, In vivo polymerization of poly(3,4-ethylenedioxythiophene) in the living rat hippocampus does not cause a significant loss of performance in a delayed alternation task, J Neural Eng. 11 (2014) 026005. doi:10.1088/1741-2560/11/2/026005.

[33] S.M. Richardson-Burns, J.L. Hendricks, B. Foster, L.K. Povlich, D.-H. Kim, D.C. Martin, Polymerization of the conducting polymer poly(3,4-ethylenedioxythiophene) (PEDOT) around living neural cells, Biomaterials. 28 (2007) 1539–1552. doi:10.1016/j.biomaterials.2006.11.026.

[34] X. Crispin, S. Marciniak, W. Osikowicz, G. Zotti, A.W. van der Gon, F. Louwet, M. Fahlman, L. Groenendaal, F. De Schryver, W.R. Salaneck, Conductivity, morphology, interfacial chemistry, and stability of poly (3, 4-ethylene dioxythiophene)–poly (styrene sulfonate): A photoelectron spectroscopy study, Journal of Polymer Science Part B: Polymer Physics. 41 (2003) 2561–2583.

[35] D. Khodagholy, T. Doublet, P. Quilichini, M. Gurfinkel, P. Leleux, A. Ghestem, E. Ismailova, T. Hervé, S. Sanaur, C. Bernard, G.G. Malliaras, In vivo recordings of brain activity using organic transistors, Nat Commun. 4 (2013) 1575. doi:10.1038/ncomms2573.

[36] M. Scanziani, M. Häusser, Electrophysiology in the age of light, Nature. 461 (2009) 930–939. doi:10.1038/nature08540.

[37] A.C. Thompson, P.R. Stoddart, E.D. Jansen, Optical Stimulation of Neurons, (n.d.) 16.

[38] J.F. Zimmerman, B. Tian, Nongenetic Optical Methods for Measuring and Modulating Neuronal Response, ACS Nano. 12 (2018) 4086–4095. doi:10.1021/acsnano.8b02758.

[39] M.P. Hortigon-Vinagre, V. Zamora, F.L. Burton, J. Green, G.A. Gintant, G.L. Smith, The Use of Ratiometric Fluorescence Measurements of the Voltage Sensitive Dye Di-4-ANEPPS to Examine Action Potential Characteristics and Drug Effects on Human Induced Pluripotent Stem Cell-Derived Cardiomyocytes, Toxicological Sciences. 154 (2016) 320–331. doi:10.1093/toxsci/kfw171.

[40] D.S. Peterka, H. Takahashi, R. Yuste, Imaging voltage in neurons, Neuron. 69 (2011) 9–21. doi:10.1016/j.neuron.2010.12.010.

[41] S.D. Antic, R.M. Empson, T. Knöpfel, Voltage imaging to understand connections and functions of neuronal circuits, Journal of Neurophysiology. 116 (2016) 135–152. doi:10.1152/jn.00226.2016.

[42] M.J. Higley, B.L. Sabatini, Calcium Signaling in Dendritic Spines, Cold Spring Harb Perspect Biol. 4 (2012). doi:10.1101/cshperspect.a005686.

[43] C. Stosiek, O. Garaschuk, K. Holthoff, A. Konnerth, In vivo two-photon calcium imaging of neuronal networks, PNAS. 100 (2003) 7319–7324. doi:10.1073/pnas.1232232100.

[44] E.S. Boyden, F. Zhang, E. Bamberg, G. Nagel, K. Deisseroth, Millisecond-timescale, genetically targeted optical control of neural activity, Nat. Neurosci. 8 (2005) 1263–1268. doi:10.1038/nn1525.

[45] R.D. Airan, K.R. Thompson, L.E. Fenno, H. Bernstein, K. Deisseroth, Temporally precise in vivo control of intracellular signalling, Nature. 458 (2009) 1025–1029. doi:10.1038/nature07926.

[46] I. Diester, M.T. Kaufman, M. Mogri, R. Pashaie, W. Goo, O. Yizhar, C. Ramakrishnan, K. Deisseroth, K.V. Shenoy, An optogenetic toolbox designed for primates, Nat. Neurosci. 14 (2011) 387–397. doi:10.1038/nn.2749.

[47] J. Wells, C. Kao, K. Mariappan, J. Albea, E.D. Jansen, P. Konrad, A. Mahadevan-Jansen, Optical stimulation of neural tissue in vivo, Opt Lett. 30 (2005) 504–506.

[48] M.G. Shapiro, K. Homma, S. Villarreal, C.-P. Richter, F. Bezanilla, Infrared light excites cells by changing their electrical capacitance, Nature Communications. 3 (2012) 736. doi:10.1038/ncomms1742.

[49] B. Migliori, M. Di Ventra, W. Kristan, Photoactivation of neurons by laser-generated local heating, AIP Advances. 2 (2012) 032154. doi:10.1063/1.4748955.

[50] E.S. Albert, J.M. Bec, G. Desmadryl, K. Chekroud, C. Travo, S. Gaboyard, F. Bardin, I. Marc, M. Dumas, G. Lenaers, C. Hamel, A. Muller, C. Chabbert, TRPV4 channels mediate the infrared laser-evoked response in sensory neurons, J. Neurophysiol. 107 (2012) 3227–3234. doi:10.1152/jn.00424.2011.

[51] A.C. Thompson, S.A. Wade, W.G.A. Brown, P.R. Stoddart, Modeling of light absorption in tissue during infrared neural stimulation, J Biomed Opt. 17 (2012) 075002. doi:10.1117/1.JBO.17.7.075002.

[52] K. Hüll, J. Morstein, D. Trauner, In Vivo Photopharmacology, Chemical Reviews. 118 (2018) 10710–10747. doi:10.1021/acs.chemrev.8b00037.

[53] A. Polosukhina, J. Litt, I. Tochitsky, J. Nemargut, Y. Sychev, I. De Kouchkovsky, T. Huang, K. Borges, D. Trauner, R.N. Van Gelder, R.H. Kramer, Photochemical restoration of visual responses in blind mice, Neuron. 75 (2012) 271–282. doi:10.1016/j.neuron.2012.05.022.

[54] J. Noh, R.P. Seal, J.A. Garver, R.H. Edwards, K. Kandler, Glutamate co-release at GABA/glycinergic synapses is crucial for the refinement of an inhibitory map, Nat. Neurosci. 13 (2010) 232–238. doi:10.1038/nn.2478.

[55] E.M. Callaway, L.C. Katz, Photostimulation using caged glutamate reveals functional circuitry in living brain slices, Proc. Natl. Acad. Sci. U.S.A. 90 (1993) 7661–7665.

[56] M.V. Keebler, C.W. Taylor, Endogenous signalling pathways and caged IP $_3$ evoke Ca $^{2+}$ puffs at the same abundant immobile intracellular sites, Journal of Cell Science. 130 (2017) 3728–3739. doi:10.1242/jcs.208520.

[57] I. Tochitsky, A. Polosukhina, V.E. Degtyar, N. Gallerani, C.M. Smith, A. Friedman, R.N. Van Gelder, D. Trauner, D. Kaufer, R.H. Kramer, Restoring visual function to blind mice with a photoswitch that

exploits electrophysiological remodeling of retinal ganglion cells, Neuron. 81 (2014) 800–813. doi:10.1016/j.neuron.2014.01.003.

[58]   P. Fromherz, Neuroelectronic Interfacing: Semiconductor Chips with Ion Channels, Nerve Cells, and Brain, in: R. Waser (Ed.), Nanoelectronics and Information Technology, 2003: pp. 781–810.

[59]   I. Schoen, P. Fromherz, The Mechanism of Extracellular Stimulation of Nerve Cells on an Electrolyte-Oxide-Semiconductor Capacitor, Biophysical Journal. 92 (2007) 1096–1111. doi:10.1529/biophysj.106.094763.

[60]   P. Fromherz, A. Offenhäusser, T. Vetter, J. Weis, A neuron-silicon junction: a Retzius cell of the leech on an insulated-gate field-effect transistor, Science. 252 (1991) 1290–1293.

[61]   P. Fromherz, Self-Gating of Ion Channels in Cell Adhesion, Phys. Rev. Lett. 78 (1997) 4131–4134. doi:10.1103/PhysRevLett.78.4131.

[62]   M.A. Colicos, B.E. Collins, M.J. Sailor, Y. Goda, Remodeling of synaptic actin induced by photoconductive stimulation, Cell. 107 (2001) 605–616.

[63]   J. Hung, M. Chansard, S.S. Ousman, M.D. Nguyen, M.A. Colicos, Activation of microglia by neuronal activity: Results from a new in vitro paradigm based on neuronal-silicon interfacing technology, Brain, Behavior, and Immunity. 24 (2010) 31–40. doi:10.1016/j.bbi.2009.06.150.

[64]   K. Mathieson, J. Loudin, G. Goetz, P. Huie, L. Wang, T.I. Kamins, L. Galambos, R. Smith, J.S. Harris, A. Sher, D. Palanker, Photovoltaic Retinal Prosthesis with High Pixel Density, Nat Photonics. 6 (2012) 391–397. doi:10.1038/nphoton.2012.104.

[65]   N. Martino, D. Ghezzi, F. Benfenati, G. Lanzani, M.R. Antognazza, Organic semiconductors for artificial vision, J. Mater. Chem. B. 1 (2013) 3768–3780. doi:10.1039/C3TB20213E.

[66]   S. Vaquero, C. Bossio, S. Bellani, N. Martino, E. Zucchetti, G. Lanzani, M.R. Antognazza, Conjugated polymers for the optical control of the electrical activity of living cells, J. Mater. Chem. B. 4 (2016) 5272–5283. doi:10.1039/C6TB01129B.

[67]   D. Ghezzi, M.R. Antognazza, M. Dal Maschio, E. Lanzarini, F. Benfenati, G. Lanzani, A hybrid bioorganic interface for neuronal photoactivation, Nat Commun. 2 (2011) 166. doi:10.1038/ncomms1164.

[68]   D. Ghezzi, M.R. Antognazza, R. Maccarone, S. Bellani, E. Lanzarini, N. Martino, M. Mete, G. Pertile, S. Bisti, G. Lanzani, F. Benfenati, A polymer optoelectronic interface restores light sensitivity in blind rat retinas, Nat Photon. 7 (2013) 400–406. doi:10.1038/nphoton.2013.34.

[69]   P. Feyen, E. Colombo, D. Endeman, M. Nova, L. Laudato, N. Martino, M.R. Antognazza, G. Lanzani, F. Benfenati, D. Ghezzi, Light-evoked hyperpolarization and silencing of neurons by conjugated polymers, Scientific Reports. 6 (2016) 22718. doi:10.1038/srep22718.

[70]   V. Benfenati, N. Martino, M.R. Antognazza, A. Pistone, S. Toffanin, S. Ferroni, G. Lanzani, M. Muccini, Photostimulation of Whole-Cell Conductance in Primary Rat Neocortical Astrocytes Mediated by Organic Semiconducting Thin Films, Advanced Healthcare Materials. 3 (2014) 392–399. doi:10.1002/adhm.201300179.

[71]   N. Martino, P. Feyen, M. Porro, C. Bossio, E. Zucchetti, D. Ghezzi, F. Benfenati, G. Lanzani, M.R. Antognazza, Photothermal cellular stimulation in functional bio-polymer interfaces, Scientific Reports. 5 (2015) 8911. doi:10.1038/srep08911.

[72]   V. Gautam, M. Bag, K.S. Narayan, Dynamics of Bulk Polymer Heterostructure/Electrolyte Devices, J. Phys. Chem. Lett. 1 (2010) 3277–3282. doi:10.1021/jz101405v.

[73]   V. Gautam, M. Bag, K.S. Narayan, Single-Pixel, Single-Layer Polymer Device as a Tricolor Sensor with Signals Mimicking Natural Photoreceptors, J. Am. Chem. Soc. 133 (2011) 17942–17949. doi:10.1021/ja207853e.

[74]   P. Thomas, T.G. Smart, HEK293 cell line: A vehicle for the expression of recombinant proteins, Journal of Pharmacological and Toxicological Methods. 51 (2005) 187–200. doi:10.1016/j.vascn.2004.08.014.

[75]   A. Varghese, E. Tenbroek, J. Colesjr, D. Sigg, Endogenous channels in HEK cells and potential roles in HCN ionic current measurements, Progress in Biophysics and Molecular Biology. 90 (2006) 26–37. doi:10.1016/j.pbiomolbio.2005.05.002.

[76]   M. Plaksin, E. Shapira, E. Kimmel, S. Shoham, Thermal Transients Excite Neurons through Universal Intramembrane Mechanoelectrical Effects, Phys. Rev. X. 8 (2018) 011043. doi:10.1103/PhysRevX.8.011043.

[77]   F. Lodola, N. Martino, G. Tullii, G. Lanzani, M.R. Antognazza, Conjugated polymers mediate effective activation of the Mammalian Ion Channel Transient Receptor Potential Vanilloid 1, Scientific Reports. 7 (2017). doi:10.1038/s41598-017-08541-6.

[78]   E. Mosconi, P. Salvatori, M.I. Saba, A. Mattoni, S. Bellani, F. Bruni, B. Santiago Gonzalez, M.R. Antognazza, S. Brovelli, G. Lanzani, H. Li, J.-L. Brédas, F. De Angelis, Surface Polarization Drives Photoinduced Charge Separation at the P3HT/Water Interface, ACS Energy Lett. 1 (2016) 454–463. doi:10.1021/acsenergylett.6b00197.

[79]   F. Bruni, J. Pedrini, C. Bossio, B. Santiago-Gonzalez, F. Meinardi, W.K. Bae, V.I. Klimov, G. Lanzani, S. Brovelli, Two-Color Emitting Colloidal Nanocrystals as Single-Particle Ratiometric Probes of Intracellular pH, Advanced Funtional Materials. 27 (2017) 1605533. doi:10.1002/adfm.201605533.

[80]   J.F. Maya-Vetencourt, D. Ghezzi, M.R. Antognazza, E. Colombo, M. Mete, P. Feyen, A. Desii, A. Buschiazzo, M. Di Paolo, S. Di Marco, F. Ticconi, L. Emionite, D. Shmal, C. Marini, I. Donelli, G. Freddi, R. Maccarone, S. Bisti, G. Sambuceti, G. Pertile, G. Lanzani, F. Benfenati, A fully organic retinal prosthesis restores vision in a rat model of degenerative blindness, Nature Materials. 16 (2017) 681–689. doi:10.1038/nmat4874.

[81]   M.R. Antognazza, M. Di Paolo, D. Ghezzi, M. Mete, S. Di Marco, J.F. Maya-Vetencourt, R. Maccarone, A. Desii, F. Di Fonzo, M. Bramini, A. Russo, L. Laudato, I. Donelli, M. Cilli, G. Freddi, G. Pertile, G. Lanzani, S. Bisti, F. Benfenati, Characterization of a Polymer-Based, Fully Organic Prosthesis for Implantation into the Subretinal Space of the Rat, Adv. Healthcare Mater. 5 (2016) 2271–2282. doi:10.1002/adhm.201600318.

[82] A. Hai, J. Shappir, M.E. Spira, In-cell recordings by extracellular microelectrodes, Nature Methods. 7 (2010) 200–202. doi:10.1038/nmeth.1420.

[83] B. Tian, T. Cohen-Karni, Q. Qing, X. Duan, P. Xie, C.M. Lieber, Three-Dimensional, Flexible Nanoscale Field-Effect Transistors as Localized Bioprobes, Science. 329 (2010) 830–834. doi:10.1126/science.1192033.

[84] X. Duan, R. Gao, P. Xie, T. Cohen-Karni, Q. Qing, H.S. Choe, B. Tian, X. Jiang, C.M. Lieber, Intracellular recordings of action potentials by an extracellular nanoscale field-effect transistor, Nature Nanotechnology. 7 (2012) 174–179. doi:10.1038/nnano.2011.223.

[85] R. Gleixner, P. Fromherz, The Extracellular Electrical Resistivity in Cell Adhesion, Biophysical Journal. 90 (2006) 2600–2611. doi:10.1529/biophysj.105.072587.

[86] A. Fendyur, M.E. Spira, Toward on-chip, in-cell recordings from cultured cardiomyocytes by arrays of gold mushroom-shaped microelectrodes, Front Neuroeng. 5 (2012). doi:10.3389/fneng.2012.00021.

[87] A. Fendyur, N. Mazurski, J. Shappir, M.E. Spira, Formation of Essential Ultrastructural Interface between Cultured Hippocampal Cells and Gold Mushroom-Shaped MEA- Toward "IN-CELL" Recordings from Vertebrate Neurons, Front Neuroeng. 4 (2011). doi:10.3389/fneng.2011.00014.

[88] A. Hai, M.E. Spira, On-chip electroporation, membrane repair dynamics and transient in-cell recordings by arrays of gold mushroom-shaped microelectrodes, Lab Chip. 12 (2012) 2865–2873. doi:10.1039/c2lc40091j.

[89] M. Dipalo, A.F. McGuire, H.-Y. Lou, V. Caprettini, G. Melle, G. Bruno, C. Lubrano, L. Matino, X. Li, F. De Angelis, B. Cui, F. Santoro, Cells Adhering to 3D Vertical Nanostructures: Cell Membrane Reshaping without Stable Internalization, Nano Letters. 18 (2018) 6100–6105. doi:10.1021/acs.nanolett.8b03163.

[90] J.W. Haycock, ed., 3D Cell Culture, Humana Press, Totowa, NJ, 2011. doi:10.1007/978-1-60761-984-0.

[91] S. Inal, A. Hama, M. Ferro, C. Pitsalidis, J. Oziat, D. Iandolo, A.-M. Pappa, M. Hadida, M. Huerta, D. Marchat, P. Mailley, R.M. Owens, Conducting Polymer Scaffolds for Hosting and Monitoring 3D Cell Culture, Advanced Biosystems. 1 (2017) 1700052. doi:10.1002/adbi.201700052.

[92] A. Ovsianikov, V. Mironov, J. Stampfl, R. Liska, Engineering 3D cell-culture matrices: multiphoton processing technologies for biological and tissue engineering applications, Expert Review of Medical Devices. 9 (2012) 613–633. doi:10.1586/erd.12.48.

[93] S.H. Oh, S.G. Kang, E.S. Kim, S.H. Cho, J.H. Lee, Fabrication and characterization of hydrophilic poly(lactic-co-glycolic acid)/poly(vinyl alcohol) blend cell scaffolds by melt-molding particulate-leaching method, Biomaterials. 24 (2003) 4011–4021. doi:10.1016/S0142-9612(03)00284-9.

[94] D. Huh, G.A. Hamilton, D.E. Ingber, From 3D cell culture to organs-on-chips, Trends in Cell Biology. 21 (2011) 745–754. doi:10.1016/j.tcb.2011.09.005.

[95] A.M.-D. Wan, S. Inal, T. Williams, K. Wang, P. Leleux, L. Estevez, E.P. Giannelis, C. Fischbach, G.G. Malliaras, D. Gourdon, 3D conducting polymer platforms for electrical control of protein conformation and cellular functions, J. Mater. Chem. B. 3 (2015) 5040–5048. doi:10.1039/C5TB00390C.

[96] S. Wang, S. Guan, W. Li, D. Ge, J. Xu, C. Sun, T. Liu, X. Ma, 3D culture of neural stem cells within conductive PEDOT layer-assembled chitosan/gelatin scaffolds for neural tissue engineering, Mater Sci Eng C Mater Biol Appl. 93 (2018) 890–901. doi:10.1016/j.msec.2018.08.054.

[97] D. Mawad, A. Artzy-Schnirman, J. Tonkin, J. Ramos, S. Inal, M.M. Mahat, N. Darwish, L. Zwi-Dantsis, G.G. Malliaras, J.J. Gooding, A. Lauto, M.M. Stevens, Electroconductive Hydrogel Based on Functional Poly(Ethylenedioxy Thiophene), Chemistry of Materials. 28 (2016) 6080–6088. doi:10.1021/acs.chemmater.6b01298.

[98] M. Sasaki, B.C. Karikkineth, K. Nagamine, H. Kaji, K. Torimitsu, M. Nishizawa, Highly Conductive Stretchable and Biocompatible Electrode-Hydrogel Hybrids for Advanced Tissue Engineering, Advanced Healthcare Materials. 3 (2014) 1919–1927. doi:10.1002/adhm.201400209.

[99] S. Wang, S. Guan, J. Xu, W. Li, D. Ge, C. Sun, T. Liu, X. Ma, Neural stem cell proliferation and differentiation in the conductive PEDOT-HA/Cs/Gel scaffold for neural tissue engineering, Biomater Sci. 5 (2017) 2024–2034. doi:10.1039/c7bm00633k.

[100] I. Giaever, C.R. Keese, Monitoring fibroblast behavior in tissue culture with an applied electric field, Proc. Natl. Acad. Sci. U.S.A. 81 (1984) 3761–3764.

[101] M. Ramuz, A. Hama, J. Rivnay, P. Leleux, R.M. Owens, Monitoring of cell layer coverage and differentiation with the organic electrochemical transistor, J. Mater. Chem. B. 3 (2015) 5971–5977. doi:10.1039/C5TB00922G.

[102] H.C. Ott, T.S. Matthiesen, S.-K. Goh, L.D. Black, S.M. Kren, T.I. Netoff, D.A. Taylor, Perfusion-decellularized matrix: using nature's platform to engineer a bioartificial heart, Nat. Med. 14 (2008) 213–221. doi:10.1038/nm1684.

[103] U.G.K. Wegst, H. Bai, E. Saiz, A.P. Tomsia, R.O. Ritchie, Bioinspired structural materials, Nat Mater. 14 (2015) 23–36. doi:10.1038/nmat4089.

[104] Y. Jiang, J.L. Carvalho-de-Souza, R.C.S. Wong, Z. Luo, D. Isheim, X. Zuo, A.W. Nicholls, I.W. Jung, J. Yue, D.-J. Liu, Y. Wang, V. De Andrade, X. Xiao, L. Navrazhnykh, D.E. Weiss, X. Wu, D.N. Seidman, F. Bezanilla, B. Tian, Heterogeneous silicon mesostructures for lipid-supported bioelectric interfaces, Nat Mater. 15 (2016) 1023–1030. doi:10.1038/nmat4673.

[105] A. Gautieri, S. Vesentini, A. Redaelli, M.J. Buehler, Hierarchical structure and nanomechanics of collagen microfibrils from the atomistic scale up, Nano Lett. 11 (2011) 757–766. doi:10.1021/nl103943u.

[106] J.L. Carvalho-de-Souza, J.S. Treger, B. Dang, S.B.H. Kent, D.R. Pepperberg, F. Bezanilla, Photosensitivity of Neurons Enabled by Cell-Targeted Gold Nanoparticles, Neuron. 86 (2015) 207–217. doi:10.1016/j.neuron.2015.02.033.

[107] Y. Wang, L. Guo, Nanomaterial-Enabled Neural Stimulation, Front Neurosci. 10 (2016) 69. doi:10.3389/fnins.2016.00069.

[108] E. Colombo, P. Feyen, M.R. Antognazza, G. Lanzani, F. Benfenati, Nanoparticles: A Challenging Vehicle for Neural Stimulation, Front Neurosci. 10 (2016) 105. doi:10.3389/fnins.2016.00105.

[109] F. Di Maria, F. Lodola, E. Zucchetti, F. Benfenati, G. Lanzani, The evolution of artificial light actuators in living systems: from planar to nanostructured interfaces, Chemical Society Reviews. 47 (2018) 4757–4780. doi:10.1039/C7CS00860K.

[110] H. Chen, L. Shao, Q. Li, J. Wang, Gold nanorods and their plasmonic properties, Chem. Soc. Rev. 42 (2013) 2679–2724. doi:10.1039/C2CS35367A.

[111] X. Huang, S. Neretina, M.A. El-Sayed, Gold nanorods: from synthesis and properties to biological and biomedical applications, Adv. Mater. Weinheim. 21 (2009) 4880–4910. doi:10.1002/adma.200802789.

[112] J. Yong, K. Needham, W.G.A. Brown, B.A. Nayagam, S.L. McArthur, A. Yu, P.R. Stoddart, Gold-nanorod-assisted near-infrared stimulation of primary auditory neurons, Adv Healthc Mater. 3 (2014) 1862–1868. doi:10.1002/adhm.201400027.

[113] C. Paviolo, P.R. Stoddart, Gold Nanoparticles for Modulating Neuronal Behavior, Nanomaterials (Basel). 7 (2017). doi:10.3390/nano7040092.

[114] E. Söderstjerna, F. Johansson, B. Klefbohm, U. Englund Johansson, Gold- and silver nanoparticles affect the growth characteristics of human embryonic neural precursor cells, PLoS ONE. 8 (2013) e58211. doi:10.1371/journal.pone.0058211.

[115] The dose makes the poison, Nat Nanotechnol. 6 (2011) 329. doi:10.1038/nnano.2011.87.

[116] M. Palner, K. Pu, S. Shao, J. Rao, Semiconducting Polymer Nanoparticles with Persistent Near-Infrared Luminescence for In Vivo Optical Imaging, Angew. Chem. Int. Ed. Engl. 54 (2015) 11477–11480. doi:10.1002/anie.201502736.

[117] M.C. Baier, J. Huber, S. Mecking, Fluorescent conjugated polymer nanoparticles by polymerization in miniemulsion, J. Am. Chem. Soc. 131 (2009) 14267–14273. doi:10.1021/ja905077c.

[118] A.J.C. Kuehne, M.C. Gather, J. Sprakel, Monodisperse conjugated polymer particles by Suzuki–Miyaura dispersion polymerization, Nature Communications. 3 (2012) 1088. doi:10.1038/ncomms2085.

[119] D. Muenmart, A.B. Foster, A. Harvey, M.-T. Chen, O. Navarro, V. Promarak, M.C. McCairn, J.M. Behrendt, M.L. Turner, Conjugated Polymer Nanoparticles by Suzuki-Miyaura Cross-Coupling Reactions in an Emulsion at Room Temperature., Macromolecules. 47 (2014) 6531–6539. doi:10.1021/ma501402h.

[120] S. Ciftci, A.J.C. Kuehne, Monodisperse Conjugated Polymer Particles via Heck Coupling—A Kinetic Study to Unravel Particle Formation in Step-Growth Dispersion Polymerization, Macromolecules. 48 (2015) 8389–8393. doi:10.1021/acs.macromol.5b01932.

[121] J.P. Rao, K.E. Geckeler, Polymer nanoparticles: Preparation techniques and size-control parameters, Progress in Polymer Science (Oxford). 36 (2011) 887–913. doi:10.1016/j.progpolymsci.2011.01.001.

[122] J. Pecher, S. Mecking, Nanoparticles of Conjugated Polymers, Chem. Rev. 110 (2010) 6260–6279. doi:10.1021/cr100132y.

[123] Y. Lyu, C. Xie, S.A. Chechetka, E. Miyako, K. Pu, Semiconducting Polymer Nanobioconjugates for Targeted Photothermal Activation of Neurons, J. Am. Chem. Soc. 138 (2016) 9049–9052. doi:10.1021/jacs.6b05192.

[124] W. Li, R. Luo, X. Lin, A.D. Jadhav, Z. Zhang, L. Yan, C.-Y. Chan, X. Chen, J. He, C.-H. Chen, P. Shi, Remote modulation of neural activities via near-infrared triggered release of biomolecules, Biomaterials. 65 (2015) 76–85. doi:10.1016/j.biomaterials.2015.06.041.

[125] F. Ye, C. Wu, Y. Jin, Y.-H. Chan, X. Zhang, D.T. Chiu, Ratiometric temperature sensing with semiconducting polymer dots, J. Am. Chem. Soc. 133 (2011) 8146–8149. doi:10.1021/ja202945g.

[126] E. Zucchetti, M. Zangoli, I. Bargigia, C. Bossio, F. Di Maria, G. Barbarella, C. D'Andrea, G. Lanzani, M.R. Antognazza, Poly(3-hexylthiophene) nanoparticles for biophotonics: study of the mutual interaction with living cells, Journal of Materials Chemistry B. 5 (2017) 565–574. doi:10.1039/C6TB02047J.

[127] M. Zangoli, F. Di Maria, E. Zucchetti, C. Bossio, M.R. Antognazza, G. Lanzani, R. Mazzaro, F. Corticelli, M. Baroncini, G. Barbarella, Engineering thiophene-based nanoparticles to induce phototransduction in live cells under illumination, Nanoscale. 9 (2017) 9202–9209. doi:10.1039/c7nr01793f.

[128] M.P. Monopoli, D. Walczyk, A. Campbell, G. Elia, I. Lynch, F.B. Bombelli, K.A. Dawson, Physical-chemical aspects of protein corona: relevance to in vitro and in vivo biological impacts of nanoparticles, J. Am. Chem. Soc. 133 (2011) 2525–2534. doi:10.1021/ja107583h.

[129] M.L. Capobianco, G. Barbarella, A. Manetto, Oligothiophenes as Fluorescent Markers for Biological Applications, Molecules. 17 (2012) 910–933. doi:10.3390/molecules17010910.

[130] C. Bossio, I. Abdel Aziz, G. Tullii, E. Zucchetti, D. Debellis, M. Zangoli, F. Di Maria, G. Lanzani, M.R. Antognazza, Photocatalytic Activity of Polymer Nanoparticles Modulates Intracellular Calcium Dynamics and Reactive Oxygen Species in HEK-293 Cells, Frontiers in Bioengineering and Biotechnology. 6 (2018). doi:10.3389/fbioe.2018.00114.

[131] R. María Girón, J. Marco-Martínez, S. Bellani, A. Insuasty, H. Comas Rojas, G. Tullii, M.R. Antognazza, S. Filippone, N. Martín, Synthesis of modified fullerenes for oxygen reduction reactions, J. Mater. Chem. A. 4 (2016) 14284–14290. doi:10.1039/C6TA06573B.

[132] E. Lanzarini, M.R. Antognazza, M. Biso, A. Ansaldo, L. Laudato, P. Bruno, P. Metrangolo, G. Resnati, D. Ricci, G. Lanzani, Polymer-Based Photocatalytic Hydrogen Generation, J. Phys. Chem. C. 116 (2012) 10944–10949. doi:10.1021/jp212107f.

[133] C. Tortiglione, M.R. Antognazza, A. Tino, C. Bossio, V. Marchesano, A. Bauduin, M. Zangoli, S.V. Morata, G. Lanzani, Semiconducting polymers are light nanotransducers in eyeless animals, Sci Adv. 3 (2017). doi:10.1126/sciadv.1601699.

[134] G. Tullii, A. Desii, C. Bossio, S. Bellani, M. Colombo, N. Martino, M.R. Antognazza, G. Lanzani, Bimodal functioning of a mesoporous, light sensitive polymer/electrolyte interface, Organic Electronics. 46 (2017) 88–98. doi:10.1016/j.orgel.2017.04.007.

[135] D.E. Markov, E. Amsterdam, P.W.M. Blom, A.B. Sieval, J.C. Hummelen, Accurate Measurement of the Exciton Diffusion Length in a Conjugated Polymer Using a Heterostructure with a Side-Chain Cross-Linked Fullerene Layer, The Journal of Physical Chemistry A. 109 (2005) 5266–5274. doi:10.1021/jp0509663.

[136] A. Haugeneder, M. Neges, C. Kallinger, W. Spirkl, U. Lemmer, J. Feldmann, U. Scherf, E. Harth, A. Gügel, K. Müllen, Exciton diffusion and dissociation in conjugated polymer/fullerene blends and heterostructures, Phys. Rev. B. 59 (1999) 15346–15351. doi:10.1103/PhysRevB.59.15346.

[137] Z. Jin, J. Wang, PIN architecture for ultrasensitive organic thin film photoconductors, Scientific Reports. 4 (2015). doi:10.1038/srep05331.

[138] E. Siebert-Henze, V.G. Lyssenko, J. Fischer, M. Tietze, R. Brueckner, T. Menke, K. Leo, M. Riede, Electroabsorption studies of organic p-i-n solar cells: Increase of the built-in voltage by higher doping concentration in the hole transport layer, Organic Electronics. 15 (2014) 563–568. doi:10.1016/j.orgel.2013.12.009.

[139] B. Maennig, J. Drechsel, D. Gebeyehu, P. Simon, F. Kozlowski, A. Werner, F. Li, S. Grundmann, S. Sonntag, M. Koch, K. Leo, M. Pfeiffer, H. Hoppe, D. Meissner, N.S. Sariciftci, I. Riedel, V. Dyakonov, J. Parisi, Organic p-i-n solar cells, Applied Physics A. 79 (2004) 1–14. doi:10.1007/s00339-003-2494-9.

[140] A.L. Ayzner, C.J. Tassone, S.H. Tolbert, B.J. Schwartz, Reappraising the Need for Bulk Heterojunctions in Polymer−Fullerene Photovoltaics: The Role of Carrier Transport in All-Solution-Processed P3HT/PCBM Bilayer Solar Cells, The Journal of Physical Chemistry C. 113 (2009) 20050–20060. doi:10.1021/jp9050897.

[141] F. Fumagalli, S. Bellani, M. Schreier, S. Leonardi, H.C. Rojas, A. Ghadirzadeh, G. Tullii, A. Savoini, G. Marra, L. Meda, M. Grätzel, G. Lanzani, M.T. Mayer, M.R. Antognazza, F. Di Fonzo, Hybrid organic–inorganic H2 -evolving photocathodes: understanding the route towards high performance organic photoelectrochemical water splitting, J. Mater. Chem. A. 4 (2016) 2178–2187. doi:10.1039/C5TA09330A.

[142] P.P. Fu, Q. Xia, H.-M. Hwang, P.C. Ray, H. Yu, Mechanisms of nanotoxicity: Generation of reactive oxygen species, Journal of Food and Drug Analysis. 22 (2014) 64–75. doi:10.1016/j.jfda.2014.01.005.

[143] T. Finkel, N.J. Holbrook, Oxidants, oxidative stress and the biology of ageing, Nature. 408 (2000) 239–247. doi:10.1038/35041687.

[144] G. Scarpa, A.-L. Idzko, S. Götz, S. Thalhammer, Biocompatibility Studies of Functionalized Regioregular Poly(3-hexylthiophene) Layers for Sensing Applications, Macromolecular Bioscience. 10 (2010) 378–383. doi:10.1002/mabi.200900412.

[145] P. Twentyman, M. Luscombe, A study of some variables in a tetrazolium dye (MTT) based assay for cell growth and chemosensitivity, British Journal of Cancer. 56 (1987) 279–285. doi:10.1038/bjc.1987.190.

[146] E. Eisenbarth, D. Velten, K. Schenk-Meuser, P. Linez, V. Biehl, H. Duschner, J. Breme, H. Hildebrand, Interactions between cells and titanium surfaces, Biomolecular Engineering. 19 (2002) 243–249. doi:10.1016/S1389-0344(02)00032-1.

[147] J.-X. Liu, D.-Z. Yang, F. Shi, Y.-J. Cai, Sol–gel deposited TiO_2 film on NiTi surgical alloy for biocompatibility improvement, Thin Solid Films. 429 (2003) 225–230. doi:10.1016/S0040-6090(03)00146-9.

[148] F. López-Huerta, B. Cervantes, O. González, J. Hernández-Torres, L. García-González, R. Vega, A. Herrera-May, E. Soto, Biocompatibility and Surface Properties of TiO_2 Thin Films Deposited by DC Magnetron Sputtering, Materials. 7 (2014) 4105–4117. doi:10.3390/ma7064105.

[149] J. Ou, J. Wang, D. Zhang, P. Zhang, S. Liu, P. Yan, B. Liu, S. Yang, Fabrication and biocompatibility investigation of TiO_2 films on the polymer substrates obtained via a novel and versatile route, Colloids and Surfaces B: Biointerfaces. 76 (2010) 123–127. doi:10.1016/j.colsurfb.2009.10.024.

[150] S. Günes, H. Neugebauer, N.S. Sariciftci, Conjugated Polymer-Based Organic Solar Cells, Chemical Reviews. 107 (2007) 1324–1338. doi:10.1021/cr050149z.

[151] A.J. Bard, M. Stratmann, S. Licht, Encyclopedia of Electrochemistry, Semiconductor Electrodes and Photoelectrochemistry, Wiley, 2002.

[152] A. Zaban, A. Meier, B.A. Gregg, Electric potential distribution and short-range screening in nanoporous TiO_2 electrodes, The Journal of Physical Chemistry B. 101 (1997) 7985–7990.

[153] B. O'Regan, J. Moser, M. Anderson, M. Graetzel, Vectorial electron injection into transparent semiconductor membranes and electric field effects on the dynamics of light-induced charge separation, Journal of Physical Chemistry. 94 (1990) 8720–8726.

[154] R. Porrazzo, S. Bellani, A. Luzio, E. Lanzarini, M. Caironi, M.R. Antognazza, Improving mobility and electrochemical stability of a water-gated polymer field-effect transistor, Organic Electronics. 15 (2014) 2126–2134. doi:10.1016/j.orgel.2014.06.002.

[155] A.J. Bard, L.R. Faulkner, Electrochemical Methods: Fundamentals and Applications, Wiley, 2000.

[156] P. Chowdhury, P. Fortin, G. Suppes, S. Holdcroft, Aqueous Photoelectrochemical Reduction of Anthraquinone Disulfonate at Organic Polymer Films, Macromolecular Chemistry and Physics. 217 (2016) 1119–1127. doi:10.1002/macp.201500440.

[157] N. Lago, A. Cester, N. Wrachien, M. Natali, S.D. Quiroga, S. Bonetti, M. Barbato, A. Rizzo, E. Benvenuti, V. Benfenati, M. Muccini, S. Toffanin, G. Meneghesso, A physical-based equivalent circuit model for an organic/electrolyte interface, Organic Electronics. 35 (2016) 176–185. doi:10.1016/j.orgel.2016.05.018.

[158] S. Cotrone, M. Ambrico, H. Toss, M.D. Angione, M. Magliulo, A. Mallardi, M. Berggren, G. Palazzo, G. Horowitz, T. Ligonzo, L. Torsi, Phospholipid film in electrolyte-gated organic field-effect transistors, Organic Electronics. 13 (2012) 638–644. doi:10.1016/j.orgel.2012.01.002.

[159] L. Kergoat, L. Herlogsson, D. Braga, B. Piro, M.-C. Pham, X. Crispin, M. Berggren, G. Horowitz, A Water-Gate Organic Field-Effect Transistor, Advanced Materials. 22 (2010) 2565–2569. doi:10.1002/adma.200904163.

[160] F. Buth, D. Kumar, M. Stutzmann, J.A. Garrido, Electrolyte-gated organic field-effect transistors for sensing applications, Applied Physics Letters. 98 (2011) 153302. doi:10.1063/1.3581882.

[161] C. Suspène, B. Piro, S. Reisberg, M.-C. Pham, H. Toss, M. Berggren, A. Yassar, G. Horowitz, Copolythiophene-based water-gated organic field-effect transistors for biosensing, J. Mater. Chem. B. 1 (2013) 2090–2097. doi:10.1039/C3TB00525A.

[162] B.E. Conway, W.G. Pell, Double-layer and pseudocapacitance types of electrochemical capacitors and their applications to the development of hybrid devices, J Solid State Electrochem. 7 (2003) 637–644. doi:10.1007/s10008-003-0395-7.

[163] H.C. Rojas, S. Bellani, F. Fumagalli, G. Tullii, S. Leonardi, M.T. Mayer, M. Schreier, M. Grätzel, G. Lanzani, F.D. Fonzo, M.R. Antognazza, Polymer-based photocathodes with a solution-processable cuprous iodide anode layer and a polyethyleneimine protective coating, Energy Environ. Sci. (2016). doi:10.1039/C6EE01655C.

[164] A. Falco, B. Matarese, P. Feyen, F. Benfenati, P. Lugli, J.C. de Mello, Investigation of the Stability and Biocompatibility of Commonly Used Electrode Materials in Organic Neurooptoelectronics, IEEE Transactions on Nanotechnology. 15 (2016) 746–753. doi:10.1109/TNANO.2016.2536946.

[165] M. Jenkner, P. Fromherz, Bistability of membrane conductance in cell adhesion observed in a neuron transistor, Physical Review Letters. 79 (1997) 4705.

[166] J. Tang, N. Qin, Y. Chong, Y. Diao, Yiliguma, Z. Wang, T. Xue, M. Jiang, J. Zhang, G. Zheng, Nanowire arrays restore vision in blind mice, Nature Communications. 9 (2018) 786. doi:10.1038/s41467-018-03212-0.

[167] B. Richter, V. Hahn, S. Bertels, T.K. Claus, M. Wegener, G. Delaittre, C. Barner-Kowollik, M. Bastmeyer, Guiding Cell Attachment in 3D Microscaffolds Selectively Functionalized with Two Distinct Adhesion Proteins, Advanced Materials. 29 (2017) 1604342. doi:10.1002/adma.201604342.

[168] M. Ikawa, T. Yamada, H. Matsui, H. Minemawari, J. Tsutsumi, Y. Horii, M. Chikamatsu, R. Azumi, R. Kumai, T. Hasegawa, Simple push coating of polymer thin-film transistors, Nature Communications. 3 (2012) 1176. doi:10.1038/ncomms2190.

[169] V. Vohra, W. Mróz, S. Inaba, W. Porzio, U. Giovanella, F. Galeotti, Low-Cost and Green Fabrication of Polymer Electronic Devices by Push-Coating of the Polymer Active Layers, ACS Appl. Mater. Interfaces. 9 (2017) 25434–25444. doi:10.1021/acsami.7b07857.

[170] V. Vohra, F. Galeotti, U. Giovanella, W. Mróz, M. Pasini, C. Botta, Nanostructured Light-Emitting Polymer Thin Films and Devices Fabricated by the Environment-Friendly Push-Coating Technique, ACS Appl. Mater. Interfaces. 10 (2018) 11794–11800. doi:10.1021/acsami.8b00137.

[171] M. Aryal, K. Trivedi, W. (Walter) Hu, Nano-Confinement Induced Chain Alignment in Ordered P3HT Nanostructures Defined by Nanoimprint Lithography, ACS Nano. 3 (2009) 3085–3090. doi:10.1021/nn900831m.

[172] V. Vohra, F. Galeotti, U. Giovanella, T. Anzai, E. Kozma, C. Botta, Investigating phase separation and structural coloration of self-assembled ternary polymer thin films, Appl. Phys. Lett. 109 (2016) 103702. doi:10.1063/1.4962390.

[173] Y. Yang, K. Mielczarek, A. Zakhidov, W. Hu, Large Molecular Weight Polymer Solar Cells with Strong Chain Alignment Created by Nanoimprint Lithography, ACS Appl. Mater. Interfaces. 8 (2016) 7300–7307. doi:10.1021/acsami.6b00192.

[174] F. Santoro, W. Zhao, L.-M. Joubert, L. Duan, J. Schnitker, Y. van de Burgt, H.-Y. Lou, B. Liu, A. Salleo, L. Cui, Y. Cui, B. Cui, Revealing the Cell–Material Interface with Nanometer Resolution by Focused Ion Beam/Scanning Electron Microscopy, ACS Nano. 11 (2017) 8320–8328. doi:10.1021/acsnano.7b03494.

[175] S. Bonde, N. Buch-Månson, K.R. Rostgaard, T.K. Andersen, T. Berthing, K.L. Martinez, Exploring arrays of vertical one-dimensional nanostructures for cellular investigations, Nanotechnology. 25 (2014) 362001. doi:10.1088/0957-4484/25/36/362001.

[176] N. Buch-Månson, S. Bonde, J. Bolinsson, T. Berthing, J. Nygård, K.L. Martinez, Towards a Better Prediction of Cell Settling on Nanostructure Arrays—Simple Means to Complicated Ends, Advanced Functional Materials. 25 (2015) 3246–3255. doi:10.1002/adfm.201500399.

[177] F. Viela, D. Granados, A. Ayuso-Sacido, I. Rodríguez, Biomechanical Cell Regulation by High Aspect Ratio Nanoimprinted Pillars, Advanced Functional Materials. 26 (2016) 5599–5609. doi:10.1002/adfm.201601817.

[178] L.E. Dickinson, D.R. Rand, J. Tsao, W. Eberle, S. Gerecht, Endothelial cell responses to micropillar substrates of varying dimensions and stiffness, Journal of Biomedical Materials Research Part A. 100A (2012) 1457–1466. doi:10.1002/jbm.a.34059.

[179] C.H. Rasmussen, P.M. Reynolds, D.R. Petersen, M. Hansson, R.M. McMeeking, M. Dufva, N. Gadegaard, Enhanced Differentiation of Human Embryonic Stem Cells Toward Definitive Endoderm on Ultrahigh Aspect Ratio Nanopillars, Advanced Functional Materials. 26 (2016) 815–823. doi:10.1002/adfm.201504204.

[180] J. Fu, Y.-K. Wang, M.T. Yang, R.A. Desai, X. Yu, Z. Liu, C.S. Chen, Mechanical regulation of cell function with geometrically modulated elastomeric substrates, Nature Methods. 7 (2010) 733–736. doi:10.1038/nmeth.1487.

[181] M. Leber, M.M.H. Shandhi, A. Hogan, F. Solzbacher, R. Bhandari, S. Negi, Different methods to alter surface morphology of high aspect ratio structures, Applied Surface Science. 365 (2016) 180–190. doi:10.1016/j.apsusc.2016.01.008.

[182] T. Limongi, F. Cesca, F. Gentile, R. Marotta, R. Ruffilli, A. Barberis, M.D. Maschio, E.M. Petrini, S. Santoriello, F. Benfenati, E.D. Fabrizio, Nanostructured Superhydrophobic Substrates Trigger the Development of 3D Neuronal Networks, Small. 9 (2013) 402–412. doi:10.1002/smll.201201377.

[183] S. Bonde, T. Berthing, M.H. Madsen, T.K. Andersen, N. Buch-Månson, L. Guo, X. Li, F. Badique, K. Anselme, J. Nygård, K.L. Martinez, Tuning InAs Nanowire Density for HEK293 Cell Viability, Adhesion, and Morphology: Perspectives for Nanowire-Based Biosensors, ACS Appl. Mater. Interfaces. 5 (2013) 10510–10519. doi:10.1021/am402070k.

[184] M.A. Bucaro, Y. Vasquez, B.D. Hatton, J. Aizenberg, Fine-Tuning the Degree of Stem Cell Polarization and Alignment on Ordered Arrays of High-Aspect-Ratio Nanopillars, ACS Nano. 6 (2012) 6222–6230. doi:10.1021/nn301654e.

[185] R. Porrazzo, A. Luzio, S. Bellani, G.E. Bonacchini, Y.-Y. Noh, Y.-H. Kim, G. Lanzani, M.R. Antognazza, M. Caironi, Water-Gated n-Type Organic Field-Effect Transistors for Complementary Integrated Circuits Operating in an Aqueous Environment, ACS Omega. 2 (2017) 1–10. doi:10.1021/acsomega.6b00256.

[186] F.J. Harding, S. Surdo, B. Delalat, C. Cozzi, R. Elnathan, S. Gronthos, N.H. Voelcker, G. Barillaro, Ordered Silicon Pillar Arrays Prepared by Electrochemical Micromachining: Substrates for High-Efficiency Cell Transfection, ACS Applied Materials & Interfaces. 8 (2016) 29197–29202. doi:10.1021/acsami.6b07850.

[187] D.-J. Kim, G. Lee, G.-S. Kim, S.-K. Lee, Statistical analysis of immuno-functionalized tumor-cell behaviors on nanopatterned substrates, Nanoscale Research Letters. 7 (2012) 637.

[188] Z. Li, J. Song, G. Mantini, M.-Y. Lu, H. Fang, C. Falconi, L.-J. Chen, Z.L. Wang, Quantifying the Traction Force of a Single Cell by Aligned Silicon Nanowire Array, Nano Letters. 9 (2009) 3575–3580. doi:10.1021/nl901774m.

[189] D.B. Chklovskii, Synaptic Connectivity and Neuronal Morphology: Two Sides of the Same Coin, Neuron. 43 (2004) 609–617. doi:10.1016/j.neuron.2004.08.012.

[190] Gomez Natalia, Chen Shaochen, Schmidt Christine E, Polarization of hippocampal neurons with competitive surface stimuli: contact guidance cues are preferred over chemical ligands, Journal of The Royal Society Interface. 4 (2007) 223–233. doi:10.1098/rsif.2006.0171.

[191] C. Simitzi, A. Ranella, E. Stratakis, Controlling the morphology and outgrowth of nerve and neuroglial cells: The effect of surface topography, Acta Biomaterialia. 51 (2017) 21–52. doi:10.1016/j.actbio.2017.01.023.

[192] E. Martínez, E. Engel, J.A. Planell, J. Samitier, Effects of artificial micro- and nano-structured surfaces on cell behaviour, Annals of Anatomy - Anatomischer Anzeiger. 191 (2009) 126–135. doi:10.1016/j.aanat.2008.05.006.

[193] D. Hoffman-Kim, J.A. Mitchel, R.V. Bellamkonda, Topography, cell response, and nerve regeneration, Annu Rev Biomed Eng. 12 (2010) 203–231. doi:10.1146/annurev-bioeng-070909-105351.

[194] T. Repić, K. Madirazza, E. Bektur, D. Sapunar, Characterization of dorsal root ganglion neurons cultured on silicon micro-pillar substrates, Scientific Reports. 6 (2016). doi:10.1038/srep39560.

[195] M. Mattotti, L. Micholt, D. Braeken, D. Kovačić, Characterization of spiral ganglion neurons cultured on silicon micro-pillar substrates for new auditory neuro-electronic interfaces, Journal of Neural Engineering. 12 (2015) 026001. doi:10.1088/1741-2560/12/2/026001.

[196] L. Micholt, A. Gärtner, D. Prodanov, D. Braeken, C.G. Dotti, C. Bartic, Substrate Topography Determines Neuronal Polarization and Growth In Vitro, PLOS ONE. 8 (2013) e66170. doi:10.1371/journal.pone.0066170.

[197] N.M. Dowell-Mesfin, M.-A. Abdul-Karim, A.M.P. Turner, S. Schanz, H.G. Craighead, B. Roysam, J.N. Turner, W. Shain, Topographically modified surfaces affect orientation and growth of hippocampal neurons, J. Neural Eng. 1 (2004) 78. doi:10.1088/1741-2560/1/2/003.

[198] J.N. Hanson, M.J. Motala, M.L. Heien, M. Gillette, J. Sweedler, R.G. Nuzzo, Textural guidance cues for controlling process outgrowth of mammalian neurons, Lab Chip. 9 (2009) 122–131. doi:10.1039/B803595D.

[199] W. Li, Q.Y. Tang, A.D. Jadhav, A. Narang, W.X. Qian, P. Shi, S.W. Pang, Large-scale Topographical Screen for Investigation of Physical Neural-Guidance Cues, Scientific Reports. 5 (2015). doi:10.1038/srep08644.

[200] D.W. Grainger, H.C. van der Mei, P.C. Jutte, J.J.A.M. van den Dungen, M.J. Schultz, B.F.A.M. van der Laan, S.A.J. Zaat, H.J. Busscher, Critical factors in the translation of improved antimicrobial strategies for medical implants and devices, Biomaterials. 34 (2013) 9237–9243. doi:10.1016/j.biomaterials.2013.08.043.

[201] C. von Eiff, B. Jansen, W. Kohnen, K. Becker, Infections associated with medical devices: pathogenesis, management and prophylaxis, Drugs. 65 (2005) 179–214. doi:10.2165/00003495-200565020-00003.

[202] J.W. Costerton, Bacterial Biofilms: A Common Cause of Persistent Infections, Science. 284 (1999) 1318–1322. doi:10.1126/science.284.5418.1318.

[203] A. Jaggessar, H. Shahali, A. Mathew, P.K.D.V. Yarlagadda, Bio-mimicking nano and micro-structured surface fabrication for antibacterial properties in medical implants, Journal of Nanobiotechnology. 15 (2017). doi:10.1186/s12951-017-0306-1.

[204] M.G. Katsikogianni, D.J. Wood, Y.F. Missirlis, Biomaterial Functionalized Surfaces for Reducing Bacterial Adhesion and Infection, in: I.V. Antoniac (Ed.), Handbook of Bioceramics and Biocomposites, Springer International Publishing, Cham, 2015: pp. 1–28. doi:10.1007/978-3-319-09230-0_32-1.

[205] S. Nir, M. Reches, Bio-inspired antifouling approaches: the quest towards non-toxic and non-biocidal materials, Current Opinion in Biotechnology. 39 (2016) 48–55. doi:10.1016/j.copbio.2015.12.012.

[206] G.D. Bixler, A. Theiss, B. Bhushan, S.C. Lee, Anti-fouling properties of microstructured surfaces bio-inspired by rice leaves and butterfly wings, Journal of Colloid and Interface Science. 419 (2014) 114–133. doi:10.1016/j.jcis.2013.12.019.

[207] C.M. Magin, S.P. Cooper, A.B. Brennan, Non-toxic antifouling strategies, Materials Today. 13 (2010) 36–44.

[208] K.J. Edwards, A.D. Rutenberg, Microbial response to surface microtopography: the role of metabolism in localized mineral dissolution, Chemical Geology. 180 (2001) 19–32. doi:10.1016/S0009-2541(01)00303-5.

[209] K. Anselme, P. Davidson, A.M. Popa, M. Giazzon, M. Liley, L. Ploux, The interaction of cells and bacteria with surfaces structured at the nanometre scale, Acta Biomaterialia. 6 (2010) 3824–3846. doi:10.1016/j.actbio.2010.04.001.

[210] W. Hartleb, J.S. Saar, P. Zou, K. Lienkamp, Just Antimicrobial is not Enough: Toward Bifunctional Polymer Surfaces with Dual Antimicrobial and Protein-Repellent Functionality, Macromolecular Chemistry and Physics. 217 (2016) 225–231. doi:10.1002/macp.201500266.

[211] S. Fuchs, X. Jiang, H. Schmidt, E. Dohle, S. Ghanaati, C. Orth, A. Hofmann, A. Motta, C. Migliaresi, C.J. Kirkpatrick, Dynamic processes involved in the pre-vascularization of silk fibroin constructs for bone regeneration using outgrowth endothelial cells, Biomaterials. 30 (2009) 1329–1338. doi:10.1016/j.biomaterials.2008.11.028.

[212] R.E. Unger, M. Wolf, K. Peters, A. Motta, C. Migliaresi, C. James Kirkpatrick, Growth of human cells on a non-woven silk fibroin net: a potential for use in tissue engineering, Biomaterials. 25 (2004) 1069–1075. doi:10.1016/S0142-9612(03)00619-7.

[213] Y. Wang, E. Bella, C.S.D. Lee, C. Migliaresi, L. Pelcastre, Z. Schwartz, B.D. Boyan, A. Motta, The synergistic effects of 3-D porous silk fibroin matrix scaffold properties and hydrodynamic environment in cartilage tissue regeneration, Biomaterials. 31 (2010) 4672–4681. doi:10.1016/j.biomaterials.2010.02.006.

[214] A.S. Lammel, X. Hu, S.-H. Park, D.L. Kaplan, T.R. Scheibel, Controlling silk fibroin particle features for drug delivery, Biomaterials. 31 (2010) 4583–4591. doi:10.1016/j.biomaterials.2010.02.024.

[215] E. Wenk, A.J. Wandrey, H.P. Merkle, L. Meinel, Silk fibroin spheres as a platform for controlled drug delivery, Journal of Controlled Release. 132 (2008) 26–34. doi:10.1016/j.jconrel.2008.08.005.

[216] D.-H. Kim, J. Viventi, J.J. Amsden, J. Xiao, L. Vigeland, Y.-S. Kim, J.A. Blanco, B. Panilaitis, E.S. Frechette, D. Contreras, D.L. Kaplan, F.G. Omenetto, Y. Huang, K.-C. Hwang, M.R. Zakin, B. Litt, J.A. Rogers, Dissolvable films of silk fibroin for ultrathin conformal bio-integrated electronics, Nature Materials. 9 (2010) 511–517. doi:10.1038/nmat2745.

[217] D.-H. Kim, Y.-S. Kim, J. Amsden, B. Panilaitis, D.L. Kaplan, F.G. Omenetto, M.R. Zakin, J.A. Rogers, Silicon electronics on silk as a path to bioresorbable, implantable devices, Appl. Phys. Lett. 95 (2009) 133701. doi:10.1063/1.3238552.

[218] S. Chang, B. Kang, Y. Dai, D. Chen, Synthesis of antimicrobial silver nanoparticles on silk fibers via γ-radiation, Journal of Applied Polymer Science. 112 (2009) 2511–2515. doi:10.1002/app.29716.

[219] L. Bai, L. Zhu, S. Min, L. Liu, Y. Cai, J. Yao, Surface modification and properties of Bombyx mori silk fibroin films by antimicrobial peptide, Applied Surface Science. 254 (2008) 2988–2995. doi:10.1016/j.apsusc.2007.10.049.

[220] M.L. Gulrajani, D. Gupta, S. Periyasamy, S.G. Muthu, Preparation and application of silver nanoparticles on silk for imparting antimicrobial properties, Journal of Applied Polymer Science. 108 (2008) 614–623. doi:10.1002/app.27584.

[221] S.T. Dubas, P. Kumlangdudsana, P. Potiyaraj, Layer-by-layer deposition of antimicrobial silver nanoparticles on textile fibers, Colloids and Surfaces A: Physicochemical and Engineering Aspects. 289 (2006) 105–109. doi:10.1016/j.colsurfa.2006.04.012.

[222] T. Arai, G. Freddi, G.M. Colonna, E. Scotti, A. Boschi, R. Murakami, M. Tsukada, Absorption of metal cations by modified B. mori silk and preparation of fabrics with antimicrobial activity, J. Appl. Polym. Sci. 80 (2001) 297–303. doi:10.1002/1097-4628(20010411)80:2<297::AID-APP1099>3.0.CO;2-Z.

[223] F. Galeotti, A. Andicsova, S. Yunus, C. Botta, Precise surface patterning of silk fibroin films by breath figures, Soft Matter. 8 (2012) 4815–4821. doi:10.1039/C2SM25089F.

[224] X. Hu, K. Shmelev, L. Sun, E.-S. Gil, S.-H. Park, P. Cebe, D.L. Kaplan, Regulation of Silk Material Structure by Temperature-Controlled Water Vapor Annealing, Biomacromolecules. 12 (2011) 1686–1696. doi:10.1021/bm200062a.

[225] G.H. Altman, F. Diaz, C. Jakuba, T. Calabro, R.L. Horan, J. Chen, H. Lu, J. Richmond, D.L. Kaplan, Silk-based biomaterials, Biomaterials. 24 (2003) 401–416. doi:10.1016/S0142-9612(02)00353-8.

[226] L. Meinel, S. Hofmann, V. Karageorgiou, C. Kirker-Head, J. McCool, G. Gronowicz, L. Zichner, R. Langer, G. Vunjak-Novakovic, D.L. Kaplan, The inflammatory responses to silk films in vitro and in vivo, Biomaterials. 26 (2005) 147–155. doi:10.1016/j.biomaterials.2004.02.047.

[227] Y. Yang, X. Chen, F. Ding, P. Zhang, J. Liu, X. Gu, Biocompatibility evaluation of silk fibroin with peripheral nerve tissues and cells in vitro, Biomaterials. 28 (2007) 1643–1652. doi:10.1016/j.biomaterials.2006.12.004.

[228] K. Bazaka, R.J. Crawford, E.P. Ivanova, Do bacteria differentiate between degrees of nanoscale surface roughness?, Biotechnology Journal. 6 (2011) 1103–1114. doi:10.1002/biot.201100027.

[229] K. Manabe, S. Nishizawa, S. Shiratori, Porous Surface Structure Fabricated by Breath Figures that Suppresses *Pseudomonas aeruginosa* Biofilm Formation, ACS Applied Materials & Interfaces. 5 (2013) 11900–11905. doi:10.1021/am4035762.

[230] G.S. Watson, D.W. Green, L. Schwarzkopf, X. Li, B.W. Cribb, S. Myhra, J.A. Watson, A gecko skin micro/nano structure – A low adhesion, superhydrophobic, anti-wetting, self-cleaning, biocompatible, antibacterial surface, Acta Biomaterialia. 21 (2015) 109–122. doi:10.1016/j.actbio.2015.03.007.

[231] D.E. Nelson, K.D. Young, Penicillin Binding Protein 5 Affects Cell Diameter, Contour, and Morphology of Escherichia coli, Journal of Bacteriology. 182 (2000) 1714–1721. doi:10.1128/JB.182.6.1714-1721.2000.

[232] N. Grossman, E.Z. Ron, C.L. Woldringh, Changes in Cell Dimensions During Amino Acid Starvation of Escherichia coli, J. BACTERIOL. 152 (1982) 7.

[233] R. Förch, H. Schönherr, H. Schonherr, A.T.A. Jenkins, Surface Design: Applications in Bioscience and Nanotechnology, John Wiley & Sons, 2009.

[234] X. Wu, S. Wang, Regulating MC3T3-E1 Cells on Deformable Poly(ε-caprolactone) Honeycomb Films Prepared Using a Surfactant-Free Breath Figure Method in a Water-Miscible Solvent, ACS Applied Materials & Interfaces. 4 (2012) 4966–4975. doi:10.1021/am301334s.

[235] G.A. Pankey, L.D. Sabath, Clinical Relevance of Bacteriostatic versus Bactericidal Mechanisms of Action in the Treatment of Gram-Positive Bacterial Infections, Clinical Infectious Diseases. 38 (2004) 864–870. doi:10.1086/381972.

[236] P.H. Raven, Biology of plants /, W.H. Freeman and Co., 2005.

[237] E. Masarovičová, K. Kráľová, Metal Nanoparticles and Plants / Nanocząstki Metaliczne I Rośliny, Ecological Chemistry and Engineering S. 20 (2013) 9–22. doi:10.2478/eces-2013-0001.

[238] D. Sun, H.I. Hussain, Z. Yi, J.E. Rookes, L. Kong, D.M. Cahill, Mesoporous silica nanoparticles enhance seedling growth and photosynthesis in wheat and lupin, Chemosphere. 152 (2016) 81–91. doi:10.1016/j.chemosphere.2016.02.096.

[239] J.P. Giraldo, M.P. Landry, S.M. Faltermeier, T.P. McNicholas, N.M. Iverson, A.A. Boghossian, N.F. Reuel, A.J. Hilmer, F. Sen, J.A. Brew, M.S. Strano, Plant nanobionics approach to augment photosynthesis and biochemical sensing, Nature Materials. 13 (2014) 400–408. doi:10.1038/nmat3890.

[240] E. Stavrinidou, R. Gabrielsson, E. Gomez, X. Crispin, O. Nilsson, D.T. Simon, M. Berggren, Electronic plants, Science Advances. 1 (2015) e1501136–e1501136. doi:10.1126/sciadv.1501136.

[241] E. Stavrinidou, R. Gabrielsson, K.P.R. Nilsson, S.K. Singh, J.F. Franco-Gonzalez, A.V. Volkov, M.P. Jonsson, A. Grimoldi, M. Elgland, I.V. Zozoulenko, D.T. Simon, M. Berggren, In vivo polymerization and manufacturing of wires and supercapacitors in plants, Proceedings of the National Academy of Sciences. 114 (2017) 2807–2812. doi:10.1073/pnas.1616456114.

[242] N. Coppedè, M. Janni, M. Bettelli, C.L. Maida, F. Gentile, M. Villani, R. Ruotolo, S. Iannotta, N. Marmiroli, M. Marmiroli, A. Zappettini, An in vivo biosensing, biomimetic electrochemical transistor with applications in plant science and precision farming, Scientific Reports. 7 (2017). doi:10.1038/s41598-017-16217-4.

[243] D.W. Meinke, Arabidopsis thaliana: A Model Plant for Genome Analysis, Science. 282 (1998) 662–682. doi:10.1126/science.282.5389.662.

[244] T. Mitchell-Olds, Arabidopsis thaliana and its wild relatives: a model system for ecology and evolution, Trends in Ecology & Evolution. 16 (2001) 693–700. doi:10.1016/S0169-5347(01)02291-1.

[245] E. Zeiger, The Biology of Stomatal Guard Cells, Annual Review of Plant Physiology. 34 (1983) 441–474. doi:10.1146/annurev.pp.34.060183.002301.

[246] A.A.R. Webb, M.R. McAinsh, J.E. Taylor, A.M. Hetherington, Calcium Ions as Intracellular Second Messengers in Higher Plants, in: Advances in Botanical Research, Elsevier, 1996: pp. 45–96. doi:10.1016/S0065-2296(08)60056-7.

[247] A.N. Dodd, J. Kudla, D. Sanders, The language of calcium signaling, Annu Rev Plant Biol. 61 (2010) 593–620. doi:10.1146/annurev-arplant-070109-104628.

[248] K. De Vriese, A. Costa, T. Beeckman, S. Vanneste, Pharmacological Strategies for Manipulating Plant Ca2+ Signalling, Int J Mol Sci. 19 (2018). doi:10.3390/ijms19051506.

[249] S. Behera, M. Krebs, G. Loro, K. Schumacher, A. Costa, J. Kudla, Ca imaging in plants using genetically encoded Yellow Cameleon Ca indicators, 2013. doi:10.1101/pdb.top066183.

[250] J.M. Widholm, The use of fluorescein diacetate and phenosafranine for determining viability of cultured plant cells, Stain Technology. 47 (1972) 189–194.

[251] L. Jiajia, M. Shinghung, Z. Jiacheng, W. Jialing, X. Dilin, H. Shengquan, Z. Zaijun, W. Qinwen, H. Yifan, C. Wei, Assessment of Neuronal Viability Using Fluorescein Diacetate-Propidium Iodide Double Staining in Cerebellar Granule Neuron Culture, Journal of Visualized Experiments. (2017). doi:10.3791/55442.

[252] M. Krebs, K. Held, A. Binder, K. Hashimoto, G. Den Herder, M. Parniske, J. Kudla, K. Schumacher, FRET-based genetically encoded sensors allow high-resolution live cell imaging of Ca^{2+} dynamics, Plant J. 69 (2012) 181–192. doi:10.1111/j.1365-313X.2011.04780.x.

[253] T. Nagai, S. Yamada, T. Tominaga, M. Ichikawa, A. Miyawaki, Expanded dynamic range of fluorescent indicators for Ca(2+) by circularly permuted yellow fluorescent proteins, Proc. Natl. Acad. Sci. U.S.A. 101 (2004) 10554–10559. doi:10.1073/pnas.0400417101.

[254] G.J. Allen, J.M. Kwak, S.P. Chu, J. Llopis, R.Y. Tsien, J.F. Harper, J.I. Schroeder, Cameleon calcium indicator reports cytoplasmic calcium dynamics in Arabidopsis guard cells, The Plant Journal. 19 (1999) 735–747. doi:10.1046/j.1365-313x.1999.00574.x.

[255] K.E. Hubbard, R.S. Siegel, G. Valerio, B. Brandt, J.I. Schroeder, Abscisic acid and CO2 signalling via calcium sensitivity priming in guard cells, new CDPK mutant phenotypes and a method for improved resolution of stomatal stimulus–response analyses, Ann Bot. 109 (2012) 5–17. doi:10.1093/aob/mcr252.

[256] Y. Yang, A. Costa, N. Leonhardt, R.S. Siegel, J.I. Schroeder, Isolation of a strong Arabidopsis guard cell promoter and its potential as a research tool, Plant Methods. 4 (2008) 6. doi:10.1186/1746-4811-4-6.

[257] P.S. Shacklock, N.D. Read, A.J. Trewavas, Cytosolic free calcium mediates red light-induced photomorphogenesis, Nature. 358 (1992) 753–755. doi:10.1038/358753a0.

[258] I.D. Volotovski, S.G. Sokolovsky, E.L. Nikiforov, V.P. Zinchenko, Calcium oscillations in plant cell cytoplasm induced by red and far-red light irradiation, Journal of Photochemistry and Photobiology B: Biology. 20 (1993) 95–100. doi:10.1016/1011-1344(93)80137-X.

[259] W.R. Briggs, J.M. Christie, Phototropins 1 and 2: versatile plant blue-light receptors, Trends in Plant Science. 7 (2002) 204–210. doi:10.1016/S1360-1385(02)02245-8.

[260] X. Zhao, Y.-L. Wang, X.-R. Qiao, J. Wang, L.-D. Wang, C.-S. Xu, X. Zhang, Phototropins Function in High-Intensity Blue Light-Induced Hypocotyl Phototropism in Arabidopsis by Altering Cytosolic Calcium, Plant Physiology. 162 (2013) 1539–1551. doi:10.1104/pp.113.216556.

[261] G.J. Allen, S.P. Chu, C.L. Harrington, K. Schumacher, T. Hoffmann, Y.Y. Tang, E. Grill, J.I. Schroeder, A de®ned range of guard cell calcium oscillation parameters encodes stomatal movements, 411 (2001) 5.

[262] S. Gilroy, M.D. Fricker, N.D. Read, A.J. Trewavas, Role of Calcium in Signal Transduction of Commelina Guard Cells., The Plant Cell. 3 (1991) 333–344. doi:10.1105/tpc.3.4.333.

[263] G.J. Allen, Alteration of Stimulus-Specific Guard Cell Calcium Oscillations and Stomatal Closing in Arabidopsis det3 Mutant, Science. 289 (2000) 2338–2342. doi:10.1126/science.289.5488.2338.

[264] B. Klüsener, J.J. Young, Y. Murata, G.J. Allen, I.C. Mori, V. Hugouvieux, J.I. Schroeder, Convergence of Calcium Signaling Pathways of Pathogenic Elicitors and Abscisic Acid in Arabidopsis Guard Cells, Plant Physiology. 130 (2002) 2152–2163. doi:10.1104/pp.012187.

[265] J.J. Young, S. Mehta, M. Israelsson, J. Godoski, E. Grill, J.I. Schroeder, CO2 signaling in guard cells: Calcium sensitivity response modulation, a Ca2+-independent phase, and CO2 insensitivity of the gca2 mutant, Proc Natl Acad Sci U S A. 103 (2006) 7506–7511. doi:10.1073/pnas.0602225103.

[266] W.L. Araújo, A.R. Fernie, A. Nunes-Nesi, Control of stomatal aperture: A renaissance of the old guard, Plant Signaling & Behavior. 6 (2011) 1305–1311. doi:10.4161/psb.6.9.16425.

[267] X. Zhang, Inhibition of Blue Light-Dependent H+ Pumping by Abscisic Acid through Hydrogen Peroxide-Induced Dephosphorylation of the Plasma Membrane H+-ATPase in Guard Cell Protoplasts, PLANT PHYSIOLOGY. 136 (2004) 4150–4158. doi:10.1104/pp.104.046573.

[268] X. Zhang, A. Takemiya, T. Kinoshita, K. -i. Shimazaki, Nitric Oxide Inhibits Blue Light-Specific Stomatal Opening Via Abscisic Acid Signaling Pathways in Vicia Guard Cells, Plant and Cell Physiology. 48 (2007) 715–723. doi:10.1093/pcp/pcm039.

[269] K.-Y. Park, A Role for Phosphatidylinositol 3-Phosphate in Abscisic Acid-Induced Reactive Oxygen Species Generation in Guard Cells, PLANT PHYSIOLOGY. 132 (2003) 92–98. doi:10.1104/pp.102.016964.

[270] C. Garcia-Mata, L. Lamattina, Abscisic acid (ABA) inhibits light-induced stomatal opening through calcium- and nitric oxide-mediated signaling pathways, Nitric Oxide. 17 (2007) 143–151. doi:10.1016/j.niox.2007.08.001.

[271] J. Yan, N. Tsuichihara, T. Etoh, S. Iwai, Reactive oxygen species and nitric oxide are involved in ABA inhibition of stomatal opening, Plant, Cell & Environment. 30 (2007) 1320–1325. doi:10.1111/j.1365-3040.2007.01711.x.

[272] G.E. Gudesblat, N.D. Iusem, P.C. Morris, Guard cell-specific inhibition of *Arabidopsis MPK3* expression causes abnormal stomatal responses to abscisic acid and hydrogen peroxide, New Phytologist. 173 (2007) 713–721. doi:10.1111/j.1469-8137.2006.01953.x.

[273] M. Haro, C. Solis, G. Molina, L. Otero, J. Bisquert, S. Gimenez, A. Guerrero, Toward Stable Solar Hydrogen Generation Using Organic Photoelectrochemical Cells, J. Phys. Chem. C. 119 (2015) 6488–6494. doi:10.1021/acs.jpcc.5b01420.

[274] D. Thorneycroft, S.M. Sherson, S.M. Smith, Using gene knockouts to investigate plant metabolism, (n.d.) 9.

[275] H. Wu, I. Santana, J. Dansie, J.P. Giraldo, In Vivo Delivery of Nanoparticles into Plant Leaves, Current Protocols in Chemical Biology. 9 (2017) 269–284. doi:10.1002/cpch.29.

[276] N.S. Lewis, D.G. Nocera, Powering the planet: Chemical challenges in solar energy utilization, Proceedings of the National Academy of Sciences. 103 (2006) 15729–15735. doi:10.1073/pnas.0603395103.

[277] J. Newman, P.G. Hoertz, C.A. Bonino, J.A. Trainham, Review: An economic perspective on liquid solar fuels, Electrochem Soc. 159 (2012). doi:10.1149/2.046210jes.

[278] M.R. Shaner, H.A. Atwater, N.S. Lewis, E.W. McFarland, A comparative technoeconomic analysis of renewable hydrogen production using solar energy, Energy Environ. Sci. 9 (2016) 2354–2371. doi:10.1039/C5EE02573G.

[279] Z. Chen, T.F. Jaramillo, T.G. Deutsch, A. Kleiman-Shwarsctein, A.J. Forman, N. Gaillard, R. Garland, K. Takanabe, C. Heske, M. Sunkara, E.W. McFarland, K. Domen, E.L. Miller, J.A. Turner, H.N. Dinh, Accelerating materials development for photoelectrochemical hydrogen production: Standards for methods, definitions, and reporting protocols, Journal of Materials Research. 25 (2010) 3–16. doi:10.1557/JMR.2010.0020.

[280] R. Sathre, J.B. Greenblatt, K. Walczak, I.D. Sharp, J.C. Stevens, J.W. Ager, F.A. Houle, Opportunities to improve the net energy performance of photoelectrochemical water-splitting technology, Energy Environ. Sci. 9 (2016) 803–819. doi:10.1039/C5EE03040D.

[281] L.M. Peter, K.G.U. Wijayantha, Photoelectrochemical Water Splitting at Semiconductor Electrodes: Fundamental Problems and New Perspectives, ChemPhysChem. 15 (2014) 1983–1995. doi:10.1002/cphc.201402024.

[282] J. Li, N. Wu, Semiconductor-based photocatalysts and photoelectrochemical cells for solar fuel generation: a review, Catal. Sci. Technol. 5 (2015) 1360–1384. doi:10.1039/C4CY00974F.

[283] M.G. Walter, E.L. Warren, J.R. McKone, S.W. Boettcher, Q. Mi, E.A. Santori, N.S. Lewis, Solar Water Splitting Cells, Chemical Reviews. 110 (2010) 6446–6473. doi:10.1021/cr1002326.

[284] J.W. Ager, M.R. Shaner, K.A. Walczak, I.D. Sharp, S. Ardo, Experimental demonstrations of spontaneous, solar-driven photoelectrochemical water splitting, Energy Environ. Sci. 8 (2015) 2811–2824. doi:10.1039/C5EE00457H.

[285] S. Bellani, M.R. Antognazza, F. Bonaccorso, Carbon-Based Photocathode Materials for Solar Hydrogen Production, Advanced Materials. (2018). doi:10.1002/adma.201801446.

[286] H.J. Son, B. Carsten, I.H. Jung, L. Yu, Overcoming efficiency challenges in organic solar cells: rational development of conjugated polymers, Energy Environ. Sci. 5 (2012) 8158–8170. doi:10.1039/C2EE21608F.

[287] G. Ding, J. Yuan, X. Huang, Z. Liu, G. Shi, S. Shi, J. Ding, H.-Q. Wang, W. Ma, Efficient all polymer solar cells employing donor polymer based on benzo[1,2-b:4,5-b']dithiophene unit, AIP Advances. 5 (2015) 117126. doi:10.1063/1.4935870.

[288] R. Søndergaard, M. Hösel, D. Angmo, T.T. Larsen-Olsen, F.C. Krebs, Roll-to-roll fabrication of polymer solar cells, Materials Today. 15 (2012) 36–49. doi:10.1016/S1369-7021(12)70019-6.

[289] H. Sirringhaus, 25th Anniversary Article: Organic Field-Effect Transistors: The Path Beyond Amorphous Silicon, Advanced Materials. 26 (2014) 1319–1335. doi:10.1002/adma.201304346.

[290] O. Ostroverkhova, Organic Optoelectronic Materials: Mechanisms and Applications, Chem. Rev. 116 (2016) 13279–13412. doi:10.1021/acs.chemrev.6b00127.

[291] A. Guerrero, M. Haro, S. Bellani, M.R. Antognazza, L. Meda, S. Gimenez, J. Bisquert, Organic photoelectrochemical cells with quantitative photocarrier conversion, Energy Environ. Sci. 7 (2014) 3666–3673. doi:10.1039/C4EE01775G.

[292] G. Suppes, E. Ballard, S. Holdcroft, Aqueous photocathode activity of regioregular poly(3-hexylthiophene), Polym. Chem. 4 (2013) 5345–5350. doi:10.1039/C3PY00143A.

[293] O.A. El-Rashiedy, S. Holdcroft, Photoelectrochemical properties of poly (3-alkylthiophene) films in aqueous solution, The Journal of Physical Chemistry. 100 (1996) 5481–5484.

[294] T. Abe, M. Ichikawa, T. Hikage, S. Kakuta, K. Nagai, Relationship between the morphology of poly(3-hexylthiophene)/methanofullerene composite and its photoelectrode characteristics in the water phase, Chemical Physics Letters. 549 (2012) 77–81. doi:10.1016/j.cplett.2012.08.053.

[295] S. Yang, L. Fan, S. Yang, Langmuir−Blodgett Films of Poly(3-hexylthiophene) Doped with the Endohedral Metallofullerene Dy@C82: Preparation, Characterization, and Application in Photoelectrochemical Cells, J. Phys. Chem. B. 108 (2004) 4394–4404. doi:10.1021/jp0375618.

[296] G. Dennler, M.C. Scharber, C.J. Brabec, Polymer-Fullerene Bulk-Heterojunction Solar Cells, Advanced Materials. 21 (2009) 1323–1338. doi:10.1002/adma.200801283.

[297] B.E. Conway, B.V. Tilak, Interfacial processes involving electrocatalytic evolution and oxidation of H2, and the role of chemisorbed H, Electrochimica Acta. 47 (2002) 3571–3594. doi:10.1016/S0013-4686(02)00329-8.

[298] T. Bourgeteau, D. Tondelier, B. Geffroy, R. Brisse, R. Cornut, V. Artero, B. Jousselme, Enhancing the Performances of P3HT:PCBM–MoS$_3$ -Based H$_2$ -Evolving Photocathodes with Interfacial Layers, ACS Applied Materials & Interfaces. 7 (2015) 16395–16403. doi:10.1021/acsami.5b03532.

[299] M. Vasilopoulou, A.M. Douvas, D.G. Georgiadou, L.C. Palilis, S. Kennou, L. Sygellou, A. Soultati, I. Kostis, G. Papadimitropoulos, D. Davazoglou, P. Argitis, The Influence of Hydrogenation and Oxygen Vacancies on Molybdenum Oxides Work Function and Gap States for Application in Organic Optoelectronics, Journal of the American Chemical Society. 134 (2012) 16178–16187. doi:10.1021/ja3026906.

[300] J. Azevedo, L. Steier, P. Dias, M. Stefik, C.T. Sousa, J.P. Araújo, A. Mendes, M. Graetzel, S.D. Tilley, On the stability enhancement of cuprous oxide water splitting photocathodes by low temperature steam annealing, Energy Environ. Sci. 7 (2014) 4044–4052. doi:10.1039/C4EE02160F.

[301] B. Seger, D.S. Tilley, T. Pedersen, P.C.K. Vesborg, O. Hansen, M. Grätzel, I. Chorkendorff, Silicon protected with atomic layer deposited TiO2: durability studies of photocathodic H2 evolution, RSC Advances. 3 (2013) 25902. doi:10.1039/c3ra45966g.

Dissemination

Publication list

- **G. Tullii**, F. Galeotti, F. Lodola, C. Bossio, F. Giona, S. Bonfadini, A. Desii, M. Pasini, C. Verpelli, C. Sala, L. Criante, M.R. Antognazza, *High Aspect Ratio semiconducting polymer pillars for 3D cell cultures*, *in preparation*

- **G.Tullii**, S. Donini, F. Galeotti, C.Bossio, E. Parisini, M. Pasini, M.R. Antognazza, *Micro and nano-patterned silk substrates for antifouling applications*, *in preparation*

- **G.Tullii**, A. Costa, M.R. Antognazza, *Conjugated polymer-mediated optical control of stomatal aperture in Arabidopsis Thaliana plants*, *in preparation*

- F. Lodola, V. Rosti, **G. Tullii**, A. Desii, L. Tapella, D. Lim, F. Moccia, M. R. Antognazza, *Conjugated polymers optically regulate the fate of Endothelial Colony Forming Cells, submitted to Science Advances.*

- **G. Tullii**, A. Desii, C. Bossio, S. Bellani, M. Colombo, N. Martino, M.R. Antognazza, G. Lanzani, *Bimodal functioning of a mesoporous, light sensitive polymer/electrolyte interface,* Org. Electron. 46 (2017) 88–98. doi:10.1016/j.orgel.2017.04.007

- C. Bossio, I. Abdel Aziz, **G. Tullii**, E. Zucchetti, D. Debellis, M. Zangoli, F. Di Maria, G. Lanzani, M.R. Antognazza, *Photocatalytic Activity of Polymer Nanoparticles Modulates Intracellular Calcium Dynamics and Reactive Oxygen Species in HEK-293 Cells*, Frontiers in Bioengineering and Biotechnology. 6 (2018). doi:10.3389/fbioe.2018.00114

- F. Lodola, N. Martino, **G. Tullii**, G. Lanzani, M.R. Antognazza, *Conjugated polymers mediate effective activation of the Mammalian Ion Channel Transient Receptor Potential Vanilloid 1*, Sci. Rep. 7 (2017). doi:10.1038/s41598-017-08541-6

- S. Bellani, L. Najafi, **G. Tullii**, A. Ansaldo, R. Oropesa-Nuñez, M. Prato, M. Colombo, M.R. Antognazza, F. Bonaccorso, *ITO nanoparticles break optical transparency/high-areal capacitance trade-off for advanced aqueous supercapacitors*, Journal of Materials Chemistry A. 5 (2017) 25177–25186. doi:10.1039/C7TA09220B

- F. Fumagalli, S. Bellani, M. Schreier, S. Leonardi, H.C. Rojas, A. Ghadirzadeh, **G. Tullii**, A. Savoini, G. Marra, L. Meda, M. Grätzel, G. Lanzani, M.T. Mayer, M.R. Antognazza, F. Di Fonzo, *Hybrid organic–inorganic H_2-evolving photocathodes: understanding the route towards high performance organic photoelectrochemical water splitting*, J Mater Chem A. 4 (2016) 2178–2187. doi:10.1039/C5TA09330A

- H.C. Rojas, S. Bellani, F. Fumagalli, **G. Tullii**, S. Leonardi, M.T. Mayer, M. Schreier, M. Grätzel, G. Lanzani, F.D. Fonzo, M.R. Antognazza, *Polymer-based photocathodes with a solution-processable*

cuprous iodide anode layer and a polyethyleneimine protective coating, Energy Environ. Sci. (2016). doi:10.1039/C6EE01655C

- R. María Girón, J. Marco-Martínez, S. Bellani, A. Insuasty, H. Comas Rojas, **G. Tullii**, M.R. Antognazza, S. Filippone, N. Martín, *Synthesis of modified fullerenes for oxygen reduction reactions,* J Mater Chem A. 4 (2016) 14284–14290. doi:10.1039/C6TA06573B

Conference presentations

- POSTER CONTRIBUTION: **G. Tullii** , A. Desii, C. Bossio, S. Bellani, N. Martino, M.R. Antognazza, G. Lanzani, *Bimodal functioning of a mesoporous, light sensitive polymer/electrolyte interface*, OrBItaly – Organic BIoelectronics Italy, 17-19 october 2018, Milan, Italy.

- ORAL CONTRIBUTION: **G. Tullii** , A. Desii, C. Bossio, S. Bellani, N. Martino, M.R. Antognazza, G. Lanzani, *Bimodal functioning of a mesoporous, light sensitive polymer/electrolyte interface*, 10th International Symposium on Flexible Organic Electronic, ISFOE17, 3-6 july 2017, Thessaloniki, Geece.

- ORAL CONTRIBUTION: **G. Tullii**, C. Bossio, S. Bellani, M.R. Antognazza, G. Lanzani, *Device engineering for the study of optical excitation of living cells,* International Winter school on Bioelectronics-Bioel2016, Kirchberg in Tirol, Austria, march 12th-19th 2016.